Computer modelling of metal oxides

Mario Burbano

School of Chemistry

Trinity College Dublin

A thesis submitted for the degree of

PhilosophiæDoctor

2014

Declaration

I hereby declare that:

This thesis has not been submitted as an exercise for a degree at this or any other University.

The work contained herein is entirely my own except where otherwise cited, referenced or acknowledged in the text.

I agree that the library of the University of Dublin may at their discretion lend or copy the thesis upon request.

.....

Mario Burbano

February 2014

Trinity College Dublin

Thesis Summary

Metal oxide ceramics constitute a group of inorganic compounds with a rich set of properties that have found use in many technological applications of present relevance. Defects in the crystalline structure of these materials account for some of their more attractive characteristics. The properties and compounds that are central to this work are the ionic conductivity in cerium dioxide electrolytes and the combination of a high electronic conductivity with transparency in cadmium oxide. The evolution of these attributes in the presence of defects are investigated using both first principles and interaction potential methods.

The optimization of the ionic conductivity in CeO_2-based electrolytes was initially approached by studying the interactions between the defects introduced upon doping CeO_2 with Y, using newly developed interaction potentials, as well as, neutron diffraction data. The advent of more advanced methods of first principles calculations made it possible to simulate the f-electrons in lanthanide elements, such as, Nd, Sm and Gd. Subsequently, a library interaction potentials was constructed for CeO_2 and ZrO_2 doped with the rare earth elements Sc, Y, La, Nd, Sm and Gd.

Furthermore, the ionic conductivity was investigated in ternary mixtures of CeO_2 electrolytes using the elements from the library of interaction potentials and the results were put in the context of contradicting reports regarding the merits of such solid solutions. This work was expanded to comprise other industrially relevant solid solutions like CeO_2-ZrO_2-Ce_2O_3, which under specific growth environments are known to display cation ordering and high oxygen storage capacities.

Lattice strain is widely recognized as one of the best ways to improve the ionic conductivity of solid electrolytes, however the magnitude of the changes undergone is still in dispute. For this reason, the work on CeO_2 conductivity was concluded with an examination of how this property is

affected by strain. These studies were performed on thin slabs which were subjected to varying amounts of strain in order to simulate the different levels of lattice mismatch.

The second type of ceramic material that was considered in this thesis was that of transparent conducting oxides, in particular, cadmium oxide. The work presented here clarifies the nature of the intrinsic defects that dominate the electronic conductivity in this material, along with the role of hydrogen as an adventitious dopant. This work is concluded with the search for the best donor dopants for cadmium oxide, with the aim to increase transparency and electronic conductivity.

Acknowledgements

Foremost, I would like to thank my supervisor, Prof. Graeme W. Watson. He has provided me with a great deal of insight regarding every aspect of my work. I would also like to thank all the people who were members of the Watson group while I was there, especially Dr. Dario Marrocchelli, Dr. Jeremy P. Allen and Dr. David Scanlon for helpful discussions and suggestions. This work was part of a collaboration with Dr. Stephen Hull, Dr. Stephan T. Norberg and Prof. Paul A. Madden.

''Wovon man nicht sprechen kann, darüber muß man schweigen."
Ludwig Wittgenstein

Contents

List of Figures

List of Tables

Glossary

η	Thermostat position
μ_{A}	Chemical potential of species A
μ_i^{α}	Dipole moment of species i along the Cartesian axis α
E_a	Activation energy
E_F	Fermi level
E_g	Energy band gap
E_g^{dir}	Direct band gap
E_g^{ind}	Indirect band gap
E_g^{FS}	Fermi level stabilization energy
E_g^{MB}	Moss-Burnstein shift
E_g^{opt}	Optical band gap
k_b	Boltzmann constant
NPT	Isothermal-isobaric ensemble
NVE	Microcanonical ensemble
NVT	Canonical ensemble
$V_{\mathrm{O}}^{\cdot\cdot}$	Oxygen vacancy with a net double positive charge
ASR	Area Specific Resistance
B88	Becke 1988 exchange correlation functional
BCC	Body Centred Cubic

BO	Born-Oppenheimer Approximation
BZ	Brillouin zone
CBM	Conduction Band Minimum
CCV	Charge Compensating Vacancy
Ce'_{Ce}	Ce^{3+} cation in its lattice site with a net negative charge
Ce^{x}_{Ce}	Ce^{4+} cation in its lattice site with a neutral charge
CG	Conjugate Gradients
CHP	Combined Heat and Power
CI	Configuration Interaction
CN	Coordination number
CZO	Ceria-Zirconia solid solutions
DFT	Density Functional Theory
DIPPIM	DIPole Polarizable Ion Model
EDOS	Electronic Density Of States
EMF	Electron Motive Force
F	Faraday Constant
FCC	Face Centred Cubic
GDC	Gadolinium doped Ceria
GGA	Generalized Gradient Approximation
H_i^{AB1}	H interstitial in anion antibonding site 1 Å from an O along the $\langle 111 \rangle$ direction
H_i^{AB2}	H interstitial in anion antibonding site 1 Å from an O along the $\langle 110 \rangle$ direction
H^{BC}	H defect in the bond centred site
h-DFT	Hybrid Density Functional Theory
HC	Hydrocarbons
HF	Hartree-Fock

HK	Hohenberg-Kohn
HOMO	Highest Occupied Molecular Orbital
HP	Hartree product
HSE06	Heyd, Scuseria and Ernzerhof hybrid exchange correlation functional
I	Electric current
ICE	Internal Combustion Engine
IP	Interaction Potential
KS	Kohn-Sham
LCAO	Linear Combination of Atomic Orbitals
LDA	Local Density Approximation
LDC	Lanthanum doped Ceria
LSM	Lanthanum Strontium Manganate
LUMO	Lowest Unoccupied Molecular Orbital
LYP	Lee, Yang, Parr exchange correlation functional
MC	Monte-Carlo
MD	Molecular Dynamics
MIGRAD	Function minimization program based on the variable metric method
MINUIT	Function minimization and error analysis program
MLWF	Maximally Localized Wannier Function
MOCVD	Metal Organic Chemical Vapour Deposition
MP	Møller-Plesset perturbation theory
MSD	Mean Square Displacement
NDC	Neodymium doped Ceria
NN	Nearest Neighbour
NNN	Next Nearest Neighbour

O_O^x	O^{2-} anion in its lattice site with a neutral charge
O_i^{per}	Peroxide-like oxygen interstitial defect
OCV	Open Circuit Voltage
OSC	Oxygen Storage Capacity
OSM	Oxygen Storage Material
p_ϵ	Barostat momentum
p_η	Thermostat momentum
PAW	Projector Augmented Wave
PBE	Perdew, Burke and Ernzerhof exchange correlation functional
PBE0	Perdew, Burke and Ernzerhof hybrid exchange correlation functional
PEDOS	Projected Electronic Density Of States
PEMFC	Polymer Electrolyte Membrane Fuel Cell
PES	Potential Energy Surface
PW91	Perdew and Wang exchange correlation functional
Q	Thermostat effective mass
QM	Quantum Mechanics
RDF	Radial Distribution Function
RE	Rare Earth elements - Lanthanides plus Sc and Y
REDC	Rare Earth doped ceria
RMC	Reverse Monte Carlo
RS	Rock salt
SC	Simple cubic
ScDc	Scandium doped Ceria
SCF	Self-consistent field
SIE	Self Interaction Error

SmDC	Samarium doped Ceria
SOFC	Solid Oxide Fuel Cell
STO	Strontium Titanate
TLD	Transition Level Diagram
TWC	Three Way Catalyst
VASP	Vienna *Ab initio* Simulation Package
VBM	Valence Band Maximum
WC	Wannier Centre
WS	Wigner–Seitz
XC	Exchange-correlation
YDC	Yttrium doped Ceria
YSZ	Yttrium stabilized Zirconia

1

Introduction

1.1 Metal oxides in everyday applications

Geopolitical and environmental concerns surrounding energy uncertainty have become a topic difficult to ignore. It is, therefore, of paramount importance for the present and long term viability of the economy and our lifestyles to find cleaner ways to exploit the resources that are commonly used at present and, to find more efficient means to produce electricity in the medium and long term. Distributed Generation of electricity has been touted by national and international agencies, such as, the Organisation for Economic Co-operation and Development (OECD) [1–3], as a possible means to incorporate nascent technologies into the energy market. Some of these technologies rely on renewable sources, e.g. wind and solar, but they are still severely limited by high production costs. As a result, it is crucial to optimize the components of these devices in order to make them competitive against the current standards. In this regard, the broad grouping of metal oxide compounds offers a wide range of properties that can be exploited by emerging technologies, from energy production and catalysis to the now ubiquitous area of optoelectronic devices. The aim of this thesis is to detail how chemical and physical changes affect the properties of two such compounds, namely cerium dioxide (ceria) and cadmium oxide. In particular, computer simulations are employed in the systematic study of the ionic conductivity of oxide ions in CeO_2 at elevated temperatures, while in the case of CdO, the simulations are used to examine the electronic structure characteristics of this material, as well, as the formation energies of intrinsic and extrinsic defects. The significance of these properties and their everyday applications are highlighted in the following sections of this Chapter.

1.2 Ionic conducting oxides

1.2.1 Solid Oxide Fuel Cells

Solid oxide fuel cells (SOFCs) [4–6] have been put forward as one of the technologies which could potentially play a significant role in the mid- and long-term future of energy conversion. SOFCs possess several advantages over existing technologies [7]. Among them are high fuel efficiencies and low pollutant emissions compared with heat engines, such as, the internal combustion engine (ICE). Standalone SOFCs have efficiencies of ~40% while ICEs operate at ~25%. In addition, SOFCs can be run using a variety of fuels, such as, natural gas, Liquefied Petroleum Gas (LPG), methanol, gasoline and hydrogen. This is a particularly important property given that it opens the possibility for SOFCs to take advantage of the increasing availability of natural gas from hydraulic fracturing, the extensive infrastructure for gasoline storage and delivery, as well as, being able to exploit future developments in the use of hydrogen as a power source. In comparison, Polymer Electrolyte Membrane Fuel Cells (PEMFCs) operate only with pure hydrogen, because any CO present in the fuel mix can poison their platinum electrodes. This represents a serious disadvantage given that hydrogen is currently very expensive to produce and difficult to store, however, PEMFCs continue to attract attention for smaller applications, such as in motor vehicles. In contrast, the relatively high working temperatures of SOFCs mean that platinum is not required as a catalyst in the electrodes and carbon monoxide acts not as a poison to the electrodes but as a fuel when it is oxidized at the anode.

Additional efficiency gains can be achieved because waste heat can be recycled by heating water, as it is done in the case of Combined Heat and Power systems (CHP). The construction of SOFCs also confers them with significant advantages; in this case, their simple and scalable modular designs where a number of units are arranged in stacks without moving parts, which significantly reduces noise pollution and component deterioration due to mechanical failure. This type of design also improves ceramic strength given that the stacks maintain the electrolyte under compressive stress.

All of these advantages make SOFCs a very attractive prospect for energy conversion. However, several challenges remain in order to make these systems economically feasible, such as the optimization of the various components of the stacks shown, in Figure 1.1, i.e. electrolyte, anode, cathode, casings and seals so as to obtain cost-effective

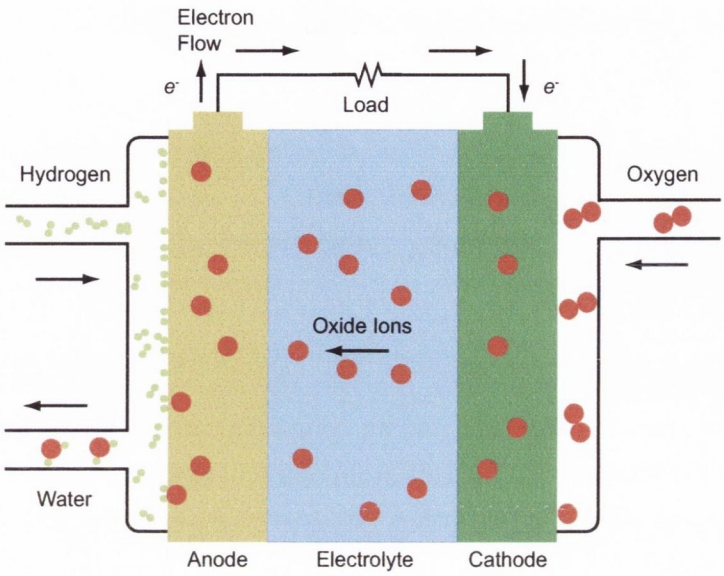

Figure 1.1: Diagramatic representation of a typical SOFC [8]. The cathode (air electrode) is light green, the anode (fuel electrode) is olive and the electrolyte is light blue.

power output per unit area in the systems. However, there are two processes which limit significantly the performance of SOFCs, namely the Oxygen Reduction Reaction (ORR) at the cathode and the ionic conductivity of the electrolyte. Most modern SOFCs use Y_2O_3 doped ZrO_2 (Yttria Stabilized Zirconia - YSZ) as their electrolyte due to its relatively high oxide conductivity; however, this material has the severe drawback of achieving this conductivity only at high working temperatures (around $\sim$1000°C), which brings with it engineering challenges such as different thermal expansion of the various components, corrosion issues, sealing problems and long start-up times. Interest in ceria-based electrolytes stems from their ability to operate at lower temperatures than current technologies. SOFCs function by a series of electrochemical reactions which take place at the electrodes. The cathode (air electrode) catalyzes the oxygen reduction (Equation (1.1)) and it is typically made of an oxide such as lanthanum strontium manganate (LSM).

$$\frac{1}{2}O_2 + 2e^- \rightarrow O^{2-} \tag{1.1}$$

The anode (fuel electrode) catalyses the oxidation of the fuel (Equations (1.2), 1.4 and 1.4), which may be hydrogen, carbon monoxide or a hydrocarbon such as methane

[8, 9]. It is usually a two-phase mixture of nickel and YSZ [9].

$$H_2 + O^{2-} \rightarrow H_2O + 2e^- \tag{1.2}$$

$$CO + O^{2-} \rightarrow CO_2 + 2e^- \tag{1.3}$$

$$CH_4 + 4O^{2-} \rightarrow 2H_2O + CO_2 + 8e^- \tag{1.4}$$

The electrolyte separates the fuel and air compartments in the cell so that the oxide anions generated at the cathode migrate from one side of the cell to the other through the electrolyte. The electric current generated is transported by an external electric circuit, *cf.* the wide variation in oxygen partial pressure from the cathode (0.2 atm) to the anode (1×10^{-15} to 1×10^{-20} atm) makes optimization of these components very difficult and it is the reason why different materials are required for each electrode. Furthermore, in order to obtain high currents from the cell it is necessary that the reactions have fast rates and high fluxes of molecules (porous electrodes), ions and electrons [8].

The Electron Motive Force (EMF) of the cell is determined by the chemical potential of oxygen, which is expressed by the Nernst equation:

$$\mathrm{EMF} = \Gamma \frac{RT}{4F} \ln\left(\frac{p(O_2)_{\mathrm{cathode}}}{p(O_2)_{\mathrm{anode}}}\right) \tag{1.5}$$

where Γ is the ionic transport number of the electrolyte and expresses the ratio of the ionic conductivity with respect to the total conductivity, $\Gamma = \sigma_i/\sigma$, its value should ideally be close to 1, i.e. conductivity is mostly ionic in nature, R is the ideal gas constant, T is the operating temperature, F is the Faraday constant, $p(O_2)_{\mathrm{cathode}}$ and $p(O_2)_{\mathrm{anode}}$ refer to the oxygen partial pressure at the cathode and anode, respectively. The EMF corresponds to the Open Circuit Voltage (OCV) when there is no external circuit connected to the cell.

Figure 1.2 (a) shows the polarization (performance) curve for a typical electrochemical power cell. The voltage drop (η) seen in the low I (current) region (i) includes the contribution from the kinetics of the chemical reactions at the solid-gas interfaces [10]. The flat region (ii) is due to the cell resitance, which includes electrolyte resistance. Region (iii) illustrates the voltage drop at high currents which is caused by depletion of acceptor sites or mobile ions at an interface of the cell. Thus, a high value of σ_i in

the low-σ_i side of the interface increases the power density by displacing region (iii) to higher currents [10]. Thermodynamic stability of the electrolyte to reactions occurring at the electrode/electrolyte and reactant/electrolyte interfaces is determined by the relative positions of the energy levels of reactants and electrodes with respect to the electrolyte's band-gap (E_g). Figure 1.2 (b) shows that the Highest Occupied Molecular Orbital (HOMO) of the reductant (fuel) should be below the energy of the electrolyte's conduction band (E_c), while the Lowest Unoccupied Molecular Orbital (LUMO) of the oxidant (oxygen) should be higher in energy than the valence band (E_v of the electrolyte. Similarly, for the Fermi energies (E_F) of the electrodes, where the E_F for the anode should rise to the value of the HOMO of the reductant while that of the cathode should fall to the level of the oxidant's LUMO [10].

1.2.2 Electrolytes for SOFCs

An ideal electrolyte for SOFC applications should display high ionic conductivity while also being an electronic insulator; this is necessary in order to avoid internal short circuits [11]. In addition, the electrolyte needs to be able to withstand the operational temperature regimes as well as being chemically stable under the oxidizing conditions of the cathode and the strongly reducing conditions of the anode. The total conductivity for these electrolytes is expressed in terms of the electronic (σ_e) and ionic (σ_i) conductivities as $\sigma = \sigma_i + \sigma_e$.

For a given operational temperature the electrolyte of choice should have an Area Specific Resistance ($ASR = R \cdot A = L/\sigma$) below 0.15 $\Omega \cdot$ cm^2, so that for an electrolyte film thickness (L) of 15 μm, the specific ionic conductivity (σ_i) should be higher than 10^{-2} S$\cdot$cm^{-1}. It must also be taken into account that ionic conductivity is a tensor (vector) quantity so its value may vary with direction along a given grain axis, i.e. σ_i is an anisotropic quantity. YSZ achieves this level of conductivity at temperatures above 700°C, whilst doped-ceria electrolytes, such as that produced by Ceres Power, [7] consisting of $Ce_{0.9}Gd_{0.1}O_{1.95}$ (CGO10) can achieve these conductivities at temperatures higher than 500°C for films of 10-30μm in thickness. The work presented in this thesis examines the factors that affect ionic conductivity in Rare Earth (RE) doped ceria (REDC) and its possible role as the electrolyte in SOFCs that operate at intermediate temperatures (IT-SOFCs), i.e., 500 - 800°C. This lower working temperature range means that standard stainless steel can be used for many of the balance-of-plant components, thus bringing down production costs. Therefore, the optimization of electrolytes for SOFCs must take into account ease of fabrication as well as the parameters

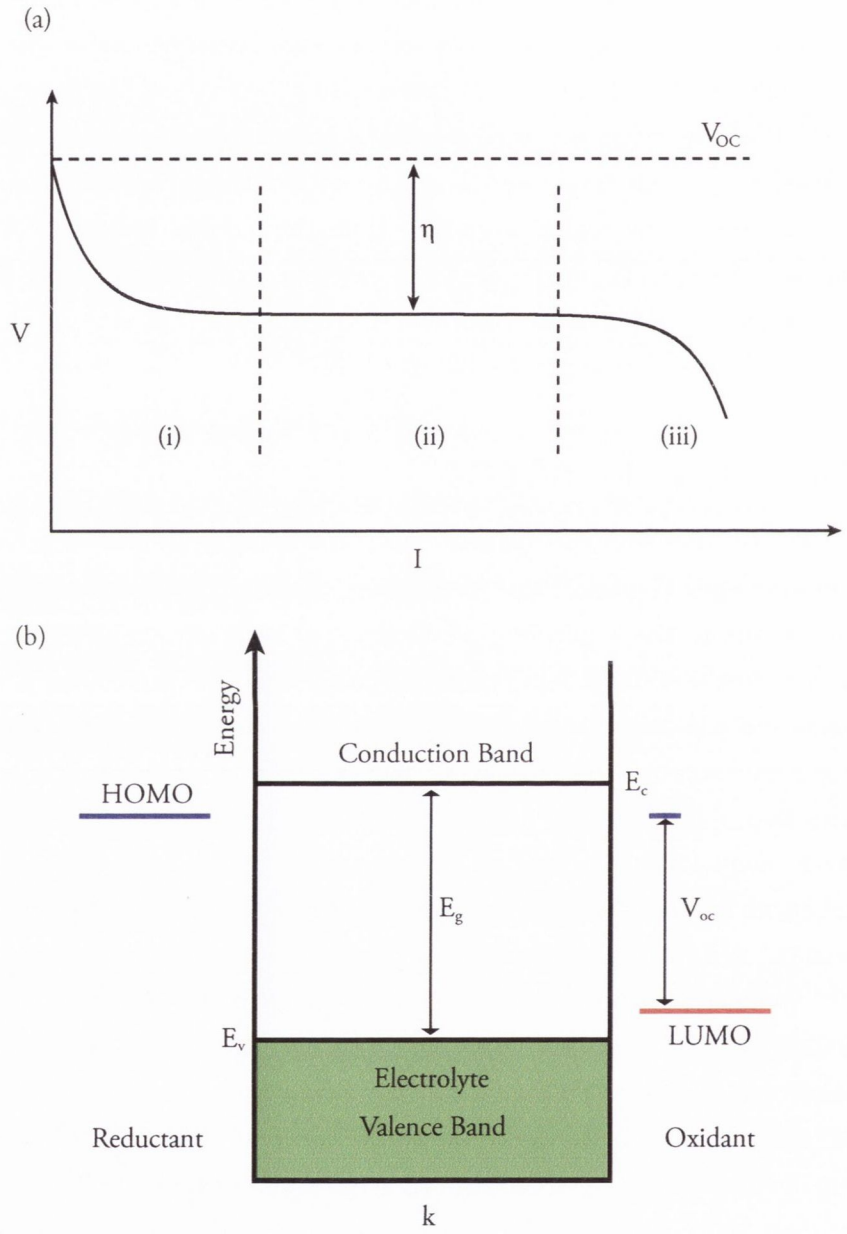

Figure 1.2: (a) Performance curve for a typical electrochemical power cell. [10] (b) Idealized (flat-band) band structure of a thermodynamically stable electrolyte. Note that the reactant energies lie within the electrolyte "window" (E_g - band gap) [10].

determining the ASR, i.e. the film should be as thin as possible (small L), yet strong enough to be durable, with high O^{2-} conductivity and a large area [10].

The very low oxygen partial pressures ($\log_{10}p(O_2)\sim$ -20) found at the fuel side electrode (anode) of SOFCs have detrimental effects on ceria-based electrodes and the electrolytes given the tendency for ceria to be reduced ($Ce^{4+} \rightarrow Ce^{3+}$) under these conditions:

$$2Ce_{Ce}^{x} + O_{O}^{x} \leftrightarrow V_{O}^{\cdot\cdot} + \frac{1}{2}O_2 + 2Ce_{Ce}^{'} \tag{1.6}$$

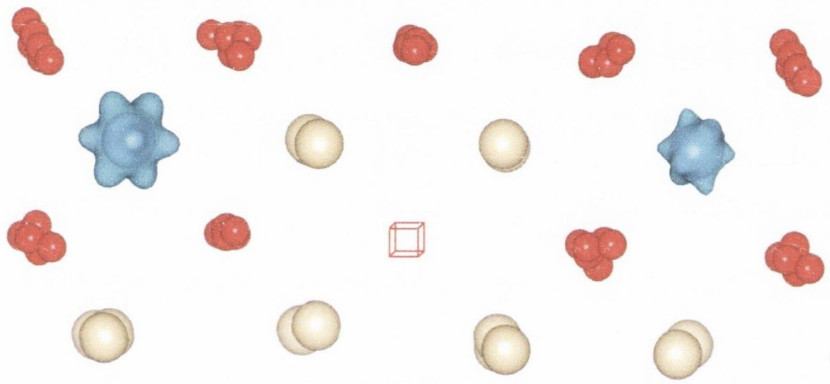

Figure 1.3: Spin density in the vicinity of an oxygen vacancy (hollow red cube) illustrates the localization of an electron in the Ce $4f$ states for Ce^{3+} (blue). Ce^{4+} ions are shown in beige and O^{2-} in red.

Where the Kröger-Vink symbols $Ce_{Ce}^{x} + O_{O}^{x}$ indicate that both the Ce^{4+} and O^{2-} are in their lattice sites, while $V_{O}^{\cdot\cdot}$ represents a vacancy in an oxygen position with a net charge of +2 and $Ce_{Ce}^{'}$ indicates that a Ce^{3+} cation is present in a Ce^{4+} lattice position, with a net negative charge. The formation of Ce^{3+} (see Figure 1.3), whose ionic radius is larger than that of Ce^{4+} (1.11 and 0.97 Å, respectively), can lead to increased lattice strain as well as increased electronic conductivity due to polaronic hopping of the $4f$ electrons [11–17]. Increased dopant concentration enhances the reduction of cerium ions for a given oxygen partial pressure. In some cases, the electronic conductivity can be considerably higher than ionic conductivity [18], where the value for the latter is 7×10^{-2} S cm^{-1} at 1000°C for pure reduced ceria (CeO_{x-1}) while the total conductivity is 2.5×10^{-1} S cm^{-1} at 1000°C. The lattice strain and relaxation caused by the formation of Ce^{3+} and additional anion vacancies due to doping can produce large stresses

and structural failure at high temperatures [7, 19–22]. However, the principal motivation for using ceria-based electrolytes is that they provide high oxide conductivities at intermediate temperatures, thus if the operating temperature is maintained within 500-600 °C the problems associated with the reduction of Ce^{4+} can be averted, according to studies by Steele [12] and Goodenough [10].

1.2.3 Thermodynamics of oxide ion mobility

The ionic conductivity (σ_i) in ceria, and other materials, can be expressed by a classical model as an Arrhenius-type equation:

$$\sigma_i = A_0/T \exp\left(-\frac{E_a}{k_B T}\right) \tag{1.7}$$

where E_a represents the activation energy of oxygen vacancy diffusion, T is the temperature, k_B is the Boltzman constant and A_0 is the composition-dependent pre-exponential factor [12, 23]. Materials with a low E_a value are better ionic conductors at low temperature regimes. One can divide E_a into different component parts with a direct physical meaning related to the lattice strain caused by the presence of defects and others which account for interactions of the form cation-cation, cation-vacancy and vacancy-vacancy, the effect of which depends on a balance between electostatic (charge-charge) and elastic interactions [24]. In this way, the ionic conductivity in pure ceria is divided into E_f, the vacancy formation energy and E_m, the migration barrier, so that:

$$E_a = E_f + E_m \tag{1.8}$$

When ceria is doped with trivalent (aliovalent) cations, such as RE^{3+}, oxygen vacancies form in order to counteract the charge imbalance. [25, 26] This process is expressed in Kröger-Vink notation as follows:

$$RE_2O_3 + 2Ce_{Ce}^{x} + O_O^{x} \rightarrow 2RE_{Ce}^{'} + V_O^{\cdot\cdot} + 2CeO_2 \tag{1.9}$$

Equation (1.9) shows that one oxygen vacancy is formed for every two trivalent metal cations. It would, therefore, be expected that the highest ionic conductivity for

doped ceria should be observed when $[V_{\ddot{O}}] = 0.5$ in

$$\sigma_i = A_0'/T[V_{\ddot{0}}]\,(1 - [V_{\ddot{O}}])\exp\left(-\frac{E_a}{k_B T}\right) \tag{1.10}$$

because this would maximize the number of charge carriers available. However, in practice it is observed that the peak in conductivity occurs at much lower concentrations, whose value depends on the dopant used. It is the nature of the dopant which determines the extent to which the various components of E_a affect the ionic conductivity of doped ceria. In its simplest form, the dopant-vacancy interaction can be thought of as that between two dopant cations with a single charge compensating vacancy (CCV) (Equation 1.11), however at large dopant concentrations larger dopant-rich nano domains are expected [27].

$$2\mathrm{RE}'_{\mathrm{Ce}} + \mathrm{V}^{\cdot\cdot}_{\mathrm{O}} \rightarrow \left((\mathrm{Re}'_{\mathrm{Ce}})_2\mathrm{V}^{\cdot\cdot}_{\mathrm{O}}\right)^{\mathrm{x}} \tag{1.11}$$

This association represents a barrier to migration in doped ceria and it is dependent on the charge, size and geometry of the dopant cations. There is, therefore, a trade-off between the increased number of oxygen vacancies formed by doping and the increased migration barrier caused by the presence of dopants. This defect association has been reported to be significant at temperatures up to 1000 K. [12] The detrimental effect of cation-vacancy association is coupled to the presence of dopant-concentration dependent resistivity at grain boundaries, thus making it necessary to separate the components of the total ionic conductivity (σ_{tot}) into lattice conductivity (σ_{lc}) and boundary conductivity (σ_{bc}), which is, unfortunately, something omitted in some of the literature [28] and which leads to wide variation in optimal dopant concentration values reported. Lattice and grain boundary contributions to ionic conductivity can be separated through the use of impedance spectroscopy methods. The sintering temperature at which the ceramics are fabricated will also affect the extent of dopant segregation, and with it the ionic conductivity of the material. [12] Furthermore, the presence of resistive grain boundaries may also have an effect on electronic conductivity and their presence may obscure the full effect of co-dopants used when preparing new electrolyte materials [12].

It has been reported, that at temperatures up to 1000 K, a plot of σT Vs $1/T$ should be curved, i.e. it displays two different slopes, because the effective vacancy

concentration in the lower temperature regime ($[V_O^{\cdot\cdot}]$) is lower than expected for a given composition of the systems $Ce_{1-x}RE_xO_{2-x/2}$ due to cation-vacancy and vacancy-vacancy association [12], while in the high temperature regime, these clusters become separated.

1.2.4 Three Way Catalysts

The advent of tighter regulations on the emissions from motor vehicles has spurred a great deal of interest in the development of catalytic materials. Ceria-zirconia solid solutions (CZO) constitute integral components of Three Way Catalysts (TWC), which are used to treat exhaust fumes [29, 30]. TWCs convert CO, NO_x and hydrocarbon (HC) gases into the less harmful CO_2, N_2 and H_2O according to the following redox reactions [31]:

$$CO + H_2O \rightarrow CO_2 + H_2 \tag{1.12}$$

$$2CO + O_2 \rightarrow 2CO_2 \tag{1.13}$$

$$C_nH_{2n+2} + \left(\frac{3n+1}{2}\right) O_2 \rightarrow nCO_2 + (n+1)\,H_2O \tag{1.14}$$

$$2H_2 + O_2 \rightarrow 2H_2O \tag{1.15}$$

$$2NO_2 \rightarrow N_2 + 2O_2 \tag{1.16}$$

$$2CO + 2NO \rightarrow N_2 + 2CO_2 \tag{1.17}$$

A stoichiometric air-to-fuel ratio is required for optimal conversion, but variations can be compensated by the use of oxygen storage materials (OSM) which act as oxygen buffers. Keeping the ratio of air to fuel within a narrow band (between 14.6:1 and 14.8:1 air:fuel) allows the metal catalyst to work at high levels of efficiency. Under operating conditions CZO releases oxygen in fuel-rich conditions through the reduction mechanism indicated in Equation 1.6, while in fuel-lean conditions the reverse takes place and the cerium cations are re-oxidized with the subsequent absorption of oxygen.

The construction of a typical monolithic TWC is depicted in Figure 1.4 [31]. In this device the exhaust gases pass through a ceramic material, which takes the form of a honeycomb-like structure in order to maximize its surface area. This ceramic block is covered with a thin coating of platinum, palladium, or rhodium and mounted on a stainless steel casing that is attached to the exhaust manifold. Given its role in TWCs, it is crucial that the processes of CZO reduction/oxidation occur rapidly as well as reversibly and, that oxygen be efficiently transported between the surface and the bulk, which means that the material should possess a fast ionic conductivity of this material.

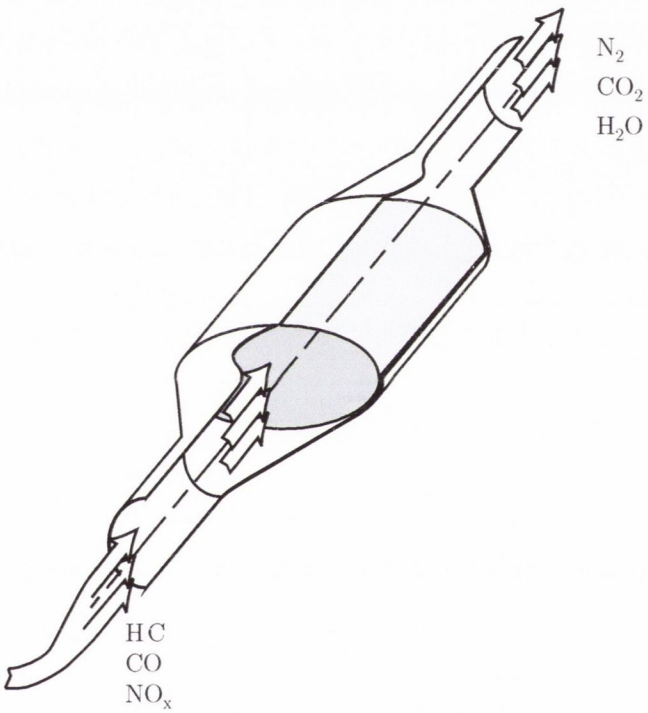

Figure 1.4: Schematic of a monolithic three-way catalyst [31].

1.3 Transparent Conducting Oxides

Transparent conducting oxides (TCOs) are compounds which combine the normally mutually exclusive properties of transparency and conductivity. Most highly transparent materials, such as glass, behave as insulators with high electrical resistivities of $> 10^{10}\,\Omega\,\mathrm{cm}$, whereas materials with low resistivities ($10^{-4} - 10^{-7}\,\Omega\,\mathrm{cm}$), such as

metals, do not transmit visible light. The combination of both properties in a single material is thus quite an unusual phenomenon and TCOs have proved indispensable in the development of optoelectronic devices such as solar cells, flat panel displays and light emitting diodes [32–35]. In practice, the combination of high conductivities and optical transparency entails some level of compromise. For example, the current industry standard n-type TCO is In_2O_3:Sn (ITO) which usually demonstrates conductivities of $\sim 10^4\,S\,cm^{-1}$, whilst retaining $> 90\,\%$ transparency [36, 37], however, ITO has some drawbacks in that it displays significant absorption in the blue–green region of the visible spectrum and corrosion in organic light-emitting diode (OLED) devices, which are gaining in popularity in the optoelectronics market. The overwhelming demand for ITO, coupled with the low abundance of indium within the earth's crust have made indium an increasingly expensive commodity, which has led to a large research drive to replace ITO as the industry standard TCO [38]. The focus of the TCO work presented here is CdO. Interest in the properties of this material can be dated back as far as 1907, when Badeker first studied its thermoelectric properties [39].

1.3.1 Electronic structure requirements

Figure 1.5 illustrates the band structure of an idealized TCO [40]. The introduction of a deep impurity band (yellow) in the bandgap of an insulating material helps to keep intense interband transitions from the valence band (blue) to the impurity band, represented by Δ_v and, similarly for transitions from the impurity band to the conduction band (red), represented by Δ_c. This requires the band gap of a host material to be more than 6.2 eV, i.e. $\Delta_v = \Delta_c = 3.1$ eV for transparency in the visible range. Furthermore, the impurity band should be narrow enough (less than 1.8 eV) to keep intraband transitions (as well as the plasma frequency) below the visible range [40].

Alternatively, the second conduction band (CBM+1) should be separated from the CBM by greater than 3.1 eV [41]. This large CBM–CBM+1 separation ensures that any donor electrons in the conduction band are not excited by visible light to the next conduction band, and therefore ensures optical transparency, which is vital for device performance. In the case of p-type TCOs, absorption must not occur from bands within ~ 3.1 eV of the VBM to the hole states near the VBM [42, 43].

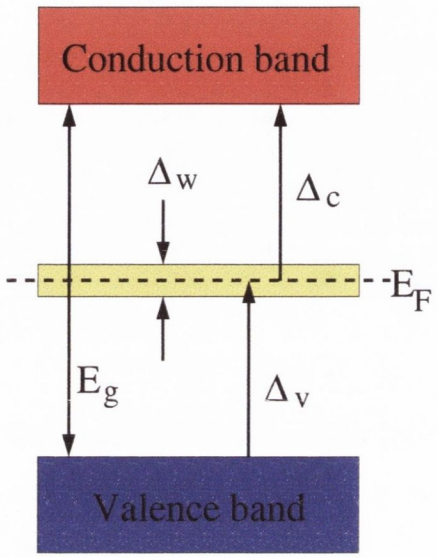

Figure 1.5: Idealized (flat-band) band structure of an ideal TCO (E_g - band gap) [40].

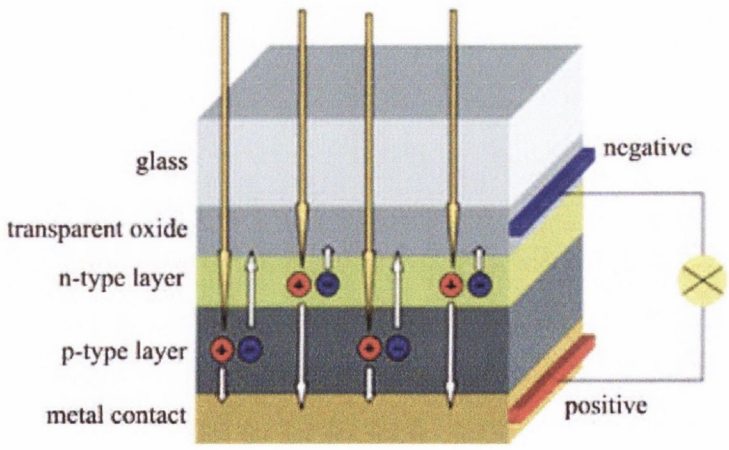

Figure 1.6: Schematic representation of a solar cell.

1.3.2 Transparent *p-n* junctions

A *p-n* junction refers to an interface between two regions in a semiconducting material, one that is doped *n*-type (excess electrons) and another which is doped *p*-type (electron holes). At these boundaries electrons may pass from the *n*-type side to the *p*-type, while holes flow in the opposite direction. These junctions are the basic building blocks of the majority of semiconductor devices, such as, transistors, diodes, integrated circuits, etc. The growing importance of optoelectronic devices over the last decade has meant that a great deal of research is currently devoted to the development of $p-n$ junctions made from TCO materials. While *n*-type TCO materials can be readily produced, as was the case for CdO in 1907, the synthesis of *p*-type TCO counterparts has proved more difficult. In wide band gap oxides, the top of the valence band is predominately composed of oxygen $2p$ states [44]. However, the introduction of positive holes in the valence band edge has little effect on the hole conductivity given that the holes are trapped by nearby oxygens, which prevents their migration. This restricts traditional *p*-type doping approaches [45]. Nevertheless, oxides where the metal possesses a closed shell valence electronic configuration of similar energy to that of oxygen can provide a solution. Interaction between the electronic states of the metal and oxygen result in covalent states at the top of the valence band. This can provide the dispersion required for the effective transport of positive holes. Metals with complete d shells such as Cu and Ag are well suited for this purpose [43, 46, 47]. One possible application of these transparent semiconductors would be a solar cell as shown in Figure 1.6 [48]. This basic scheme shows how sunlight is absorbed upon impacting a thin semiconducting layer. This leads to electron loss from the semiconducting material, with subsequent flow to produce electricity. The most efficient solar cells on the market are based on silicon, which elevates the production costs, and are usually designed around a $p-n$ junction scheme, which allows current flow in only one direction. CdTe, GaAs and SnS are among the candidate thin film materials suggested as possible replacements for silicon [49]. CdO with its metallic-like conductivities could also serve as a possible candidate, however these efforts have been hampered thus far by the fact that no *p*-type CdO has been observed.

1.4 Thesis Outline

The work presented here is divided into two broad categories. Firstly, the study of ionic conductivity in ceria-based electrolytes by detailed analysis of defect interactions and the application of strain to thin slabs of the material. Secondly, a detailed analysis of the intrinsic defects in cadmium oxide, the case of adventitious H-doping, as well as, the study of a number of single electron donors from groups 3, 13 and 17. This Chapter provided the motivation and background to study these materials.

Chapter 2 introduces the underlying theory to be used throughout this work. It follows the broad categories enumerated above in the sense that Interaction Potentials (IP) were the main tool for the study of ionic conductivity in doped ceria, while the the *ab initio* methods were used in the treatment of defects in CdO. Chapter 3 presents the concepts in solid state physics/chemistry that are basic to this work, as well as, the simulation techniques that allow the implementation of the theory from Chapter 2.

Yttrium-doped ceria (YDC) is the first ionic conductor considered in this work. A thorough study of the factors that determine its conductivity is presented in Chapter 4 using simulations and experimental data from our collaborators Dr. Steve Hull and Dr. Stefan Norberg. In addition, the concept of an ideal dopant radius is formulated, as well as, the consequences of doping ceria with one such ideal cation. This chapter also introduces the method of potential fitting that is used to generate IPs from *ab initio* simulations.

Chemical optimization of ceria's ionic conductivity is carried forward to Chapter 4 where a self-consistent IP is used to study the effect of doping ceria with more than one dopant species. The study of ionic conductivity is concluded with an investigation of how this property is affected by elastic strain.

Chapter 7 is devoted to the *ab initio* study of the changes in the electronic structure of CdO that result from defects, as well as, their associated formation energies. These results, are then used to make predictions about the likelihood of producing *p*-type CdO, as well as the determination of the optimal dopant species from a variety of aliovalent cations and an anion, F.

2

Calculation of the energies of microscopic systems

2.1 Intoduction

The chief aim of this thesis is to make use of computer simulation techniques in order to gain a deep understanding of the factors that determine the properties of metal oxides. This chapter details the theories underlying the two branches of simulation employed throughout this work. Section 2.2 introduces the concepts behind Quantum Mechanical (QM) or *ab initio* simulations, while Section 2.3 is concerned with Interaction Potential (IP) simulations.

The principal differentiating factor between these two levels of theory is the way in which electrons are represented. In the case of QM simulations, the electronic wave function is modelled directly by solving the Schrödinger equation. This is in contrast to IP simulations, where the electrons are not considered explicitly; rather, it is their resulting attractive and repulsive interactions which are taken into account. This intrinsic distinction between QM and IP methods has important ramifications for the kinds of problems and the answers that can be accessed by using either technique. For instance, IP simulations are less computer intensive than QM, and thus can be performed on much larger systems; however, IPs are not typically able to account for instances where electronic redistribution occurs.

2.2 Quantum mechanical techniques

2.2.1 Schrödinger Equation

In its time-independent form, the Schrödinger equation (Equation 2.1) provides information about the stationary states (standing waves) of a quantum system [50–52]. Such states are more commonly known as orbitals in atomic or molecular systems and their properties underpin most of what is known about interatomic interactions. This relationship takes the form of a partial differential eigenvalue equation, where E corresponds to the total energy (eigenvalue), Ψ is the wave function (eigenvector) and $\hat{H}$ is the Hamiltonian operator (second-order differential operator):

$$\hat{H}\Psi = E\Psi \tag{2.1}$$

The Hamiltonian consists of kinetic and potential energy operators as shown below:

$$\hat{H} = -\frac{\hbar}{2m}\nabla^2 + V(r) \tag{2.2}$$

and

$$\nabla^2 = \left(\frac{\partial^2}{\partial x^2} + \frac{\partial^2}{\partial y^2} + \frac{\partial^2}{\partial z^2}\right) \tag{2.3}$$

where $\hbar = \frac{h}{2\pi}$, ∇^2 is the Laplacian (Equation 2.3) and $V(r)$ is the configuration-dependent potential energy operator. The wave function obtained from the Schrödinger equation completely describes a quantum system, and thus is fundamental to quantum theory. But despite this central role, it is typically conceived of as an abstract concept with no explicit definition or physical meaning, and although several interpretations exist, it is the Born interpretation of the wave function that is most prevalent in quantum chemistry [53]. This interpretation postulates that Ψ^2 is to be understood as a probability distribution of the particle to which it corresponds. A consequence of this interpretation is that:

$$\int \Psi^* \Psi d\tau = 1 \tag{2.4}$$

In this case Ψ^* is the complex conjugate of the wave function and $d\tau$ indicates integration over all space. Wave functions which satisfy Equation 2.4 are said to be *normalized*. Solutions to the Schrödinger equation are also typically required to be

orthogonal:

$$\int \Psi_m^* \Psi_n d\tau = 0 \ \ (m \neq n) \tag{2.5}$$

The orthonormality (orthogonality and normality) of wave functions is conveniently expressed using Kronecker delta notation:

$$\int \Psi_m^* \Psi_n d\tau = \delta_{mn} \tag{2.6}$$

where

$$\delta_{mn} = \begin{cases} 0 & \text{if } m \neq n \\ 1 & \text{if } m = n \end{cases} \tag{2.7}$$

The crux of the vast majority of quantum chemical methods involves finding solutions to the Schrödinger equation. The various levels of theory available are differentiated from one another by the assumptions and approximations inherent to each. The next sections outline the reasons why these approximations are necessary and introduce some of the most important ones for the purpose of computer simulation.

2.2.2 The Born-Oppenheimer Approximation

The Schrödinger equation can be solved exactly, in terms of an analytical expression, for only a few cases, such as the particle in a box, the harmonic oscillator, the particle on a ring, the particle on a sphere and the hydrogen atom [50, 51]. Common to these examples are the *boundary conditions* imposed on the solutions and the fact that these systems are composed of at most two interacting particles, as in the case of the hydrogen atom. To understand why more complex systems require approximate solutions to the Schrödinger equation it is necessary to first consider the kinetic ($\hat{T}$) and potential energy ($\hat{V}$) terms that are associated with the nuclei (n) and electrons (e) of the system, as shown below:

$$\hat{H} = \hat{T}_n + \hat{V}_{nn} + \hat{T}_e + \hat{V}_{ne} + \hat{V}_{ee} \tag{2.8}$$

which is equivalent to

$$\hat{H} = -\sum_A \frac{1}{2M_A} \nabla_A^2 + \sum_{A<B} \frac{Z_A Z_B}{r_{AB}} - \sum_i \frac{1}{2} \nabla_i^2 - \sum_{i,A} \frac{Z_A}{r_{iA}} + \sum_{i>j} \frac{1}{r_{ij}} \tag{2.9}$$

where the suffixes $A, B, C...$ refer to nuclei, while $i, j, k...$ correspond electrons, Z refers to the nuclear charge and M is the mass. The first term in Equations 2.8 and 2.9 is usually exluded from calculations in what is known as the Born-Oppenheimer (BO) approximation, which attempts to decouple the wave function of a system into nuclear and electronic degrees of freedom:

$$\Psi_{Total} = \psi_n \times \psi_e \tag{2.10}$$

Justification for Equation 2.10 comes from the large mass disparity between electrons and nuclei, which means that the electronic wave function (Ψ_e) depends only on the positions of the much heavier nuclei and not their momenta. In practice this means that the electrons are assumed to be under a constant nuclear potential formed by a fixed atomic configuration ($\hat{V}_{nn}$), and any changes to it can be accommodated rapidly by the electrons. This approximation greatly simplifies the process of obtaining the total energy of a system, because terms like the kinetic energy of the nuclei ($\hat{T}_n$) can be completely excluded from the calculation, while $\hat{V}_{nn}$ need only be updated when there are changes to the geometry, and thus forms part of the external potential of fixed nuclear charges acting on the system of electrons. Therefore, the Hamiltonian becomes:

$$\hat{H} = \hat{T}_e + \mathcal{V}_{ext}\left(\mathbf{R}_A\right) + \hat{V}_{ee} \tag{2.11}$$

Here, $\mathcal{V}$ is the external potential imposed by the nuclear positions ($\mathbf{R}_A$) on a system of N electrons. Despite the simplification achieved by applying this approximation, the many-body nature of the problem still remains. In particular, the quantum correlations that give rise to the electron-electron interactions ($\hat{V}_{ee}$) are not addressed by the BO description of the system. It is, therefore, necessary to introduce further approximations that deal with this problem directly or indirectly.

2.2.3 Hartree self-consistent-field

According to Hartree's self-consistent-field (SCF) model, the motion of each electron in the effective field of the other $N-1$ electrons in the system is governed by a one-particle Schrödinger equation. Self-consistency of the electronic charge distribution with its own electrostatic field leads to a set of coupled integro-differential equations (Hartree equations) for N one-particle wave functions. The resulting total wave function for the

system takes the form of a product of these one-electron wave functions:

$$\Psi\left(x_1, ..., x_N\right) = \chi_i(x_1)\chi_j(x_2)\chi_k(x_3)....\chi_N(x_N) \tag{2.12}$$

where N is the number of electrons. This expression is typically known as the Hartree product (HP), where the terms such as $\chi_i(x_1)$ signify occupancy of spin orbital χ_i by electron 1. The system energy from this wave function is given by:

$$\langle\Psi|\,\hat{H}\,|\Psi\rangle = \epsilon_i + \epsilon_j + \epsilon_k + ...\epsilon_n = E \tag{2.13}$$

In practice, the exact wave function is unknown due to the many-body nature of the problem; hence, the *variational principle* is introduced in order to compare trial wave functions (Ψ_T). This theorem states that the energy obtained from a given Ψ_T is always greater than or equal to the true ground state energy:

$$\langle\Psi_T|\,\hat{H}\,|\Psi_T\rangle = E_T \geq E_0 = \langle\Psi_0|\,\hat{H}\,|\Psi_0\rangle \tag{2.14}$$

By this prescription it is necessary to iteratively improve the trial wave function.

2.2.4 Hartree-Fock Approximation

When written in the from given in Equation 2.12 the wave function does not satisfy the antisymmetry principle of Pauli which requires the sign of the wave function to be inverted when the coordinates of two electrons are interchanged:

$$\Psi\left(x_1, x_2...., x_N\right) = -\Psi\left(x_2, x_1...., x_N\right) \tag{2.15}$$

This problem was addressed by Slater [54], who expressed the wave function not as a simple product, but as a determinant of an orbital matrix:

$$\mathbf{\Psi} = \frac{1}{\sqrt{N!}} \begin{vmatrix} \chi_i(x_1) & \chi_j(x_1) & ... & \chi_N(x_1) \\ \chi_i(x_2) & \chi_j(x_2) & ... & \chi_N(x_2) \\ \vdots & \vdots & \vdots & \vdots \\ \chi_i(x_N) & \chi_j(x_N) & ... & \chi_N(x_N) \end{vmatrix} \tag{2.16}$$

Interchanging electron coordinates is equivalent to swapping two rows of the determinant, which causes the sign to be inverted, as required. Within this approximation

each electron experiences a slightly different potential field, which is obtained from a mean field representation of the electrostatic charges of the system, both positive and negative. In HF, the Hamiltonian is replaced by the Fock operator ($\hat{f}$):

$$\hat{f}_i(1) = \hat{H}^{\text{core}}(1) + \sum_{j=1}^{N} \left\{ \hat{J}_j(1) - \hat{K}_j(1) \right\} \tag{2.17}$$

where the label (1) indicates that the operator is one-electron in nature. The motion of a single electron moving in the field generated by bare nuclei is represented by $\hat{H}^{\text{core}}$:

$$\hat{H}^{\text{core}}(1) = -\frac{1}{2}\nabla_1^2 + \sum_{A=1}^{M} \frac{Z_A}{r_{1A}} \tag{2.18}$$

By applying relationship in Equation 2.17 the Schrödinger equation now becomes:

$$\hat{f}_i(1)\chi_i = \epsilon_i \chi_i \tag{2.19}$$

The interelectron interactions of the system are accounted for by two additional operators, the first of which is the Coulomb operator ($\hat{J}_j(1)$), which describes the average potential due to an electron in χ_j:

$$\hat{J}_j(1) = \int d\tau_2 \chi_j(2) \frac{1}{r_{12}} \chi_j(2) \tag{2.20}$$

The exchange operator ($\hat{K}_j(1)$) is a quantum mechanical effect that arises from the Pauli exclusion principle, which requires that the wave functions of electrons be anti-symmetric. It is defined with respect to its effect on the spin orbital χ_i:

$$\hat{K}_j(1)\chi_i(1) = \left[\int d\tau_2 \chi_j(2) \frac{1}{r_{12}} \chi_i(2) \right] \chi_j(1) \tag{2.21}$$

this term is only non-zero for electrons of the same spin, in which case $\hat{K}_j(1)\chi_i(1)$ is a negative term that lowers the total energy of the system. This is the most computationally intensive part of a HF calculation in practical applications.

2.2.5 Roothan-Hall Equations

Direct solution of the Hartree-Fock equations for complex systems, like molecules, is not practical because of their integro-differential form [51]. Instead, common implementations express them as matrices, which are more amenable to computation. In this approach each spin orbital is represented as a Linear Combination of Atomic Orbitals (LCAO):

$$\chi_i = \sum_{\nu}^{K} c_{\nu i}\phi_\nu \tag{2.22}$$

where ϕ_ν represents the one-electron orbitals typically referred to as *basis functions*, while $c_{\nu i}$ corresponds to the respective coefficient associated with each one of these orbitals. The Roothan-Hall approach incorporates these orbitals into a secular equation as follows:

$$\mathbf{FC} = \mathbf{SCE} \tag{2.23}$$

The $\mathbf{F}$ term corresponds to the $K \times K$ square Fock matrix whose elements correspond to the Fock operators for each electron from Equation 2.17. $\mathbf{S}$ is the overlap matrix that describes the interactions between the elements of basis set. $\mathbf{C}$ is another $K \times K$ matrix and it contains the orbital coefficients $c_\nu i$:

$$\mathbf{C} = \begin{pmatrix} c_{1,1} & c_{1,2} & \cdots & c_{1,K} \\ c_{2,1} & c_{2,2} & \cdots & c_{2,K} \\ \vdots & \vdots & \vdots & \vdots \\ c_{K,1} & c_{K,2} & \cdots & c_{K,K} \end{pmatrix} \tag{2.24}$$

while the diagonal matrix $\mathbf{E}$ contains the orbital energies:

$$\mathbf{E} = \begin{pmatrix} \epsilon_1 & 0 & \ldots & 0 \\ 0 & \epsilon_2 & \ldots & 0 \\ \vdots & \vdots & \vdots & \vdots \\ 0 & 0 & \ldots & \epsilon_K \end{pmatrix} \tag{2.25}$$

2.2.6 Hartree-Fock limitations

The HF method was developed shortly after the introduction of the Schrödinger equation and, from this time onward it positioned itself as one of the most important techniques available to quantum chemists. It performs well at predicting physical

properties, such as equilibrium interatomic distances, bond angles and total energies. However, HF suffers from significant limitations that are related to the fashion in the wave function is described, i.e. by means of a mean-field expressed as a single Slater determinant. This treatment of the wave function neglects instantaneous correlations between the electrons. Thus, contrary to predictions from HF, the probability of finding two of these charged particles close to each other in a real system is lower than would be expected from their overall density. In quantifying the HF error, Lowdin [55] introduced the concept of correlation energy, which is defined as the difference between the true energy of the system and the HF energy:

$$E_{\mathrm{C}} = E_0 - E_{\mathrm{HF}} \tag{2.26}$$

where E_{C} is the correlation energy, E_0 is the exact energy and E_{HF} is the HF energy. Note that this definition uses the variational principle to define the error, see Equation 2.14. By further decomposing this effect it is possible to identify two types of correlation, namely dynamical and non-dynamical correlation. The case of dynamical correlation refers to the way in which the actual motion of electrons affects others in their vicinity. This means that HF is unsuited for the simulation of systems with delocalized states such as metals, and in the case of metallic states, HF is unable to account for the Coulombic screening that results from delocalized electrons. Non-dynamical (static) correlation occurs in systems where the ground state is only described by more than one degenerate determinant and can be accounted for by the inclusion of a small number of excited states close to the highest occupied molecular orbital. Neglecting correlation leads to physically incorrect results, especially close to the dissociation limit, where, for example HF predicts that the electrons in a H_2 molecule would spend equal time on both nuclei, even after the atoms have been fully separated.

Despite accounting for only $\sim 0.1\%$ of the total energy, the E_{C} has a significant impact on the energetics of HF simulations, because this value is similar in magnitude to total energy differences, hence large errors are expected from calculations of cases where electrons are redistributed, i.e. reaction energies and binding energies.

For the purposes of this thesis it is worth noting that HF scales nominally as N^4, where N is the number of basis functions, and although implemented for calculations on periodic systems like those reported throughout this work, it is seldom used nowadays due to its inherent inadequacies. Post-HF methods aim at accounting for electron correlation in a variety of ways. For example, Configuration Interaction (CI) expresses

the many body wave function as a linear combination of determinants, starting with a reference HF wave function and adding several excited states, all of which are weighted by coefficients. Another post-HF method is the Møller-Plesset (MP) perturbation theory, which adds electronic correlation to the HF wave function in the form of small perturbations to the Hamiltonian. These post-HF methods are, however, much more computationally expensive than standard HF, of scaling N^5 and higher depending on the level of theory chosen. This limits their applicability to only small systems, although, increased computer power could change this in the future. In the interim, researchers have sought different methods for the simulation of periodic supercells that are sufficiently large to simulate defects in a realistic manner. One such method is density functional theory, which is the subject of the next section.

2.2.7 Density Functional Theory

The method of Density Functional Theory (DFT) hinges upon the relationship between the electron density of a system and its corresponding energy. This representation has an advantage over HF (see Section 2.2.4) in that the electron density function ($\rho(\mathbf{r})$) used in DFT is an *observable* that is always 3-dimensional, unlike the complex $3N$-dimensional wave functions of HF, where N is the number of electrons. The quantum chemical framework of DFT relevant to this thesis starts with the work by Hohenberg and Kohn [56], who in 1964 derived the theorems that describe the dependence of the total energy on the electron density. They proved that the ground state energy of a system can be written as a functional of the ground state density, $\rho_0(\mathbf{r})$:

$$E_0\left[\rho_0(\mathbf{r})\right] = T\left[\rho_0(\mathbf{r})\right] + E_{ee}\left[\rho_0(\mathbf{r})\right] + E_{Ne}\left[\rho_0(\mathbf{r})\right] \tag{2.27}$$

where $\mathbf{r}$ is the position vector upon which the electronic density depends, $T\left[\rho(\mathbf{r})\right]$ is the kinetic energy, $E_{ee}\left[\rho(\mathbf{r})\right]$ corresponds to the electron-electron interactions and $E_{Ne}\left[\rho(\mathbf{r})\right]$ represents the interactions between nuclei and electrons. In addition, Hohenberg and Kohn showed the existence of a unique ground state electron density and defined the universal density functional, which if known, would contain the information necessary to determine all the ground state properties of a system.

This work was closely followed by that of Kohn and Sham [57], who provided a solution to the Schrödinger equation by writing the theorems that underlie DFT as equations resembling those of HF. In their prescription of DFT, Kohn and Sham (KS) made use of the fact that the electron density is given by the square of the wave

function under the Born interpretation (see Equation 2.4), thus, effectively providing a link between the HF wave function and the method of DFT. They showed that it is possible to devise a fictitious non-interacting system of electrons (uniform electron gas) generated from a HF wave function and which is assumed to have the same density as the fully interacting electron system:

$$\rho_{KS}(\mathbf{r}) = \sum_i \left|\chi^2_{KS}(\mathbf{r})\right| = \rho_{exact}(\mathbf{r}) \tag{2.28}$$

Kohn and Sham introduced the wave function in their definition of DFT, because previous attempts by Thomas-Fermi, Dirac and Slater [58] had failed to properly account for the electronic kinetic energy. Hence, $T_S[\rho(\mathbf{r})]$ corresponds to the kinetic energy from non-interacting electrons which requires a correction ($T_C[\rho(\mathbf{r})]$) to account for electron-electron interactions:

$$T[\rho(\mathbf{r})] \longrightarrow T_S[\rho(\mathbf{r})] + T_C[\rho(\mathbf{r})] \tag{2.29}$$

where

$$T_S[\rho(\mathbf{r})] = -\frac{1}{2}\sum_i \langle\chi_i|\nabla^2|\chi_i\rangle \tag{2.30}$$

In DFT the kinetic and electron-electron terms can be condensed into the Hohenberg-Kohn *universal* functional, $F[\rho(\mathbf{r})]$ as follows:

$$E[\rho(\mathbf{r})] = F[\rho(\mathbf{r})] + \int \rho(\mathbf{r})V_{ext}(\mathbf{r})d\mathbf{r} \tag{2.31}$$

The term universal means that it is system independent, in contrast to the integral on the right hand side of Equation 2.31 which corresponds to the *system dependent* interaction between the electron density and the external potential created by the nuclei and/or an external field. From this equation it is clear that if the ground state electron density ($\rho_0(\mathbf{r})$) is known, then minimization of this relationship will yield the ground state electronic energy, provided there is an expression for the HK universal functional. Thus, similarly to HF, the vatiational principle is applied in DFT because neither the true ground state energy nor the form of the universal density functional are unknown. To gain further insight into why this is the case it is first necessary to reexamine the

components of $F[\rho(\mathbf{r})]$:

$$F[\rho(\mathbf{r})] = T_S[\rho(\mathbf{r})] + J[\rho(\mathbf{r})] + E_{XC}[\rho(\mathbf{r})] \tag{2.32}$$

The term $J[\rho(\mathbf{r})]$ in Equation 2.32 corresponds to the classical Coulomb interaction:

$$J[\rho(\mathbf{r})] = \frac{1}{2}\sum_{i}^{N}\sum_{j}^{N}\int\int |\chi_i^2| \frac{1}{r_{ij}} |\chi_j^2| \, dr_i dr_j \tag{2.33}$$

while the remaining non-classical (NC) parts of the electron-electron interaction, exchange and correlation, are now accounted for explicitly by $E_{XC}[\rho(\mathbf{r})]$, which is known as the *exchange-correlation energy*:

$$\begin{aligned} E_{XC}[\rho(\mathbf{r})] &= (T[\rho(\mathbf{r})] - T_{KS}[\rho(\mathbf{r})]) + (E_{ee}[\rho(\mathbf{r})] - J[\rho(\mathbf{r})]) \\ &= T_C[\rho(\mathbf{r})] + E_{NC}[\rho(\mathbf{r})] \end{aligned} \tag{2.34}$$

Having defined the energy in terms of the electron density calculated using the wave function, it is now possible to apply the variational principle. This calculation results in the set of orbitals, χ_i, which minimize the energy, subject to the constraint that these orbitals are orthonormal (see Equation 2.6). Having defined all the components of the DFT energy it is now possible to express the equations that describe how a potential acts on the wave functions to produce the eigenvalues and eigenvectors:

$$\left(-\frac{1}{2}\nabla^2 + \left[\int \frac{\rho(\mathbf{r})}{\mathbf{r}_{12}} d\mathbf{r}_2 + V_{XC}(\mathbf{r}) + \sum_{A}^{M} \frac{Z_A}{\mathbf{r}_{1A}}\right]\right)\chi_i = \epsilon_i \chi_i \tag{2.35}$$

which is condensed to:

$$\left(-\frac{1}{2}\nabla^2 + V_{eff}(\mathbf{r})\right)\chi_i = \epsilon_i \chi_i \tag{2.36}$$

These equations define the KS operator, which like that used in HF (see Equation 2.17), is one electron in nature . Figure 2.1 illustrates the various steps in the SCF loop of DFT calculations. The diagram depicts how an initial electron density is used to determine the effective potential, V_{eff}, which acts upon it. This procedure, therefore, requires an iterative approach for its solution because, as the diagram shows, the improved orbitals from subsequent iterations will serve to also improve their own description of V_{eff}. Although similar in many respects to HF, DFT offers the advantage of being able to, at least in theory, fully account for electronic interactions provided there exists

an exact term for $V_{XC}(\mathbf{r})$. In practice, rather than having the exact exchange and zero correlation of HF, the various versions of the $V_{XC}(\mathbf{r})$ that are available for DFT incorporate varying amounts of both exchange and correlation. The significance of these exchange-correlation functionals is further expanded upon in the next section.

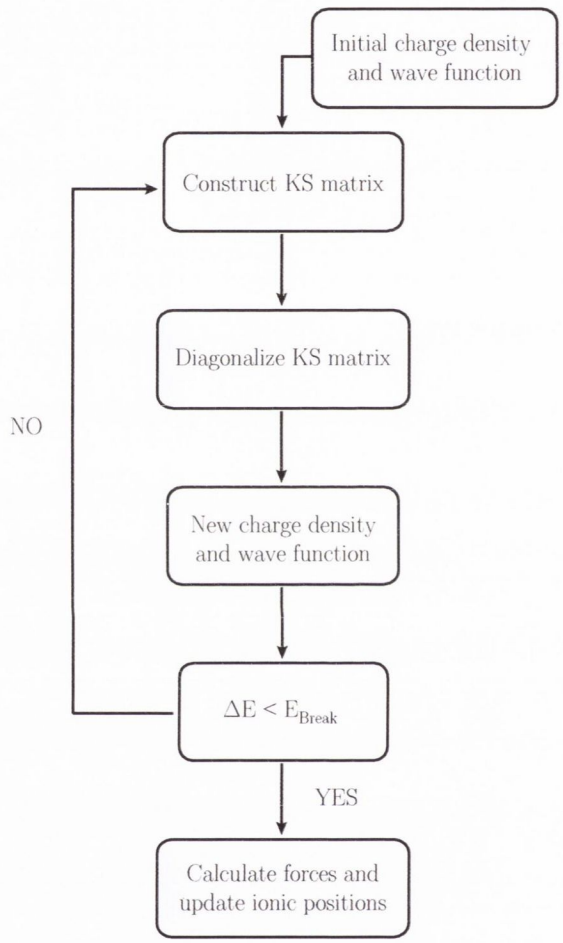

Figure 2.1: Schematic representation of the self-consistent field (SCF) loop used in DFT calculations.

2.2.8 Exchange-Correlation functional

By now it has been shown that DFT depends on an accurate description of the electronic density of the system under study in order to compute its energy and other properties. The development of this theory presented in Section 2.2.7 illustrated how KS DFT separates the components of the effective potential that acts on the elec-

trons; namely, those related to Coulombic intearactions of the kind electron-electron and electron-nuclei, while corrections to the electronic kinetic energies and the non-classical (quantum) effects of electron self interaction, exchange and correlation are grouped into a single functional, $V_{\mathrm{XC}}(\mathbf{r})$, whose actual form is unknown [58]. That is, $V_{\mathrm{XC}}(\mathbf{r})$ accounts for the many-body interactions between electrons, and is given by the functional derivative of E_{XC} with respect to the electron density ρ:

$$V_{\mathrm{XC}} = \frac{\partial E_{\mathrm{XC}}}{\partial \rho} \tag{2.37}$$

The majority of XC functionals are based on a hypothetical *uniform electron gas*, where the electrons are acted upon by a positive background charge distribution which balances out their total charge [58]. In this model both the number of electrons (N) and the system volume (V) approach infinity, while the density (ρ) is constant, thus $N \to \infty$, $V \to \infty$, $N/V = \rho$. This representation is reminiscent of metals, however it does not account for the rapidly varying electron densities of atoms and molecules. Nonetheless, the homogeneous electron gas is the starting point of most XC functionals because it is the only system for which there already exist such functionals in exact or very accurate forms. The central assumption in this case is that E_{XC} can be written as follows

$$E_{\mathrm{XC}}[\rho(\mathbf{r})] = \int \rho(\mathbf{r})\, \epsilon_{\mathrm{XC}}(\rho(\mathbf{r}))\, d\mathbf{r} \tag{2.38}$$

where the term $\epsilon_{\mathrm{XC}}(\rho(\mathbf{r}))$ corresponds to the exchange-correlation energy per particle of a uniform electron gas of density $\rho(\mathbf{r})$. In this case the density also acts as a weighting factor, representing the probability that there is an electron at a given point in space. This constitutes the definition of the Local Density Approximation (LDA), which is one of the commonly used DFT functionals. Decoupling the exchange and correlation parts of ϵ_{XC} yields:

$$\epsilon_{\mathrm{XC}}(\rho(\mathbf{r})) = \epsilon_{\mathrm{X}}(\rho(\mathbf{r})) + \epsilon_{\mathrm{C}}(\rho(\mathbf{r})) \tag{2.39}$$

where the exchange part has an analytical expression known as Slater exchange:

$$\epsilon_{\mathrm{X}}(\rho(\mathbf{r})) = -\frac{3}{4}\sqrt[3]{\frac{\rho(\mathbf{r})}{\pi}} \tag{2.40}$$

In view of the lack of such an explicit form for the correlation part ϵ_{C}, Ceperley and Alder [59] used highly accurate numerical quantum Monte-Carlo (MC) simulations of

the homogeneous electron gas with different densities and subtracted $\epsilon_X(\rho(\mathbf{r}))$ from the total energies to yield ϵ_C. This work was followed by that of Vosko *et al.* [60], who used sophisticated interpolation schemes for this data to derive analytical expressions of ϵ_C. Further work on this approach lead Perdew and Wang in 1992 to derive what is now the more commonly used version of this type of functional [61].

In the case of LDA, the biggest approximation made is the assumption that $E_{XC}[\mathbf{r}]$ depends only on the density at point $\mathbf{r}$ and does not take into account changes in its local environment. This means that better approximations must be used for systems where the electron density varies rapidly. As a result, the first step in the improvement of this description starts with the expression of the exchange-correlation energy in terms of not only the local density, but also its derivatives:

$$E_{XC}[\mathbf{r}] = \int \left(\rho(\mathbf{r}), \nabla\rho(\mathbf{r}), \nabla^2\rho(\mathbf{r}), ...\right) \epsilon_{XC}(\mathbf{r})\, d\mathbf{r} \tag{2.41}$$

Hence, corrections to LDA can be included in the form of the gradient, $\nabla\rho(\mathbf{r})$, and the resulting functionals are known as the Generalized Gradient Approximation (GGA). By including this term, GGA functionals achieve more flexibility and accuracy than LDA at determining the electronic structure and of molecules and solids. Over the course of GGA functional development there emerged two broad families that differ in how the functional form was parameterized. Becke's 1988 exchange-correlation functionals (B88) [62] as well as that from Lee *et al.* (LYP) [63] utilize data from molecules and atoms from the first row of the periodic table; a fact that makes them inappropriate for simulation of heavier elements. The second family of GGA functionals comprises those for which there are no fitted parameters, which includes that by Perdew and Wang (PW91) [61, 64] and the one by Perdew, Burke and Ernzerhof (PBE)[65]. The latter two, and in particular PBE, are the most common exchange-correlation functionals in use for solid state simulations.

2.2.9 LDA/GGA limitations

DFT simulations have become an indispensable tool for the study of solid state systems. This is despite the limitations inherent from the approximations made in the widely used LDA and GGA functionals. As outlined in the previous section, these approximations relate to the way in which electron-electron interactions are represented. The first of these inherent problems becomes apparent upon examination of Equation 2.33, where the Coulombic term ($J[\rho(\mathbf{r})]$) includes a spurious interaction of an electron with

itself that is not present in the HF definition. This Self Interaction Error (SIE) manifests itself in systems that contain highly localized orbitals where the electrons are in close proximity to each other, e.g. *d*- and *f*-orbitals and results in electron delocalization in order to minimize this self interaction. In the case of semiconductors/insulators with such electrons, standard DFT functionals like LDA and GGA delocalize these electron (or hole) states over many atoms, often predicting metallic behaviour, rather than activated deep levels. This is typically encountered when the simulated band structures predict metallic properties for systems that are known to be semiconductors. This inherent "band gap problem" is due to a discontinuity that occurs even in the exact exchange-correlation functional [66].

In addition, there is no systematic way for improving the current XC functionals in use. This is in contrast to HF where addition of more determinants or inclusion of excited levels are guaranteed to reach the exact wave function of the one-electron basis set used. The closest analogue to this in DFT is the inclusion of more derivatives of the density, as shown in Equation 2.41.

2.2.10 The DFT+U approach

The DFT+U method was developed in order to correct the SIE inherent in standard functionals. This problem arises from the use of approximate amounts of electronic exchange which only partially cancel the interactions between electrons on the same atomic centre (on-site interactions). The DFT+U method treats only the specific on-site interactions of electrons with a quantum number l by means of a parameterized Hamiltonian. The rotationally invariant form put forward by Dudarev [67] is shown below:

$$E_{\mathrm{DFT}+U} = E_{\mathrm{DFT}} + \frac{U-J}{2}\sum_{\sigma m}\left(n_{l,m,\sigma} - n_{l,m,\sigma}^2\right) \tag{2.42}$$

where $n_{l,m,\sigma}$ is the occupation number of an orbital l with quantum magnetic number m and a spin of σ. The parameters U and J correspond to the average Coulomb and exchange interactions between electrons of the same angular momentum on the same atom. What this implies is that the $+U$ correction acts as an energetic penalty to partial orbital occupancy, i.e. the correction is zero when $n = 0\mathrm{or}1$ and non-zero when there is fractional occupation, as illustrated in Figure 2.2.

Given its small impact on computer time performance with respect to standard LDA/GGA, the DFT+U method has become a very popular way to correct the SIE,

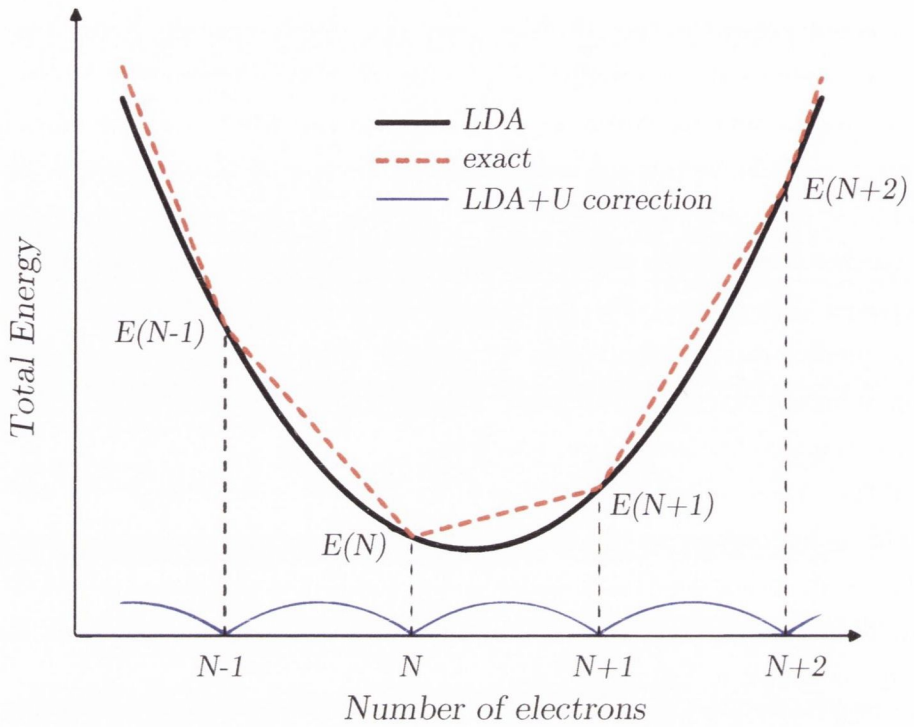

Figure 2.2: Sketch of the total energy profile as a function of number of electrons in a generic atomic system in contact with a reservoir. The bottom curve is simply the difference between the other two (the LDA energy and the exact result for an open system). [68]

e.g. *d*-electrons in transition metals. Its biggest drawback, however, is the fact that the $+U$ term is a fitted parameter and there is not a clear formalism for determining its true value, although first principles derivations have been put forward [68]. Finding a single value of this parameter is also made difficult by the fact that it is geometry dependent, which represents problems when simulating systems of low symmetry like defects and surfaces [69]; thus potentially it is necessary to have different $+U$ values for these inequivalent sites and they could vary during large structural relaxations. In addition, DFT+U should not be used to solve problems that are not fully caused by the SIE such as the band gap error. For example, fitting the U parameter to reproduce experimental band gaps rather than to localize polaronic defects can lead to artificially high values which completely distort the nature of defect states [70]. In practice, the preferred approach is to fit the U value to the *relative* position of the defect state in the band gap obtained from experiments like XPS and UPS. This has been successfully applied to the oxides of metals with highly correlated electrons, such as V_2O_5 [70],

TiO_2 [71] and also CeO_2 [72].

2.2.11 Hybrid DFT

Hybrid DFT (h-DFT) methods represent another approach for correcting the SIE mentioned above by mixing DFT with HF. This is justified by the fact that HF does not suffer from SIE given that its exact exchange completely cancels this spurious effect, and also the fact that HF lacks correlation. In essence the shortcomings of both methods are complementary to each other and as a result, a mixed approach should reduce the SIE and give rise to better $E_{\mathrm{XC}}[\mathbf{r}]$ functionals. In practice this combination is achieved by means of a linear combination of HF exchange and the DFT functional:

$$E_{\mathrm{XC}} = \alpha E_{\mathrm{X}}^{\mathrm{HF}} + (1-\alpha) E_{\mathrm{XC}}^{\mathrm{DFT}} \tag{2.43}$$

where α controls the amount of HF exchange included in the calculation and is typically fitted to reproduce experimental data. More sofisticated methods like PBE0 have been developed and have been shown to work well for metals and semiconductors [73]. This functional combines 25% HF exchange with 75% PBE exhange and 100% PBE correlation, with these values deriving from perturbation theory [74]:

$$E_{\mathrm{XC}}^{\mathrm{PBE0}} = \frac{1}{4} E_{\mathrm{X}}^{\mathrm{HF}} + \frac{3}{4} E_{\mathrm{X}}^{\mathrm{PBE}} + E_{\mathrm{C}}^{\mathrm{PBE}} \tag{2.44}$$

However, this type of h-DFT is very computationally expensive in a plane wave formalism caused by the slow decay of the exchange interaction in real space. Hence, to solve this problem it is necessary to partition the exchange interaction into long range (LR) and short range (SR) parts [75], wchich is the case in the functional by Heyd, Scuseria and Ernzerhof known as HSE06, where 25% of non-local HF exchange is added to PBE, although this value is regarded as empirical by some [76]. A screening value $\omega = 0.11$ bohr^{-1} is applied to partition the Coulomb potential:

$$E_{\mathrm{XC}}^{\mathrm{HSE06}}(\omega) = E_{\mathrm{X}}^{\mathrm{HSE06,SR}} + E_{\mathrm{X}}^{\mathrm{PBE,LR}} + E_{\mathrm{C}}^{\mathrm{PBE}} \tag{2.45}$$

where

$$E_{\mathrm{X}}^{\mathrm{HSE06,SR}} = \frac{1}{4} E_{\mathrm{X}}^{\mathrm{HF,SR}} + \frac{3}{4} E_{\mathrm{X}}^{\mathrm{PBE,SR}} \tag{2.46}$$

It is worth noting that setting $\omega = 0.00$ bohr^{-1} is equivalent to PBE0, while $\omega = \infty$ bohr^{-1} corresponds to the PBE functional.

2.3 Interaction potential techniques

The preceding discussion in Section 2.2 detailed the fundamental aspects of the theories that underlie a family of simulations known as first-principles or *ab initio*. In contrast to those approaches, potential-based methods do not consider electrons in an explicit manner, but rather, they model the attractions and repulsions between atoms by means of parameterized analytical functions. This crucial difference makes potential-based approaches capable of modelling much larger systems due to their reduced computational expense. The general form of the interaction potentials used to study ions in the solid state is derived from the Born model [77], which separates the interactions between the various species into interactions among pairs of ions, triplets, quadruplets, etc:

$$U^{\text{Tot}}_{(r_1,\ldots,r_n)} = \sum_{ij}^{n} \Phi_2(r_{ij}) + \sum_{ijk}^{n} \Phi_3(r_{ijk}) + \sum_{ijkl}^{n} \Phi_4(r_{ijkl}) + \ldots \tag{2.47}$$

However, in practice the representation of these interactions requires truncation in order to remain computationally tractable. This gives rise to the most common type of potentials where interactions are considered up to the pair-wise level, though many-body character is achieved through the inclusion of effects like polarization and dispersion. In this way, most interaction potentials used nowadays are composed of separate elements that represent Coulombic interactions, repulsion interactions in the short-range, dispersion and polarization:

$$U^{\text{Tot}} = U^{\text{Coulomb}} + U^{\text{Rep}} + U^{\text{Disp}} + U^{\text{Pol}} \tag{2.48}$$

The following discussion illustrates how a detailed consideration of the environmental effects present in ionic systems can lead to a rationalized approach to the development of potentials for ionic materials which account for the components listed in Equation 2.48.

2.3.1 Long-range interactions

Coulomb interaction

Interactions are classified into long-range or short-range depending on how rapidly the expressions that are used to represent them decay with distance. In the case of inverse power laws, r^{-n}, those where $n < 3$ are generally deemed to be long-range in character. This is the case of the Coulombic interaction between between point charges (q):

$$U^{q-q} = \sum_{i<j} \frac{q_i q_j}{r_{ij}} = \sum_{i<j} q_i \mathbf{T}_{ij} q_j \tag{2.49}$$

In Equation 2.49 and throughout the remainder of this work the following tensor notation will be used when representing electrostatic interactions:

$$\mathbf{T}_{ij} = (r_{ij})^{-1} \tag{2.50}$$

$$\mathbf{T}^{\alpha}_{ij} = \nabla_{\alpha} \mathbf{T}_{ij} = -r^{\alpha}_{ij} (r_{ij})^{-3} \tag{2.51}$$

$$\mathbf{T}^{\alpha\beta}_{ij} = \nabla_{\alpha} \nabla_{\beta} \mathbf{T}_{ij} = (3 r^{\alpha}_{ij} r^{\beta}_{ij} - (r_{ij})^2 \delta_{\alpha\beta})(r_{ij})^{-5} \tag{2.52}$$

$$\mathbf{T}^{\alpha\beta\ldots\nu}_{ij} = \nabla_{\alpha} \nabla_{\beta} \ldots \nabla_{\nu} \mathbf{T}_{ij} \tag{2.53}$$

where the indices α, β and γ represent the Cartesian axes x, y and z. The long-range Coulomb interactions typically account for close to 80% of all the interactions within a simulation, however the form of Equation 2.49 is unsuitable for atomistic simulation due to its slow decay with distance. The most commonly used solution to this problem is the Ewald summation described below.

Ewald summation

Within the formalism of the Ewald summation [78], the system being simulated is considered to be infinite and each particle interacts with all the periodic images of other particles (See Section 3.2.3 for more details on Periodic Boundary Conditions). This is realized in practice by separating the potential into three components which converge more rapidly than the original expression in Equation 2.49. These sums comprise

a term in real space that represents screened interactions at short distances; another term in reciprocal space contains the long-range interactions and a self-interaction term which corrects the total interaction energy by removing "self" interactions of a particle with its periodic images.

In real space, screening is achieved by surrounding each point charge with a neutralizing Gaussian distribution of opposite sign. The resulting screened charges rapidly converge to zero at long-distances and are therefore short-ranged. This allows the electrostatic interactions between screened charges to be determined by direct summation in real space:

$$U^{\text{Real}} = \sum_i \sum_{j>i} \left(q_i \widehat{\mathbf{T}}_{ij} q_j - q_i \widehat{\mathbf{T}}^{\alpha}_{ij} \mu^{\alpha}_j + q_j \widehat{\mathbf{T}}^{\alpha}_{ij} \mu^{\alpha}_i - \mu^{\alpha}_i \widehat{\mathbf{T}}^{\alpha\beta}_{ij} \mu^{\beta}_j \right) \tag{2.54}$$

where the screened multipole interactions are considered up to the level of induced dipoles (See Section 2.3.2 for more details); that is q_i corresponds to the point charge on ion i and μ_i is its induced dipole [79, 80]. The circumflex accents over the tensors indicate that they correspond to their screened versions as given by:

$$\widehat{\mathbf{T}}_{ij} = \widehat{\frac{1}{r_{ij}}} = \frac{erfc(\kappa r_{ij})}{r_{ij}} \tag{2.55}$$

$$\widehat{\frac{1}{(r_{ij})^{2n+1}}} = \frac{1}{(r_{ij})^2} \left(\widehat{\frac{1}{(r_{ij})^{2n-1}}} + \frac{(2\kappa^2)^n}{\sqrt{\pi}\kappa(2n-1)} e^{-\kappa^2 (r_{ij})^2} \right) \tag{2.56}$$

where $erfc$ is the complementary error function:

$$erfc(r) = \frac{2}{\sqrt{\pi}} \int_r^{\infty} e^{-t^2} dt \tag{2.57}$$

The additional contributions to the energy in reciprocal space are calculated from the following expressions:

$$U^{q-q}_{\text{Recip}} = \frac{4\pi}{V} \sum_{h>0}^{\infty} \frac{e^{-h^2/4\kappa^2}}{h^2} \left(\left[\sum_i q_i \cos(\mathbf{h} \cdot \mathbf{r}_i) \right]^2 + \left[\sum_i q_i \sin(\mathbf{h} \cdot \mathbf{r}_i) \right]^2 \right) \tag{2.58}$$

where U^{q-q}_{Recip} corresponds to the charge-charge interactions in reciprocal space summed over the reciprocal lattice $\mathbf{h} = 2\pi \left(i\hat{\mathbf{x}}/L_x + j\hat{\mathbf{y}}/L_y + k\hat{\mathbf{z}}/L_z \right)$, κ is an adjustable param-

eter that represents an inverse length and determines the relative emphasis given to the real- and reciprocal-space terms; the reciprocal-space series becomes increasingly more important as κ increases. V is the simulation cell volume $|L_x \cdot L_y \times L_z|$. The interaction potential model used throughout this work also accounts for the Coulombic interactions of the form charge-dipole ($U^{q-\mu}$) and dipole-dipole ($U^{\mu-\mu}$). Their contributions in reciprocal space are as follows:

$$U^{q-\mu}_{\text{Recip}} = \frac{8\pi}{V} \sum_{h>0}^{\infty} \frac{e^{-h^2/4\kappa^2}}{h^2} \left(\sum_i q_i \sin(\mathbf{h} \cdot \mathbf{r}_i) \times \sum_i (\boldsymbol{\mu}_i \cdot \mathbf{h}) \cos(\mathbf{h} \cdot \mathbf{r}_i) - \sum_i q_i \cos(\mathbf{h} \cdot \mathbf{r}_i) \times \sum_i (\boldsymbol{\mu}_i \cdot \mathbf{h}) \sin(\mathbf{h} \cdot \mathbf{r}_i) \right) \tag{2.59}$$

$$U^{\mu-\mu}_{\text{Recip}} = \frac{4\pi}{V} \sum_{h>0}^{\infty} \frac{e^{-h^2/4\kappa^2}}{h^2} \left(\left[\sum_i (\boldsymbol{\mu}_i \cdot \mathbf{h}) \cos(\mathbf{h} \cdot \mathbf{r}_i) \right]^2 + \left[\sum_i (\boldsymbol{\mu}_i \cdot \mathbf{h}) \sin(\mathbf{h} \cdot \mathbf{r}_i) \right]^2 \right) \tag{2.60}$$

Finally, the self-interaction corrections are given by:

$$U^{q-q}_{\text{Self}} = \frac{\kappa}{\sqrt{\pi}} \sum_i (q_i)^2 \tag{2.61}$$

$$U^{\mu-\mu}_{\text{Self}} = \frac{2\kappa^3}{3\sqrt{\pi}} \sum_i (\boldsymbol{\mu}_i)^2 \tag{2.62}$$

where the charge-dipole self-interaction term is cancelled on the grounds of symmetry.

2.3.2 Short-range interactions

Ion compression in perfect crystals

Discussion of the forces that act upon ions in the solid state requires a detailed consideration of how their electronic charge densities are affected by their in-crystal surroundings. Figure 2.3 (top panel) illustrates an arrangement of cations and anions in a crystal structure of cubic symmetry. In this environment, the central anion is subjected to a potential ($U(r)$) caused by the electrostatic charges of the other ions in the crystal

and, in addition, by the repulsion from the region occupied by the electron density of the neighbouring ions which originates from Pauli's exclusion principle [81, 82]. The form of this potential is expressed mathematically in Equation 2.63 where it is divided into a spherical part ($U_0(\mathbf{r})$) and an angularly dependent part ($U_l(r)Y_{l,m}(\mathbf{r})$) which varies rapidly with the orientation of the electronic position $\mathbf{r}$:

$$U(\mathbf{r}) = U_0(r) + \sum_{l>4} \sum_{m} U_l(r) Y_{l,m}(\mathbf{r}) \tag{2.63}$$

Here, the angular part is expressed by means of a spherical harmonic expansion that involves terms of angular momentum $l = 4$ or higher. In the case of ions with *sp* valence electrons such as O^{2-}, it is the spherical component that is expected to be dominant. This is rationalized by the fact that the ground state (S) of such closed shell ions can only mix with excited states of even symmetry (G), which tend to be prohibitively high in energy. As a result, the electronic density of the ion is unable to adjust to the angularly dependent part of the potential and thus remains spherical. This effect is coupled to the exclusion of the central ion's electrons from the volume occupied by those of the neighbouring cations and results in an overall repulsive interaction. Thus, as shown in Figure 2.3 (bottom panel) the spherical potential U_0 tends to compress the ion's electron density (dark shading) relative to that of the free ion (light shading), with a subsequent decrease of its polarizability. This confining of the electron density can have profound effects, as in the case of the oxide anion, O^{2-}, which is unstable in the gas phase, but commonly occurs in condensed matter [83–85].

Polarization effects

The development of a complete description of the environmental effects on ions in the solid state naturally leads to the consideration of environments that are less symmetrical than those discussed above; this is particularly true for simulations at finite temperatures, simulations of melts and surfaces. Changing the environment around the idealized central anion from Section 2.3.2 affects the spherical harmonic expansion (Equation 2.63), which will likely contain $l = 0$, 1 and 2 angular momentum terms; where $l = 1$ corresponds to deformations of the ion's electron density with dipolar symmetry, while $l = 2$ corresponds to quadrupolar deformations. The concomitant change in polarization energy occurs because of the electrostatic interactions between the dipole and quadrupole moments of the central ion and those of the ions around it.

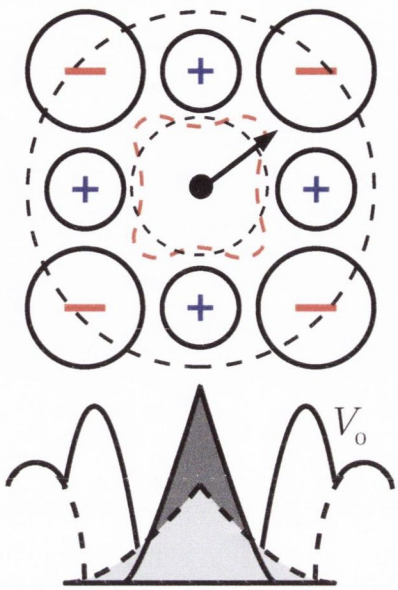

Figure 2.3: Top panel: Arrangement of anions and cations in a crystal of cubic symmetry. The *sp* valent electrons of the central anion are unable to respond to the rapid angular variation in the potential, illustrated by the red dashed contour. Bottom panel: Schematic representation of a cross section through the confining spherical potential (U_0). The dashed line corresponds to the Coulombic (Madelung) contribution due to the ionic point charges. Confinement is enhanced by exclusion from the region occupied by the electronic density of neighbouring ions. U_0 compresses the free-anion charge density (light shading) to the in-crystal charge density (heavy shading).

In the long range, that is, at distances exceeding the first coordination shell, the displacement of an ion off its lattice site affects the potential experienced by the central ion through an induced field (E_β, $l = 1$) and a field gradient ($E_{\gamma\beta}$, $l = 2$). The resulting dipoles $\boldsymbol{\mu}^i_{\alpha,AS}$ and quadrupoles $\boldsymbol{\theta}^i_{\alpha\beta,AS}$ are expressed according to the multipole expansion [86]:

$$\boldsymbol{\mu}_i^{\alpha,\mathrm{AS}} = \boldsymbol{\alpha}^{\alpha\beta} E^{\beta}(\mathbf{r}_i) + \frac{1}{3}\mathbf{B}^{\alpha\beta,\gamma\delta} E^{\beta}(\mathbf{r}_i) E^{\gamma\beta}(\mathbf{r}_i) + \ldots \tag{2.64}$$

$$\boldsymbol{\theta}_i^{\alpha\beta,\mathrm{AS}} = \frac{1}{2}\mathbf{B}^{\alpha\beta,\gamma\delta} E^{\gamma}(\mathbf{r}_i) E_{\delta}(\mathbf{r}_i) + \mathbf{C}^{\alpha\beta\gamma\delta} E^{\gamma\delta}(\mathbf{r}_i) + \ldots \tag{2.65}$$

where the Greek superscripts α, β correspond to the Cartesian axes and repeated subscripts represent summation over the three values x, y and z of that subscript. The

superscript AS indicates that these moments are appropriate when the sources of the fields are *asymptotically* far away from the central ion i. The terms $\boldsymbol{\alpha}$ and $\mathbf{C}$ are the dipole and quadrupole polarizabilities, while $\mathbf{B}$ represents the dipole-dipole-quadrupole hyperpolarizability. For spherical ions, $\boldsymbol{\alpha}$, $\mathbf{B}$ and $\mathbf{C}$, can be specified by a single scalar [86]. These are the in-crystal polarizabilities, and thus, are smaller than those of the free ions due to the confinement effects discussed above.

The top panel in Figure 2.4 illustrates the displacement of a nearest neighbour (NN) cation away from the central anion considered thus far. This symmetry breaking in the short range modifies the anion's confining potential. The bottom panel of Figure 2.4 shows cross sections the confining potential before (dashed line) and after (solid line) the distortion. As is evident from the diagram, the repulsive wall of the confining potential has been pushed away from the anion and, in the process, more space has been made available to its electron density. This latter effect results in an additional dipole (μ^{SR})that is in a direction antiparallel to that caused by distortions that are asymptotically far away (μ^{AS}). The net effect of these opposing dipoles has been found to cause fluctuations of up to 50 % in the total dipole on the central anion [83]. The experimental manifestation of these two effects can be studied in the far-infrared spectra and light scattering of disordered ionic systems [87, 88]. For cation polarization, the relative sign of the short range and asymptotic moments is the same, therefore the short range effect enhances the dipoles above their electrostatically induced moments.

The form of the interaction potential

The full expression used throughout this work for the short-range repulsion is as follows:

$$U^{\mathrm{Rep}} = \sum_{i<j} \frac{A^{ij} e^{-a^{ij} r_{ij}}}{r_{ij}} + \sum_{i \leq j} B^{ij} e^{-b^{ij} r_{ij}^2} \tag{2.66}$$

where the first term on the right hand side of the equation represents the exponentially decaying electron density of each ion that leads to short-range repulsions. In Equation 2.66, those terms where i and j are cations are set to zero due to the small size of their electron clouds and the considerable distance between them at the temperatures of interest. Inclusion of the $\frac{1}{r_{ij}}$ factor has been shown to provide a better fit in the parameterization process for the short-range interactions and, in addition, it has also been shown improve the potential's stability [89]. The second term is a Gaussian which

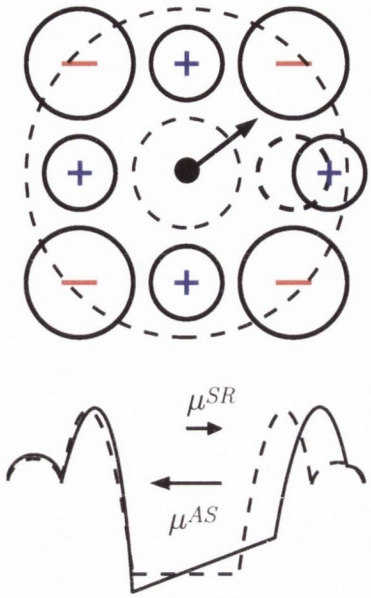

Figure 2.4: Top panel: Symmetry breaking in the first coordination shell of a central anion in a cubic crystal. Bottom panel: Cross sections of the confining potential for the anion in the undistorted crystal (dashed line) and the resulting potential after symmetry breaking (solid line). The arrows represent the direction of electron displacement, and are, therefore antiparallel to the associated dipoles.

acts as a steep repulsive wall and accounts for the anion hard core; these extra terms are used in cases where the ions are strongly polarized to avoid instability problems at very small anion-cation separations [89].

The polarization part of the potential incorporates dipolar effects only and is thus called DIPole Polarizable Ion Model (DIPPIM) [90, 91]:

$$\begin{aligned} U^{\text{pol}} &= \sum_{i,j} \left(q_i \mu_j^\alpha f_4^{ij}(r_{ij}) \delta_{ij} - q_j \mu_i^\alpha f_4^{ji}(r_{ij}) \delta_{ij} \right) \mathbf{T}_{ij}^\alpha \\ &\quad - \sum_{i,j} \mu_i^\alpha \mu_j^\beta \mathbf{T}_{ij}^{\alpha\beta} + \sum_i \frac{1}{2\alpha_i} \mid \boldsymbol{\mu}_i \mid^2 \end{aligned} \tag{2.67}$$

Here, α_i is the polarizability of ion i, $\boldsymbol{\mu}_i$ are the dipoles δ_{ij} is the Kronecker delta function from Equation 2.7. The terms $\mathbf{T}_{ij}^\alpha$ and $\mathbf{T}_{ij}^{\alpha\beta}$ are the charge-dipole and dipole-dipole interaction tensors from Equations 2.51 and 2.52, respectively. The instantaneous values of these moments are obtained by minimization of this expression with respect to the dipoles of all ions in the system at each step of the simulation (See Section 3.4).

The short-range induction effects on the dipoles discussed in Section 2.3.2 above are taken into account by means of the Tang-Toennies damping functions [92, 93]:

$$f_n^{ij}(r_{ij}) = 1 - c^{ij} e^{-b^{ij} r_{ij}} \sum_{k=0}^{n} \frac{(b^{ij} r_{ij})^k}{k!} \tag{2.68}$$

where the parameter b^{ij} determines the range at which the overlap of the charge densities affects the induced dipoles and the parameter c^{ij} determines the strength of the ion response to this effect. Figure 2.5 illustrates how this function tends to 1 for large r and to $1 - c^{ij}$ when r goes to 0. The value of n determines the form of the Tang-Toennies function between these values.

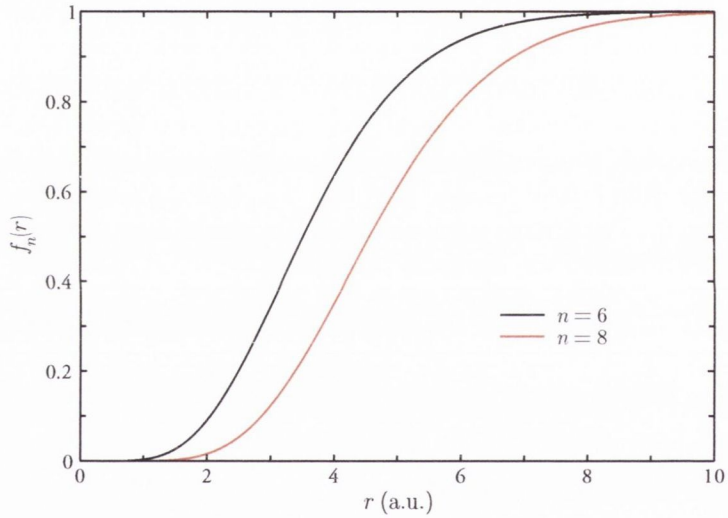

Figure 2.5: The Tang-Toennies damping function from Equation 2.68 for $n = 6$, 8, $c^{ij} = 1$ and $b^{ij} = 1.9$ atomic units (a.u.)

The dispersion interactions account for the mutually induced temporary multipoles between ions:

$$U^{\text{Disp}} = -\sum_{i \leq j} \left[\frac{C_6^{ij} f_D(r_{ij})}{r_{ij}^6} + \frac{C_8^{ij} f_Q(r_{ij})}{r_{ij}^8} \right] \tag{2.69}$$

where the terms C_6^{ij} and C_8^{ij} correspond to the dipole-dipole and dipole-quadrupole dispersion coefficients, respecitvely. The Tang-Toennies dispersion damping functions $f_D(r_{ij})$ and $f_Q(r_{ij})$ are similar to those in Equation 2.68 but here $n = 6$ and 8 for C_6^{ij}

and C_8^{ij}, respectively and $c^{ij} = 0$ in both cases. Damping is introduced in order to account for the short-range corrections to the asymptotic dispersion term.

2.4 Summary

This chapter provided an overview of the techniques that will be used throughout this thesis for the study of the forces between the component species in ionic materials. The development of these topics illustrated the theory that underlies *ab initio* methods in Section 2.2, with special emphasis being given to the modern implementations of DFT. In addition, a comprehensive discussion of IP developement was provided in Section 2.3. The general simulation methods where these techniques are implemented will be described in detail in the next chapter.

3

Solid State Simulations

3.1 Introduction

This chapter consolidates the *ab initio* and potential-based techniques introduced in Chapter 2 into methods that can be applied in computer simulations of the solid state. Section 3.2 develops concepts that are fundamental to the simulation of periodic systems. Section 3.3 introduces static lattice calculations and Section 3.4 describes the method of Molecular Dynamics (MD). In static lattice calculations the goal is to minimize the energy of an input structure by optimizing its geometry, that is, when the forces on each component species are below a certain predetermined cutoff. MD simulations, on the other hand, calculate the time-dependent trajectory of each species from the forces that act upon it by numerical integration of Newton's equations of motion.

3.2 Properties of periodic systems

3.2.1 Crystal lattices

Bravais Lattice

The concept of the Bravais lattice is one that is fundamental to the description of the periodic arrangement of atoms in crystals. A Bravais lattice is defined as an infinite array of discrete points with an arrangement and orientation that appears exactly the

same regardless of which point it is viewed from [94]. Mathematically, it is given by a set of discrete position vectors $\mathbf{R}$, which in three dimensions take the form:

$$\mathbf{R} = n_1\mathbf{a}_1 + n_2\mathbf{a}_2 + n_3\mathbf{a}_3 \tag{3.1}$$

where n_i are integers, while $\mathbf{a}_i$ are a set of non–coplanar vectors typically known as the primitive vectors which are said to generate or span the lattice. Figure 3.1 illustrates a portion of a two-dimensional (2D) square Bravais lattice with primitive vectors $\mathbf{a}_1$ and $\mathbf{a}_2$ and a lattice spacing of a.

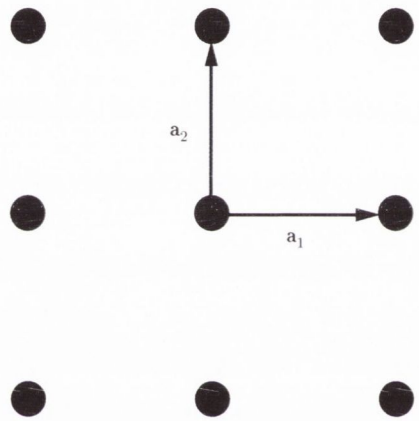

Figure 3.1: Two-dimensional square Bravais lattice with primitive vectors $\mathbf{a}_1$ and $\mathbf{a}_2$ with lattice spacing a.

Similarly, Figure 3.2 presents portions of the two three-dimensional (3D) lattices that will be encountered throughout this work: a) the simple cubic (SC) lattice and b) the face–centred cubic (FCC) lattice. The points in a Bravais lattice that are closest to a given point are called its nearest neighbours and this number is known as the coordination number (CN) of the lattice, whose value is 6 for the SC lattice and 12 for the FCC lattice.

Primitive unit cell

Another important concept typically encountered in the study of the solid state is that of the primitive unit cell. It is defined as the volume of space which, when translated through all the vectors in a Bravais lattice fills all of space without overlapping or leaving voids [94]. A primitive cell must contain only one lattice point, unless it is positioned in such a way that there are points on its surface. A common example of

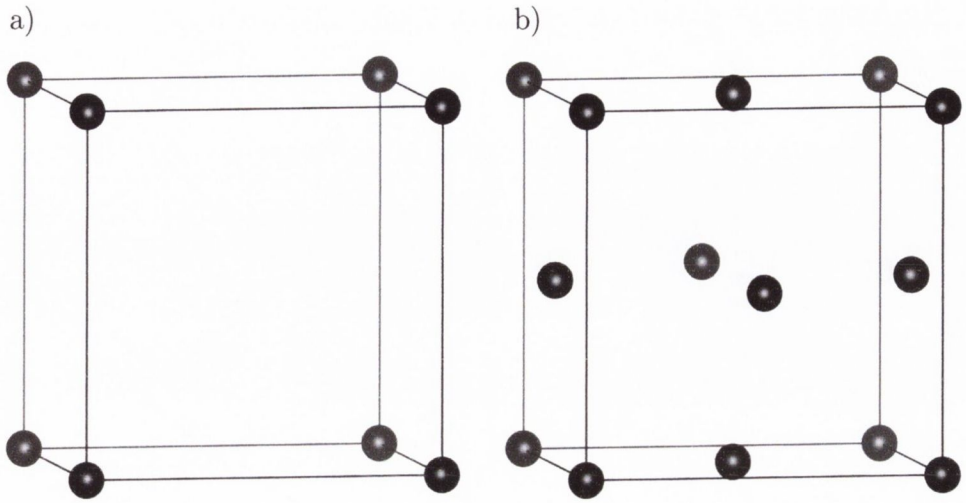

Figure 3.2: a) Simple cubic Bravais lattice. b) Face–centred cubic Bravais lattice.

this type of cell is the Wigner–Seitz (WS) primitive cell, which is defined as the region of space about a lattice point that is closer to that point than to any other lattice point. It is constructed by drawing lines connecting the point to all its neighbours, then bisecting each of these lines with a plane (or line in the case of 2D), and then taking the smallest polyhedron enclosed by these planes as shown in Figure 3.3a for the two–dimensional square lattice presented above. In three–dimensions, the WS cell for the SC lattice is simply a cube with sides that are half the length of the original cell, while in the case of the FCC lattice the WC cell is a rhombic dodecahedron as shown in Figure 3.3b.

In practice, real crystals are finite in extent and, it is discontinuities in their periodicity (defects) which typically impart the material with interesting properties as will be shown in the reminder of this thesis. Moreover, physical crystals are constructed from an underlying Bravais lattice, together with a description of the arrangement of the species within it, such as atoms, molecules, or ionic species. Therefore, a distinction must be made between the abstract pattern of points in a Bravais lattice and an actual crystal subject so simulation by introducing the term crystal structure to refer to a Bravais lattice which has identical copies of the same repeating unit, known as the basis, located at each point.

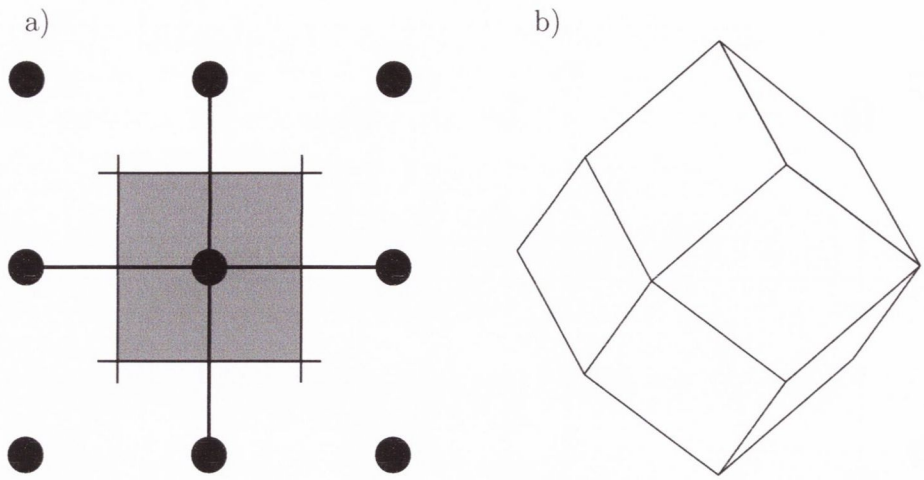

Figure 3.3: a) Wigner–Seitz primitive cell for the square lattice in two dimensions. b) The rhombic dodecahedron that is the Wigner–Seitz primitive cell for the FCC Bravais lattice.

The reciprocal lattice

Just as the concept of the Bravais lattice is fundamental to the description of crystalline systems, so is that of the reciprocal lattice to the analytical study of their structure. It is often encountered in the theory of crystal diffraction, as well as, in the description of functions which have the same periodicity as the Bravais lattice. The reciprocal lattice for a Bravais lattice described by $\mathbf{R}$ is constructed by fixing the periodicity of a plane wave $e^{i\mathbf{k}\cdot\mathbf{r}}$ to that of the lattice. This is achieved when the set of wave vectors $\mathbf{K}$ satisfy the relation

$$e^{i\mathbf{K}\cdot\mathbf{R}} = 1 \tag{3.2}$$

for all $\mathbf{R}$ in the Bravais lattice [94]. Note that the resulting reciprocal lattice is defined with reference to a specific Bravais lattice, also called the *direct lattice* in this context:

$$\mathbf{b}_1 = 2\pi\left(\frac{\mathbf{a}_2 \times \mathbf{a}_3}{\mathbf{a}_1 \cdot \mathbf{a}_2 \times \mathbf{a}_3}\right); \quad \mathbf{b}_2 = 2\pi\left(\frac{\mathbf{a}_1 \times \mathbf{a}_3}{\mathbf{a}_2 \cdot \mathbf{a}_1 \times \mathbf{a}_3}\right); \quad \mathbf{b}_3 = 2\pi\left(\frac{\mathbf{a}_1 \times \mathbf{a}_2}{\mathbf{a}_3 \cdot \mathbf{a}_1 \times \mathbf{a}_2}\right) \tag{3.3}$$

or more concisely

$$\mathbf{b}_i \cdot \mathbf{a}_j = 2\pi\delta_{ij} \tag{3.4}$$

where δ_{ij} is the Kronecker delta function encountered in Section 2.2.1. These reciprocal vectors have units of the form 1/length and are said to belong to k–space, also known as momentum space, as opposed to r–space for the direct lattice. The reciprocal lattice

is a Bravais lattice itself and it is given by:

$$\mathbf{k} = k_1\mathbf{b}_1 + k_2\mathbf{b}_2 + k_3\mathbf{b}_3 \tag{3.5}$$

where k_i are integers, i.e. any vector $\mathbf{k}$ can be written as a linear combination of $\mathbf{b}_i$.

The first Brillouin zone

As mentioned above, the reciprocal lattice is a Bravais lattice itself. Moreover, the reciprocal of the reciprocal lattice is the original direct lattice. The WS cell of a lattice in k–space is commonly known as the first Brillouin zone. Its volume is given by $\mathbf{b}_1 \cdot \mathbf{b}_2 \times \mathbf{b}_3$. Shown in Figure 3.4 is the Brillouin zone for the space group $Fm\bar{3}m$–O_h^5 (225) which is common to crystals with an FCC lattice as is the case of the cubic systems discussed in this thesis. The shape of the BZ illustrated in Figure 3.4 is known as the truncated octahedron. Each of the high symmetry points and lines is given a special label, depending on the symmetry operations associated with them. These "special" k–points indicate locations within the BZ where energy degeneracies occur due to symmetry restrictions [95]. The high symmetry positions $\Gamma = (0, 0, 0)$, $X = \left(\frac{1}{2}, 0, \frac{1}{2}\right)$; $W = \left(\frac{1}{2}, \frac{1}{4}, \frac{3}{4}\right)$, $K = \left(\frac{3}{8}, \frac{3}{8}, \frac{1}{2}\right)$, $L = \left(\frac{1}{2}, \frac{1}{2}, \frac{1}{2}\right)$ will be used in Chapter 7 for the calculation of the band structure of cadmium oxide (CdO).

3.2.2 Periodic potential in crystals

As shown in Section 2.2.1 the electrons in crystalline systems can be thought of as a group of non-interacting particles which are acted upon by a static one-electron effective potential $U(\mathbf{r})$:

$$H\psi = \left(-\frac{1}{2}\nabla^2 + U(\mathbf{r})\right)\psi = E\psi \tag{3.6}$$

As this potential originates from a periodic array of nuclei in a crystal like those shown in Figure 3.2 it has the same periodicity of the underlying Bravais lattice

$$U(\mathbf{r} + \mathbf{R}) = U(\mathbf{r}) \tag{3.7}$$

where $\mathbf{R}$ corresponds to the primitive vectors from Equation 3.1. Electrons that are subject to a periodic potential are known as Bloch electrons.

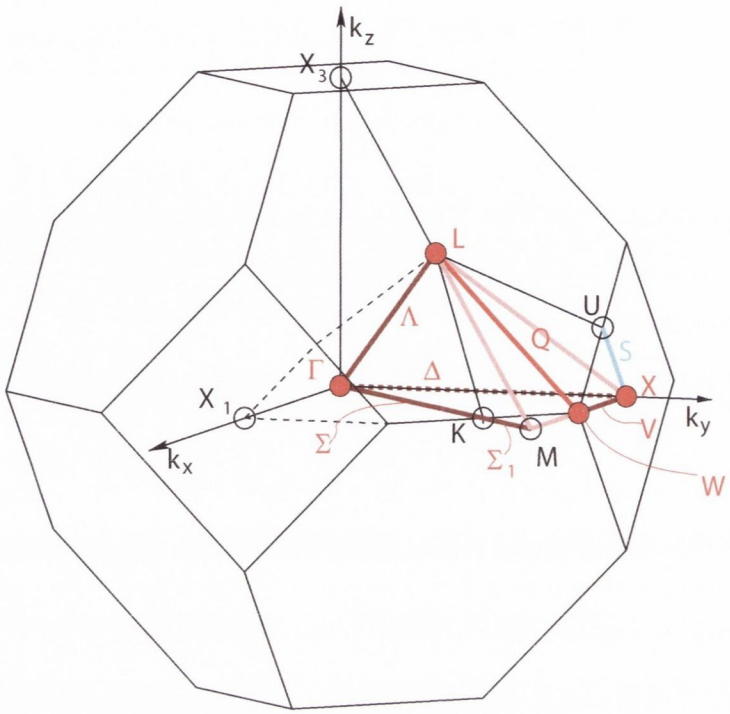

Figure 3.4: Brillouin Zone for the space group $Fm\bar{3}m$–O_h^5 (225) (FCC) showing the high symmetry points.

3.2.3 Bloch's Theorem

Bloch's theorem sets forth that the eigenstates ψ of the one-electron Hamiltonian in a periodic potential (Equation 3.6) can be chosen to be a plane wave times a function with the periodicity of the Bravais lattice [94, 96]:

$$\psi(\mathbf{r}) = u_{n\mathbf{k}}(\mathbf{r})e^{i\mathbf{k}\cdot\mathbf{r}} \tag{3.8}$$

where the periodic function is described by $u_{n\mathbf{k}}(\mathbf{r}+\mathbf{R}) = u_{n\mathbf{k}}(\mathbf{r})$ and n is an integer quantum number called the band index $n = 1, 2, 3,...$ This quantum number corresponds to the appearance of independent eigenstates of different energies, but with the same $\mathbf{k}$ values. Any value of $\mathbf{k}$ that is outside the first BZ can be reduced to the first zone as indicated by an alternative formulation of Bloch's thorem:

$$\psi(\mathbf{r}+\mathbf{R}) = e^{i\mathbf{k}\cdot\mathbf{R}}\psi(\mathbf{r}) \tag{3.9}$$

Allowing **k** to range outside the first BZ is unnecessary as the properties of Bloch electrons are fully described within this volume as shown in Figure 3.5 for a reciprocal vector **G** in k–space.

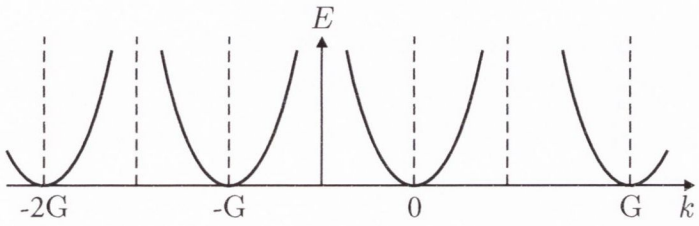

Figure 3.5: Periodicity of the energy with respect to the reciprocal lattice.

The Born–von Karman boundary conditions are applied to the wave functions in order to arrive at the set of allowed values of **k**. The general form of these boundary conditions is as follows:

$$\phi(\mathbf{r} + N_j\mathbf{a}_j) = \phi(\mathbf{r}), \quad i = 1, 2, 3, ... \tag{3.10}$$

where N_j is the number of unit cells along the jth direction. This boundary condition implies that $e^{iN_j\mathbf{k}\cdot\mathbf{a}_j} = 1$. From this relationship it is possible to define the allowed values for the wave vector

$$\mathbf{k} = \sum_{j=1}^{3} \frac{m_j}{N_j}\mathbf{A}_j \tag{3.11}$$

Computer simulations are usually performed on relatively small systems which contain between several hundred and several thousand atoms. This is quite small compared to physical systems typically found in the laboratory, whose size is in the order of Avogadro's number, i.e. $\mathcal{O}(10^{23})$ particles. The simulation of relatively small systems is the result of the computational cost involved. A problem inherent to the direct simulation of a small number of particles is that it will likely lead to disproportionately high surface effects with respect to the bulk solid. This is because a typical simulation box contains a higher proportion of particles near the surface than the much larger physical system being simulated given the high area:volume ratio of a small simulation cell. Nonetheless, it is possible to take advantage of the periodic symmetry found in crystals in order to reduce the computational cost and overcome the unphysical representation of surfaces in the bulk. The simulation schemes presented in this thesis make

use of a technique called periodic boundary condition (PBC) for the ionic species in the simulation cell, as illustrated in Fig. 3.6. In this case a primary cell or simulation box is defined by a set of non-coplanar vectors **a**, **b** and **c**, as well as, the positions of the particles within it. It is then replicated in all directions to better represent a macroscopic sample and simplify the calculation. As the simulation proceeds, the movement of each particle in the primary cell is replicated by each of its images, and in cases where a particle leaves the simulation box one of its images from a contiguous box enters it through the opposite face.

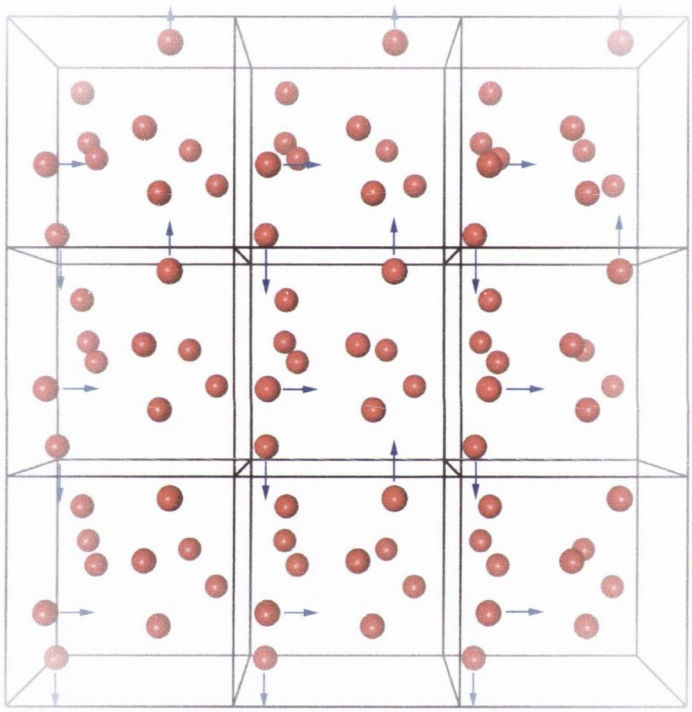

Figure 3.6: Periodic boundary conditions: The primary cell (centre) is replicated in all directions. The figure shows how as one particle leaves this box, one of its images from a contiguous box enters from the opposite side.

3.2.4 Basis sets and pseudopotentials

Practical implementations of the *ab initio* methods from Section 2.2 call for the representation of the wave function in a way that is both accurate and computationally inexpensive. This is usually achieved by means of linear combinations of functions

known as a *basis set*. As shown above, for periodic systems plane waves can be used as a basis set because of the intrinsic connection that exists between free electrons and plane waves. In addition, they provide an efficient and accurate representation of the wave function [97, 98]. The wave function can, thus, be described by a basis set made up of plane waves, which in three dimensions can be written as follows:

$$\psi_{i\mathbf{k}}(\mathbf{r}) = \sum_{\mathbf{G}} c_{i\mathbf{k}}(\mathbf{G}) e^{i(\mathbf{k}+\mathbf{G})\cdot\mathbf{r}} \tag{3.12}$$

Where $\mathbf{G}$ is a reciprocal vector like that in Equation 3.5 and $c_{i\mathbf{k}}(\mathbf{G})$ are the plane wave coefficients that must be optimized in order to solve the Schrödinger equation. The wave vector $\mathbf{k}$ can also be thought of as a frequency factor, with high values indicating rapid oscillation, and thus high kinetic energy. The allowed values for $\mathbf{k}$ are determined by the unit cell translational vector $\mathbf{t}$, where $\mathbf{k} \cdot \mathbf{t} = 2\pi m$, with m being a positive integer. In this way the typical spacing between $\mathbf{k}$ vectors is $\sim$ 0.01 eV (electron volts). The size of the basis set is uniquely characterized by the $\mathbf{k}$ vector with the highest energy that is included, known as the cutoff, i.e. $|\mathbf{G}|^2 < E_{\text{cutoff}}$. For example, a cutoff of 200 eV corresponds to approximately 20000 functions in the basis set, hence the cutoff value should be chosen in order to increase accuracy and minimize computational cost. Note that the size of a plane wave basis set depends only on the size of the periodic cell and not on the actual system described within it, i.e. the basis set is not system dependent. This is in contrast with other popular basis sets that use nucleus–centred Gaussian functions which increase linearly with system size. This means that plane wave basis sets are more favourable for larger systems. An additional advantage of plane wave basis sets over localised basis sets, like those which use Gaussian functions, is that they do not suffer from basis set superposition error. This error occurs due to the mixing of functions in the short range, i.e. there is an overlap and hence mixing between the functions centred on different atoms that are in close proximity to each other.

Plane wave basis functions are ideally suited for the simulation of delocalized and slowly varying electron densities as is the case of the valence bands in metals. However, the electrons in the atomic core are strongly localized in the vicinity of the nucleus and, in addition, the valence electrons undergo rapid oscillations in this region in order to mantain ortogonality. Therefore, the cutoff required to simulate these properties would be very high if only plane waves were used. To circumvent this problem, a pseudopotential is normally introduced to be able to describe the interaction between the valence

electrons with the core electrons and the nucleus. Pseudopotentials are derived from all-electron calculations from which the parameters of the pseudopotential are defined in order to reproduce the behaviour and properties of the valence electrons. Figure 3.7 illustrates this concept, where the pseudopotential wave function has the same form as the all-electron wave function beyond the region limited by the core radius r_c, but it has fewer nodes within. This representation decreases the magnitude of the plane wave basis set required to carry out the simulation [99]. In 1990 Vanderbilt [100] demonstrated that by relaxing the constraint that the real and pseudo wave function represent the same charge (norm–conservation) it is possible to achieve the same accuracy using a smoother function and therefore a *smaller* cutoff. These advances were followed by the

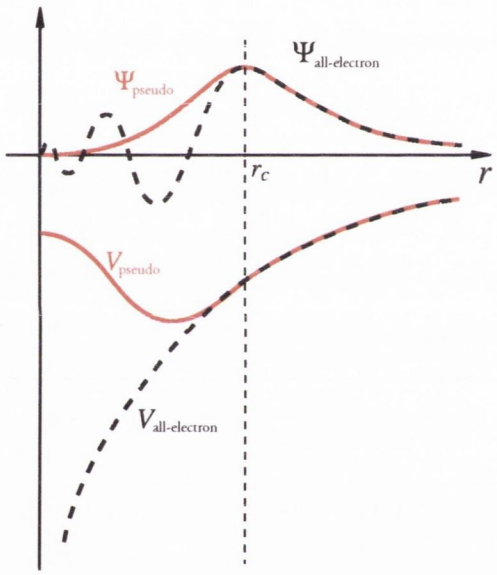

Figure 3.7: Top: Schematic representations of the relationship between the all–electron wave function (dashed black line) and a pseudopotential (solid red line) wave function. Bottom: Nuclear Coulomb potential (dashed black line) and pseudopotential (solid red line). Note that both wave functions and potentials are matched beyond the radius cutoff r_c.

introduction of the Projector Augmented Wave (PAW) method developed by Blöchl [101] to accurately and efficiently calculate the electronic structure of materials within the framework of DFT. In the PAW method, localized basis sets are used to represent the core electrons, with the effect of these core states being projected onto the valence electrons. This approach retains the numerical advantages of pseudopotential calculations, while retaining the physics of all–electron calculations, including the correct

nodal behaviour of the valence electron wave functions. The PAW fixed core states are generated from all-electron scalar relativistic calculations.

3.3 Static Lattice Calculations

3.3.1 Structural Optimisation and Convergence

The search for the minimum energy geometry of a particular material necessitates a number of criteria to be considered *a priori*: i) the optimization of the forces acting upon all the species of the system, ii) the resolution of the basis set, which is related to the plane wave cut-off, and iii) the k-point sampling density. In DFT, the forces acting upon the ions in the system are computed at the end of an SCF cycle (See Section 2.2.7). These values are calculated using classical mechanics, which prescribes that the forces acting on the nuclei are given by the derivative of the energy with respect to position. This problem could, at first, be approached by moving the ions in all directions, however, for a system composed of N ions, this method would require 6N *costly* evaluations of the system's energy. Practical applications of this procedure employ the Hellmann–Feynman theorem [102], which states that the forces on any fixed nucleus in a system of nuclei and electrons are given by the *classical* electrostatic attraction exerted on the nucleus. This means that by using the Hellmann–Feynman theorem, all the forces acting on all the ions can be calculated directly from the wave function by calling the energy subroutine only once and on a single ionic configuration, which results in a considerable speed-up. The optimization methods most commonly used are highlighted in the following section.

The structural optimization described so far has a main drawback in that it ignores an additional term that is required in order to represent the derivative of the basis set with respect to the ionic position. This term is known as the Pulay stress, or also as the Pulay force, and it should always be considered in calculations when localized basis sets are used. In plane wave basis set calculations, however, this error arises due to the basis set being incomplete with respect to changes in volume. Thus, non-constant volume calculations result in an underestimation of the equilibrium volume unless a very large plane wave cut-off is used. This issue is addressed by optimizing the unit cell at a series of volumes (lattice constants), where the atomic positions, lattice vectors and angles are allowed to relax within the constrained total volume. Usually, the starting configuration is obtained from databases that contain experimental and/or

computational data for the material of interest, as well as, related ones. The variational principle thus establishes that the ground state of a system has the lowest energy, hence the equilibrium value is the minimum energy obtained from the resulting energy-volume data fitted to the Murnaghan equation of state [103], as shown below

$$E(V) = E_0 + \frac{B_0 V}{B_1(B_1 - 1)}\left[B_1\left(1 - \frac{V_0}{V_1}\right) - 1 + \left(\frac{V_0}{V}\right)B_1\right] \tag{3.13}$$

where B_0 corresponds to the bulk modulus and B_1 is its pressure derivative, V_0 is the equilibrium cell volume and E_0 is the ground state energy. To test for convergence, a series of energy-volume curves are plotted using different plane wave cut-off energies and k-point densities. A plane wave cut-off energy of 300-500 eV is sufficient for the simulation of the metal oxide systems studied in this work. The minimum energy for each curve is then compared to ensure convergence to within 0.01 eV/atom as shown in Figure 3.8 which depicts a plot of the energy as a function of small fractional variations in the lattice constant of CdO for a cut-off of 400 eV. Through years of undertaking electronic structure calculations within the Watson research group, it has been observed that a k-point sampling density of approximately 0.04 Å^{-1} results in acceptable convergence for most non-metallic systems. Table 3.1 shows a simple convergence table between lattice vector magnitude, k-point sampling density and the number of k-points. The number of k-points is taken as a whole integer, and is rounded to the nearest even number for continuity in the convergence. Even numbers produce a distribution in which the zone centre is not included, while odd numbers give distributions that include the zone centre. Using all even numbers ensures equivalent distributions, varying only in the density of points.

Once an equilibrium volume has been obtained from the fit to Equation 3.13, a final geometry relaxation is performed at this value, which results in the optimized structure for the material.

3.3.2 Energy Minimization and Optimization

The goal of static lattice calculations is to determine the structural configuration which yields the lowest energy for the system under study. This kind of simulation belongs to a general type of optimization problems. In static lattice calculations, the atomic coordinates of a structure are adjusted in order to minimize the potential energy of the

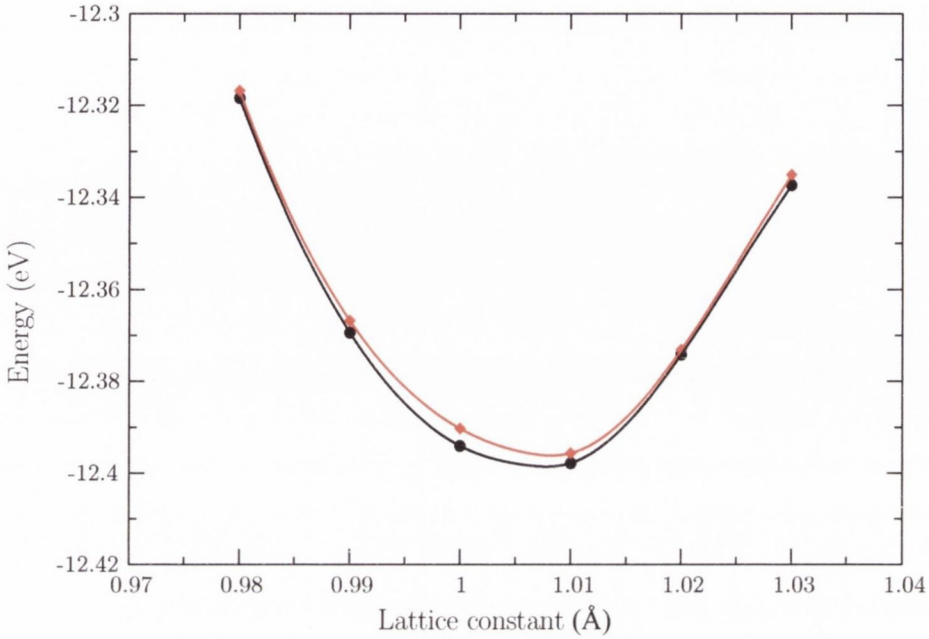

Figure 3.8: Different k-point sampling densities for CdO. Shown in black is a k-point sampling density of 8×8×8 and 12×12×12 shown in red.

Table 3.1: Relationship between the magnitude of the lattice vector to the k-point density, with a sampling rate 0.04 Å^{-1}.

Lattice Vector (Å)	LV^{-1}	LV^{-1}/0.04	k-point density
2.00	0.5000	12.50	12
4.00	0.2500	6.26	6
6.00	0.1667	4.17	4
8.00	0.1250	3.13	4
10.00	0.1000	2.50	2
12.00	0.0834	2.09	2

system. This is expressed mathematically as:

$$\frac{\partial U_L}{\partial \mathbf{r}} = 0 \tag{3.14}$$

where U_L is the lattice energy and $\mathbf{r}$ represents the atomic positions. In practice this entails reducing the force acting on each atomic coordinate (i) to zero, i.e. $\mathbf{F}_i = -\frac{\partial U}{\partial \mathbf{r}_i}$. Here, V is the potential energy calculated using either the first principles or potential-based methods from Chapter 2. The basis of this approach is to express the lattice

energy by means of a Taylor expansion in terms of the basis strain $\delta\mathbf{r}$:

$$U_L(\mathbf{r}+\partial\mathbf{r}) = U_L(\mathbf{r}) + \frac{\partial U_L(\mathbf{r})}{\partial\mathbf{r}}\partial\mathbf{r} + \frac{1}{2!}\frac{\partial^2 U_L(\mathbf{r})}{\partial\mathbf{r}^2}\delta\mathbf{r}^2 + \mathrm{K} \tag{3.15}$$

As the position vector $\mathbf{r}$ is made up of three components, this gives rise to a $3N$ matrix for an N-atom system. The numerous methods that have been developed to solve this problem operate by iteratively reducing the energy until a minimum is found. This is done by gradually changing the atomic coordinates as the system moves closer to the minimum. The starting point for each iteration ($\mathbf{r}_{n+1}$) is the configuration obtained from the previous step ($\mathbf{r}_n$). Minimization methods are broadly differentiated by how many terms from Equation 3.15 they include. The most commonly used minimization techniques encountered in solid state physics/chemistry are either first or second derivative methods. One can generally expect higher accuracies from those methods that include higher derivatives at the cost of computational expense.

As is the case with other simulation techniques, static lattice calculations have a number of drawbacks. Firstly, if more than one energy minimum is present in the system then the calculation may only find a local rather than the global minimum; this is a problem common to all optimization schemes. Secondly, static lattice calculations ignore the vibrational properties of the crystal, thereby effectively simulating the system at 0 K and also neglecting the zero point energy. Despite these shortcomings, however, this family of simulation techniques represents a powerful tool in solid state simulations given their excellent agreement with experimental results. Some of the details of these methods will be highlighted in the following sections. For further details, please consult Leach (2001) [51].

First-order Minimization Methods

Steepest Descents

The method of steepest descents is an example of a first-order derivative minimization technique. This method starts with an initial configuration $\mathbf{r}_0$ and each iteration advances along a line in the direction parallel to the net force, represented by the vector $\mathbf{s}_n$ below

$$\mathbf{s}_n = -\frac{\mathbf{g}_n}{|\mathbf{g}_n|} \tag{3.16}$$

where $\mathbf{g}_n$ is a vector containing the gradients (first derivatives) of the function. Figure 3.9 illustrates a one-dimensional example of this method for the function $f(x) = x^3 -$

$2x^2+2$, with the initial guess $x_0 = 2$ and subsequent iterations marked by a red dot until the minimum is reached [104]. As the direction of the gradient is determined by the largest interatomic forces, the steepest descent method is often useful for relieving the highest energy features in an initial configuration. A major drawback of this technique is found in locations where the function resembles a narrow valley; in such cases, the fact that the direction of displacement is orthogonal to the gradient means that the method will proceed in a large number of small successive steps.

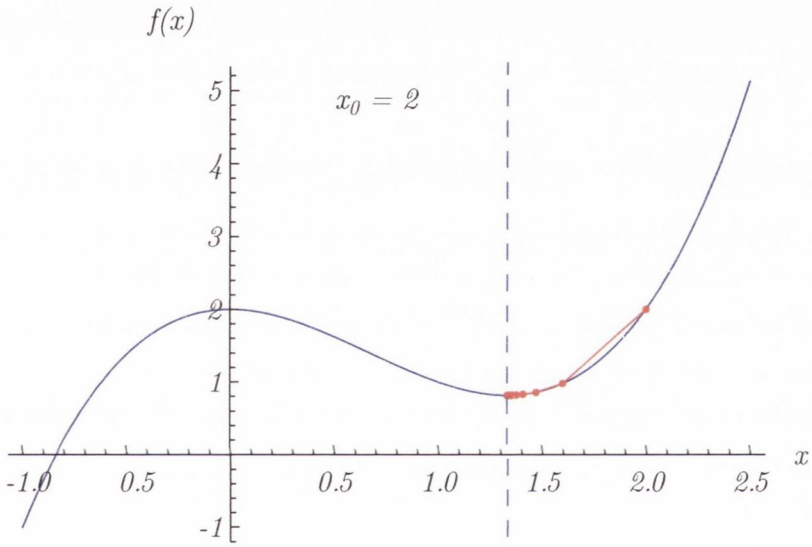

Figure 3.9: Illustration of the steepest descent method for the one-dimensional function $f(x) = x^3 - 2x^2 + 2$.

Conjugate Gradients

The method of conjugate gradients (CG) is a modification of the steepest descents method. In fact, the first step of a CG calculation uses the steepest descent direction, however subsequent iterations use the information from previous gradients to calculate the new displacement vector:

$$\mathbf{s}_n = -\mathbf{g}_n + \gamma_n \mathbf{s}_{n-1} \tag{3.17}$$

where

$$\gamma_n = \frac{\mathbf{g}_n \cdot \mathbf{g}_n}{\mathbf{g}_{n-1} \cdot \mathbf{g}_{n-1}} \tag{3.18}$$

This modification imparts more efficiency to the CG method over what can be achieved using steepest descent, particularly when evaluating potential energy surfaces (PES) with long narrow valleys.

Second-order Minimization Methods

Newton-Raphson

Being a second-order method, Newton-Raphson is expected to be more efficient than CG in terms of the number of iterations required to reach the minimum, but with a higher cost per step. Addition of second-order derivative terms captures information about the function curvature as expressed below for the gradient at step n:

$$\mathbf{g}_n = \frac{\partial U_L}{\partial \mathbf{r}_{n-1}} + \frac{\partial^2 U_L}{\partial \mathbf{r}_{n-1}^2} \delta \mathbf{r}^2 = \mathbf{g}_{n-1} + \mathbf{H}_{n-1} \cdot \delta \mathbf{r} \tag{3.19}$$

Here, $\mathbf{H}_{n-1}$ is the Hessian of second-order partial derivatives and $\delta \mathbf{r}$ is the displacement of ions between iterations $n-1$ to n, i.e. $\delta \mathrm{r} = \mathrm{r}_n - \mathrm{r}_{n-1}$. At the minimum energy, where $\mathbf{g}_n$ is equal to zero, the atom displacements are given by

$$\delta \mathbf{r} = -\mathbf{g}_n \cdot \mathbf{H}_n^{-1} \tag{3.20}$$

where $\mathbf{H}_{n-1}$ is the inverse Hessian matrix. Thus, the working equation for calculating the atomic positions using the Newton-Raphson method is:

$$\mathbf{r}_n = \mathbf{r}_{n-1} - \mathbf{g}_{n-1} \cdot \mathbf{H}_{n-1}^{-1} \tag{3.21}$$

In theory, this method is capable of determining the minimum of a purely quadratic (harmonic) function in a single step. However, this is rarely the case for the problems encountered in simulations of the solid state and, hence, the minimization proceeds iteratively. In order to successfully apply the Newton-Raphson method, it is necessary that the Hessian be positive definite, which refers to a matrix whose eigenvalues are all positive. Instances where this is not the case will lead the minimum search towards saddle points where the energy increases. In addition, far from a minimum, the harmonic approximation is not appropriate and the minimization can become unstable. Therefore, the standard approach is to initially employ a more robust method

such as CG in order to move the system close to the minimum and, then to apply the Newton-Raphson method.

Quasi-Newton

The calculation and inversion of the Hessian matrix performed in course of a Newton-Raphson method have a deleterious effect on its overall efficiency. One way to speed up the minimization is to use quasi-Newton methods. These techniques still apply the working equation of the Newton-Raphson method (Equation 3.21), but rather than explicitly calculating the inverse Hessian at each iteration an approximate form is used. The full inverse Hessian is only recalculated after a fixed number of iterations, or when the energy changes are too large for the approximation to be valid. Precisely how the inverse Hessian is approximated is what distinguishes the several types of quasi-Newton methods, e.g. the Davidon-Fletcher-Powell (DFP) and the Broyden-Fletcher-Goldfarb-Shanno (BFGS) methods [51].

The inverse Hessian is approximated in the DFP method as follows:

$$\mathbf{H}_n^{-1} \approx \mathbf{H}_{n-1}^{-1} + \frac{\delta\mathbf{r} \otimes \delta\mathbf{r}}{\delta\mathbf{r} \cdot \delta\mathbf{g}} - \frac{\left(\mathbf{H}_{n-1}^{-1} \cdot \delta\mathbf{g}\right) \otimes \left(\mathbf{H}_n^{-1} \cdot \delta\mathbf{g}\right)}{\delta\mathbf{g} \cdot \mathbf{H}_{n-1}^{-1} \cdot \delta\mathbf{g}} \tag{3.22}$$

where $\delta\mathbf{g} = \mathbf{g}_n - \mathbf{g}_{n-1}$ and the symbol $\otimes$ when interposed between two vectors means that a matrix must be formed. An alternative, and more efficient, approach to that in Equation 3.22 is the BFGS method, which includes an additional term

$$\mathbf{H}_n^{-1} \approx \mathbf{H}_{n-1}^{-1} + \frac{\delta\mathbf{r} \otimes \delta\mathbf{r}}{\delta\mathbf{r} \cdot \delta\mathbf{g}} - \frac{\left(\mathbf{H}_{n-1}^{-1} \cdot \delta\mathbf{g}\right) \otimes \left(\mathbf{H}_n^{-1} \cdot \delta\mathbf{g}\right)}{\delta\mathbf{g} \cdot \mathbf{H}_{n-1}^{-1} \cdot \delta\mathbf{g}} \tag{3.23}$$

$$+ \left(\delta\mathbf{g} \cdot \mathbf{H}_{n-1}^{-1} \cdot \delta\mathbf{g}\right) \mathbf{u} \otimes \mathbf{u} \tag{3.24}$$

where

$$\mathbf{u} = \frac{\delta\mathbf{r}}{\delta\mathbf{r} \cdot \delta\mathbf{g}} - \frac{\mathbf{H}_n^{-1} \cdot \delta\mathbf{g}}{\delta\mathbf{g} \cdot \mathbf{H}_n^{-1} \cdot \delta\mathbf{g}} \tag{3.25}$$

Common to all of these methods is their use of just the new and current points to update the inverse Hessian. Assuming that this approximation holds, as the minimization progresses, the estimate of the inverse Hessian becomes closer to the true inverse Hessian matrix and, on approaching the minimum these methods have a similar accuracy to the Newton-Raphson method.

3.3.3 Electronic Structure Calculations

Band Structure

The band structure of a solid depicts the ranges of energy that its electrons may possess. Band structures consist of plots of the Kohn-Sham eigenvalues from DFT calculations as a function of k. To obtain this data, it is first necessary to calculate the charge density and wave function self-consistently with a homogeneous k-point sampling. The following step requires the calculation of the eigenvalues non-self-consistently along a selection of high symmetry directions of the reciprocal cell (as shown in Figure 3.4) using the self-consistent charge density which defines the potential. The choice of high symmetry points is specific for the Brillouin zone of the structure. The band structure, thus shows the evolution of the band energy along these specific directions. This type of sampling is necessary because it is not feasible to plot the bands at all possible k-points. The changes in the band energy observed provide information on the types of interactions that occur among the electrons of the material. For example, band dispersion indicates the interaction strength, while the band energy at a certain point reveals the interaction's symmetry and topology. Other important information that can be obtained from the band structure is the position of the valence band maximum and the conduction band minimum, which are used to estimate the band gap of the material. Materials intended for SOFC electrolyte applications like ceria, should possess wide band gaps, i.e. to be electronic insulators. On the other hand, TCOs are wide band gap semiconductors whose optimization ultimately depends on the balance between electrical conductivity and optical transparency. These requirements impose very specific demands on the properties observed in the band structure of the material such as conduction bands that are highly dispersed at the bottom, which result in small effective masses and, thus highly mobile electrons, as well as, a band gap of more than 3.1 eV [40].

Electronic Density of States

The electronic density of states (EDOS) is another way of visualizing information about the electronic structure of a material. The total EDOS shows the density of eigenvalues as a function of energy, i.e. it is essentially a band structure integrated with respect to the energy. The EDOS provides an intuitive and accessible view of the electronic structure; one which is readily comparable to photoemission experiments. Investigation of the EDOS can give an idea of the underlying bonding in a crystal, thus making it

possible to monitor any changes that occur due to different composition, pressure or structure.

It is also commonplace to calculate the partial electronic density of states (PEDOS), which decomposes the information in terms of the ionic species, as well as the orbitals and the spins. This is carried out by projecting the wave functions onto spherical harmonics that are non-zero within spheres of a specified radius around each ion, the same way that an atomic orbital basis set represents the wave function in a region of space. This radius around a given ion with which wave function will be associated is an user determined parameter that is estimated by monitoring the electron distribution around each ion in plots of the charge density as the projection radii are varied until the number of electrons associated with each ion is correct.

Effective mass

In semiconductor physics, one quantity which is often used to gauge the likely conductivity of a material is its transport effective mass. This gives an estimate of the conductive ability of the bulk material. A low effective mass is associated with a higher mobility and therefore greater conductivity. For a material to have good n-type conductivity, it should have a low electron effective mass at the CBM and similarly, a good p-type conductor should have a low hole effective mass at the VBM. Bands with low effective masses possess a high degree of curvature and conversely, flat bands have high effective masses. Highly dispersed bands lead to a high degree of electron/hole delocalisation which results in high conductivity. In contrast, flat bands result in localised electrons/holes which are not very mobile. In this work, the transport effective mass, $\mathrm{m}_{\tau}^{*}(\mathrm{E}_{k})$, was calculated using the following equation for a free electron [105, 106]:

$$\frac{1}{m_{\tau}^{*}\left(E_{k}\right)}=\frac{1}{\hbar^{2}k}\frac{dE_{k}}{dk} \tag{3.26}$$

where E_{k} is the band edge energy as a function of the wave vector k, which is obtained directly from DFT calculations. This assumes that the first derivative of E_{k} is the same as that of a parabolic band at the same k-point. However, this is only an initial approximation as in many of the materials of interest, the VBM and CBM are not parabolic due to band gap renormalization [106]. This approach also assumes a band-like conduction mechanism, hence, if a polaronic hopping mechanism is dominant, the calculated masses may not be accurate and can only be used to provide a rough estimate of the conductive ability of the material in question.

Bader Charge Analysis

Atomic charges in molecules or solids are not defined explicitly in quantum chemical theory. For example, in the case of DFT calculations the output obtained is the electron density. In addition for plane wave basis set simulations, the determination of how the electrons should be partitioned amongst the ions is not a straightforward task, as illustrated in the determination of the ionic radius used in PDOS calculations. The most commonly used scheme used in quantum chemistry to assign charges is the Mulliken analysis, which relies on a localized orbital basis set for the determination of charges. On the other hand, the partitioning scheme proposed by Bader takes an alternative approach [107]. In this case, partial charges are derived directly from the electron density itself. The optimized charge density is placed on a three dimensional grid and analyzed to assign regions of charge defined by surfaces that run through minima in the electron density. This method is therefore independent of the basis set employed. The fastest implementation for assigning the regions of electron density is based on the steepest ascent method [107]. In this case, each point in the grid is taken in turn and a steepest ascent optimization is performed until a maximum of charge density is reached. This results in the assignment of finite regions for each maximum in the charge density.

3.3.4 Defect Calculations

The principal focus of the work presented in this thesis is the study of how the properties of metal oxides are altered by defects in their crystalline structures. In the case of SOFC electrolytes, simulations were used to investigate the ordering of oxygen vacancies in systems with high defect concentrations (See Chapter 4). This section, however, pertains mostly to the work presented in Chapter 7, where relatively low defect concentrations in CdO were studied using DFT. These simulations of isolated defects, such as ion vacancies or substituents, were carried out using supercells which were generated from optimized unit cells. The introduction of these larger cells is necessary in order to model relatively small defect concentrations and also to avoid spurious interactions between neighbouring images of the defects under the periodic boundary conditions of the simulations. However, the increased system size makes their simulation more computationally expensive, which means that a compromise between system size and computational cost is routinely required. In practice this means that for the simulations of the type presented here some kind of image correction is necessary [108]. The

following discussion details the techniques employed to calculate the energies of defects in supercells.

Formation Enthalpy of a Neutral Defect

The formation energy of a neutral defect D is calculated using the following relation

$$\Delta H_f(D,0) = \left(E^{D,q} - E^H\right) + \sum_i n_i \left(E_i + \mu_i\right) \tag{3.27}$$

where E^H is the total energy of the host supercell, $E^{D,0}$ is the energy of the supercell with the neutral defect (charge 0), while E_i corresponds to the energies of the species in the simulation in their standard states, e.g. Cd(s) and O_2(g), n corresponds to the change in the number of atoms in an external reservoir of the element, thus n takes positive values when atoms are added to the reservoir and negative values when atoms are removed from it. Formation energies depend on the *relative* abundance of each species in the environment, which are represented by the chemical potentials μ_i. For example, the chemical potential of the metal (Me) in a generic oxide (MeO) corresponds to the energy of a reservoir of Me atoms in equilibrium with the system. Those Me atom states with energy values that are higher than μ_{Me} by a few k_BT will be empty, while those that are lower by same amount will be filled [109–111]. Hence high values of μ_{Me} correspond to Me-rich enrvironments, while low values correspond to Me-poor environments.

Formation Enthalpy of a Charged Defect

For a defect D in charge state q the formation energy is given by adding extra parameters to the equation already encountered for neutral defects as shown below:

$$\begin{aligned}\Delta H_f(D,q) = \; & \left(E^{D,q} - E^H\right) + \textstyle\sum_i n_i \left(E_i + \mu_i\right) \\ & + q\left(E_F + \epsilon^H_{VBM}\right) + E_{align}[q]\end{aligned} \tag{3.28}$$

The additional terms in this equation account for the exchange of electrons with the Fermi level (E_F), which is the chemical potential for the electrons and ranges from the VBM ($E_F = 0$eV) to the calculated CBM, ϵ^H_{VBM} is the VBM eigenvalue of the host bulk.

$E_{align}[q]$ is a correction used to align the VBM of the bulk and the defective supercells and also to correct for finite-size effects in the calculations of charged defects, performed using the freely available SXDEFECTALIGN code by Freysoldt *et al* [108]. The only extra parameter required for this scheme is the dielectric constant of the system, which is taken from experimentally determined values. An additional correction was made in order to account for band-filling effects [112, 113], and is especially necessary in the case of materials like CdO where defect states occupy strongly dispersive bands.

Chemical Potential Limits

As already discussed, the chemical potentials reflect the experimental growth conditions, which in the case of oxides can be metal-rich or oxygen-rich, and anything in between. However, their values are constrained by the condition that, in equilibrium, their sum must equal the calculated enthalpy of the host (H_f^{MeO}), which in the case of CdO corresponds to the total energy of the two atom unit cell:

$$\mu_{Me} + \mu_O \leq \Delta H_f^{\mathrm{MeO}} \tag{3.29}$$

The lower limit of μ_{O}, corresponds to a Me-rich/O-poor environment is determined by Me metal formation:

$$\Delta\mu_{\mathrm{Me}} = 0eV, \rightarrow \Delta\mu_O = \Delta H_f^{\mathrm{MeO}} \tag{3.30}$$

The upper bound of μ_{O} (Me-poor/O-rich) is limited by the formation of O_2:

$$\mu_{\mathrm{Me}} = \Delta H_f^{\mathrm{MeO}}, \rightarrow \Delta\mu_O = 0 \tag{3.31}$$

Note that this generalized description of the chemical potential limits for MeO does not take into account other stoichiometries of the metal oxide, such as MeO_2. An additional constraint is necessary in order to include this compound if its formation enthalpy lies within the limits already imposed by MeO, i.e. if MeO_2 has a lower

formation energy than MeO

$$\mu_{Me} + 2\mu_O \leq \Delta H_f^{\mathrm{MeO_2}} \tag{3.32}$$

Solution of this system of linear equations thus provides the set of chemical potential limits.

Thermodynamic Transition Levels

The presence of impurities and point defects often leads to the formation of new defect levels in the band gap of a material. These defect levels can be identified experimentally, however, there is no definite way of assigning a given defect level to a particular defect. The high degree of detail afforded by DFT simulation techniques means that they are becoming increasingly popular as a means to carry out this assignment. However, it is generally not possible to compare the single particle levels (SPLs), i.e. the raw eigenvalues (Kohn Sham states) of the defect state in the band structure, because experimental data is usually based on transitions from one charge state to another. Thus, to compare simulation results with experiment it is necessary to first calculate thermodynamic ionization (transition) levels. The thermodynamic transition levels (ionization levels) of a given defect, $\epsilon_D(q/q')$, correspond to the Fermi-level positions at which a given defect changes from charge state q to q':

$$\epsilon_D(q/q') = \frac{\Delta H^f(D,q) - \Delta H^f(D,q')}{q' - q} \tag{3.33}$$

The transition levels derived from this relation are typically plotted in a transition level diagram (TLD) and compared to experimentally derived trap levels. An example of how to generate one such diagram is presented in Figure 3.10, where the formation energies of oxygen defects in CdO for different charge states are plotted as a function of the Fermi energy (E_F) under both metal-rich/oxygen-poor and metal-poor/oxygen-rich conditions. The n-type defects (V_O) are shown as blue lines whereas the p-type ($\mathrm{O}_i^{\mathrm{per}}$) are shown as orange lines. For each defect type, the solid line corresponds to

the charge state with the lowest energy for a given value of E_F. The dots indicate where the transitions between charge states occur. Also shown in this diagram is the conduction band minimum (CBM) of the material [44].

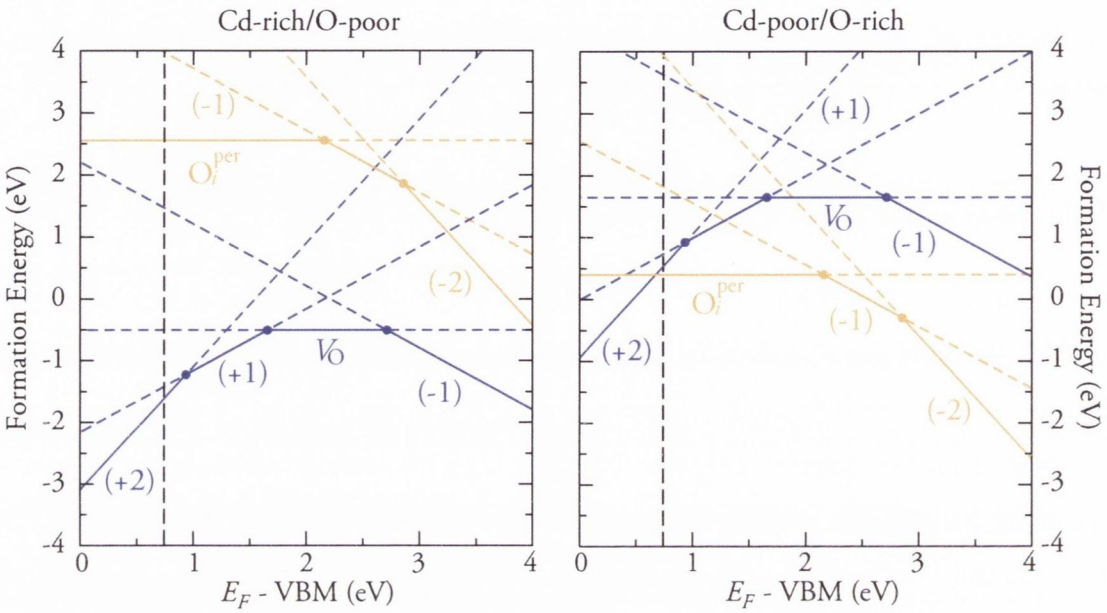

Figure 3.10: Transition level diagram for oxygen defects in CdO (a) cadmium-rich/oxygenpoor conditions and (b) cadmiumpoor/oxygenrich. The n-type defects (V_O) are shown as blue lines whereas the p-type (O_i^{per}) are shown as orange lines. The dots represent the transition levels ($\epsilon_D(q/q')$). The black dashed line indicates the position of the conduction band minimum (CBM) in CdO.

3.4 Molecular Dynamics

Molecular Dynamics can be thought of as a Determinist's dream; the ability to follow an individual atom's motion as a part of a bigger system of interacting particles and in this way gather information is a concept that provides as much appeal now as it did when the laws of motion were first elucidated. The equations of motion provide the relationships that govern the interactions between the various species that constitute the system under study as a function of time. In this way, it is possible to overcome energy barriers in the system in order to find the global minimum, *c.f.* static lattice

calculations. However, as the amount of real time modelled is currently very short, this is only true for small energy barriers in the order of a few k_BT, where k_B is the Boltzmann constant.

The motion of the particles in a system is governed by Newton's second law, which relates the forces acting on each particle to changes in their positions as follows

$$\mathbf{F}_i = m_i \frac{\partial^2 \mathbf{r}_i}{\partial t^2} = m_i \mathbf{a}_i \tag{3.34}$$

which indicates that the force $\mathbf{F}_i$ imparts an acceleration $\mathbf{a}_i$ to a particle i of mass m_i. Details on how this equation is applied in practice are provided in the sections below.

3.4.1 Finite Difference Method

Once the forces between the particles have been calculated it is necessary to integrate the equations of motion in order to obtain the time-correlated trajectories of the particles in the simulated system. The integration can be done in a variety of ways, but it generally involves using the Taylor expansion of the function (or integral) of interest and truncating it at different points; then, in some cases, one can make use of derivatives from previous steps to obtain better estimates of the quantities being calculated, namely, positions, velocities and forces.

A good integration algorithm must meet certain criteria. Firstly, it should allow for use of long timesteps, typically of the order of $10^{-14} - 10^{-15}$s. This is necessary because long timesteps allow exploration of a greater portion of the phase space (See Section 3.4.2), from which the thermodynamic data are calculated, for the same number of cycles. Secondly, the algorithm must conserve the total energy and momentum, as well as being time-reversible. The time reversibility of an algorithm refers to the ability to retrace the trajectory of the system in phase space if the momenta of the particles are reversed. Time-irreversible algorithms are not compatible with energy conservation, hence one expects long-term energy drift to affect these algorithms. Thirdly, the algorithm should follow closely the true phase space trajectory of the system, thus making

it possible to sample the desired constant energy surface. It is not expected that the algorithm exactly duplicates the true trajectory due to the finite precision available from computers and the accumulation of errors as the simulation proceeds, neither is it necessary to have the true trajectory because the properties calculated from the MD data depend on statistical averages [50].

Other important properties desirable in an integration algorithm are that it is fast, although its speed only has limited impact given that most of the CPU time is devoted to calculation of the forces, thus it is preferable to search for ways of optimizing the latter aspect of the calculation rather than the integration algorithm. In the early days of MD it was also important to keep memory usage to a minimum, however this restriction only applies to very large systems these days given that these hardware constraints have been reduced. Finally, maintaining the program is facilitated if the algorithm is easy to code.

Equation 3.35 represents the Taylor series expansion of particle positions from time t forward by a time step of δt to $t+\delta t.$, assuming the acceleration to be constant during the timestep

$$\mathbf{r}_i(t+\delta t) = \mathbf{r}_i(t) + \mathbf{v}_i(t)\delta t + \frac{\mathbf{a}_i(t)}{2!}\delta t^2 + \frac{\mathbf{b}_i(t)}{3!}\delta t^3 + \mathcal{O}(\delta t^4) \tag{3.35}$$

Similarly, the backward expansion is given by

$$\mathbf{r}_i(t-\delta t) = \mathbf{r}_i(t) - \mathbf{v}_i(t)\delta t + \frac{\mathbf{a}_i(t)}{2!}\delta t^2 - \frac{\mathbf{b}_i(t)}{3!}\delta t^3 + \mathcal{O}(\delta t^4) \tag{3.36}$$

By adding Equations 3.35 and 3.36 one eliminates all odd-order terms. This is the functional form of the time reversible Verlet algorithm

$$\mathbf{r}_i(t+\delta t) = 2\mathbf{r}_i(t) - \mathbf{r}_i(t-\delta t) + \mathbf{a}_i\delta t^2 + \mathcal{O}(\delta t^4) \tag{3.37}$$

Note that the local truncation error is of order $\mathcal{O}(\delta t^4)$, however the algorithm is said to be of third order. One source of error in this algorithm is the fact that the acceleration term $\mathbf{a}_i\delta t^2$, which is much smaller than $(2\mathbf{r}_i(t) - \mathbf{r}_i(t-\delta t))$, is added to this

difference thus leading to loss of precision. Also, in equation (3.37) there is no explicit calculation of the velocity $\mathbf{v}_i(t)$, which is required to calculate the kinetic energy. If one truncates after the second term in Equation 3.37 and rearranges the variables the following expression for the velocity is obtained

$$\mathbf{v}_i(t) = \frac{\mathbf{r}_i(t+\delta t) - \mathbf{r}_i(t-\delta t)}{2\delta t} + \mathcal{O}(\delta t^2) \tag{3.38}$$

Equation 3.38 is the first-order central difference estimator. Note however that this equation shows a second order truncation error, as a result the kinetic energies calculated from these velocities are less accurate than the potential energies calculated using Equation 3.37. An alternative version is the Verlet Leapfrog algorithm. This algorithm is numerically equivalent to the Verlet algorithm and it produces identical trajectories. However, instead of expanding the positions around t by $+\delta t$ and $-\delta t$ one expands the velocities at half-integer timesteps and uses these velocities to compute the new positions:

$$\mathbf{v}_i(t+\frac{\delta t}{2}) = \mathbf{v}_i(t-\frac{1}{2}\delta t) + \mathbf{a}(t)\delta t \tag{3.39}$$

$$\mathbf{r}_i(t+\delta t) = \mathbf{r}_i(t) + \mathbf{v}_i(t+\frac{1}{2}\delta t)\delta t \tag{3.40}$$

$$\mathbf{v}_i(t) = \frac{1}{2}\left[\mathbf{v}_i(t+\frac{1}{2}\delta t) + \mathbf{v}_i(t-\frac{1}{2}\delta t)\right] \tag{3.41}$$

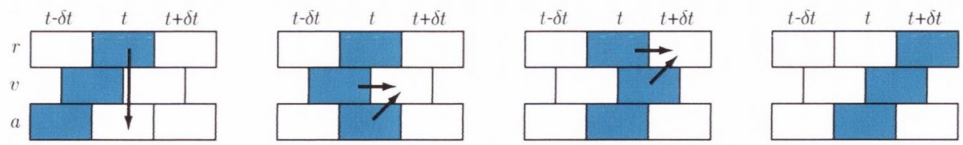

Figure 3.11: Schematic representation of the Verlet leapfrog algorithm.

The leapfrog algorithm updates the velocities before the positions are changed, as illustrated in Figure 3.11 [114]. The main advantage of this algorithm over the original Verlet (Equation 3.37) is that here the small difference between two large quantities

is no longer computed as was the case with Equation 3.38. Moreover, having the velocities explicitly stated in the algorithm makes further manipulations like velocity scaling much easier.

In choosing a time step δt for calculations one must also take into consideration that there are two types of errors involved in the numerical integration of the equations of motion, namely the truncation error and the round-off error. The truncation error appears when terms in the Taylor expansion are omitted from the calculation; this means that in the Verlet algorithm the acceleration is assumed to be constant for the duration of the timestep, but this assumption is only true in the limit of an infinitely small timestep. On the other hand, the round-off error comes from the finite precision at which the values being calculated can be stored; therefore, as the calculation proceeds these errors increase exponentially and after a number of steps the dynamic connection between points along the trajectory becomes disrupted (this effectively means that Molecular Dynamics is not a truly deterministic method); both truncation and round-off errors combine into a global error. One must then compromise on the time step chosen for the simulation in order to sample the phase space at a good resolution level, whilst reducing the effect of truncation and round off errors. In order to decide upon an acceptable timestep it is necessary to carry out a number of trial runs and monitor the conservation of total energy to a given level of accuracy; this will allow the identification of a critical value for δt at which the algorithm becomes unstable, then the chosen timestep should be smaller than the critical value. Fortunately, the time averages that are calculated in MD can tolerate errors in particle trajectories. In fact, the errors introduced as the calculation proceeds could be thought of as uncontrolled perturbations that are expected also in physical systems.

3.4.2 Ensembles

Microcanonical ensemble

A statistical ensemble relates macroscopic observables, like temperature and pressure, to the microscopic information from MD simulations. Direct solution of Equation

3.34 provides the simplest form of molecular dynamics simulations, which are those performed on thermodynamically isolated systems, i.e. those which do not exchange matter or energy with their surroundings, thus their number of particles (N), total energy (E) and volume (V) remain constant, while the temperature (T) and the pressure (P) are allowed to fluctuate. For this reason this ensemble is typically known as NVE. Under this set of conditions the total Hamiltonian (H_{Tot}) of the system is given by

$$H_{NVE}(\mathbf{p}_N, \mathbf{r}_N) = E_K(\mathbf{p}_N) + U(\mathbf{r}_N) \tag{3.42}$$

where E_K is the kinetic energy and U is the potential energy and the phase space of the system is described by the position ($\mathbf{r}_N$) and momentum ($\mathbf{p}_N$) of each particle. This ensemble is seldom used in practice, however, because of the severe restriction presented by the fact that it corresponds to isolated systems with few experimental counterparts.

Canonical ensemble

In the canonical ensemble (NVT) the system temperature is held constant by coupling it to a heat bath. In this case, each point in phase space is sampled with a probability equal to the the Boltzmann factor e^{-H/k_BT}. Traditionally, phase space sampling along the NVT ensemble has been performed using Monte-Carlo methods, however these simulations do not provide time-correlated particle trajectories, but instead each step depends only on the previous one. One of the most popular implementations of the canonical ensemble is the method proposed by Nosé [115, 116] and improved by Hoover [117]. Within this formalism, the Lagrangian of the system is increased by an additional degree of freedom that is coupled to the kinetic energy of the system. It can be thought of as a friction factor that is added in order to adjust the velocities of the system. To understand how this thermostat is implemented it is first necessary to clarify how the

temperature is related to the kinetic energy

$$T(t) = \sum_{i=1}^{N} \frac{|\mathbf{p}_i^2|}{2m_i} = \frac{k_B T}{2}(3N - N_c) \tag{3.43}$$

In Equation 3.43 N_c is the total number of independent internal constraints (fixed bond lengths and angles), which in the case of a periodic box with total linear momentum of zero, as used here, is 3. The term $(N - N_c)$ is also expressed as N_{df} to indicate the total number of degrees of freedom in the system. The mechanism by which the Nosé-Hoover method modifies the laws of motion [118], and thus the temperature, is as follows

$$\mathbf{a}_i = -\frac{\partial U(\mathbf{r}_i)}{\partial \mathbf{r}_i} - \mathbf{p}_i \frac{p_\eta}{Q} \tag{3.44}$$

where η is the friction coefficient whose time dependence is given by

$$\frac{d\eta}{dt} = \frac{p_\eta}{Q} \tag{3.45}$$

and Q corresponds to the effective mass of the thermostat

$$Q = N_{df} k_B T_{ext} \tau^2 \tag{3.46}$$

Here, T_{ext} is the temperature of the extended system, i.e. that which is being simulated as well as the reservoir, τ is typically called the relaxation time and it is a free parameter that models the strength of the coupling of the system to the thermostat. A small value of τ yields a large derivative for η and hence a large additional friction coefficient acting on the motion of the particles; thus, this case is said to be strongly coupled. The effective Hamiltonian used in this method is therefore given by

$$H_{NVT} = U + \sum_{i=1}^{N_{df}} \frac{\mathbf{p}_i^2}{2m_i} + \frac{\mathbf{p}_\eta^2}{2Q} + N_{df} k_B T \eta \tag{3.47}$$

Notwithstanding, Martyna *et al.* [119, 120] demonstrated that the dynamics from the Nosé-Hoover thermostat are not guaranteed to produce a canonical distribution.

The solution they proposed prescribes the use of chains of thermostats rather than a single one. The thermostat chains (M) couple the system to a first thermostat η_1, which is in equilibrium with the system under study, while successive thermostats η_j are at equilibrium with the next thermostat in the chain η_{j+1}. The equations of motion now become

$$\mathbf{a}_i = -\frac{\partial U(\mathbf{r}_i)}{\partial \mathbf{r}_i} - \mathbf{p}_i \frac{p_{\eta_1}}{Q_1} \tag{3.48}$$

$$\frac{d\eta_j}{dt} = \frac{p_{\eta_j}}{Q_j} \tag{3.49}$$

$$\mathbf{a}_{\eta_1} = \left(\sum_i^{N_{df}} \frac{\mathbf{p}_i^2}{m_i} - N_{df} k_B T \right) - p_{\eta_1} \frac{p_{\eta_2}}{Q_2} \tag{3.50}$$

$$\mathbf{a}_{\eta_j} = \left[\frac{p_{\eta_{j-1}}^2}{Q_{j-1}} - k_B T \right] - p_{\eta_j} \frac{p_{\eta_{j+1}}}{Q_{j+1}} \tag{3.51}$$

$$\mathbf{a}_{\eta_M} = \left(\frac{p_{\eta_{M-1}}^2}{Q_{M-1}} - k_B T \right) \tag{3.52}$$

and the Hamiltonian is

$$H_{NVT} = U + \sum_{i=1}^{N_{df}} \frac{\mathbf{p}_i^2}{2m_i} + \frac{p_\eta^2}{2Q} + N_{df} k_B T \eta_1 + \sum_{j=2}^{M} k_B T \eta_j \tag{3.53}$$

Isothermal-isobaric ensemble

The isothermal-isobaric, or NPT, ensemble produces phase space averages that can be directly compared to experimental data given that these are the typical conditions that are encountered. The equations of motion were derived by Martyna *et al.* [120] and couple a thermostat of position η and momentum p_η with a barostat of momentum p_ϵ as follows

$$\mathbf{v}_i = \frac{\mathbf{p}_i}{m_i} + \mathbf{r}_i \frac{p_\epsilon}{W} \tag{3.54}$$

$$\mathbf{a}_i = -\frac{\partial U(\mathbf{r}_i)}{\partial \mathbf{r}_i} - \mathbf{p}_i \frac{p_\epsilon}{W} - \mathbf{p}_i \frac{p_\eta}{Q} \tag{3.55}$$

where the change in volume with time is given by

$$\frac{dV}{dt} = \frac{dV p_\epsilon}{W} \tag{3.56}$$

for a given set of internal, P_{int}, and external, P_{int}, pressures

$$a_\epsilon = dV \left(P_{\text{int}} - P_{\text{ext}}\right) - \frac{p_\eta p_\epsilon}{Q} \tag{3.57}$$

the thermostat parameters thus become

$$\frac{d\eta}{dt} = \frac{p_\eta}{Q} \tag{3.58}$$

$$a_\eta = \sum_{i=1}^{N_{df}} \frac{\mathbf{p}_i^2}{m_i} + \frac{p_\epsilon^2}{W} - \left(N_{df} + 1\right) k_B T \tag{3.59}$$

The Hamiltonian for this ensemble is

$$H_{NPT} = \sum_{i=1}^{N_{df}} \frac{\mathbf{p}_i^2}{2m_i} + \frac{p_\epsilon^2}{2W} + \frac{p_\eta^2}{2Q} + U + \left(N_{df} + 1\right) k_B T \eta + P_{\text{ext}} V \tag{3.60}$$

3.4.3 Equilibration and production dynamics

In order to initialize an MD simulation it first necessary to assign random velocities to each particle using a random number generator under the constraint of the Maxwell-Boltzmann distribution in order to reach the desired thermodynamic state point. The system is then allowed to come to equilibrium from the initial positions and velocities *prior* to data collection at a given temperature and pressure. The aim of this process is to create a thermalized distribution of velocities. This equilibration period usually lasts in the order of several pico seconds. The subsequent production period is characterized by simulations that are sufficiently long to allow the convergence of the properties

under study. Throughout this period, data is collected at a set number of intervals. The process by which properties of the bulk material are drawn out of the mass of trajectory data is known as ensemble averaging (Section 3.4.2).

3.4.4 Ergodicity

Thus far it has been shown that the MD method proceeds by repeatedly integrating the trajectories in phase space along the constant energy hyper surface for a relatively small number of particles. The ergodic hypothesis assumes that the calculated time average for a small number of particles over a long time is equivalent to averaging over a large number of particles for a short time

$$\langle X \rangle = \lim_{\tau \to \infty} \frac{1}{\tau} \int_0^{\tau} X(t) dt = \lim_{M \to \infty} \frac{1}{M} \sum_{i=1}^{M} X_i \tag{3.61}$$

Where X is the property being measured, $\langle X \rangle$ is its average, τ is the time and M is the number of steps.

3.4.5 Mean Square Displacement

The ionic conductivity (σ) of a material can be found from MD by calculating the Mean Square Displacements (MSD) for each species in the system. The MSD ($\langle \Delta r(t)^2 \rangle$) is given by:

$$\left\langle \Delta r(t)^2 \right\rangle = \frac{1}{N} \sum_{i=1}^{N} \Delta \mathbf{r}_i(t)^2 \tag{3.62}$$

for every particle i, which has travelled a distance $\Delta \mathbf{r}_i(t)$ in time t. Information about ionic conductivity is obtained from an MSD vs time plot given that

$$D = \lim_{t \leftarrow \infty} \frac{1}{6t} \left\langle \Delta r(t)^2 \right\rangle \tag{3.63}$$

where D is the self-diffusion coefficient [121], i.e., the slope of the plot. One can then

use this value to calculate σ by using the Nernst-Einstein equation:

$$\sigma = \frac{Nq^2D}{k_BTH_R} \tag{3.64}$$

In Equation (3.64) N is the number of charge carriers per unit volume, q is the charge on the carriers, T is the temperature and H_R is the Haven coefficient, which is normally set to 1. [122] Another important feature of MD simulations is that one is able to follow the trajectory of individual species so that properties of interest can be calculated separately, for example, the anionic and cationic mobilities can be calculated independently.

3.4.6 Pair correlation function

The pair correlation function $g_{ij}(r)$, also known as Radial Distribution Function (RDF), gives an indication of the probability of finding a particle at a certain distance from another particle (these may be of the same or different species) and it provides valuable structural information which can be compared with data obtained from experiment. It is expressed as follows:

$$g_{ij} = \frac{1}{4\pi r^2 \Delta r} \frac{n_{ij}(r)}{\rho_j} \tag{3.65}$$

where $n_{ij}(r)$ is equal to the number of atoms of type j located at a distance between r and $r+\Delta r$ from an atom of type i and ρ_j is the number density of atoms of type j, given by $\rho_j = c_j\rho_0$. These partial radial distribution functions can be easily calculated from the simulation output and is obtained as average over the simulation. The total radial distribution function $G(r)$ is calculated from the individual partial radial distribution functions $g_{ij}(r)$ by using weighting parameters, which in this case are the concentrations of each species c_i and their neutron scattering lengths b_i:

$$G(r) = \sum_{i,j=1}^{n} c_i c_j b_i b_j g_{ij}(r) / \sum_{i=1}^{n} (b_i c_i)^2 \tag{3.66}$$

3.5 Summary

This chapter highlighted some of the underlying theory necessary to perform the simulations presented throughout this work. Section 3.2 illustrated how the periodicity in crystals can be exploited to facilitate the simulation process. Sections 3.3 and 3.4 provided the framework necessary to utilize the potential energy models from Chapter 2 in both static and time dependent calculations.

4

Interaction Potential for doped ceria

4.1 Introduction

This Chapter details the methods used to parametrize IPs. The parameter set obtained for doped ceria is tested by means of comparison to structural and dynamic experimental data. Finally, the model system YDC is employed to investigate the effects that determine the drop in ionic conductivity as the dopant concentration is increased as was mentioned in Section 1.2.3.

4.2 Properties of pure and doped ceria

In its pure stoichiometric form CeO_2 is pale yellow and has a cubic fluorite-type structure with space group $Fm\bar{3}m$ and lattice constant 5.411 AA at room temperature [123], Figure 4.1 (a) [124], which is maintained up to its melting point. This represents an advantage in terms of stability over the more commonly used SOFC electrolyte YSZ which only adopts this structure after it is stabilized by doping [15]. The fluorite structure is advantageous because it provides the space required for oxide anion mobility. In addition to its role as an electrolyte in SOFCs, ceria has found applications in several

technologically relevant areas such as catalysis [8, 125, 126]. In catalysis, it plays an important role due to its oxygen storage capacity, which stems from the change in oxidation state undergone by the Ce^{4+} cations and release/absorption of oxygen under different environments [125]. These properties of CeO_2 are made use of in Three-Way Catalysts (TWC), where it assists in the oxidation of CO to CO_2 under reducing conditions through the reduction of Ce^{4+} to Ce^{3+}. Under fuel-lean conditions, the reduction of NO to N_2 is assisted by the oxidation of Ce^{3+} to Ce^{4+}.

Doping ceria with RE cations, such as Sm, Gd, or Y leads to high ionic conductivity in the intermediate temperature range (500 – 800°) [18, 127]. The remainder of this thesis abbreviates the names of RE-Doped Ceria systems ($Ce_{1-x}RE_xO_{2-x/2}$) to ScDC, YDC, GDC, SmDC, NDC and LDC. Several synthetic routes for producing doped CeO_2 ceramics have been reported in the literature, in particular Y-doping has been achieved by methods such as precipitation of metal oxides from the corresponding nitrates [121, 128], solid state reactions of pelletized mixtures of Y_2O_3 and CeO_2 [15, 129], as well as the sol-gel method [130]. Y is highly soluble in ceria, in fact, at 1500°C ceria can accommodate 20.5 mol% Y_2O_3 into its lattice [129].

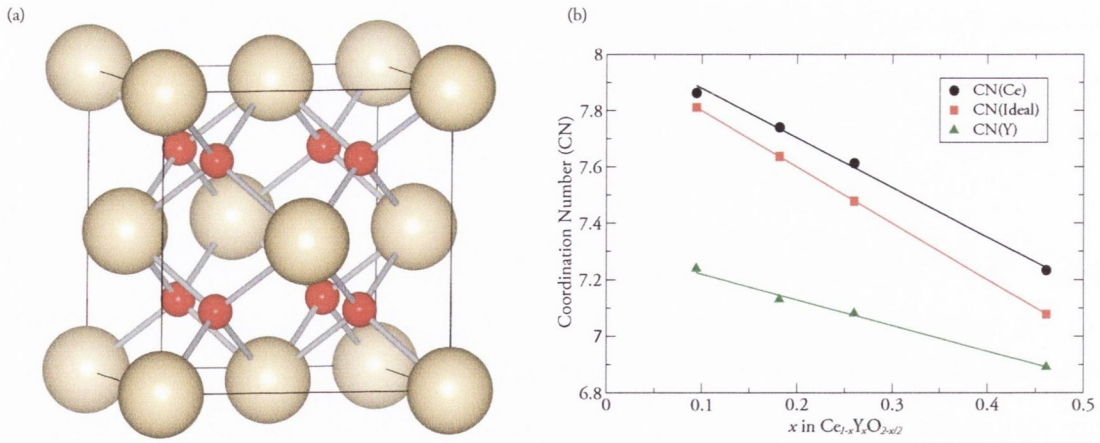

Figure 4.1: (a) Fluorite-type structure seen in CeO_2 [10]. It consists of an array of anions (red) occupying the tetrahedral sites in an fcc array of cations (gold). (b) Variation in the average cation coordination number (CN) with Y^{3+} content [15].

However, Magic-Angle-Spinning NMR (^{89}Y MAS-NMR) studies [15] have shown

that the average coordination number of Y cations in YDC is smaller than expected if the oxygen vacancies were randomly distributed, suggesting association between the dopant cations and the vacancies in the system, such as, Y^{3+}-$V_O^{\cdot\cdot}$-Y^{3+}. Figure 4.1 (b) shows the change in average coordination numbers as a function of Y^{3+} concentration. The coordination numbers observed were all below those for a system where the same number of vacancies are distributed at random, however, depending on the fabrication method, Y_2O_3-like clustering cannot be excluded. X-ray diffraction data from the same study showed that increasing the Y content reduces the unit cell volume due to the oxygen vacancies generated, despite the fact that the Y^{3+} cation is slightly larger than Ce^{4+}, 1.019Å and 0.97Å respectively [131]. Previous studies have looked at ageing effects in YDC and found that the conductivity increases with time (heating at 1000°C for 8 days) for samples with Y^{3+} contents up to 20%, due to improved grain boundary conductivity. This is in sharp contrast to YSZ electrolytes whose conductivity decreases with time due to phase transitions that take place under different conditions [129].

As with all other materials of industrial significance, it is very important to characterize the fabrication process of doped-ceria electrolytes to ensure reproducible results are obtained. To this end, the availablity of high purity powders with SiO_2 concentrations below 50 ppm is essential to dispel confusion regarding the optimum dopant concentration required to achieve the highest ionic conductivity. SiO_2 is seen to accummulate at the grain boundaries, forming amorphous phases [12, 18, 129], and it is associated with reduced oxide ion conductivity. These impurities may come from the ore, the furnace refractories, where the sintering takes place, and even from silicone grease used in the SOFC test apparatus [12]. It is this reduced ionic (and electronic) conductivity at grain boundaries with varying levels of impurities which is reported to cause, at least in part, the discrepancies observed in total conductivities. Another reason to exclude siliceous impurities from the samples is that they can segregate to electrode-electrolyte three-phase boundary regions and dramatically increase the electrode resistance. The negative effect of grain boundaries on the ionic conductivity is minimized by fabrication of electrolytes with large grain sizes and the pure reagents.

4.3 Potential Parametrization

The DIPPIM potential is parametrized by simultaneously minimizing the objective functions presented in Equations (4.1) and (4.2) using a non-gradient simplex and MIGRAD method [132], as implemented in the package MINUIT [133, 134]. These functions use χ^2 testing to compare the dipoles and forces obtained from DFT calculations for a given ionic configuration. Here, $\mu_{i,\alpha}^{\mathrm{DFT}}$ represents the dipole along the α Cartesian axis for ion i as given by DFT, while $\mu_{i,\alpha}^{\mathrm{IP}}$ represents the value obtained from the potential model. The forces are handled in a similar manner, i.e. $F_{i,\alpha}^{\mathrm{DFT}}$ is the DFT value against which $F_{i,\alpha}^{\mathrm{IP}}$ is compared. Therefore, the values for A_P and A_F are an indication of how well the potential model describes a given set of *ab initio* data. This method to generate IPs is commonly known as force matching [135–137]. Both the dipole and the force components are given an equal weighting in the calculation of the total χ^2.

$$A_P\left(\{\chi\}\right) = \frac{\sum_{i,\theta,A}\left|\zeta_{i,\theta}^{A}\left(\{\chi\}\right) - \zeta_{i,\theta}^{A,DFT}\right|^2}{\sum_{i,A}\left|\zeta_{i,\theta}^{A,DFT}\right|^2} \tag{4.1}$$

$$A_F\left(\{\chi\}\right) = \frac{\sum_{i,\theta,A}\left|F_{i,\theta}^{A}\left(\{\chi\}\right) - F_{i,\theta}^{A,DFT}\right|^2}{\sum_{i,A}\left|F_{i,\theta}^{A,DFT}\right|^2} \tag{4.2}$$

Figure 4.2 illustrates the steps carried out in the development of an IP. The process starts by first performing DFT calculations on a number of high temperature ionic configurations. Such configurations may be obtained using an initial ansatz interatomic potential model or from *ab initio* MD simulations. The forces on each species were then determined directly from each DFT calculation and the dipoles were obtained from a Wannier analysis of the Kohn-Sham (KS) wave functions [138, 139]. The set of MLWFs generated made it possible to associate orbitals with each ion (cf. the KS description where they are delocalized throughout the simulation cell), this, in turn, provided a detailed account of the polarization undergone by each ion due to the electrostatic field of the surrounding environment [137]. Once the information about forces and dipoles

is gathered from the *ab initio* calculations, the parameters in the IP were fitted to them [137] DFT's known failure to include Van der Waals (dispersion) interactions [58] made it necessary to add the empirically derived dispersion terms after the fit. A correct representation of the dispersion interactions is necessary in order to accurately represent the material's density and stress tensor.

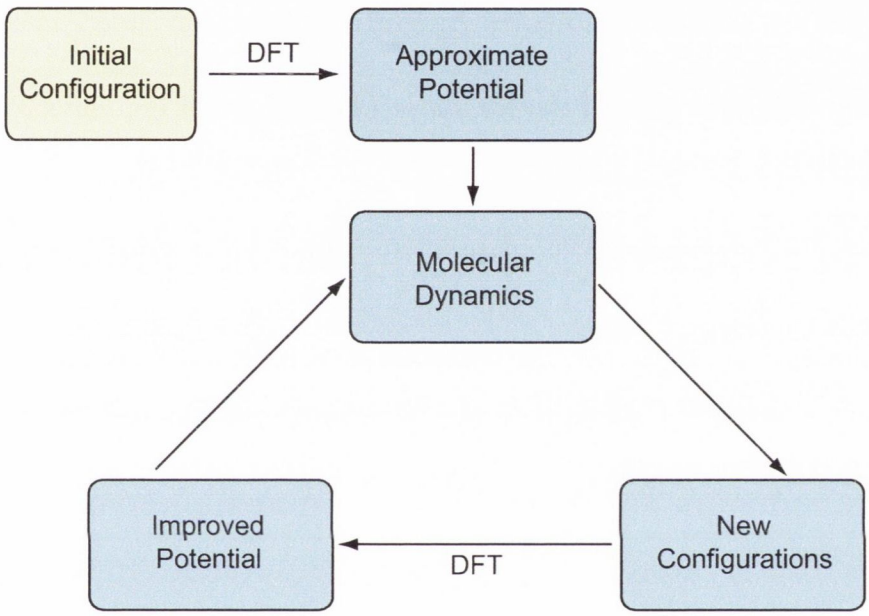

Figure 4.2: Flow chart illustrating the potential development process.

The YDC potential was parametrized by performing DFT calculations, in the local density approximation parametrized (LDA), using the CPMD code [140]. For this system, the simple DFT approach is known to give the correct valence states (Ce^{4+} and Y^{3+}), so that a correction like DFT+U functional was not needed. Twelve 2 $\times$ 2 $\times$ 2 supercells with $Ce_{0.5}Y_{0.5}O_{1.75}$ compositions and a total of 88 atoms were constructed. Each model supercell was obtained from high temperature (2500 K) MD simulations that were run for 50 ps in order to reach structural equilibrium. Figure 4.4 illustrates one of the cells used in the parametrization process. The forces on each species were determined directly from each DFT calculation, and the dipoles were obtained from a Wannier analysis of the Kohn-Sham (KS) wave functions [138]. In this case, the delocalized optimal KS eigenvectors $\left(\{\Psi_n\}_{n=1,N}\right)$ are transformed into a set of

Maximally Localized Wannier Functions (MLWFs) that are associated with individual ions and from which the ionic multipole moments can be calculated [138, 139]. In this work, MLWFs were determined by unitary transformation of the KS eigenvectors according to the following relationship

$$|w_n\rangle = \sum_{m=1}^{N} \mathbf{U}_{mn} |\Psi_n\rangle \tag{4.3}$$

where the sum runs over all the KS states $\{\Psi_n\}_{n=1,N}$, and the unitary matrix $\mathbf{U}$ was determined by iterative minimization of the wannier spread Ω

$$\Omega = \sum_{n=1}^{N} \left(\langle r^2 \rangle_n - \langle \mathbf{r} \rangle_n^2 \right) \tag{4.4}$$

For each ion i in the system, the component along the α Cartesian axis of the dipole moment, μ_i^α, is calculated from the Wannier function Centre (WC) positions, r^n, according to

$$\mu_i^\alpha = -2 \sum_{i=1}^{N} r_\alpha^n \tag{4.5}$$

Once the information about *both* forces and dipoles was gathered from the *ab initio* calculations, the parameters in the interatomic potential were fitted to them. The value of the objective functions obtained were 0.289 and 0.145 for the forces and dipoles, respectively, and an average of 0.217. These values compare favourably with those previously reported for $Zr_2Y_2O_7$–Y_3NbO_7 [90, 141]. Figure 4.3 provides a visual representation of the match between the forces (top panel) and dipoles (bottom panel) along the x-axis obtained from DFT (black) and DIPPIM (red). Only six of the twelve configurations used to parametrize the potential are shown. Each point along the abscissa represents an ion, i.e., the first 56 ions in each configuration are O, followed by 16 Y and 16 Ce. The close agreement seen indicates that the potential model used in this study is able to reproduce the *ab initio* data. However, there is a clear tendency for the DIPPIM values to deviate from those obtained from DFT for all species in cases where the forces have large magnitudes. This issue might arise from the parametrization

procedure employed or because a more complex potential model is required. An important property of this model is that the parameter values derived for a given species are transferable across different coordination environments and system compositions, thus, values for Ce and O can be used in systems with a different dopant or in studies of ceria co-doping, as shall be seen in Chapter 5. The resulting parameters are reported in 4.1. One problem with DFT calculations is the uncontrolled representation of the dispersion interaction. Although dispersion energies constitute only a small fraction of the total energy, they have a considerable influence on transition pressures and, in particular, on the material density and stress tensor. For this reason, the dispersion parameters were not included in the fits, as discussed by Madden *et al.* [91], but were added afterward. The parameters from refs. [90, 142] were used.

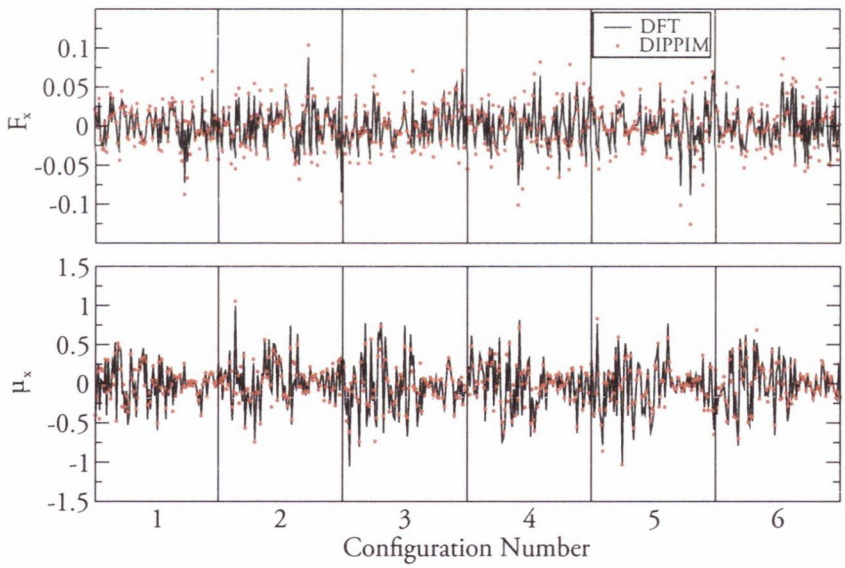

Figure 4.3: Comparison of forces, F_x, (top) and dipoles, μ_x, (bottom) along the x-axis for six of the twelve configurations used to parametrize the interaction potential. Configuration 4 corresponds to Figure 4.4. All values reported are reported in atomic units.

A potential was parametrized for reduced CeO_2 as well. Similarly as above, first a short *ab initio* MD simulation was performed on $CeO_{1.875}$ at high temperature. This configuration was used to calculate the forces acting on the ions and these, in turn,

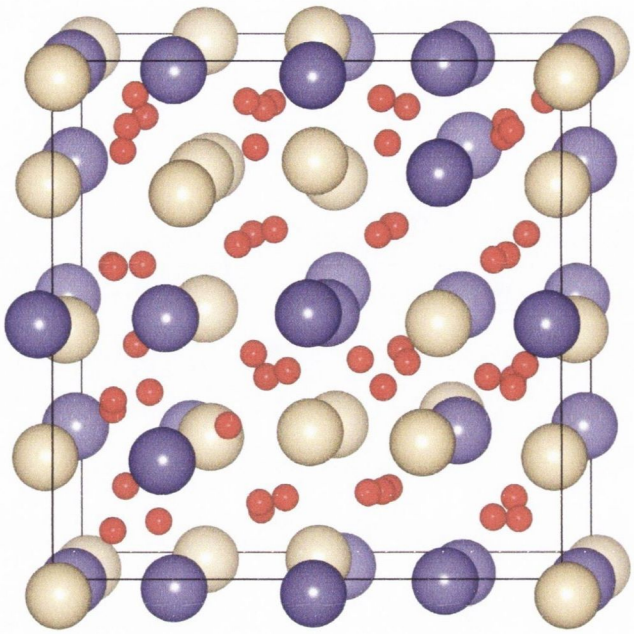

Figure 4.4: One of the twelve configurations used to parametrize the DIPPIM potential. Gold, blue and red represent cerium, yttrium and oxygen, respectively.

were used for the fitting procedure. These calculations were performed with the Vienna Ab-Initio Simulation Package (VASP) [98, 143] within the DFT+U framework. A value of $U = 7\,\text{eV}$ was chosen to ensure correct localization of the f electrons. The Ce^{3+} cations were identified as those with spin 1, while the Ce^{4+} ones have no spin. The Ce^{3+} and Ce^{4+} cations are then treated as two *different* cationic species in the potential parametrization and separate terms are obtained to describe the interactions between, for instance, Ce^{4+} - O^{2-} and Ce^{3+} - O^{2-}. The parameters for the Ce^{4+} - O^{2-} and O^{2-} - O^{2-} were then fixed to the values obtained before for the Y-doped CeO_2 system, so that these parameters are all consistent and can be used together. This procedure is equivalent to treating the Ce^{3+} cations as a dopant species, in the same way as was done for Y. While an ionic model for reduced CeO_2 might not be justified *a priori*, the picture arising from DFT+U calculations and experiments seems to confirm this model. The f electrons are, indeed, found to be strongly localized on the Ce^{3+} cations in agreement with an ionic picture. Also, a recent study on Ce^{3+}/Ce^{4+} ordering

in ceria nanoparticles [144] showed that strikingly similar relative energy ordering of the isomers and atomic scale structural trends (e.g., cation–cation distances) are obtained in both the DFT and interionic-potential calculations, which, again, proves the validity of this approach. The resulting parameters for the Ce^{3+} cations are reported in 4.1. The potential parametrization was performed using two DFT codes because the CPMD package does not have an implementation of the DFT+U framework needed to describe reduced CeO_2, while functionality required for the Wannier analysis was not available in VASP at the time of writing.

Finally, the same procedure was repeated to include other cations. In this case we obtained parameters for La^{3+} and Gd^{3+}. This was again done by performing a short MD simulation on Gd and La-doped CeO_2 at high temperature and using the final configuration to calculate forces to which the potential parameters can be fitted. Once again, we fixed the parameters for the $Ce^{4+} - O^{2-}$ and $O^{2-} - O^{2-}$ to the values obtained before for the Y doped CeO_2 system. This ensures that these parameters are all consistent and allows the study of mixed systems - such as, for instance, partially reduced, and Y and La doped CeO_2. The resulting parameters for the dopant cations are reported in 4.1. This procedure can be repeated for as many dopant cations as desired.

The quality of the potentials can be assessed by comparing model predictions to experimental data, since no experimental data was used in the optimization of the model parameters. In the following section we present our predictions, using the herein developed IPs, for lattice parameters, local crystalline structure, thermal and chemical expansion, and elastic constants, and their comparison with the experimental values. The way these quantities are calculated is described in each section.

4.4 Potential Validation

In a recent paper, Xu *et al.*[145] compared six different interatomic potentials for ceria available in the literature [146–151] and tested their accuracy by reproducing a series of

Table 4.1: Parameters of the LDA DIPPIM potential. All values are in atomic units.

	O-O	Y-O	Ce^{4+}-O	Ce^{3+}-O	Gd-O	La-O
A^{ij}	55.3	111.1	105.9	218.7	236.9	98.6
a^{ij}	6.78	1.377	1.269	1.473	1.566	1.257
B^{ij}	50000	50000	50000	50000	50000	50000
b^{ij}	0.85	1.35	1.4	1.35	1.35	1.35
b_D^{ij}	1.67	0.58	0.75	1.82	1.93	1.69
c_D^{ij}	1.62	-.33	-.45	2.92	-.44	0.00
b_D^{ji}	1.73	1.67	1.75	3.50	3.5	3.5
c_D^{ji}	0.45	-.91	-0.47	0.00	0.00	0.00
C_6^{ij}	53	12	12	12	12	12
C_8^{ij}	1023	240	240	240	240	240
b_{disp}^{ij}	1.0	1.5	1.5	1.5	1.5	1.4
$\alpha_{O^{2-}}$	14.9					
$\alpha_{Y^{3+}}$	2.60					
$\alpha_{Ce^{4+}}$	5.0					
$\alpha_{Ce^{3+}}$	11.2					
$\alpha_{Gd^{3+}}$	6.8					
$\alpha_{Sm^{3+}}$	10.8					

experimental data (lattice constants, thermal expansion, chemical expansion, dielectric properties, oxygen migration energy and mechanical properties). Two main limitations were found. The first was that none of the reviewed potentials could reproduce all the fundamental properties under study, although some displayed higher accuracy than others. While all the potentials could reproduce the static properties, such as lattice parameters and elastic constants, they all failed at reproducing the thermal expansion coefficient, and to a lesser degree the oxygen migration energy, for pure CeO_2. Indeed, some potentials gave thermal expansion coefficients which were one order of magnitude smaller than the experimental one and also severely underestimated the oxygen migration energy. Thermal and chemical expansion properties of ceria are particularly important in the context of SOFCs given that differential expansion of the components has a detrimental effect on the long term durability of the fuel cells [152, 153]. A second problem evinced from the study by Xu *et al.* was that not all the interatomic

potentials have a complete set of parameters available for the study of both doped and reduced CeO_2. The potential by Inaba *et al* [148], for instance, properly reproduces the thermal expansion coefficient and the elastic properties, but cannot be tested for chemical expansion because it does not have parameters for Ce^{3+}.

The first limitation can be easily understood by looking at 4.5, where we show the shape of a typical interatomic potential. Such a potential is harmonic in the vicinity of the equilibrium position (red curve is a parabola fitted to the potential) but at distances away from the equilibrium position, it deviates from that shape and becomes anharmonic. It is this anharmonicity which is responsible for the thermal expansion observed in solid materials. A potential's failure to reproduce the experimental thermal expansion means that it is not properly parametrized and/or the potential's shape is not correct at distances greater than the equilibrium position. In particular the strong underestimation of the thermal expansion coefficient, as observed by Xu *et al.*, indicates that the potential maintains a harmonic description of the system in regions where this approximation is not valid. The potential also deviates from the harmonic behavior at distances shorter than the equilibrium one, with the interatomic potential being more repulsive than its harmonic approximation. This feature plays an important role in the calculation of the oxygen migration barrier. When an oxygen ion hops from one site to another, it has to squeeze between neighboring cations, so that the average interatomic distance between the oxygen and these cations is much smaller than at equilibrium. If a potential's description of this interaction is predominantly harmonic, then the repulsion between these ions will be underestimated and, consequently, the migration energy barrier will be underestimated, as observed by Xu *et al.*

It would seem from the above analysis that the limitations of the existing potentials are due to the fact that they are too harmonic. This might be due to the way they are parametrized, given that they are optimized by fitting their parameters to a small data set of experimental properties, usually elastic constants and lattice parameters. These

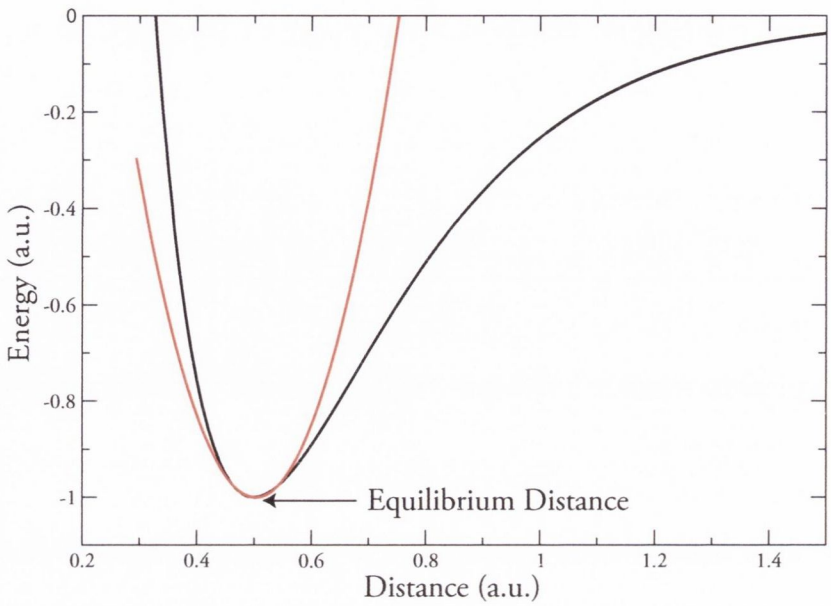

Figure 4.5: The shape of a typical interaction potential (black line) and of its harmonic approximation (red line).

are equilibrium or near-to-equlibrium properties, which allow the sampling of only a small region of the potential energy surface (PES) of the system, around the equilibrium distance. Little or no information is provided about the long- or short-distance behavior where the potential becomes anharmonic. In this work we use a different methodology, which was used successfully for similar oxide systems [90, 142, 154–162], to parametrize interatomic potentials for stoichiometric, reduced and doped CeO_2. The key idea of this methodology is that the potential's parameters are fitted to a series of DFT calculations on high-temperature, distorted CeO_2 configurations. This allows sampling wider regions of the PES than those accessed by macroscopic equilibrium observables. We obtain parameters for stoichiometric, reduced and doped (La, Gd and Y) CeO_2 and test them against the experimental data. The agreement is quite good for all the studied properties, including thermal expansion and oxygen migration energy barriers. This methodology can be easily extended to other dopant cations in ceria or similar materials.

4.4.1 Thermal expansion

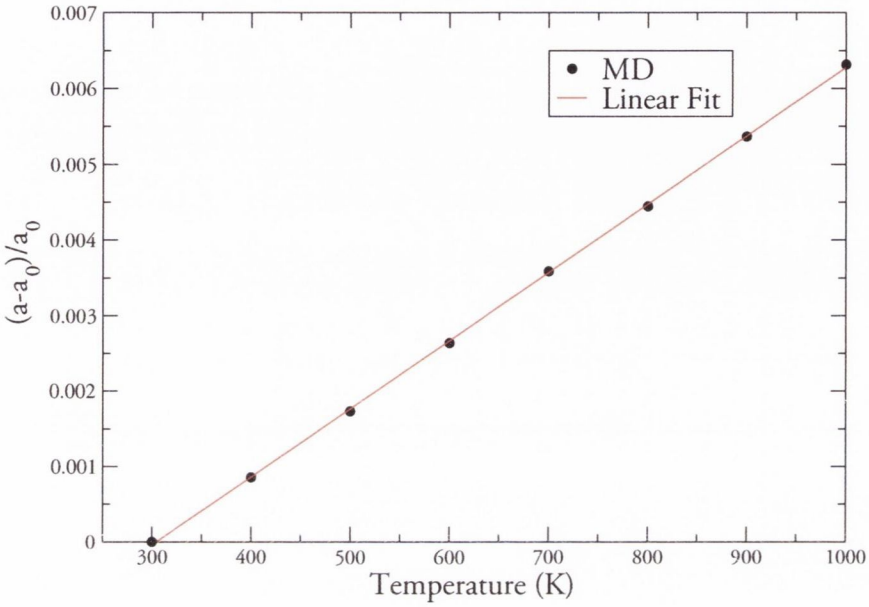

Figure 4.6: Simulated lattice expansion (points) *Vs* temperature for stoichiometric CeO_2. The red line represents a linear fit of the MD data. The thermal expansion, α, extrapolated from the fit is 9.0 x 10^{-6} K^{-1}.

Xu *et al.* [145] found that most potentials in the literature fail to reproduce the thermal expansion of this material. For this reason, we test our potential with this quantity first. Figure 4.6 shows the calculated expansion of the lattice parameter, in the 300 - 1000 K temperature range. This was calculated by performing molecular dynamics simulations with 4 x 4 x 4 supercells in an NPT ensemble, at the required temperatures. We used barostats and thermostats as described by Martyna *et al*[119, 120] and we set the external pressure to zero. The lattice parameters were averaged over a 0.1 ns long simulation and used to calculate the percentage expansion. In 4.6 the corresponding thermal expansion coefficient is extracted by fitting a straight line to our data. The obtained value is α = 9.0 x 10^{-6} K^{-1} which is within 15-20 % the experimental values (see 4.2). This is a substantial improvement compared to the Grimes [146], Gotte 2004 [149] and Gotte 2007 [150] potentials which gave a thermal expansion coefficient of 1.27 x 10^{-6} , 6.65 x 10^{-6} , 7.31 x 10^{-6} K^{-1}, respectively. We

remind the reader that no empirical data was used in the parameterization of this potential, so that this potential was not manually optimized in order to reproduce the thermal expansion coefficient.

Table 4.2: Comparison between the experimental and simulated thermal expansion coefficients (α).

α (10^{-6} K^{-1})	Reference
9.0	This work
10.7	Ref. [163]
11.1	Ref. [164]
11.6	Ref. [165]

4.4.2 Elastic properties

Elastic constants and the bulk modulus were calculated and compared to the experimental values. The three independent elastic constants were obtained by straining an optimized simulation cell in different directions by a small amount (typically a fraction of a percent) and the resulting stress tensor is recorded after relaxation of the atomic positions. After repeating this procedure for several magnitudes of positive or negative strain, the linear relationship between strain and stress is used to obtain the elastic constants at 0 K. The bulk modulus was extracted from a volume versus pressure curve.

Table 4.3 reports the three elastic constants and the bulk modulus. These are within 15% of the reported experimental values, with the exception of C_{11}, whose value is overestimated by 32%. We believe this agreement to be quite good, especially considering that the experimental data for these properties are quite scattered.

One of the main motivations of the work of Xu *et al.* [145] was to find a reliable potential to describe - and perhaps explain - the observed elastic softening of ceria with decreasing oxygen partial pressure (P_{O_2}). For this reason in 4.7 we report the Young modulus for reduced ceria as a function of the lattice constant, together with

Table 4.3: Experimental and simulated elastic constants and bulk modulus for stoichiometric CeO_2.

Property (GPa)	MD	Experimental [166, 167]
C_{11}	552	386 - 450
C_{12}	137	105 – 124
C_{44}	66	60 – 73
B	270	204 – 236

the experimental data from the work of Wang *et al.* [145, 168] and the ones obtained with the Grimes and Gotte 2007 potentials [145]. The scale of the plot is the same as in Fig. 3 in ref [145] to facilitate a comparison. Our interatomic potential shows the expected elastic softening as a function of the lattice constant (or analogously, as a function of the non-stoichiometry). The values obtained with our simulations are within the experimental error. The level of accuracy is indeed better than the Grimes potential and comparable with the Gotte 2007 potential.

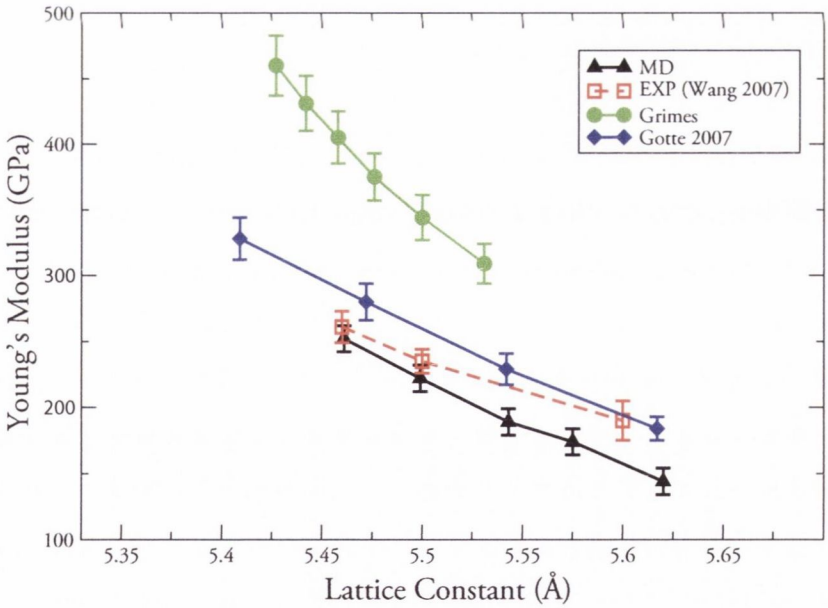

Figure 4.7: Young modulus Vs the lattice parameter in CeO_{2-x}. Red symbols are the experimental data from Wang *et al.* [168], green and blue symbols are the simulated data obtained with the Grimes [146] and Gotte 2007 [150] potentials, while the black ones are from our own potential.

4.4.3 Structural properties of reduced ceria

The local crystal structure of reduced ceria has been recently studied with neutron diffraction experiments [11]. From that set of data, total radial distribution functions were extracted for different values of x in CeO_{2-x}. In Figure 4.8, we report the calculated total radial distribution functions, $G(r)$(from Equation 3.66), for different non-stoichiometries and we compare them with the ones extracted from the neutron diffraction data. The agreement is good for all the studied compositions. The first peak in the simulated $G(r)s$ appears as a doublet while in the experimental data it appears as a single broad peak . This is probably caused by the lower spacial resolution of the experimental data and has been observed in previous studies as well [90, 162]. A visual analysis of the oxygen-oxygen radial distribution functions (not shown) shows an increased broadening as a function of x, which is indicative of an increased disorder within the anion sublattice [11].

4.4.4 Chemical expansion

The conditions found at the anode side of SOFCs lead to the reduction of Ce^{4+} to Ce^{3+} with a subsequent change in the lattice parameter. This chemical expansion affects the performance of the electrolyte as it creates a strain in the cell and can eventually cause fractures. For this reason, in this section, we test the ability of our potential to describe this behavior accurately. In Figure 4.9 we report the calculated lattice parameter as a function of the oxygen non-stoichiometry in CeO_2 at 1273 K and compare this with the neutron data from Hull *et al.* [11] at the same temperature. The agreement is excellent and the simulated chemical expansion coefficient, 0.338 Å, is within 7 % of the experimentally determined chemical expansion coefficient, 0.362 Å. Such a good agreement is encouraging and also indirectly confirms that our "ionic" approach, in which we see Ce^{3+} as a different cation species, carries the correct physics.

In Table 4.4 we report the calculated lattice parameters for $Ce_{0.8}RE_{0.2}O_{1.9}$ at room temperature, where RE = Gd^{3+}, La^{3+} and compare them with the experimental val-

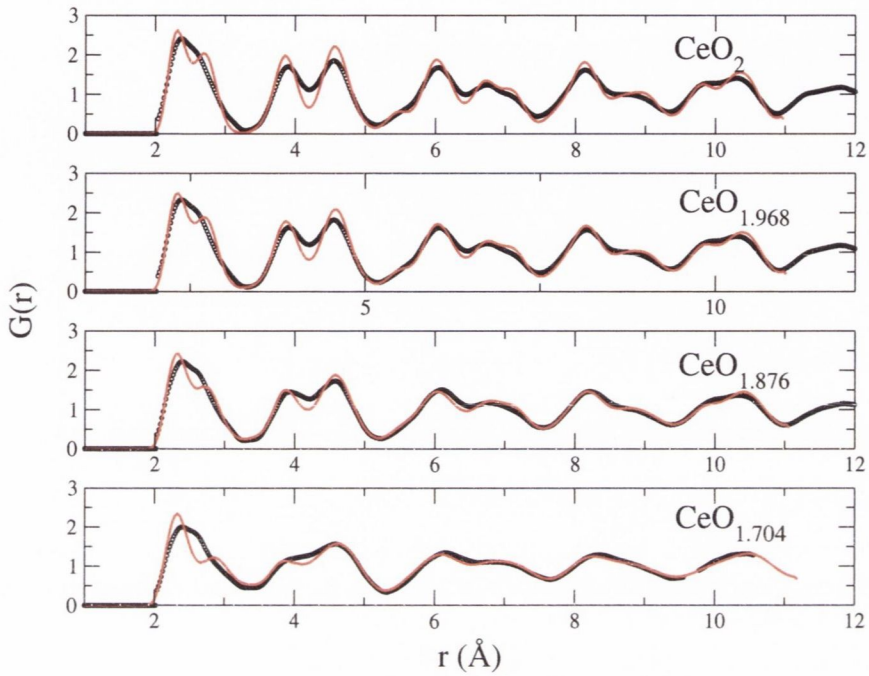

Figure 4.8: Radial distribution functions, $G(r)$, for different values of x in CeO_{2-x}, at 1273 K. Red lines and black empty dots correspond to the MD and experimental [11] $G(r)s$ respectively.

ues. The agreement is within 1% and the trend of increasing lattice parameter with increasing cation radius is properly reproduced.

Table 4.4: Comparison between experimental [169] and simulated lattice parameters for $Ce_{0.8}RE_{0.2}O_{1.9}$ at room temperature (RE = Gd^{3+}, La^{3+}).

Lattice parameter	MD (Å)	Experimental (Å) [169]
Gd^{3+}	5.426	5.423
La^{3+}	5.494	5.476

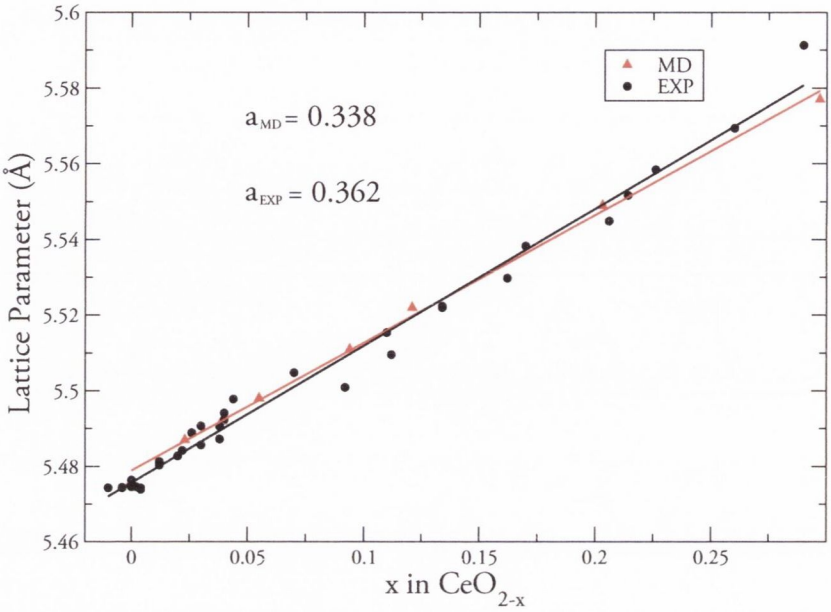

Figure 4.9: Lattice parameter (red line) as a function of the nonstoichiometry, x, in CeO_{2-x}. The simulations were performed at 1273 K, the same temperature as the reported experimental data [11] (black empty circles).

4.5 Defect interactions and the ionic conductivity in YDC

This Section examines the factors that affect the ionic conductivity of YDC at its working temperature as an electrolyte in SOFC applications. In particular, we investigate the effect of oxygen vacancy ordering on the conductivity of YDC using a combination of experimental neutron diffraction, ionic conductivity data and molecular dynamics simulations using the potential parameters reported in Table 4.1.

4.5.1 Simulation details

All molecular dynamics simulations on the cubic $Ce_{1-x}Y_xO_{2-x/2}$ system were performed using a supercell of 4 x 4 x 4 unit cells for a range of x values (Table 4.5). Each model was set up by distributing the ions randomly over their average crystallographic positions. Coulombic and dispersion interactions were summed using Ewald summations

Table 4.5: Number of atoms of each species in the $Ce_{1-x}Y_xO_{2-x/2}$ systems used throughout this study

$Ce_{1-x}Y_xO_{2-x/2}$	Ce^{4+} ions	Y^{3+} ions	O^{2-} ions	oxygen vacancies
0	256	0	512	0
0.04	246	10	507	5
0.08	236	20	502	10
0.12	226	30	497	15
0.18	210	46	489	23
0.20	204	52	486	26
0.24	194	62	481	31
0.26	190	66	479	33
0.30	178	78	473	39
0.36	164	92	466	46
0.40	152	104	460	52

[78] whilst the short-range part of the potential was truncated to half the length of the simulation box (~ 10 Å). Each concentration was initially equilibrated at a temperature of 2073 K for 120 ps; the temperature was then scaled down to room temperature at a rate of 1.64 K ps^{-1}. The diffusion coefficients were calculated for temperatures of 873 K and above. All simulations were performed at constant temperature and pressure (NPT ensemble), as described by Martyna et al. [119, 120] using a timestep of 1 fs. In addition to these calculations, we also constructed model systems (referred to as average cation ac-YDC) where both cations are assigned the same short-range potential parameters as those of the Ce^{4+} ions in the original potential. In this model both cations are given the same charge so that the total for all cations balances that of the O^{2-} ions present in the simulation for the same concentration ranges that were used in the calculations described above for $Ce_{1-x}Y_xO_{2-x/2}$. These idealized systems allow us to eliminate the effects of differing charges and lattice strain induced by having both host and dopant cations and serve as reference systems in which the cation-vacancy ordering effects are absent.

4.5.2 Structural properties of YDC

Figure 4.10 shows the change in cubic lattice parameter, a_0, at 300 K as a function of dopant concentration in $Ce_{1-x}Y_xO_{2-x/2}$, obtained from the MD simulations (blue squares) and from previous XRD experiments (red diamonds and black circles [15, 129]). The trend observed is that the lattice constant decreases as the dopant concentration increases. This is caused by vacancy formation upon doping, which counteracts the increased number of the slightly larger Y^{3+} cations. This effect is discussed in detail in ref [20]. Figure 4.11 compares the total radial distribution function, $G(r)$, generated from the MD simulations (using Equation 3.66) with those obtained from the neutron diffraction experiments, both at 1073 K and represented by red dashed lines and black solid lines, respectively. The range of concentrations shown is from $x = 0.04$ to 0.26. In addition, the results for a 10 ps Local Density Approximation (LDA) Car-Parrinello MD [170] simulation performed for the composition $x = 0.12$, shows the high level of agreement between our IP and *ab initio*. Overall, the agreement between the MD simulations and the neutron diffraction data in Figure 4.11 is good, the only deviation (common to both MD and ab initio simulations) being that the simulated peak at around 2.7Å is slightly sharper that the experimental one.

Figure 4.12 shows a plot of the partial radial distribution functions, $g_{ij}(r)$, for $Ce_{0.88}Y_{0.12}O_{1.94}$ at 1073 K, from MD, RMC and ab initio simulations. Overall, the high level of agreement between the data sets confirms that the DIPPIM potential used here is able to account well for the structural properties of YDC at various dopant concentrations. The plots for $g_{Ce-O}(r)$ and $g_{Y-O}(r)$ show that the Y-O distance is slightly longer than Ce-O, which is explained by the stronger Coulombic attraction exerted by the Ce^{4+} cation and is in good agreement with Shannon's radii of 0.97 Å and 1.019 Å for Ce^{4+} and Y^{3+}, respectively [131]. Overall, this comparison shows that the DIPPIM potential can satisfactorily reproduce the experimental structural data for this system. In the next section, we will therefore focus on cation-vacancy and vacancy-vacancy ordering tendencies (which can be probed only with computer simulations) and their effects on the conductivity of this material.

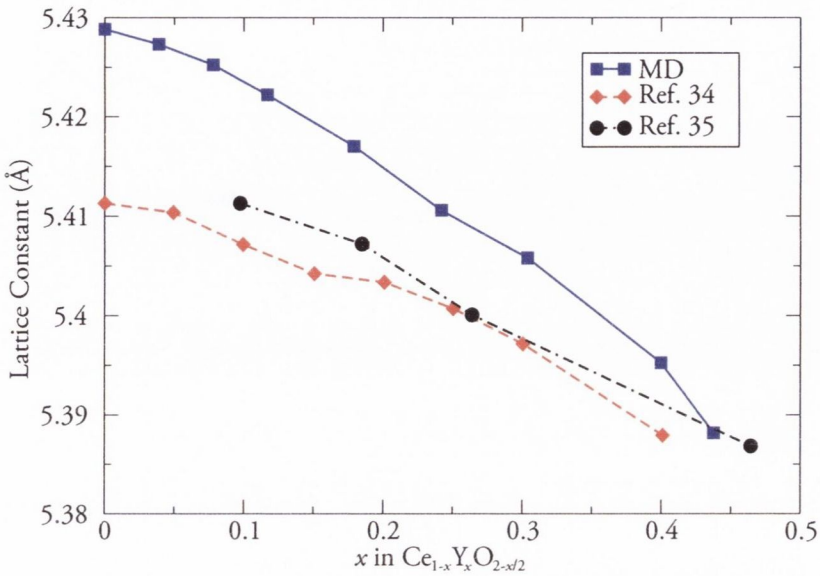

Figure 4.10: Room temperature lattice constants from experiment (red diamonds and black circles), taken from previously published XRD data [15, 129] and DIPPIM (blue squares) lattice constants as a function of dopant concentration x in $Ce_{1-x}Y_xO_{2-x/2}$.

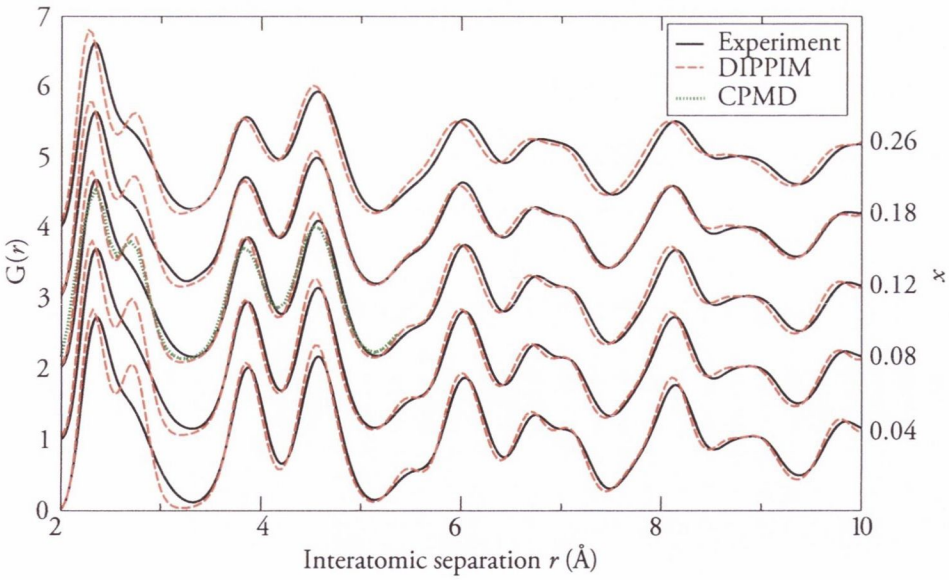

Figure 4.11: Total radial distribution functions $G(r)$ for $Ce_{1-x}Y_xO_{2-x/2}$ where x = 0.04, 0.08, 0.12, 0.18 and 0.26 from experiment (black solid lines) and MD (red dashed lines). The green dotted line represents a Car-Parrinello MD simulation for $x = 0.12$.

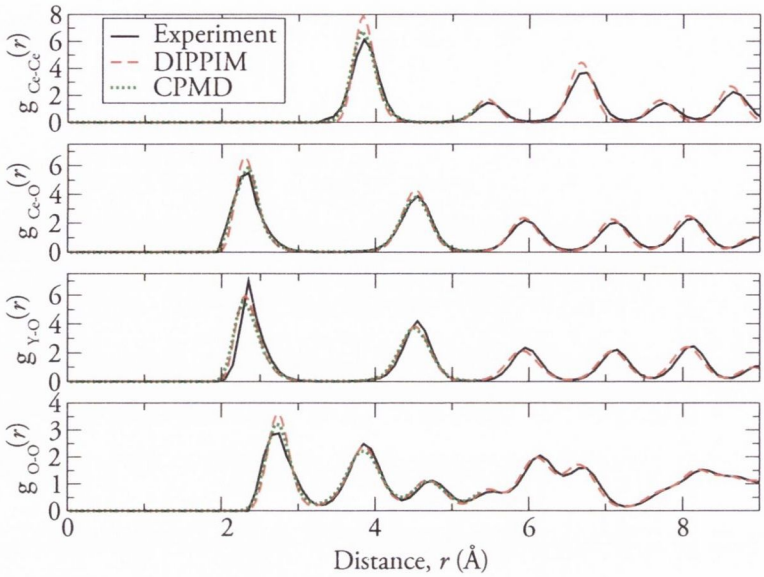

Figure 4.12: Partial distribution functions, $g_{ij}(r)$, from MD simulations (red dashed lines) and experiment (black solid lines) for $Ce_{0.88}Y_{0.12}O_{1.94}$. The green dotted lines represent a Car-Parrinello MD simulation for x = 0.12.

4.5.3 Cation-vacancy interactions

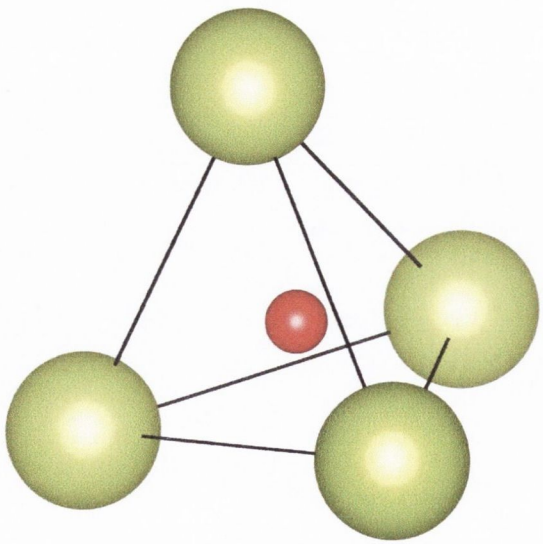

Figure 4.13: Cations (green) are coordinated tetrahedrally around the anions (red) in the fluorite structure. Four planes can be delineated using the cations at the vertices of the tetrahedron.

The vacancy analysis of fluorite structured materials probes the occupancy changes of the tetrahedral sites formed by the face centred cubic cation sublattice shown in Figure 4.13. As the picture illustrates, these are the sites where the oxide ions and, thus, their vacancies are normally present. The oxygen vacancy analysis is performed making use of the fact that the cations in the systems under study do not diffuse, even at high temperatures. Thus, it is possible to specify the cation sublattice in terms of tetrahedra, each of which may be empty (vacancy) or occupied by an oxide anion. For a set of time-correlated instantaneous ionic configurations, i.e., frames in an MD simulation, one can determine which tetrahedral sites are empty. However, distinction must be made between the vibrations undergone by the oxide anions, which are large in amplitude at the temperatures of interest, and instances when a given oxide anion has truly vacated a given tetrahedron. This distinction is made by imposing the condition that a site be considered a vacancy only if it has been vacant for a period of at least two frames. The position of each vacancy is then defined as the centre of the tetrahedron formed by the average positions of the four surrounding cations. These positions can then be used to calculate partial radial distribution functions (RDFs), from which vacancy ordering in real space can be studied. Integration of these partial RDFs ($g(r)$) peaks from zero out to the position r_c gives the coordination number:

$$n = 4\pi\rho \int_0^{r_c} r^2 g(r) dr \tag{4.6}$$

where ρ is the vacancy density in the simulation cell. This method has been previously used to study similar materials, such as, $Zr_2Y_2O_7$–Y_3NbO_7 [158], YDC [171] and PbO_2 [89, 172].

Figure 4.14 shows the $g_{\text{cat}-\text{vac}}(r)$ at 1073 K for $x = 0.18$ (a), 0.26 (b), 0.30 (c) and 0.36 (d) in $Ce_{1-x}Y_xO_{2-x/2}$. The first two peaks in the RDFs represent the number of vacancies that are in the nearest neighbour and next-nearest neighbour position of each cation, respectively. The results show that there is no clear tendency for the vacancies to associate with either cation at the nearest neighbour position, although the next

nearest neighbour position shows, especially for low dopant concentrations, enhanced association of the vacancies with the Y^{3+} cations with respect to the Ce^{4+} cations, which indicates repulsion of the vacancies by the former species.

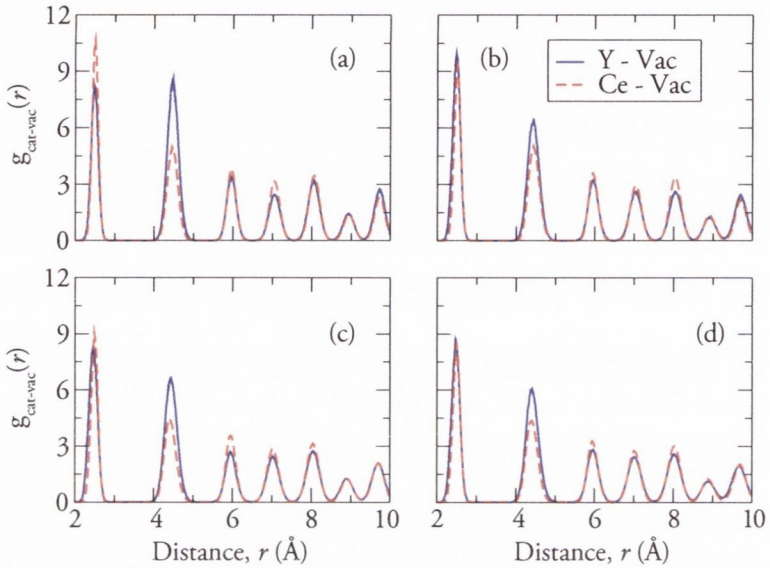

Figure 4.14: Cation-vacancy partial distribution functions, $g_{\mathrm{cat-vac}}(r)$, obtained from MD simulations at 1073 K for $x = 0.18$ (a), 0.26 (b), 0.30 (c) and 0.36 (d) in $Ce_{1-x}Y_xO_{2-x/2}$. Y–vacancy and Ce–vacancy $g(r)$s are represented by blue (solid) lines and red (dashed) lines, respectively.

At first, our results might seem at odds with previous evidence from the literature. Indeed, room temperature MAS NMR measurements on YDC show clearly that the Y coordination number is smaller than that of the Ce cations (See Figure 4.1 (b)), thus implying that vacancies associate with Y cations [15, 173]. Static calculations, based on interatomic potentials or DFT, also show that there is a preference for vacancies to be nearest-neighbour to Y, as opposed to next nearest neighbour. However, this preference is rather weak and the energy difference between these two configurations is smaller than 0.1 - 0.2 eV [15, 173]. This explains why we do not observe such ordering in our simulations. Indeed, since our calculations are performed at high temperatures (> 873 K), this weak ordering tendency is washed out by entropic effects. This argument is confirmed by recent calorimetric measurements, performed at 973 K, which show that little defect ordering is observed in YDC compared to YSZ and yttria-doped HfO_2. Kim

et al. [15] performed ^{17}O MAS NMR studies and found evidence of different resonances, which they assigned to oxygen atoms with different numbers of yttrium cations in the first coordination sphere. However, when the temperature is raised to 673 K, these resonances coalesce, indicating that at this temperature this ordering effect vanishes.

4.5.4 Vacancy-vacancy interactions

Figure 4.15 illustrates the $g_{\text{vac}-\text{vac}}(r)$ at a range of dopant concentrations at 1073 K. For the purpose of comparison, a $g_{\text{vac}-\text{vac}}(r)$ for CeO_2 at the same temperature is also included as it represents that expected from a random distribution of vacancies. The directions/distances in the simple cubic oxygen sublattice are indicated by <100>, <110>, <111>, <200>, etc. The patterns observed indicate that there is an enhanced ordering of oxygen vacancies along the <210> and <211> that is not dependent on the dopant concentration. Figure 4.15 also indicates that as the Y^{3+} content increases the vacancies tend to pair along the <111> direction with respect to the random distribution. This has been observed in several fluorite structured oxides [11, 161, 162]

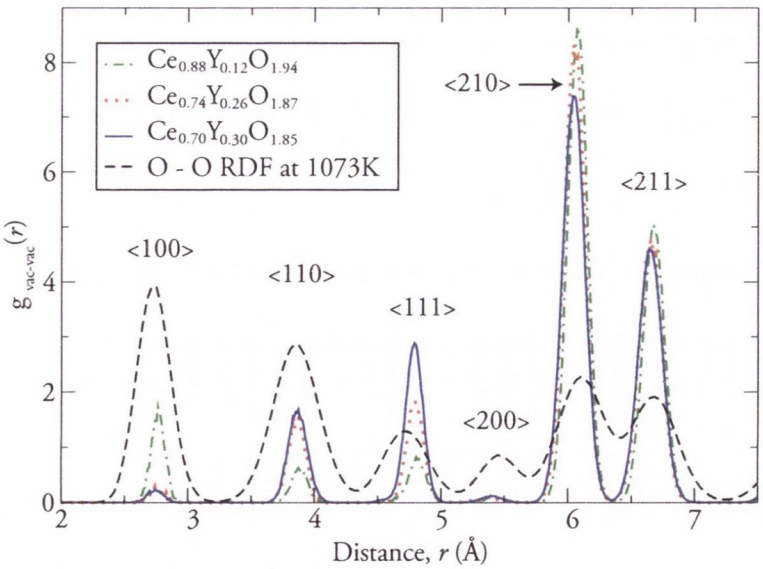

Figure 4.15: Vacancy-vacancy partial radial distribution function, $g_{\text{vac}-\text{vac}}(r)$, obtained from MD simulations at 1073 K for $x = 0.12, 0.26, 0.30$ in $Ce_{1-x}Y_xO_{2-x/2}$.

4.5.5 Ionic conductivity

The ionic conductivity was estimated using the diffusion coefficients from MD simulations according to the Nernst-Einstein formula shown in Equation 3.64. Figure 4.16 shows the ionic conductivity as a function of dopant concentration at 1073 K and 873 K obtained from experiments and simulations. At the temperatures in question there is a peak in the conductivity (σ) with increasing Y^{3+} content at $x \approx 0.12$ for the experimental data. This maximum is less pronounced in the MD simulation data, but it also occurs at $x \approx 0.12$ in the case of the 1073 K simulations. This peak becomes less pronounced at 873 K for both data sets. These data are in excellent agreement with those reported elsewhere and highlight the predictive capabilities of the DIPPIM potential. The data from simulations at multiple temperatures can be used to generate Arrhenius plots, from which activation energies can be obtained. Figure 4.17 illustrates the observed behavior of an increasing migration energy as a function of Y_2O_3 concentration, which is in excellent agreement with the experimental findings of Tian *et al.* [174].

If the migration energy in Figure 4.17 is extrapolated to $x = 0$, a value of approximately 0.47 eV is obtained. This corresponds to the oxygen migration energy in CeO_2 and compares well with the experimental results and with previous DFT calculations, as shown in Table 4.6. This further demonstrates that this potential can successfully reproduce the ionic conductivity properties of this material.

Table 4.6: Comparison between experimental and simulated oxygen migration energies for CeO_{2-x}, for $x \to 0$.

Migration energy (eV)	Reference
0.47	This work
0.52	Ref. [175]
0.40	Ref. [176]
0.47	Ref. [177]

As discussed above, the shape of the conductivity versus composition plot is usually attributed to two types of interactions, namely, those between cations and vacancies

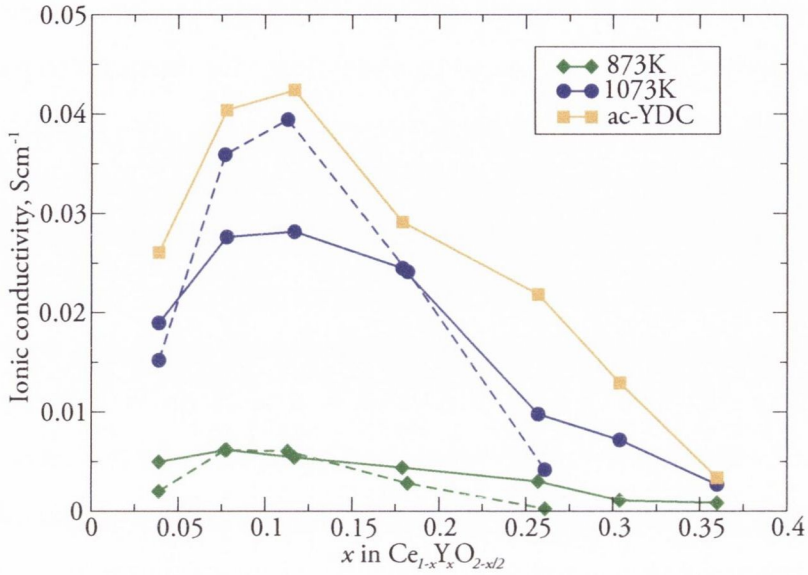

Figure 4.16: Ionic conductivity as a function of dopant concentration at 1073 K (blue lines with circles) and 873 K (green lines with diamonds). Dashed and solid lines represent experimental and MD results, respectively. The orange line with squares corresponds to the conductivity at 1073 K of the average cation systems (ac-YDC) where the cations carry the same charge.

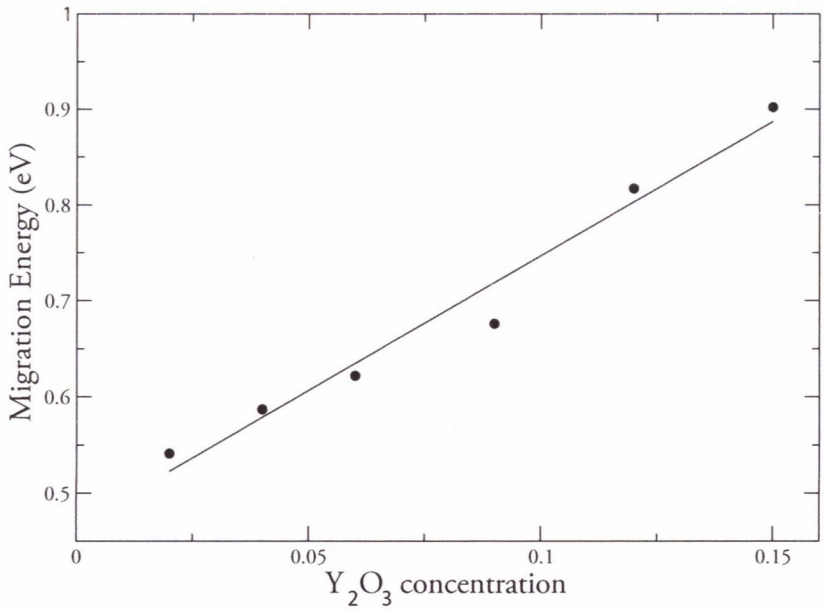

Figure 4.17: Oxygen migration energy in $Ce_{1-x}Y_xO_{2-x/2}$ *Vs* Y_2O_3 concentration, x. These migration energies were extracted from an Arrhenius plot of the MD diffusion coefficients at high temperatures.

and those between vacancies themselves. Our study of these interactions has shown no clear evidence for the former, but a strong tendency for vacancies to pair along the <111> direction with increasing dopant concentration. In order to confirm which of these effects dominates the observed maximum in conductivity, Figure 4.16 also shows a plot of the conductivities at 1073 K for the average cation systems, ac-YDC, where both cationic species carry the same charge and have the same short-range repulsion interactions with the oxide ions. These calculations were included in order to explore the effects of the vacancy-vacancy interaction in a more direct manner, given that cation-vacancy effects are, *de facto*, eliminated in ac-YDC. In this case we see that the conductivity has a peak at the same dopant concentration, although all values are higher than either the experimental or the simulated results for the real system at the same temperature. The latter is probably a consequence of the potential which has, on average, less repulsive short-range interactions [162]. Figure 4.16 shows that, even if all the differences between the cation species are removed, a maximum in the conductivity is still observed in ac-YDC, which happens at the same vacancy concentration as in the real material, $x = 0.12$. This serves to confirm that the observed maximum in the conductivity, and its subsequent drop, are predominantly caused by vacancy-vacancy interactions in cases where there is small cation size mismatch, as is the case in YDC.

4.6 Conclusions

Section 4.2 provided some background on the properties of ceria and presented the main challenges that must be considered in its optimization for use as an SOFC electrolyte. Section 4.3 detailed the method of force-matching that is employed to parametrize the IPs used throughout this thesis. The reliability of the new interionic potential was studied for stoichiometric, reduced and doped CeO_2 in Section 4.4, where a series of fundamental properties of these materials were calculated and compared to experimental data. The agreement for all these properties (thermal and chemical expansion coefficients, lattice parameters, oxygen migration energies, local crystalline structure and elastic constants) is very good, with the calculated values being within 10-15%

of the experimental ones. We note that such accuracy is comparable to that of DFT calculations, but the computational cost is reduced significantly. These potentials can thus be used to predict and elucidate the atomic-scale properties of CeO_2 in situations where DFT calculations are not practical due to their size limitations. With such potentials, nano-second long simulations on 1000s of atoms can be performed and these can be used to understand the structural, chemical, mechanical and conducting properties of this material, as previously done in similar systems [90, 142, 154–162].

In Section 4.5.5 the potential set that was parametrized served to assess the role of the processes which affect the conductivity in $Ce_{1-x}Y_xO_{2-x/2}$ (YDC), namely, the local ordering of the anion vacancies and their preference to reside in the vicinity of either cationic species. The former was found to have a more pronounced effect with increasing x, whilst there was no clear tendency for the vacancies to be located near the host Ce^{4+} or dopant Y^{3+} cations in the intermediate temperature range. In fact, it was found that vacancy ordering along the <111> direction, driven by their strong repulsion at closer distances [24, 178], dominates at high x values. The decreasing ionic conductivity with increasing x is, therefore, for the most part dominated by vacancy-vacancy interactions in YDC. This was confirmed by performing simulations on average cation, ac-YDC, systems, where both cationic species carry the same charge and have the same short-range repulsion interactions with the oxide ions. Our results showed that the ac-YDC systems displayed the same maximum in conductivity as those where the ions carry their formal charges, namely $x \approx 0.12$.

Recent studies of the local ordering of anion vacancies in a series of fluorite-structured materials such as YSZ, ScSZ, $CeO_{2-\delta}$, $Zr_{0.50.5x}Y_{0.5+0.25x}Nb_{0.25x}O_{1.75}$ [11, 158, 161, 162] also showed a strong ordering of the vacancies along <111> directions, together with a preference for the vacancies to reside in the vicinity of the smaller cationic species - when these have ionic radii that are quite different, such as the case of YSZ. The results presented in this Chapter indicate that the same arguments apply to YDC. As result of this, we conclude that the vacancy ordering tendencies in these fluorite-structured materials are very similar and share the same features, even though the local

structure of these materials can be very different [11, 90, 158, 162] Most importantly, the tendency for vacancies to order along the <111> direction is still observed even when the differences between the host and dopant cations are completely removed. These results therefore appear to indicate that vacancy-vacancy interactions in these materials are an intrinsic effect, rather like a property of the fluorite lattice and that, consequently, they cannot be minimized/avoided by changing the chemistry of these compounds . This has significant consequences as these interactions ultimately limit the conductivity of these materials for $x > 0.12$. For this reason, different optimization strategies are considered in the remainder of this thesis. In Chapter 5, the use of multiple dopant species (co-doping) is assessed as a means to improve the conductivity beyond that of the best single dopants. Chapter 6 diverges from this compositional approach by examining how the application of strain to thin films of YDC affects their conductivity.

5

Solid solutions of ceria with multiple cationic species

5.1 Introduction

5.2 Co-doped ceria electrolytes

Traditionally, ionic conductivity optimization has been approached from a compositional perspective. This has meant that, in order to improve the conductivity of ceria-based electrolytes, researchers have mostly focused on parameters such as the ionic radius of the dopant cation and its concentration, x in $Ce_{1-x}RE_xO_{2-x/2}$. The chief aim has been to minimize defect interactions, especially those between dopants and vacancies [23, 24, 151, 179–181]. These studies have variously identified a number of RE elements, such as Gd^{3+}, Y^{3+}, Sm^{3+} and Pm^{3+} as the best candidate dopants, given that their radius mismatch with the host cation (Ce^{4+}) balances the competing electrostatic and elastic components of the defect interactions which control their association [182]. Nevertheless, recent studies have shown that in the limit where cation-vacancy interactions are reduced to a minimum, it is vacancy-vacancy association which ultimately determines the ionic conductivity drop as a function of dopant concentration in fluorite-structured materials, such as, Yttria Doped Ceria (YDC) [171], Yttria Sta-

bilized Zirconia (YSZ) and Scandia Stabilized Zirconia (ScSZ) [162]. This means that different optimization strategies must be sought if IT-SOFCs are to realize their potential in commercial applications [183–186].

An interesting route for improving the ionic conductivity of fluorite-structured electrolytes is co-doping, i.e. doping these materials with more than one cation species. This approach has been successfully employed on ZrO_2 by Politova and Irvine [187]. In this case, the material is doped with two different cation species, each of which plays a *different* role. Sc is added to improve the ionic conductivity, since its radius is very close to that of Zr, thus minimizing cation-vacancy interactions; while Y, on the other hand, is introduced because its larger ionic radius fully stabilizes the fluorite structure and removes a phase transition to a lower-symmetry phase observed in pure Sc-doped ZrO_2. It is important to note that Y addition to Sc-doped ZrO_2 is found to *lower* the conductivity of this material. There is therefore a *trade-off* between stability and ionic conductivity in this co-doped zirconia system. In the case of Politova and Irvine, the authors found that very *small* concentrations of Y are necessary to stabilise the cubic fluorite structure and that this has a small effect on the conductivity.

It has been suggested that co-doping can also be used to improve the ionic conductivity of ceria based electrolytes [130, 188–199]. However, contrary to the stabilizing role it plays in zirconia, co-doping in ceria is done in order to either reproduce the ionic radius of an ideal dopant, or the lattice constant of ceria doped with said dopant. Co-doping with two or more different cations aims to obtain an *average* or "effective" cation radius that is very close to that of Ce^{4+} and, thus the average strain introduced by the dopant cations is minimized. This is substantiated by different interpretations of how a dopant with a critical radius (r_C) is likely to affect defect–defect interactions. For example, in 1989 Kim suggested that the ideal dopant would not change the volume of the host lattice upon its introduction, hence minimizing elastic strain, and identified $r_C = 1.038$ Å [200]. More recently, researchers have had access to a more

detailed view of the interplay between strain and electrostatics with the use of *ab initio* methods, which in 2006 lead Andersson *et al.* [23] to ascertain that r_C should be that which maximizes oxygen vacancy disorder. Their simulations showed that when ceria is doped with relatively small cations, vacancies prefer to sit in a nearest neighbour (NN) position with respect to the dopant cation, whereas, for larger cations, vacancies prefer to sit in a next nearest neighbour (NNN) position. The crossover between these two tendencies was observed at Pm^{3+}, for which the NN and NNN positions have the same energy, which was rationalized in terms of a perfect balance between the elastic (related to the dopant's radius) and Coulombic interactions between Pm^{3+} and a vacancy. This finding implies that Pm^{3+} is the ideal dopant for ceria and this material should display the highest ionic conductivity. Unfortunately, Pm^{3+} is radioactive, so the authors suggested, instead, to try a mixture of Sm/Nd which have slightly smaller/larger ionic radii than Pm^{3+}.[1] Based on these ideas, multiple research groups have carried out experiments in order to test several co-doping schemes for ceria, e.g. Y/Sm co-doping [193], La/Y co-doping [130], Lu/Nd co-doping [201] and Sm/Nd co-doping [192], of which the latter two were specifically aimed at reproducing the r_C values predicted by Kim and by Andersson, respectively. In general, co-doping studies have pointed to increases in the ionic conductivity with respect to singly doped systems, which has lead to the conclusion that there exists a "co-doping" effect in ceria.

Modern simulation techniques have become a mainstay within the materials science community, not only because they afford researchers information which is complementary to their experiments, but also because they can serve as predictive tools [202]. Hence, the implementation of reliable computer simulations can be used to clarify the role of particular effects present in physical experiments in a targeted and controlled manner. To this end, the interaction potentials reported here are shown to perform with the accuracy of state-of-the-art *first-principles* calculations, i.e. hybrid Density Functional Therory (DFT), but at the computational cost of classical (polarizable)

[1]We note here that the radii of these three elements (1.079, 1.093, 1.109 Å for Sm, Pm and Nd, respectively [131]) are all very similar and almost within the associated experimental error.

molecular dynamics. This approach allows us to study, for the first time, systems with realistic doped/co-doped defect concentrations within the temperatures of interest for SOFC applications (600-1000 C°), and to accumulate sufficiently long trajectories to calculate the conductivity. This is in contrast to most of the previous computational work on doped ceria which has typically used static DFT calculations or *ad hoc* emprirical potentials. The use of computer simulations allows us to focus on the *bulk* behaviour of this material, excluding factors like grain size and boundaries, sintering conditions, impurity levels, etc, which are known to also (negatively) affect the conductivity of these materials [10, 203]. We show that co-doping does not significantly improve the conductivity of these materials, but rather, we find that the conductivity of the co-doped systems lies within the range spanned by the singly doped systems, i.e. it is an average of the two. The reason for this is that introducing two cation species with radii which are bigger or smaller than that of a given r_C affects the local structure of ceria and results in deep traps for the vacancies.

5.2.1 Methods

Interionic Potential

The highly correlated nature of the f-electrons found in lanthanide elements makes necessary the use of high levels of theory in order to correctly describe their electronic structure. Such demands have been found to be satisfied by the inclusion of a fraction of non-local Hartree-Fock exchange within the framework of Density Funcional Theory (DFT), which gives rise to hybrid functionals (h-DFT) [204, 204–206]. Alternative DFT functionals are also available, namely, those which include a Hubbard parameter U (DFT+U). They represent a viable alternative to h-DFT and their ability to describe the properties of ceria has been widely documented [207–211]. Nonetheless, h-DFT provides a better agreement with experimental lattice constants and does not require fitting a $+U$ value for the f-electron systems. In either case, however, DFT calculations are prohibitively expensive from a computational point of view for this type of study

regardless of the functional; this is because of the long Molecular Dynamics (MD) simulation times and large systems required to study the ionic conductivity of doped ceria. For this reason interionic potentials (IP) implemented in an in-house MD code (PIMAIM) and derived from static h-DFT calculations were used in this work, as they accurately reproduce the structural *ab initio* data at a fraction of the computational cost. This approach has been successfully used for a series of related oxides [20, 155, 157, 158, 160–162], including Y-doped ceria [17, 171], as well as a variety of ionic systems [212–214]. The RE dopant cations studied in this article included La, Nd, Sm and Gd, as well as, Y and Sc. A crucial feature of this potential set is that they were fitted with a *common* O – O term, which made it possible to perform simulations with several dopant cations within the same cell, i.e. to co-dope ceria. Details on the interionic potential used (DIPPIM - DIPole Polarizable Ionic Model) are found in Chapters 2 4.

Potential parameterization

A total of 19 2 x 2 x 2 fluorite-structured supercells were used to fit this IP set. They included YSZ (1), ScSZ (1), ceria-zirconia (3), pure ceria (1), reduced ceria (1) and two configurations of composition $Ce_{0.5}RE_{0.5}O_{1.75}$ for each of the systems. Each model supercell was obtained from high temperature (2000 K) *ab initio* MD simulations that were run for a few pico seconds in order to reach structural equilibrium. The forces on each species were determined directly from each DFT calculation, and the dipoles were obtained from a Wannier analysis of the Kohn-Sham (KS) wave functions [138]. In each case, hybrid density functional theory (h-DFT) calculations using the Heyd, Scuzeria, Ernzerhof (HSE06) functional [75, 215], as implemented in the VASP code [216] were performed. The inclusion of a fraction of nonlocal Hartree-Fock exchange to standard DFT in functionals such as HSE is known to be necessary to correctly describe the electronic strucuture of lanthanide oxides, such as, reduced ceria [204, 205] due to the highly correlated f-electrons present in these elements. This DFT functional also represents an improvement over other more commonly used functionals like LDA (Local

Density Approximation) or GGA (Generalized Gradient Approximation) in terms of a closer agreement to experimental lattice constants [204] in cases where there are no f-electrons present, e.g. YDC, LDC, etc.

Although dispersion energies constitute only a small fraction of the total energy, they have a considerable influence on transition pressures and, in particular, on the material density, thus the lattice constant, and the stress tensor. However, the dispersion terms were not included in the initial fit due to the well known uncontrolled representation of dispersion within the framework of DFT [58]. Instead, values for the C_6^{ij} and C_8^{ij} terms were determined from the dipole polarizabilities for each element that resulted from the initial potential fit. The α values thus obtained have been previously found to be in very good agreement with other theoretically derived values [17, 217]. The relationship between the dispersion coefficients and the dipole polarizability is given by the Slater-Kirkwood equation [218, 219]. The final values for the DIPPIM parameters were then obtained by fixing the values of the polarizabilities and dispersion terms in a last round of optimization and re-fitting. The final χ^2 values for fit were 0.216 for dipoles and 0.335 for forces. Table 5.1 presents the parameters for the DIPPIM interionic potential set that was obtained.

Simulation Details

All MD simulations on the singly doped $Ce_{1-x}RE_xO_{2-x/2}$ and co-doped systems were performed using 6 x 6 x 6 supercells ($\sim$ 2592 atoms, depending on the dopant concentration). Three different co-doped systems formed part of this study. Firstly, $Ce_{1-x}Nd_{0.5x}Sm_{0.5x}O_{2-x/2}$, which, as was mentioned in Section 5.1, has been previously studied experimentally [192] because the average radius of both dopants matches that of Pm. Similarly, $Ce_{1-x}Sc_{0.22x}La_{0.78x}O_{2-x/2}$ was included given that in this ratio of La and Sc the ionic radius Pm is also reproduced. Three different supercells were set up for each dopant concentration, $x = 0.05, 0.10, 0.15, 0.20, 0.25$ and the values reported here, such as, ionic conductivities, lattice constants and activation energies were ob-

Table 5.1: Parameters for the HSE DIPPIM potential. All values are in atomic units, except those corresponding to the ionic radii (Å) which are shown in parentheses alongside the dipole polarizabilities α. The parameters $b_D^{O^{2-}-\square}$ and $b_D^{\square-O^{2-}}$ were given the same value. Here, $\square$ represents a placeholder for the identity of the ionic species specified in a given column

Interaction	A^{ij}	a^{ij}	B^{ij}	b^{ij}	C_6^{ij}	C_8^{ij}	b_6^{ij}	b_8^{ij}
O^{2-} – O^{2-}	7.15	18.52	50000	1.00	83	1240	1.30	1.70
Ce^{4+} – O^{2-}	82.20	1.19	50000	1.55	47	595	1.50	1.96
Zr^{4+} – O^{2-}	89.79	1.29	50000	1.75	21	271	1.62	2.10
La^{3+} – O^{2-}	102.63	1.25	50000	1.30	57	731	1.46	1.88
Ce^{3+} – O^{2-}	100.02	1.25	50000	1.20	71	902	1.47	1.90
Nd^{3+} – O^{2-}	94.24	1.25	50000	1.36	56	709	1.49	1.94
Sm^{3+} – O^{2-}	87.79	1.25	50000	1.38	49	630	1.51	1.97
Gd^{3+} – O^{2-}	79.98	1.25	50000	1.38	23	293	1.54	2.00
Y^{3+} – O^{2-}	118.0	1.38	50000	1.50	21	264	1.60	2.08
Sc^{3+} – O^{2-}	61.66	1.28	50000	1.75	15	197	1.77	2.30

Ion	α	radius (Å)	$b_D^{O^{2-}-\square}$	$c_D^{O^{2-}-\square}$	$c_D^{\square-O^{2-}}$
O^{2-}	13.97	1.38	2.18	3.03	–
Ce^{4+}	5.86	0.97	1.75	1.85	0.17
Zr^{4+}	2.38	0.84	1.74	1.56	-0.60
La^{3+}	7.51	1.16	1.50	1.43	-0.20
Ce^{3+}	9.72	1.143	1.59	1.71	0.05
Nd^{3+}	7.24	1.109	1.67	1.94	0.00
Sm^{3+}	6.28	1.079	1.67	1.97	-0.14
Gd^{3+}	2.56	1.053	1.69	1.75	-0.89
Y^{3+}	2.31	1.019	1.47	1.08	-0.60
Sc^{3+}	1.70	0.87	1.67	1.36	-0.39

tained from the averages of these three configurations per system. Each calculation was set up by randomly distributing the dopants over the cation sublattice and the oxygen vacancies over the anion sublattice. The supercells were initially equilibrated at a temperature of 1673 K for 40 ps; the temperature was then scaled down to room temperature at a rate of 2 K ps^{-1}. The diffusion coefficients were calculated for temperatures between 873 K and 1473 K from simulations that were up to 3 ns long in the case of the lowest temperature. The 300 K lattice constants were obtained from 10 ps long runs. All simulations were performed at constant temperature and pressure (NPT ensemble), as described by Martyna et al. [120] using a time step of 1 fs. The Coulombic and dispersion interactions were summed using Ewald summations [78], while the

short-range part of the potential was truncated at 12.96 Å.

5.2.2 Results and discussion

The reliability of the models used in the computer simulations presented throughout this work is assessed in Section 5.2.3 by means of comparison against experimental and computational results for singly doped ceria. We also note that this approach has already been successfully used to model yttria-doped ceria, as reported in ref. [17]. Section 5.2.4 builds upon these results to determine whether co-doping is likely to improve the ionic conductivity in these solid electrolytes. The co-doped systems are referred to as Sc:LDC and Nd:SmDC.

5.2.3 Potential assesment

Lattice constants of singly doped ceria

The DIPPIM simulated lattice constants for $Ce_{0.90}RE_{0.10}O_{1.95}$ at 300 K are shown in Figure 5.1 as a solid black line. Their associated errors are represented by the standard deviation of the values from the three simulations carried out for each system. The dashed red line in Figure 5.1 corresponds to the values for the same systems predicted by Hong and Virkar [220], who derived an empirical expression for the relationship between the ionic radius of the dopant and the lattice constant of RE-doped ceria:

$$a(x, r_{\mathrm{RE}}) = \tfrac{4}{\sqrt{3}}[x r_{\mathrm{RE}} + (1-x) r_{\mathrm{Ce}} + (1-0.25x) r_{\mathrm{O}} + 0.25x r_{\mathrm{v_O}}] \times 0.9971 \quad (5.1)$$

In Equation 5.1, x corresponds to the dopant concentration in $Ce_{1-x}RE_xO_{2-x/2}$, while r_{Ce}, r_{O}, r_{RE} and $r_{\mathrm{v_O}}$ correspond to the ionic radius of Ce^{4+} (0.970 Å) [131], O^{2-} (1.380 Å) [131], the ionic radii of the dopants (See Table 5.1 in the Appendix) and the radius of a vacancy (1.164 Å) [220], respectively. Figure 5.1 also presents experimental (open symbols) and computational (closed symbols) lattice constant values for the

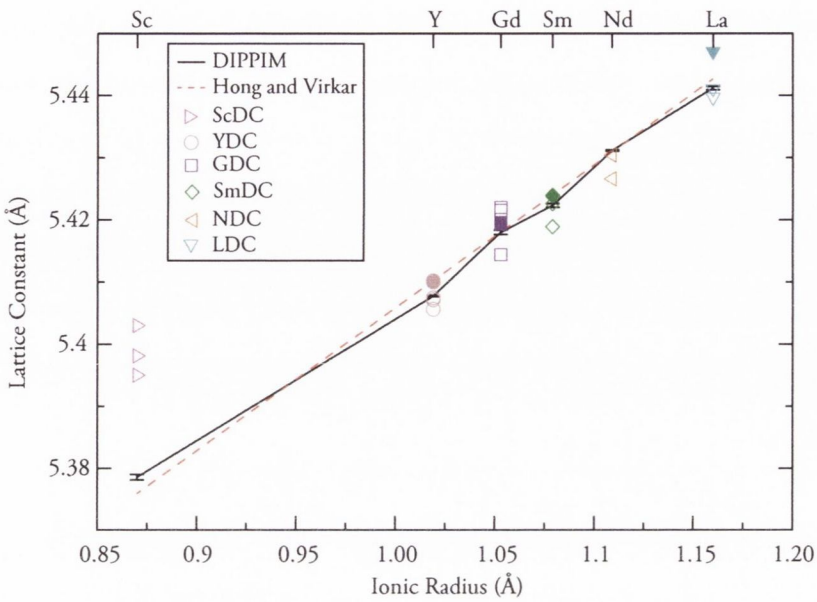

Figure 5.1: Lattice constants for $Ce_{0.90}RE_{0.10}O_{1.95}$. DIPPIM values at 300 K (this work) are shown as a solid black line. The errors correspond to the standard deviation obtained from three simulations. Hong and Virkar [220] values are represented by a dashed red line. Experimental data from [221–223] for ScDC, [129, 191, 224, 225] for YDC, [191, 225, 226, 226, 227] for GDC, [191, 225, 228] for SmDC, [191, 228] for NDC and [163, 225, 229] for LDC.

same compositions (10% cation doped) of ScDC, YDC, GDC, SmDC, NDC and LDC. As shown in Chapter 4, DIPPIM simulations are expected to perform as well as the DFT functional from which they were parameterized [171]. In this case, the use of hybrid DFT functionals means that errors in the calculated value of lattice constants with respect to experiment for doped ceria should be in the order of 0.20% [204]. This is borne out by the results presented in Figure 5.1, which show an excellent agreement with the range of experimental data available in the literature and also with the values calculated from Equation 5.1. In the case of ScDC, the simulations provide a better estimation of the lattice constant than that obtained from Equation 5.1 with respect to experiment, however both models underestimate the value of a_0. For DIPPIM simulations of ScDC, the largest error is 0.45% compared to the value from Grover *et al.* [221]. Despite this being a relatively small error, it is likely that this discrepancy arises from sources other than the DFT functional employed in this work. In fact, of

the three experimental sources cited, Grover *et al.* (highest value for a_0), as well as, Gerhardt-Anderson and Nowick [223] (lowest value for a_0) predict low solubilities for scandia (Sc_2O_3) and thus, formation of C-type phases in $Ce_{0.90}Sc_{0.10}O_{1.95}$ which are characteristic of sesquioxides that crystallize in the cubic bixbyite structure, such as scandia. Although similar, the F-type phase (cubic fluorite, Figure 4.1(a)) differs from the C-type phase in that the latter has an ordered array of oxygen vacancies along the $< 111 >$ direction, leaving the Sc metal with a 6-fold coordination (Figure 5.2(b)).

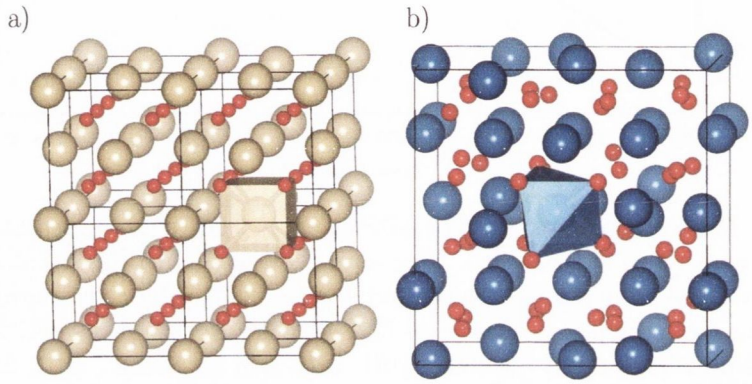

Figure 5.2: a) CeO_2 crystal structure illustrating the 8-fold coordination of Ce^{4+}. b) Sc_2O_3 crystal structure illustrating 6-fold coordination of Sc^{3+}.

Ionic conductivity of singly doped ceria

The ionic conductivities for the singly doped ceria systems under study are presented in Figure 5.3. In agreement with the literature for singly doped ceria, the best dopants were found to be Gd and Sm [12, 151, 228]. In particular, GDC was found to have the highest conductivity among all dopants for the simulations at all temperatures. The size of the errors in this plot illustrates why it is often the case that different studies assign the highest conductivity to different elements, depending on the fabrication conditions or the type of simulation performed. These errors become larger at lower temperatures because of the slower diffusion. Furthermore, the concentration which gives the highest conductivity varies from one doped system to another for a particular temperature. The dashed red line (vertical) shown in Figure 5.3 represents the critical

ionic radius put forward by Andersson *et al.* [23] (r_c) for the ideal dopant cation, which corresponds to that of Pm.

Figure 5.4 presents the DIPPIM simulated ionic conductivities at 873 K, as well as, a range of conductivity values from other studies for the same singly doped ceria ($Ce_{0.90}RE_{0.10}O_{1.95}$) systems at the same temperature. Individual literature values are labelled a) to m), with open symbols indicating experimental values and filled symbols those from other computational studies. This figure shows that there is a significant spread in the experimental data set, as exemplified by GDC which shows a variation in conductivity of $\sim 2.5\times$ (from 0.01 [230] to 0.025 [12]). Such fluctuations are typically ascribed to different fabrication methods, sintering times and temperatures, grain sizes and impurities [12, 230], all of which are excluded from the our computational bulk models. Nonetheless, what is clear from Figure 5.4 is that the DIPPIM potentials used in this work deliver conductivity values which lie in the lower end of the range of the experimental ones, but constitute a good predictor of the overall tendencies in doped ceria.

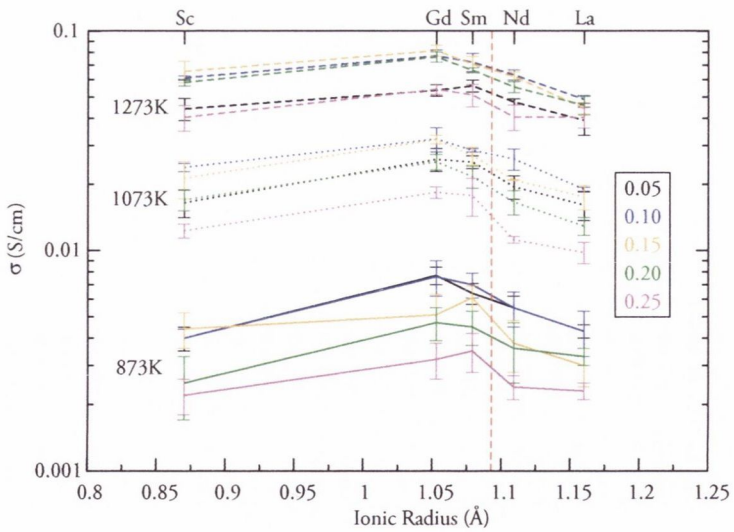

Figure 5.3: Ionic conductivities for singly doped ceria ($Ce_{0.90}RE_{0.10}O_{1.95}$) at 1273 K (blue diamonds), 1073 K (black dots) and 873 K (red triangles). The dashed red line represents the critical ionic radius (r_C) introduced by Andersson *et al.* [23].

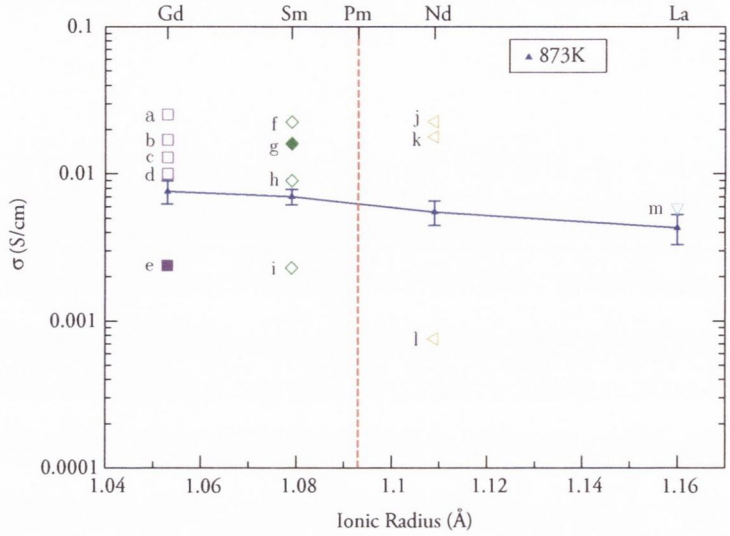

Figure 5.4: Ionic conductivities for $Ce_{0.90}RE_{0.10}O_{1.95}$ at 873 K from this work (solid blue triangles). Open symbols correspond to experimental values, while filled symbols were obtained from computational data in the literature: a) Steele [12], b) Huang *et al.* [226] and Omar *et al.* [192] c) Xia and Liu [231], d) Zhou *et al.* [230], e) Dholabhai *et al.* [232], f) Kasse and Nino [199], g) Grope *et al.* (at 893 K) [233] and Omar *et al.* [191], h) Shemilt and Williams [234], i) Jung *et al.* [235], j) Kasse and Nino [199], k) Omar *et al.* [191] l) Aneflous *et al.* [236] and m) Dikmen *et al.* [229]. The dashed red line represents the critical ionic radius (r_C) introduced by Andersson *et al.* [23]

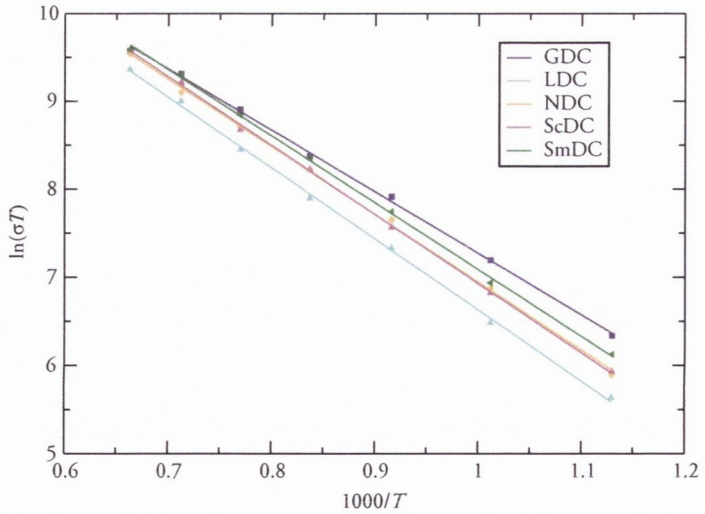

Figure 5.5: Arrhenius plots for singly doped ceria systems, $Ce_{0.90}RE_{0.10}O_{1.95}$, where RE = GDC, LDC, NDC, ScDC, SmDC. The temperature range is 873 K - 1473 K.

The E_a values for these systems were calculated from Arrhenius plots are shown in Figure 5.5. These plots of $\ln(\sigma T)$ vs $1/T$ within this range of temperatures were found to be linear for all dopants. This is important as it indicates that there is no extensive clustering of dopants and vacancies, which would occur if the simulations spanned both sides of the critical temperature (T^*) below which nucleation centres form around the dopants leading to progressive trapping of the vacancies into such clusters as the temperature decreases [10, 226]. If the calculations had been carried out at sufficiently low temperatures ($T^* \approx 856\,\mathrm{K}$ for GDC [226]), then two different E_a values would have be obtained for the $T > T^*$ and $T < T^*$ temperature regimes. For this reason, the literature data presented in Figure 5.6 corresponds to the $T > T^*$ region only. Their corresponding E_a values are presented in Figure 5.6 (filled black circles) as a function of dopant ionic radius and were obtained from simulations between 1473 K and 873 K. Experimental values are distinguished with the same open symbols from Figure 5.4 and labelled a) to o). Just as was found to be the case with ionic conductivities, Figure 5.6 illustrates that the self-consistent DIPPIM potentials used in this work are able to predict the activation energies for the various RE dopants used in this study. This is particularly impressive since no experimental data were used at any stage of the potential parameterazation. We can therefore proceed to study co-doping in this material, with the confidence that the employed simulation technique can reliably predict the properties of these materials.

5.2.4 Co-doped ceria

Lattice constants of co-doped ceria

Figure 5.7 presents the DIPPIM calculated (filled symbols) and experimental lattice constants (open symbols) from Buyukkilic *et al.* [228] at 300 K for $Ce_{1-x}RE_xO_{2-x/2}$, where $x = 0.05$, 0.10, 0.15, 0.20, 0.25 and RE = Sm, Nd, Nd:SmDC and Sc:LaDC. The co-doped systems shown correspond to an effective dopant cation radius of 1.093 Å for the stoichiometries specified in Section 5.2.1. It is evident from the figure that the calculations predict the correct lattice constant for the singly doped systems over the

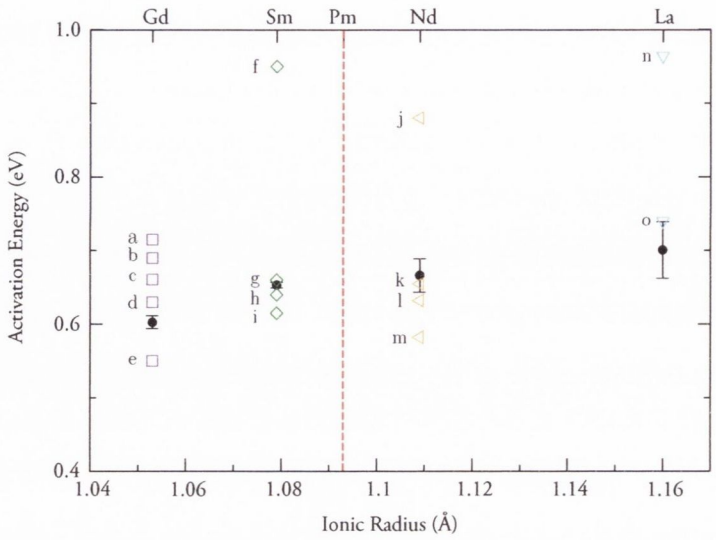

Figure 5.6: Activation energies from this work (filled black circles) between 1473 K and 873 K for $Ce_{0.90}RE_{0.10}O_{1.95}$. Open symbols correspond to experimental values: a) Zhang *et al.* [237], b) Omar *et al.* [192], c) Omar *et al.* [191], d) Huang *et al.* [226], e) Xi and Liu [231], f) Jung *et al.* [235], g) Shemilt and Williams [234], h) Omar *et al.* [191], i) Kasse and Nino [199], j) Aneflous *et al.* [236], k) Omar *et al.* [191], l) Kasse and Nino [199], m) Stephens and Skinner [238], n) Lang *et al.* [239] and o) Dikmen *et al.* [229]. The dashed red line represents the critical ionic radius (r_C) introduced by Andersson *et al.* [23]

entire composition range, and that this carries over to the co-doped cerias under study. The agreement is particularly good for the systems that are the focus of this study, namely $Ce_{0.90}RE_{0.10}O_{1.95}$. The results show that co-doping can be successfully used to reproduce the lattice constant of a cation with a critical dopant radius, r_C.

Ionic conductivity of co-doped ceria

Thus far the results presented for the ionic conductivity of singly doped ceria have shown only progressive changes in both the bulk ionic conductivities and activation energies as a function of dopant ionic radius. Hence, the question of whether co-doping is a viable alternative for substantially improving these properties becomes: *Do co-doped systems show a marked increase (decrease) in ionic conductivity (activation energy) or is this property simply the average of the singly doped systems?*

To answer this question it is necessary to compare directly the ionic conductivity

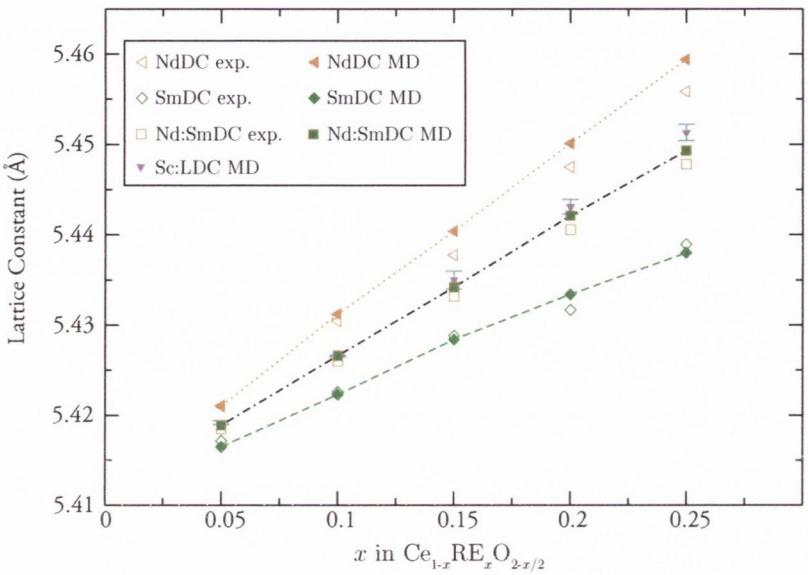

Figure 5.7: DIPPIM calculated (filled symbols) and experimental (open symbols) lattice constants from Buyukkilic *et al.* [228] at 300 K for for $Ce_{1-x}RE_xO_{2-x/2}$, where $x = 0.05$, 0.10, 0.15, 0.20, 0.25 and RE = Sm (diamonds), Nd (triangles pointing left), Nd:SmDC (squares) and Sc:LaDC (triangles pointing down). The lines shown are intended as a guide to the eye only.

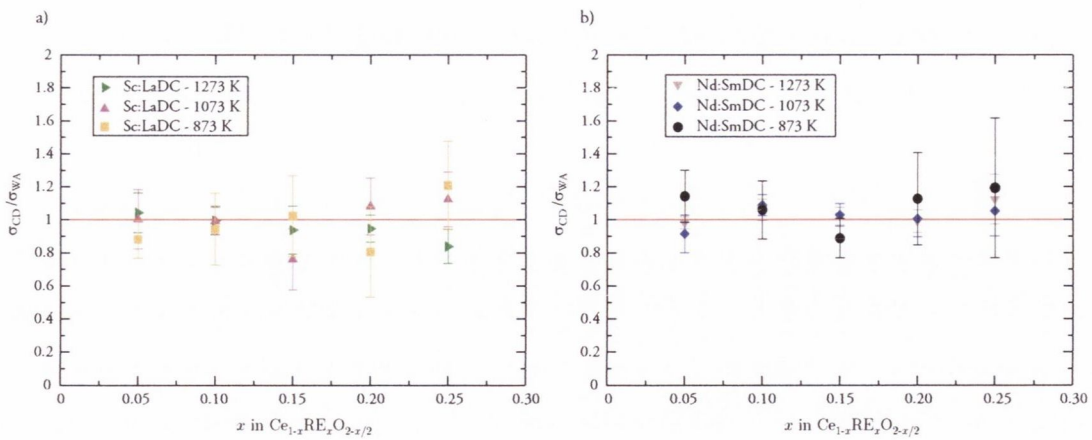

Figure 5.8: DIPPIM ionic conductivities shown as a ratio of the values for co-doped (CD) ceria divided the weighted average (WA) of their singly-doped parent oxides. Panel a) corresponds to the Sc:LaDC system and panel b) corresponds to Nd:SmDC.

of the co-doped systems with that of their "parent" singly doped ceria compounds. Hence if there exists a co-doping effect it would be expected that such systems display ionic conductivities that are higher than the average of the values obtained for singly doped ceria. These data are presented in Figure 5.8 (a) for the Sc:LaDC system and Figure 5.8 (b) for Nd:SmDC. The data in these plots is presented as a ratio of the calculated conductivities for the co-doped systems (σ_{CD}) with respect to the weighted average for the singly doped parent compounds with the same total number of dopant cations (σ_{WA}). The weighting factors are given by the ratio of each co-dopant as specified in Section 5.2.1, namely 0.50 for both Nd and Sm in Nd:SmDC, as well as, 0.22 and 0.78 for Sc and La, respectively in Sc:LaDC. The solid red line indicates a linear correspondence between both data sets (co-doped vs weighted average of singly doped), i.e. no co-doping effect. It is clear from these plots that any deviations in σ_{CD} away from the σ_{WA} values are within the margin of error of these measurements (standard deviation). This indicates that the conductivities of co-doped ceria can be predicted by simply calculating the average of the two parent singly doped cerias for all temperatures and dopant concentrations.

Accordingly, it is expected that the corresponding activation energies for the ionic conductivity of co-doped ceria display the same averaging effect. This is confirmed in Figure 5.9, which depicts the DIPPIM E_a (eV) for $Ce_{0.90}RE_{0.10}O_{1.95}$ from Figure 5.6 (filled black circles), along with those for the co-doped systems, Nd:SmDC (filled blue triangle) and Sc:LaDC (filled black triangle). Experimental values from a) Omar *et al.* [191] (open squares) and b) Kasse and Nino [199] (open circles), with green for SmDC, maroon for Nd:SmDC and orange for NdDC. Both data sets show that despite having the same effective r_{C} value of 1.093 Åand taking into account the errors intrinsic to these calculations, the co-doped Sc:LaDC system has a higher activation energy than Nd:SmDC; that is, the DIPPIM simulations, as well as, the experimental data for these co-doped systems show changes in bulk ionic conductivities and activation energies that are in line with an averaging effect with respect to the singly doped "parent" oxides, with small deviations from this behaviour likely due to sampling error. The simple,

yet often overlooked, explanation for these patterns is found by analyzing the local structure around the dopants in these systems as shown in the next section.

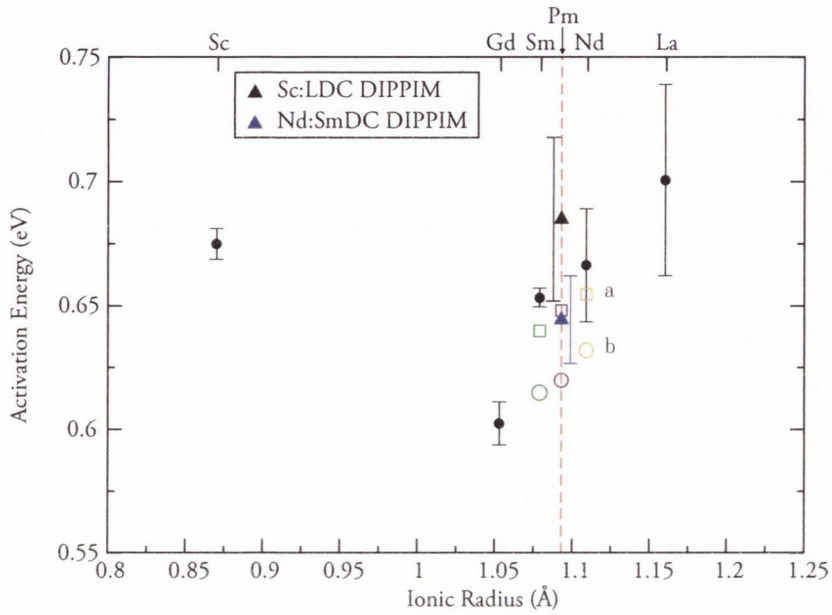

Figure 5.9: DIPPIM activation energies (eV) for $Ce_{0.90}RE_{0.10}O_{1.95}$ from Figure 5.6 along with those for the co-doped systems, Nd:SmDC (filled blue triangle) and Sc:LaDC (filled black triangle). Experimental values from a) Omar *et al.* [191] (open squares) and b) Kasse and Nino [199] (open circles) with green for SmDC, maroon for Nd:SmDC and orange for NdDC.

Local structure of co-doped systems

A configurational analysis of the MD simulations for 10% cation doped LaDC, ScDC and Sc:LaDC is illustrated in Figure 5.10 in the form of the cation-vacancy partial radial distribution functions ($g_{Cat-Vac}(r)$) obtained from the average of the three configurations used for each system. Appendix 4.5.4 details the process of oxygen vacancy identification and subsequent calculation of g(r). The average values are presented in order to eliminate any possible configuration–dependent ordering of the cations. The La/Sc doubly and singly doped systems are illustrated given that the large radius mismatch between the dopant cations with the host facilitates visualization of the small changes undergone, however the conclusions were confirmed for the other co-doped

systems. The top panel shows the g(r)s for La – Vac in Sc:LaDC (dashed orange line) vs La – Vac in LaDC (dotted turquoise line); the bottom panel contains the g(r)s for Sc – Vac in Sc:LaDC (dashed green line) vs Sc – Vac in ScDC (dotted magenta line). The solid black lines in both panels correspond to the Ce – O g(r) in bulk ceria at the same temperature, which exemplifies a random vacancy distribution, but with a slightly different lattice constant due to the absence of dopants. The number of vacancies coordinated to the cations in these systems were obtained by integrating the peaks in Figure 5.10 and are reported in Table 5.2, with the addition of the values for GdDC of the same concentration which are included for comparison as it is the best single dopant system. These results show that Sc acts as a vacancy scavenger in ScDC, with the vacancies ordering in the first coordination shell of this cation. This is a well known effect which has been documented by experiments [223, 240] and simulations [151, 241]. In fact, dopant cations that are smaller in radius than Ce^{4+} are generally expected to have vacancies in Nearest Neighbour (NN) positions, while those that are larger are expected to have the vacancies in the Next Nearest Neighbour (NNN) position. The latter effect is observed in the case of the larger La and Gd (Table 5.2) cations as indicated by the pronounced second peak. The results in Figure 5.10 and Table 5.2 clearly show that the local environment, and thus the local strain, of the dopant cations undergoes few changes in going from singly doped systems to those with more than one dopant species.

Table 5.2: Number of vacancies in the Nearest Neighbour (NN) and Next Nearest Neighbour (NNN) positions with respect to the cations in a random distribution, GdDC, Sc:LaDC, LaDC and ScDC. These values were obtained from the integration of the peaks in Figure 5.10

Peak	Random	GdDC	LaDC	Sc:LaDC	ScDC	Sc:LaDC
	Ce-O	Gd-Vac	La-Vac	La-Vac	Sc-Vac	Sc-Vac
1^{st} (NN)	0.200	0.168	0.062	0.059	0.734	0.878
2^{nd} (NNN)	0.600	1.356	1.502	1.578	0.412	0.467

Previous studies have shown that concomitant with cation–vacancy ordering, there also exist inherent vacancy–vacancy ordering interactions in fluorite-structured mate-

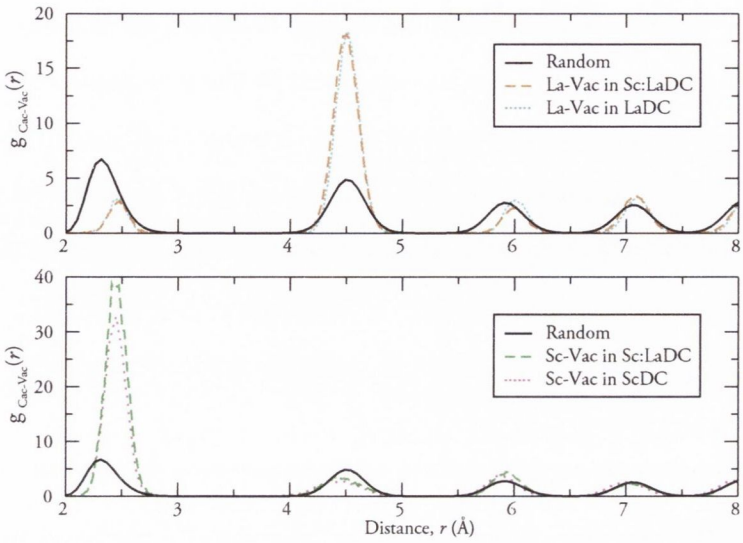

Figure 5.10: Cation–vacancy partial radial distribution functions ($g_{Cat-Vac}(r)$) at 873 K. Top panel: Random (solid black line), La^{3+} – Vacancy in Sc:LaDC (dashed orange line) and La^{3+} – Vac in LaDC (dotted turquoise line). Bottom panel: Random (solid black line), Sc^{3+} – Vacancy in Sc:LaDC (dashed green line) and Sc^{3+} – Vacancy in ScDC (dotted magenta line)

rials [11, 162, 171, 242]. Figure 5.11 presents the three configuration average vacancy–vacancy partial radial distribution functions ($g_{Vac-Vac}(r)$) at 873 K for Sc:LaDC (solid black line), LaDC (dot–dashed turquoise line), ScDC (dotted magenta line), GdDC (dot-dot-dashed green line) as well as a random vacancy distribution, which is simply the O – O g(r) from CeO_2 at the same temperature. The <100>, <110> and <111>, <210>, etc labels indicate different directions along the simple cubic anion sublattice. The values obtained upon integration of these peaks are reported in Table 5.3. The results show that for this dopant concentration vacancies display some degree of long range ordering as evidenced by the sharp peaks in the <210> and <211> positions, while the positions that are at shorter distance in the simple cubic lattice are underpopulated with respect to a random vacancy distribution. This effect arises from the Coulomb repulsions between the vacancies. Common to all the doped ceria systems is also a deleterious redistribution of the vacancies which favours short range occupancy along the <111> direction with respect to an idealized random system. This effect is larger in inferior conductors, like LaDC and ScDC than in the better ones like GdDC,

for example; in the case of Sc:LaDC, co-doping is shown to enhance this ordering, because the small Sc^{3+} cations trap the vacancies in the NN positions, while the large La^{3+} cations repel them towards NNN but also increase their migration barrier [241], which leads to an overall increase in the vacancy ordering of co-doped systems. This indicates that the "synergistic" effect on bulk ionic conductivity from co-coping is not realized.

Table 5.3: Number of vacancies surrounding another vacancy along the <100>, <110> and <111> directions of the simple cubic anion sublattice of 10% cation doped GdDC, LaDC, ScDC and Sc:LaDC, as well as a random distribution of the same number of vacancies. These values were obtained from the integration of the peaks in Figure 5.11

System	<100>	<110>	<111>
Random	0.150	0.300	0.200
GdDC	0.001	0.010	0.056
LaDC	0.06	0.007	0.107
ScDC	0.001	0.062	0.170
Sc:LaDC	0.006	0.023	0.213

5.2.5 Ceria co-doping in perspective

Despite the significant improvements in the ionic conductivity of co-doped ceria reported by several previous studies [130, 192–195, 197, 201, 243, 244] this work found that this property is simply an average of the singly doped materials. This is in accordance with an early experimental/computational study by Yoshida *et al.* [245, 246], as well as, recent experimental data reported Figure 5.9 for Nd:SmDC [191, 199]. Similar results were reported by Ralph *et al.* for Yb:LaDC and Sm:YDC, and by Li *et al.* [240] for Sc:GdDC, who observed a worsening in these properties for co-doped cerias with substantially mismatched dopant cations. The interpretation provided in both cases was that the localized nature of the strains caused by each dopant species does not change substantially in the co-doped systems compared to singly doped materials.

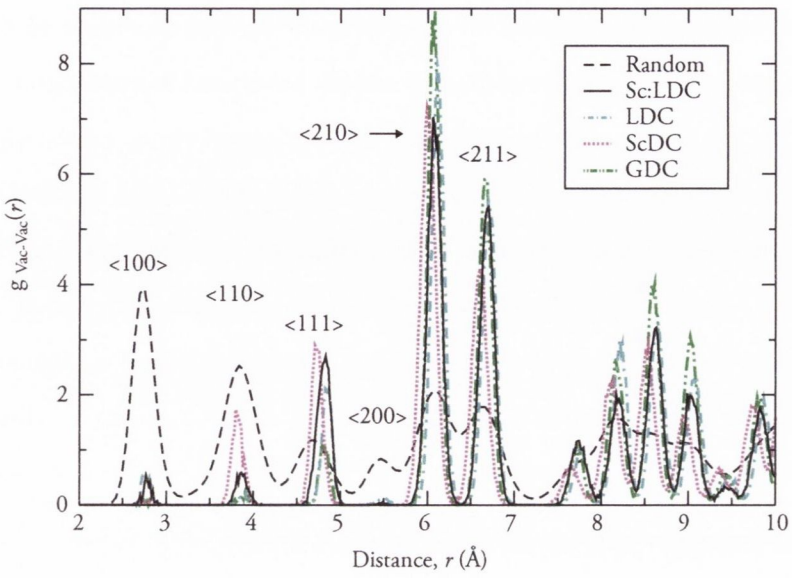

Figure 5.11: Vacancy–vacancy partial radial distribution functions at 873 K for Sc:LaDC (solid black line), LaDC (dot-dashed turquoise line), ScDC (dotted magenta line), GdDC (dot-dot-dashed green line) and a random vacancy distribution (O–O g(r)). The <100>, <110> and <111> labels indicate different directions along the simple cubic anion sublattice.

We point out that our investigation has left out a series of factors, such as long-range cation ordering, grain boundaries, impurities, etc, that might also affect the total conductivity of these materials. This was done on purpose, because the focus of this investigation was on bulk properties of perfect fluorite-structured materials. We note here that these factors have usually a detrimental effect on the conductivity of these materials, so that our conclusions are not invalidated by leaving them out. For instance, cation ordering might be expected in Sc:LaDC[247], because the cations have significantly different ionic radii. This was not taken into account in these calculations, because the cations were randomly distributed and the simulation timescale does not allow them to diffuse. Cation ordering is known to lead to a decrease of the ionic conductivity, as observed in several oxides [158, 248], so that the effects of co-doping might be even more detrimental to the material's conductivity that what we predict in this investigation.

Finally, we wonder why many studies have found an enhancement of the ionic conductivity in some co-doped materials, while others have not. We note that, as discussed above, there are many factors (grain boundaries, cation ordering, phase separation and nano-domain formation, impurity levels, etc) that affect the ionic conductivity of these materials and it is very hard to separate their effects. As an example, the conductivity of 10% GdDC, as shown in figure 5.4, varies by as much as a factor of 2.5 in different experiments. Such a huge variation is probably caused by a combination of these factors and shows that it is not trivial to compare the conductivity of these materials.

5.3 Ceria-zirconia solid solutions

Ceria-zirconia ceramics are essential components within automotive exhaust catalysts, where the $Ce^{3+} \leftrightarrow Ce^{4+}$ redox reactions allow them to operate as oxygen ion buffers that provide oxygen to convert harmful CO and hydrocarbon gases to more benign CO_2 and H_2O species [249, 250]. Under reducing conditions, the ZrO_2-CeO_2 system should transform into the ZrO_2-Ce_2O_3 one, though their phase diagrams are rather different and only tentative suggestions for the ternary ZrO_2-CeO_2-Ce_2O_3 phase diagram have been presented (see Ref. [251], and references therein). However, particular attention has focused on the systems with a Zr:Ce ratio of 1:1. Conventional high temperature solid-state synthesis under oxidizing conditions produces $Zr_{0.5}Ce_{0.5}O_2$ with a tetragonal distortion of the fluorite structure (labelled t'), which transforms to the cubic fluorite phase with randomly distributed cations at 1831 K [252]. Reduction of the same material at temperatures in excess of 1323 K favours the loss of oxygen and ordering of the two cation species along the <110> direction to form a pyrochlore structured phase of stoichiometry $Ce_2Zr_2O_7$ in which the oxygen vacancies are next to the smaller Zr^{4+} cations, leaving them with a 6-fold coordination (see Figure 5.12) [253, 254].

Oxidation of the $Ce_2Zr_2O_7$ phase at temperatures of $\sim$873 K incorporates additional O_2 into the lattice, forming the phase κ-$CeZrO_4$ [255]. Remarkably, the pyrochlore-like long-range ordering of the cations is retained throughout the intercalation of anions from $Ce_2Zr_2O_7$ to κ-$CeZrO_4$, though the latter phase is metastable and reverts to the

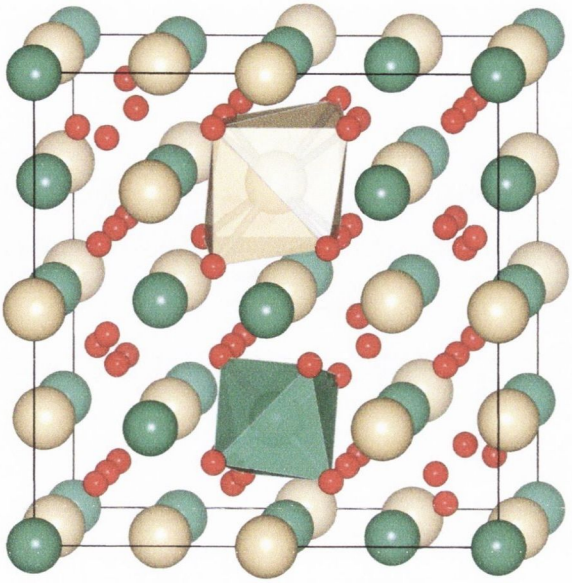

Figure 5.12: Pyrochlore structure of the $Ce_2Zr_2O_7$ system. The Ce^{4+} cations are shown in beige, Zr^{4+} cations are shown in green and the oxygen anions in red.

(cation disordered) t'-$Zr_{0.5}Ce_{0.5}O_2$ phase at $\sim$1123 K [256]. The crystal structure of κ-$CeZrO_4$ can be described as a 'filled pyrochlore', though diffraction studies indicate that the symmetry is either cubic [254] or rhombohedral [257] and involves partially occupied anion sites significantly displaced from the ideal positions within the equivalent cubic fluorite arrangement.

It has been observed that κ-$CeZrO_4$ possesses a remarkably high oxygen storage capacity (OSC), which is defined as the ratio of reduced cerium ions in the system, i.e. $[Ce^{3+}]/([Ce^{3+}]+[Ce^{4+}])$. In the case of κ-$CeZrO_4$ it is around 89% of the theoretical maximum value [254, 258], which is close to twice that of other ZrO_2-CeO_2-Ce_2O_3 compositions, including t'-$Zr_{0.5}Ce_{0.5}O_2$, and roughly 50 times that of pure CeO_2.

The OSC of CZO is very important for its applications in TWCs and, in order to better understand its origins it is necessary to make use of the atomic-level information gleaned from computer simulations. The macroscopic observable of OSC depends on two properties that can be calculated, namely, the reduction energy and the ionic

conductivity. Thus, a low reduction energy is essential in order to facilitate the release of oxygen, while a high oxygen diffusivity will ensure that this material can respond quickly to changes in the oxygen content of the exhaust chamber. As a result, the aim of this section is to investigate the evolution of the ionic conductivity of CZO as a function of $[Ce^{3+}]$, and, in doing so, to study the role of ordering and crystal structure on the conducting properties of CZO. These simulated conductivity results are of great information

5.3.1 Methods

MD simulations were performed on cation ordered (pyrochlore-like) and cation disordered (fluorite-like) $Ce^{4+}_{0.5-2\delta}Ce^{3+}_{2\delta}Zr^{4+}_{0.5}O^{2-}_{2-\delta}$ solid solutions on 6 x 6 x 6 supercells. These cells contained $\sim$ 2592 atoms, depending on the level of reduction being simulated, which ranged from fully oxidized systems, $\delta = 0.00$, to fully reduced systems, $\delta = 0.25$ in increments of 0.025. These concentrations are reported in terms of the vacancy concentration as it is the most common form found in the CZO literature and because it facilitates the comparison with the other doped-ceria systems already discussed, given that $2\delta = x$. The supercells were initially equilibrated at a temperature of 1673 K for 40 ps; the temperature was then scaled down to room temperature at a rate of 2 K ps^{-1}. The diffusion coefficients were calculated for 1273 K from simulations that were up to 1.5 ns long. The remaining details of the simulations were the same as those in Section 5.2.1.

5.3.2 Results

The ionic conductivities (S/cm) at 1273 K for $Ce^{4+}_{0.5-2\delta}Ce^{3+}_{2\delta}Zr^{4+}_{0.5}O^{2-}_{2-\delta}$ are presented in Figure 5.13. The black diamonds indicate the conductivities of the fluorite-structured (disordered cations) systems, while the red triangles correspond to those calculated for the pyrochlore-like (ordered cations) systems. Although the data is somewhat scattered given the relatively large errors associated with the slow diffusions observed and the fact that a single configuration was used for each concentration of Ce^{3+}, it is clear

that the conductivity of the disordered systems is on average 20 times larger than that observed in the ordered systems. Also shown in Figure 5.13 are the conductivities of GDC and LDC with equivalent numbers of vacancies at the same temperature. In this case, the difference between the best ionic conductor (GDC) and the fluorite-structured CZO systems is in the order of 5 times, while the conductivity of LDC is 3 times higher on average than that of disordered CZO. These results are expected given the large ionic radius mismatch mismatch between Ce^{4+}, Ce^{3+} and Zr^{4+}. The conductivities of pyrochlore-structured CZO systems are also impacted by the underlying cation order of these compounds. In fact, the conductivities of the pyrochlore systems were so low that a step-like MSD was observed (Figure 5.14).

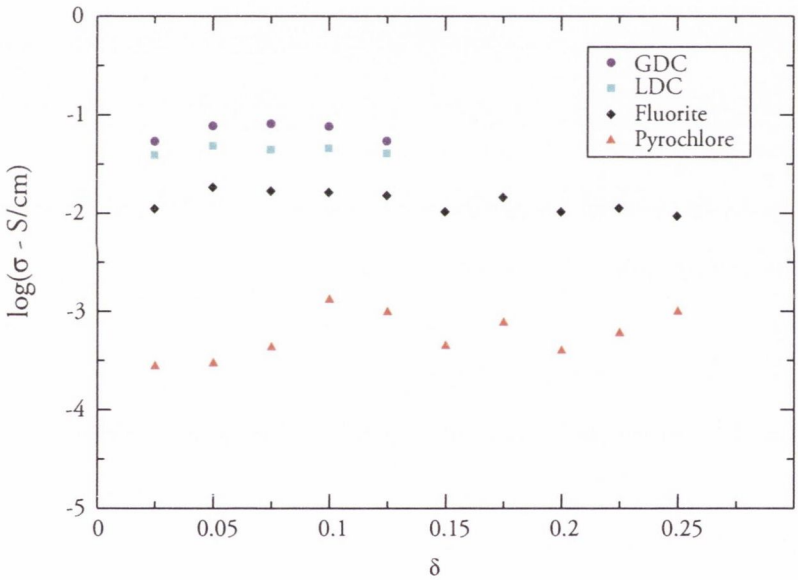

Figure 5.13: Ionic conductivities (S/cm) of CZO solid solutions. The black line indicates the conductivities of the fluorite structured systems, while the red line corresponds to those calculated for the pyrochlore-like systems. The conductivity values for GDC are shown in purple and those for LDC in turquoise. Concentrations are expressed in terms of δ, which corresponds to the vacancy concentration in $Ce^{4+}_{0.5-2\delta}Ce^{3+}_{2\delta}Zr^{4+}_{0.5}O^{2-}_{2-\delta}$.

The cation-vacancy $g(r)$s for $Ce^{4+}_{0.35}Ce^{3+}_{0.15}Zr^{4+}_{0.5}O^{2-}_{1.925}$ solid solutions at 1273 K are illustrated in Figure 5.15). Panel (a) shows that the vacancies reside in the NN position to the small Zr^{4+} cation in both fluorite and pyrochlore CZO, although enhanced occopancy is observed in the latter due to the structural characteristics of this crystal

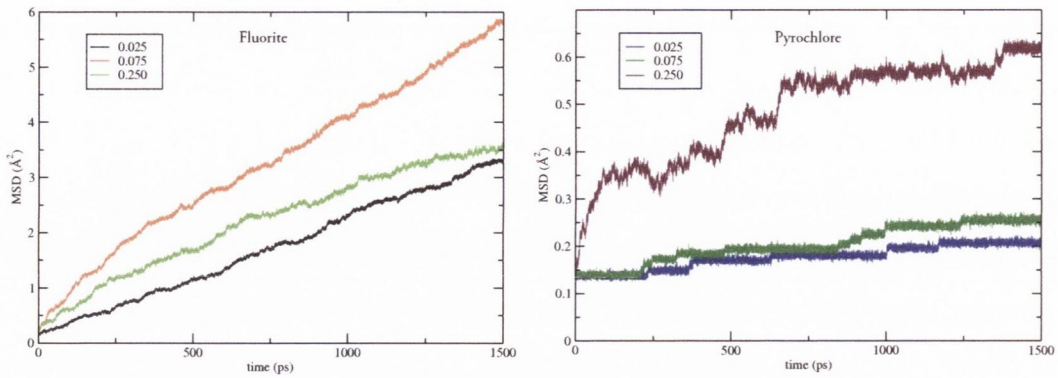

Figure 5.14: MSDs for $Ce^{4+}_{0.5-2\delta}Ce^{3+}_{2\delta}Zr^{4+}_{0.5}O^{2-}_{2-\delta}$ solid solutions at 1273 K for selected concentrations. The data for fluorite-structured CZO is shown on the left panel, while those for the pyrochlore-structured CZO is shown on the right.

system. In the case of the larger cations, Ce^{4+} (b) and Ce^{3+} (c), there is a substantial difference in the first coordination shell between both structures; the vacancies in pyrochlore systems are NNN to both large cations. The large height of the peaks for the preferred positions of vacancies with respect to Zr^{4+} and Ce^{3+} indicate that there is trapping of the vacancies at these sites.

The most striking evidence for this vacancy trapping is observed in the $g_{V-V}(r)$ of these compounds, which are plotted in Figure 5.16. Although, disordered CZO is a poor conductor, it still retains tha main features of vacancy ordering that are found in high performance electrolytes like GDC. However, the positioning of the vacancies in the pyrochlore-like systems confirms that the low vacancy mobilities result from trapping.

Thus far the simulations indicate that pyrochlore-structured CZO is a rather poor ionic conductor. Hence, to understand why this ordered structure performs better as an OSM than its cation-disordered counterpart, it is necessary to quantify the differences in the reduction energy in both structures. Figure 5.17 presents the DFT+U calculated values for this property as a function of δ. These calculations were performed by Dr Dario Marrocchelli using a $2 \times 2 \times 2$ fluorite supercell with 96 atoms where the cations were either ordered in a pyrochlore-like structure or placed at random. The reduction energies is given by $E_{\text{Reduction}} = E_{\text{Bulk}} - E_{\text{Defect}} - 1/2E^{O_2}_{\text{Form.}}$ were then calculated by

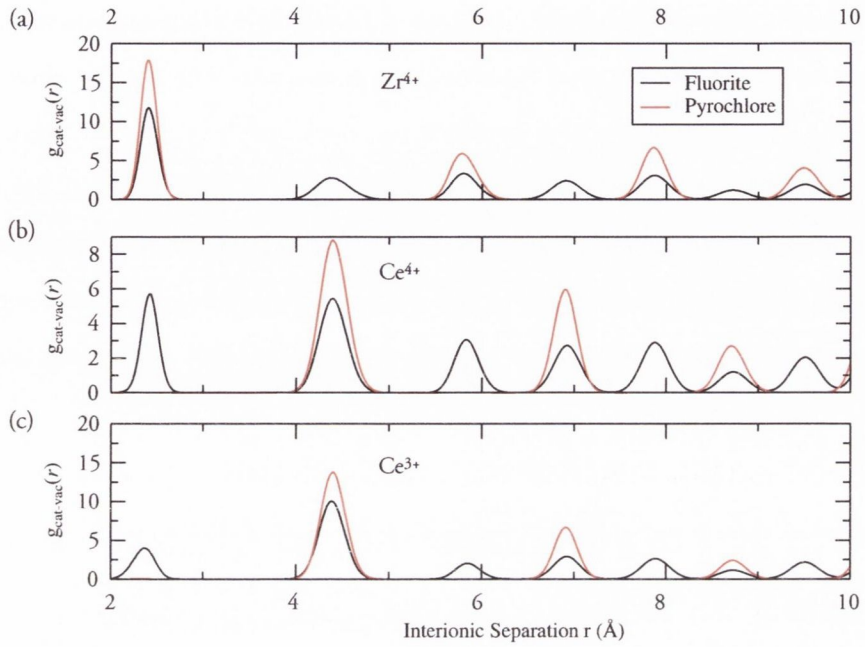

Figure 5.15: Cation-vacancy partial RDFs for $Ce^{4+}_{0.35}Ce^{3+}_{0.15}Zr^{4+}_{0.5}O^{2-}_{1.925}$ solid solutions at 1273 K: (a) Zr^{4+}-Vac in Fluorite (black) and Pyrochlore (red) CZO. (b) Ce^{4+}-Vac in Fluorite (black) and Pyrochlore (red) CZO. (c) Ce^{3+}-Vac in Fluorite (black) and Pyrochlore (red) CZO.

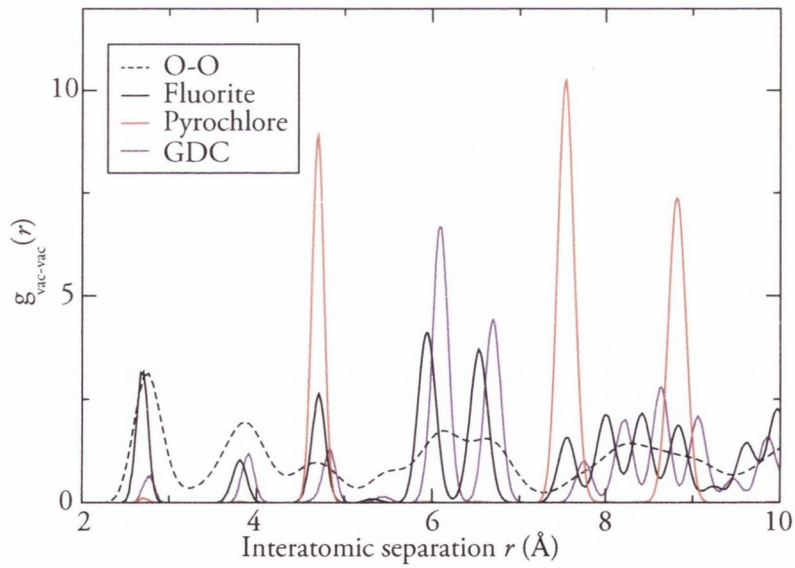

Figure 5.16: Vacancy–vacancy partial radial distribution functions for $Ce^{4+}_{0.35}Ce^{3+}_{0.15}Zr^{4+}_{0.5}O^{2-}_{1.925}$ at 1273 K, with fluorite CZO shown in orange and pyrochlore shown in green. The $g_{O-O}(r)$ of pure ceria at the same temperature is shown in black, while the $g_{V-V}(r)$ of $Ce_{0.85}Gd_{0.15}O_{1.925}$ is shown in blue.

removing individual oxygens from the lattices until all the cerium cations were reduced, which is achieved when a total of 8 anions are removed. The results show that the reduction energies of both systems coalesce as successive oxygens are removed from the structures. However, the average reduction energy of the fluorite CZO system is 2.02 eV, while that of pyrochlore CZO is 0.58 eV. This difference between both systems is likely the cause for enhanced OSC in pyrochlore CZO with respect to fluorite CZO. Similar observations have been made experimentally by [259] and using DFT+U by [30].

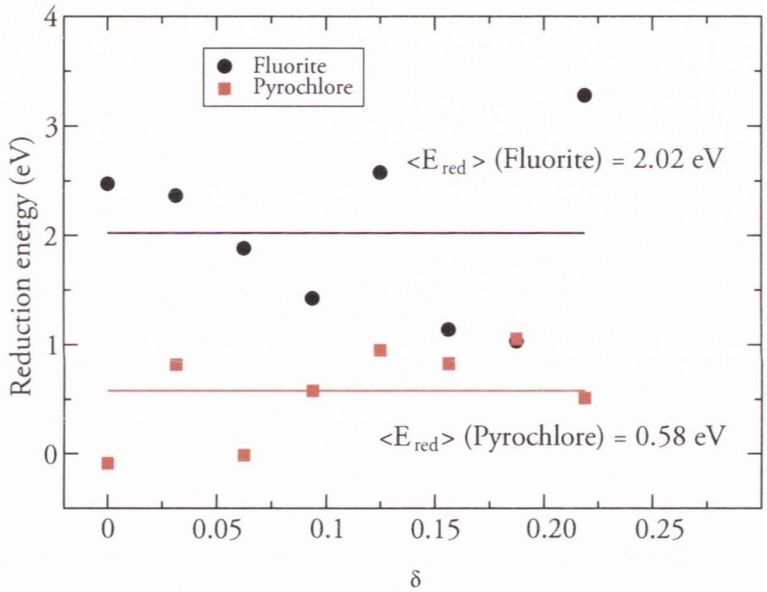

Figure 5.17: Reduction energy as a function of non-stoichiometry in $Ce^{4+}_{0.5-2\delta}Ce^{3+}_{2\delta}Zr^{4+}_{0.5}O^{2-}_{2-\delta}$ for the fluorite-structured (black dots) and pyrochlore-structured (orange) systems.

5.4 Conclusions

This work was motivated by the conflicting evidence that surrounds the merits of ceria co-doping as a means to improve this electrolyte's ionic conductivity. Here we used Molecular Dynamics simulations that employ accurate interionic potentials, parameterized with respect to *first-principles* calculations. No experimental data was used to

parameterise these potentials. This methodology allowed the study of large systems at realistic operating temperatures ($\sim$ 873-1273 K) and defect concentrations. The conclusions pertain only to *bulk* properties, because the models that were simulated do not include grain boundaries, impurity segregation, dislocations, etc.

The results show that co-doping can be successfully used to reproduce the lattice constant of ceria doped with a single cation which has an ionic radius equal to the effective radius from two co-dopants. However, close examination of the *bulk* ionic conductivity of co-doped ceria revealed that this property is not enhanced by co-doping and can be described as an average of the conductivities of the "parent" singly-doped compounds. This result was explained by the fact that the vacancy ordering tendencies of individual dopant cations remain largely unchanged in co-doped systems. For this reason, co-doping with cations that are bigger/smaller than a given ideal dopant radius (r_C) leads to the combination of unwanted defect trapping tendencies, as exemplified by the case of the significantly mismatched Sc:LaDC system, where Sc^{3+} is an oxygen vacancy scavenger while La^{3+} repels vacancies. In conclusion it is the *local* structure of these materials, rather than their average structure, that dictates their conducting properties. These results effectively reject co-doping as a possible avenue for improving ceria conductivity. More fruitful outcomes are likely to be achieved in other intensely investigated areas such as the application of strain [186, 260, 261].

6

Strain effects on the ionic conductivity of ceria-based electrolytes

6.1 Introduction

Current thin film deposition techniques allow for the fabrication of epitaxially grown oxides with high levels of control over the microstructure, stoichiometry and lattice mismatch of individual layers [262–266]. These developments have attracted much attention to this area of research because they might open a new avenue for SOFC electrolyte optimization in a way similar to that which has been achieved in Si-based semiconductors [267]. Changes in the ionic conductivity of thin film electrolytes, whether detrimental or beneficial, are ascribed to interfacial effects present at phase boundaries. One such effect is the formation of space charge regions which have been shown to cause a dramatic increase in the fluoride ion conductivity of materials with a low concentration of bulk defects, such as, BaF_2/CaF_2 heterostructures [268, 269]. However, heavily doped extrinsic ionic conductors like doped ceria/zirconia possess narrow space charge regions, and thus, are not expected to display a significant enhancement of their ionic conductivity as a result of this effect [262, 266, 270]. Coherent growth of

a thin film on a substrate, or heterostructure, leads to *strain* (ϵ) due to the structural mismatch which arises from differences in their lattice vectors (Equation 6.1).

$$\epsilon = \frac{a_1 - a_0}{a_0} \tag{6.1}$$

Thin films can elastically accommodate strains of $\epsilon \sim 0.03$, depending on the thickness of the film and the elastic properties of the material [263, 271]. Strain levels beyond this value are typically released by the films through the formation of dislocation networks, defect clustering at the interface and rotations with respect to the substrate or other layers [272–275].

Substantial research efforts have been devoted, over the last decade, to the elucidation of how interfacial effects alter ionic conductivity. Many such studies have focused on YSZ as it is the prevalent electrolyte in SOFCs. The results reported in the literature for this material show significant scatter in the range of conductivities achieved through the formation of interfaces. Experimental investigations have observed conductivity enhancements varying from a colossal 10^8 increase in σ_i [276] down to neglegible changes [277] and myriad values in between [266, 270, 271, 278–283]. Early theoretical work using Molecular Dynamics (MD) simulations found only a small enhancement in σ_i for YSZ mediated by a lowering of the activation barrier [284]. Similar conclusions were arrived at more recently by Dezanneau *et al.* [285], who also performed MD simulations, and found enhancements of up to $2\times$ for strains of 3% at 833 K. These results are further corroborated by recent Density Functional Theory (DFT) calculations which have predicted a maximum enhancement of up to four orders of magnitude in this property, at 400 K for relatively high strains ($\epsilon = 4\%$) [260, 261].

In the case of REDC, the conductivity enhancements observed have been more modest. For example, Chen *et al.* studied thin GDC films grown on MgO (lattice mismatch of 28%) and found only a small increase in the ionic conductivity with respect to the bulk system [272]. Suzuki *et al.* [286] spin coated sapphire substrates

with CeO_2 thin films, as well as, GDC films of different concentrations. Their study found that the conductivity increased with diminishing film thickness. However, this change may be attributed to a lowering of the oxygen vacancy formation energy which leads to reduction of Ce^{4+} to Ce^{3+} (Equation 1.6), and thus, to electronic conductivity [287].

This is an undesirable effect in SOFC electrolytes as it causes an internal short circuit and cell delamination through lattice expansion [11, 19–21, 126, 263, 288]. Similar results were obtained by Perkins *et al.*, who saw the formation of discrete micro-domains containing Ce^{3+} in SDC/CeO_2 heterostructures ($\epsilon \sim 0.0035$) grown on MgO substrates [289]. Studies of the ionic conductivity in epitaxial SDC films grown on MgO substrates using $SrTiO_3$ (STO) buffer layers ($\epsilon \sim 0.016$) found a conductivity of 0.07 $S\,cm^{-1}$ at 973 K compared to ~0.02 $S\,cm^{-1}$ for dense polycrystalline pellets at the same temperature [265]. In the case of STO-buffered SDC/YSZ heterostructures ($\epsilon \sim 0.055$)) grown on MgO, the same group found a conductivity increase of two orders of magnitude with respect to SDC polycrystaline pellets and about one order of magnitude increase compared to either SDC or YSZ thin films [266]. A recent computational study, which employed static calculations with interatomic potentials, predicted an enhancement in σ_i of up to four orders of magnitude when tensile strain ($\epsilon = 0.040$) was applied to bulk CeO_2 [290]. These enhancements in conductivity were attributed by Rushton *et al.* to a lowering of the binding energy between oxygen vacancies and dopant cations [291].

This brief survey of our current understanding of interfacial effects highlights the need for further investigation in this area of materials research. To this end, computer simulations can play an important role because the various processes which underlie complex phenomena can be treated in a direct and controlled manner, thus, making it possible to evaluate their contribution to the overall changes observed in experiments. In this work we have assessed how the ionic conductivity in YDC is modified when bulk and thin films are subjected to isotropic and anisotropic biaxial strain, respectively. Our study has a series of distinctive features that set it apart from previous

work. Firstly, we use molecular dynamics simulations coupled with accurate dipole-polarizable interatomic potentials derived directly from *ab initio* calculations [17, 171]. Secondly, our use of the slab method allows us to account for the relaxation perpendicular to the plane where strain is applied (Poisson effect), as well as the effect on the ionic conductivity that results from the presence of surfaces on this material; all under realistic dopant concentrations (10-20 %) and high temperatures (1273-1673 K). Also, this paper differs from previous ones [260, 261, 290, 292] in that we only study small strain levels ($\epsilon \leq 0.021$), that can be elastically accommodated in thin films. Finally, in our simulations, the Ce cation reduction reaction (Ce^{4+} to Ce^{3+}), observed in some studies [286], is not allowed. This makes it possible to isolate the effects of strain on the *ionic* conductivity only.

6.2 Methods

6.2.1 Interatomic Potential

The computational methods used in this study are well established and have been described elsewhere for doped ceria and other oxides [17, 155, 158, 160, 171], as well as fluoride systems [212, 213]. The interatomic potential that was employed is known as the DIPole Polarizable Ion Model (DIPPIM) [91] and was described in Chapter 2. The derivation of parameters for the IP is described in Chapter 5, where h-DFT, rather than LDA was employed as was the case for the potential in Chapter 4. The parameters used are listed in Table 5.1. The inclusion of a fraction of nonlocal Hartree-Fock exchange to standard DFT in functionals such as HSE is known to be necessary to correctly describe the electronic strucuture of lanthanide oxides such as ceria [204, 205]. This is important in cases where highly correlated f-electrons are present. However, for YDC this potential represents an improvement in terms of a closer agreement to experimental lattice constants [204].

6.2.2 MD Simulation Details

All Molecular Dynamics simulations were performed with an in-house code (PIMAIM) which uses three-dimensional periodic boundary conditions. The ionic conductivities of three different dopant concentrations were studied, namely $Ce_{1-x}Y_xO_{2-x/2}$ where $x = 0.08, 0.12, 0.18$. This choice of values originated from our previous work, described in Chapter 4, where it was found that the conductivity maxium in YDC is at $x = 0.12$ [171]. The other two values for the dopant concentration were included in order to investigate if straining YDC causes a shift in the position of the conductivity maximum. As was the case in previous studies, the dopant cations and their corresponding charge compensating vacancies were distributed at random within their respective sublattices. Short MD simulations were carried out for each concentration at constant temperature and pressure (NPT ensemble) [120] in order to obtain the equilibrium lattice constants at three temperatures, $T = 1673\,\mathrm{K}$, $1473\,\mathrm{K}$ and $1273\,\mathrm{K}$. Isotropic tensile strain was simulated by expanding the axes of $6 \times 6 \times 6$ fluorite supercells (henceforth referred to as bulk) under constant temperature and volume conditions (NVT ensemble). Each bulk simulation cell was subjected to three different strain levels $\epsilon_x = \epsilon_y = \epsilon_z = \{0.007, 0.014, 0.021\}$ for each temperature. YDC thin films of the same concentrations as bulk were simulated using slabs that exposed the (111) surface which has been found to be the most stable for ceria both in experiments and simulations [293, 294]. The size of the simulation cells along x and y were ~ 30Å and ~ 26Å (Figure 6.1a), respectively, depending on the dopant concentration and temperature. The length along the z-axis for the slab simulation cells was 80 Å. This corresponded to a vacuum gap of $\sim$ 40 Å depending on the dopant concentration and temperature (Figure 6.1b). The vacuum gap is necessary in order to avoid interactions between periodic images of the slabs along this direction. By using slabs with these dimensions it was possible to have similar numbers of ions of each species as in the bulk YDC cells. Table 6.1 reports the number of atoms from each species in these systems. The simulation of anisotropic biaxial strain on YDC was performed by applying every combination of strain to the slabs, where $\epsilon_x, \epsilon_y = \{0.007, 0.014, 0.021\}$ (Picture 6.1a). These simulations were run

in the NVT ensemble resulting in the lattice vectors along the x and y directions of the slabs being fixed while relaxation was allowed along the direction normal to the slab surface (z-axis) in order to account for the Poisson effect (Picture 6.1b). Note also that the effective strain applied to the slabs is different to that applied to the bulk systems given their different orientations, thus a certain strain along <100> direction will have a different effect to the same strain along <111> direction [295].

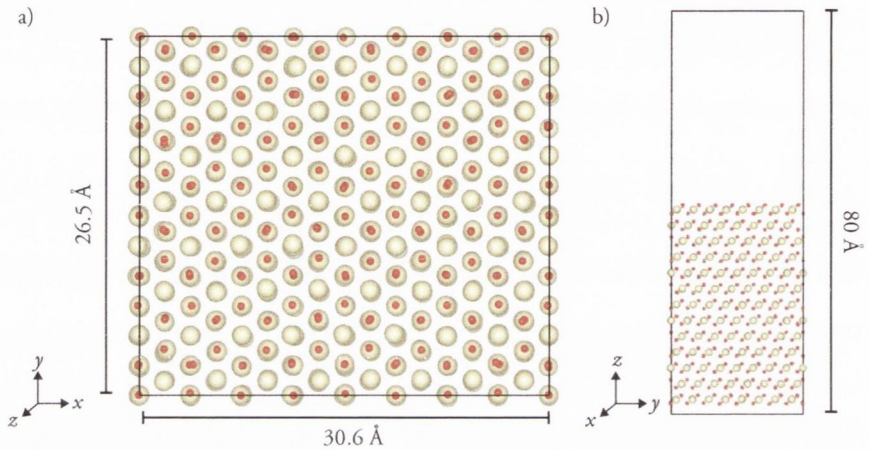

Figure 6.1: a) CeO_2 slab xy-plane b) Slab yz-plane. Ce^{4+} and O^{2-} are shown in as beige and red spheres, respectively.

Table 6.1: Number of ions from each species in the bulk and slab simulation cells for each concentration of YDC.

	Bulk			Slab		
x in $Ce_{1-x}Y_xO_{2-x/2}$	Ce	Y	O	Ce	Y	O
0.08	796	68	1694	766	66	1631
0.12	762	102	1677	734	98	1615
0.18	710	154	1651	684	148	1590

The use of the DIPPIM interatomic potential made it possible to perform the long simulations required to measure the diffusion coefficients of these systems, which in the case of the lowest temperature considered was 600 ps with a timestep of 1 fs for all calculations. Coulombic and dispersion interactions were handled using Ewald summa-

tions, while the short-range part of the potential was truncated at 12.7 Å. The errors associated with the reported values for conductivities and activation energies were estimated from the calculations on YDC presented in Chapter 5, where the three different supercell configurations were used for each concentration under study.

6.3 Results and discussion

6.3.1 Bulk YDC conductivity

Figure 6.2 presents the activation energies, E_a (eV), for vacancy migration in bulk YDC obtained from DIPPIM simulations using both the HSE IP parameters (Table 5.1) from Chapter 5 and those presented in Chapter 4, which were obtained from LDA calculations (Table 4.1), as well as, from experimental data available in the literature. The E_a values predicted by the h-DIPPIM potential were calculated from Arrhenius plots of the ionic conductivity in the temperature range 1273 K – 1673 K (NVT ensemble) for each of the three concentrations considered in this study. The errors associated with this data set were found to be in the order of 3%. The previous LDA-DIPPIM (l-DIPPIM) work used 4 × 4 × 4 cells under NPT conditions [17] and a wider temperature range (1073 K – 2073 K). As expected, both sets of computational data are very similar despite being parameterized using different DFT functionals (h-DIPPIM shown as green circles and l-DIPPIM as black triangles). Moreover, the values from the simulations are in good agreement with the range of available experimental results (blue diamonds [296] and red squares [26]). Table 6.2 contains the DIPPIM calculated bulk σ_i (S cm^{-1}) as a function of dopant concentration at 1473 K. Both the h-DIPPIM and the l-DIPPIM potentials predict $x = 0.12$ to be the ionic conductivity maximum in YDC. The same level of agreement was observed between the potentials for all temperatues studied. This indicates that the h-DIPPIM potential maintains the previous potential's ability to account for the properties of YDC, but with the added advantages discussed above (Section 6.2). As a result, all subsequent parts of this study were

performed using the h-DIPPIM potential.

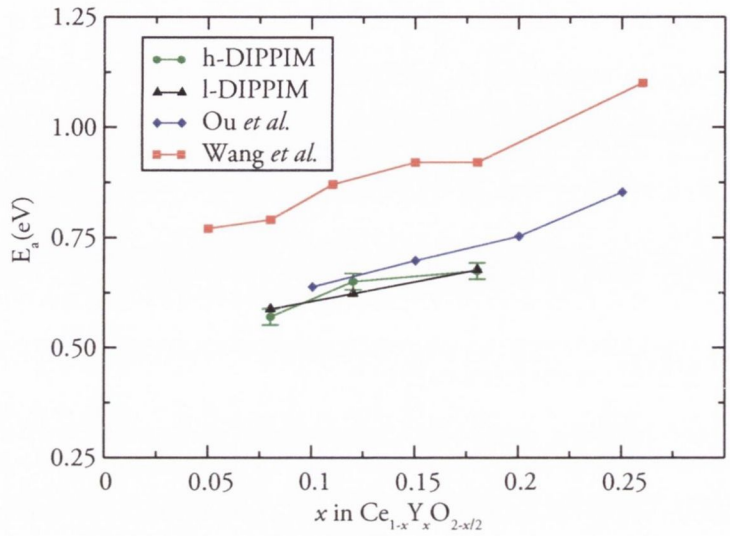

Figure 6.2: Bulk activation energies, E_a (eV), calculated using the h-DIPPIM (green circles) and l-DIPPIM potentials (black triangles. Experimental bulk activation energies from Ou *et al.* [9, 296] (blue diamonds) and Wang *et al.* [26] (red squares)

Table 6.2: Bulk ionic conductivities, σ_i ($\mathrm{S\,cm^{-1}}$), at 1473 K from LDA (l-DIPPIM) [17, 171] and HSE (h-DIPPIM) DIPPIM potentials (present work). The errors associated with the h-DIPPIM data set are 1.58%, 0.64%, 1.25%, respectively for $x = 0.08$, 0.12 and 0.18. The l-DIPPIM data set is expected to have slightly larger error values due to the use of smaller simulation cells.

x in $Ce_{1-x}Y_xO_{2-x/2}$	l-DIPPIM	h-DIPPIM
0.08	0.110	0.125
0.12	0.132	0.136
0.18	0.125	0.122

Application of isotropic strain to bulk YDC caused an increase in the material's ionic conductivity, σ_i. Figure 6.3 presents σ_i of bulk $Ce_{1-x}Y_xO_{2-x/2}$ when $\epsilon = 0.021$ relative to $\epsilon = 0.000$ ($\sigma^{2.1}/\sigma^0$) as a function of temperature. The conductivity maximum remains at $x = 0.12$ (red squares) for all the temperatures considered, however the highest increase in σ_i with strain (3.50 ×) is observed for $x = 0.18$ (blue triangles)

at 1273 K. These results also show that the impact of strain on σ_i increases as the temperature decreases from 1673 K to 1273 K. This effect can be explained in terms of the decrease in the activation energy of vacancy migration, E_a (eV) (Table 6.3) due to the activated nature of the conduction mechanism. The intrinsic error in these results (up to 3%) is small in comparison to magnitude of the changes observed in E_a for YDC. The changes observed are also similar to those reported by De Souza *et al.* [290], who found a decrease of up to 40% for CeO_2 at $\epsilon \sim 0.02$. Lower temperatures were not included in this study as they are more difficult to simulate because they require longer MD trajectories (in the order of several ns of simulation time). Unfortunately, isotropic strain is difficult to realize experimentally and is presented here due to its theoretical interest. As a consequence, the changes in conductivity experienced by YDC under these conditions will be used only as a benchmark when compared to those of anisotropically strained slabs in the next section.

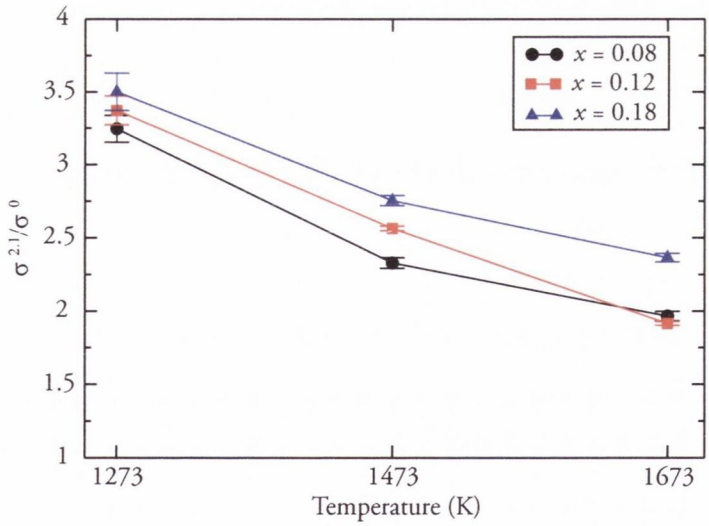

Figure 6.3: Ionic conductivities of bulk $Ce_{1-x}Y_xO_{2-x/2}$ when $\epsilon = 0.021$ relative to $\epsilon = 0.000$ ($\sigma^{2.1}/\sigma^0$) as a function of temperature. The different concentrations are indicated as $x = 0.08$ (black dots), 0.12 (red squares) and 0.18 (blue triangles).

Table 6.3: Activation energies, E_a (eV), as a function of strain, ϵ, for bulk YDC. The values in square brackets correspond to the percentage change with respect to the activation energy without strain for a given concentration. The reported values for unstrained systems have errors of 1.86%, 3.00% and 1.80% for x = 0.08, 0.12, 0.18, respectively. It was found that the magnitude of these errors decreases with strain.

x in $Ce_{1-x}Y_xO_{2-x/2}$	0.000	0.007	0.014	0.021
0.08	0.570	0.487 [-14.6]	0.397 [-30.4]	0.338 [-40.7]
0.12	0.650	0.580 [-10.8]	0.554 [-14.8]	0.392 [-39.6]
0.18	0.674	0.651 [-3.3]	0.567 [-15.9]	0.493 [-26.8]

6.3.2 YDC slabs: surface effects

The YDC slabs discussed in this section serve as models for the study of ionic conductivity of epitaxially grown thin films, in particular, coherently grown films where the lattice mismatch does not exceed $\epsilon = 0.03$. Figure 6.4 presents the 2D ionic conductivities, σ_i ($S\,cm^{-1}$), at 1273 K for unstrained YDC as a function of dopant concentration for bulk (blue triangles) and slabs (black diamonds). These conductivities were calculated from the diffusion coefficients along the x and y directions only (D_{xy} - 2D lateral diffusion). The MD simulations reveal that, for zero strain, the conductivities of the slabs are 50% higher than those of bulk YDC of the same concentration. This pattern remains unaffected when all three components of the diffusion coefficient (D_x, D_y, D_z) are included in the calculation of the conductivity of bulk YDC and when this value is obtained from the average of the conductivities along the *xy*, *yz*, *xz* planes (3D conductivity shown as red dots). To the authors' knowledge, this is the first time that such a behaviour is observed in YDC. Apart from the increase in the conductivity, the behaviour of the two systems is similar, with the highest conductivity achieved for a dopant concentration of $x = 0.12$.

The MD technique makes it possible to perform a detailed examination of the conductivity within each atomic layer along the z-axis of the slabs (delimited by horizontal blue dashed lines on the left in Figure 6.5). The diffusion coefficients for each of these 13 layers of $Ce_{0.88}Y_{0.12}O_{1.94}$ at 1273 K are presented on the right hand side of Figure

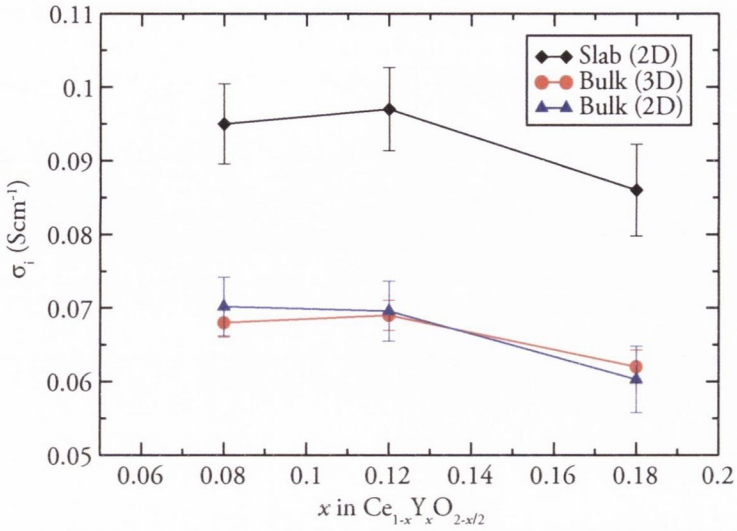

Figure 6.4: 2D (lateral) ionic conductivities, σ_i ($\mathrm{S\,cm^{-1}}$), for unstrained bulk (blue triangles) and slabs (black diamonds) as a function of dopant concentration at 1273 K. Bulk 3D ionic conductivities are shown as red dots.

6.5 as a function of depth (black dots aligned to their corresponding layers). These values have an associated error of up to 5%. It is immediately clear that the layers with exposed surfaces show a significantly higher conductivity ($\sim 4\times$) than those in the bulk region of the slab, with the lowest conductivities seen in the subsurface layers. The diffusion coefficient for bulk YDC of the same concentration as the slab is shown for comparison (vertical red dashed line). The increased conductivity in the surface regions is likely due to the substantial changes to the coordination environment around the oxygen anions in these layers. This is evident when the positions of the oxide anions on the surface regions (solid blue circle in Figure 6.5) are compared to those in the low conductivity subsurface (dashed black circle in Figure 6.5).

6.3.3 YDC slabs: strain effects

All combinations of strains, where $\epsilon_x, \epsilon_y = \{0.007, 0.014, 0.021\}$, were applied to the YDC slabs. However, it was found that, although the conductivity tended to increase whenever there was strain along either direction, the change was generally larger when

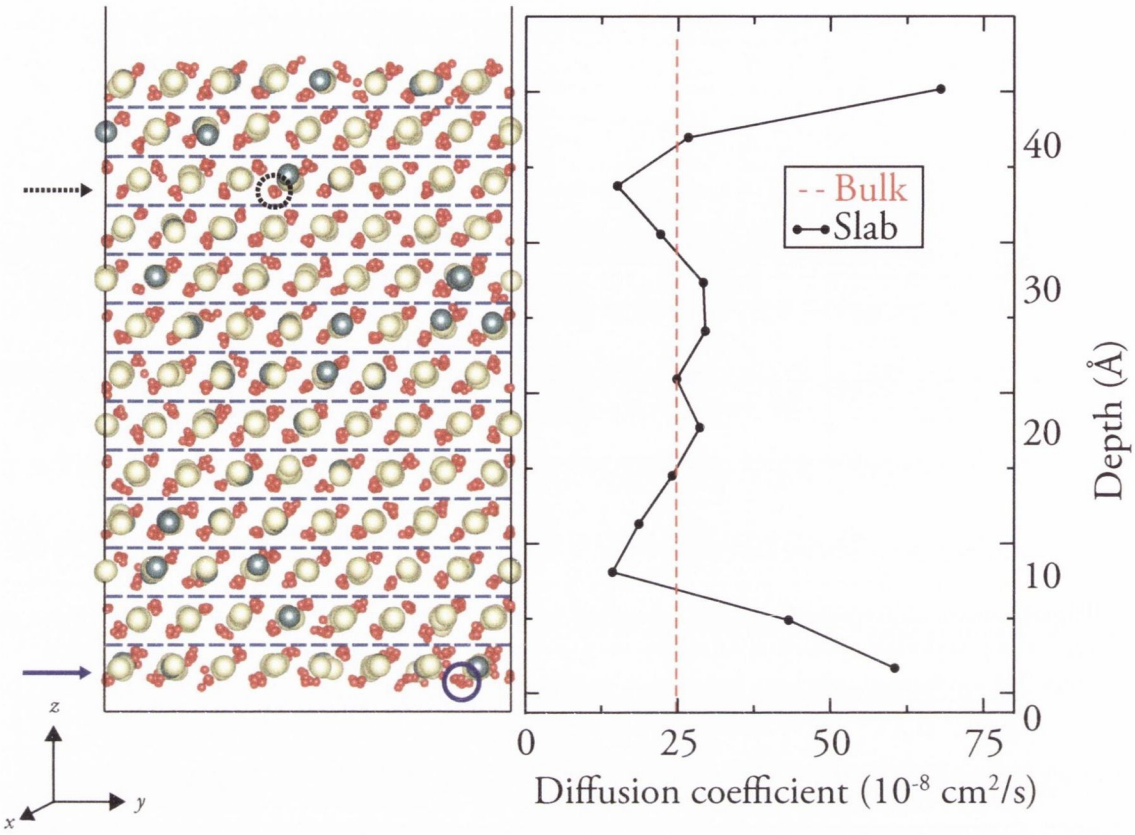

Figure 6.5: 3D diffusion coefficients for each atomic layer along the z-axis for $Ce_{0.88}Y_{0.12}O_{1.94}$ at 1273 K (black dots). The vertical red dashed line indicates the bulk conductivity at the same dopant concentration and temperature. Attention is drawn to the high degree of disorder in anion sublattice on surface layers (solid blue circle) compared to the ordered subsurface layers (dashed black circle). Ce^{4+}, Y^{3+} and O^{2-} are shown in as beige, blue and red spheres, respectively.

$\epsilon_x = \epsilon_y$ (which is to be expected since YDC adopts a cubic fluorite structure). For this reason, we will only report strain where $\epsilon_x = \epsilon_y$ for the slabs. In Figure 6.6 we report the conductivity vs strain for $Ce_{1-x}Y_xO_{2-x/2}$ slabs at 1273 K, where $x = 0.08$ (black dots), 0.12 (red squares) and 0.18 (blue triangles). The plots show that σ_i increases with strain for all concentrations of YDC, and just as in the bulk system, $x = 0.12$ displays the highest conductivity. The inset shows the change in conductivity of the same YDC systems when $\epsilon_x = \epsilon_y = 0.021$ with respect to the unstrained slabs ($\sigma^{2.1}/\sigma^0$) for all temperatures under study. As was seen in bulk YDC (Figure 6.3), applying strain to YDC causes a larger increase in conductivity at lower temperatures. In the case of

slabs, this change corresponds to a 1.44 × rise with respect to the unstrained slab at the same temperature for $x = 0.18$ (*cf.* the increase for isotropically strained bulk was 3.5 ×). This increase may appear modest when compared to the orders of magnitude seen in some of the YSZ literature [276], but it is in very good agreement with the latest reports on ceria and zirconia-based electrolytes [265, 266, 277, 289]. Our findings are in also reasonable agreement with previous calculations [260, 261, 290], when the differences in strain values and temperatures are factored in. The activation energies, E_a (eV), of the YDC slabs (Table 6.4) decrease as the strain increases, nevertheless, these changes are not as pronounced as was the case of bulk YDC (Table 6.3), especially when $\epsilon = 0.021$. Again, since the ionic conductivity is an activated process, the conductivity enhancement is expected to be higher at lower temperatures, as observed by Kushima and Yildiz for YSZ [260, 261].

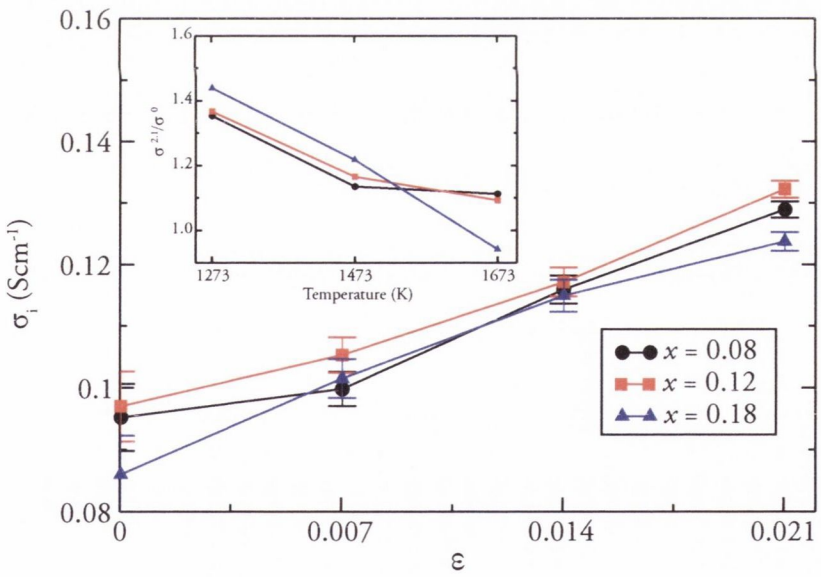

Figure 6.6: Ionic conductivities of $Ce_{1-x}Y_xO_{2-x/2}$ slabs at 1273 K as a function of strain. The different concentrations are indicated as $x = 0.08$ (black dots), 0.12 (red squares) and 0.18 (blue triangles). Inset: 2D ionic conductivities of $Ce_{1-x}Y_xO_{2-x/2}$ slabs when $\epsilon_x = \epsilon_y = 0.021$ relative to $\epsilon_x = \epsilon_y = 0.000$ ($\sigma^{2.1}/\sigma^0$) as a function of temperature.

The ionic conductivities of the YDC slabs manifest a high degree of anisotropy,

Table 6.4: Activation energies, E_a (eV), as a function of strain, where $\epsilon_x = \epsilon_y$ for YDC slabs. The values in square brackets correspond to the percentage change with respect to the activation energy without strain for a given concentration. The reported values for unstrained systems have errors of 4.00%, 5.13% and 3.92% for $x = 0.08$, 0.12 and 0.18, respectively.

x in $Ce_{1-x}Y_xO_{2-x/2}$	0.000	0.007	0.014	0.021
0.08	0.511	0.479 [-6.3]	0.477 [-6.6]	0.419 [-18.1]
0.12	0.608	0.528 [-13.2]	0.510 [-16.1]	0.504 [-17.1]
0.18	0.691	0.643 [-6.9]	0.588 [-14.9]	0.499 [-27.7]

which is evidenced when the diffusion coefficients , D ($10^{-8}\,cm^2/s$), are decomposed into the individual components along each Cartesian direction. The values reported in Table 6.5 correspond to the diffusion coefficients along the x (D_x), y (D_y) and z (D_z) directions for biaxially strained $Ce_{0.88}Y_{0.12}O_{1.94}$ slabs and isotropically strained bulk (square brackets) of the same concentration. The results show that D_x and D_y increase more slowly in the slabs than they do in bulk when strain is applied. This anisotropy likely arises from the compression along the z direction of the slabs (Poisson effect). The D_z values of our simulation slabs are constrained by the non-periodicity along this direction and they will ultimately tend to zero as a result, provided the simulation time is long enough. However, in the timescales presented here the results indicate that the relaxation perpendicular to the surface plane does not lead to a diffusion enhancement.

Table 6.5: Slab diffusion coefficients (10^{-8} cm^2/s) along each Cartesian axis for $Ce_{0.88}Y_{0.12}O_{1.94}$ at 1273 K under different strain, where $\epsilon_x = \epsilon_y$ levels. Isotropically strained bulk diffusion coefficients are shown in square brackets for comparison. These uni-axial diffusion coefficients values have an associated error in the order of 5%.

$\epsilon_x = \epsilon_y$	D_x (10^{-8} cm^2/s)	D_y (10^{-8} cm^2/s)	D_z (10^{-8} cm^2/s)
0.000	33.5 [23.0]	33.7 [26.8]	23.3 [24.4]
0.007	38.1 [42.9]	37.5 [42.4]	24.5 [39.9]
0.014	40.5 [59.2]	44.1 [62.5]	25.4 [59.1]
0.021	49.3 [89.8]	47.1 [89.9]	26.7 [87.0]

6.4 Conclusions

This work attempts to rationalize the impact of strain in epitaxially strained RE-doped ceria. The simulations used accurate dipole-polarizable interatomic potentials derived directly from *ab initio* calculations. The simulation conditions were realistic from the point of view of the strains applied, dopant cation concentrations and the temperatures employed. Also, for the first time, the slab method was applied to this problem which allowed for a more realistic representation of biaxially strained systems. In addition, the results from the slab calculations illustrated the effects of surfaces on the ionic conductivity. The results obtained from our calculations indicate that there is a clear enhancement of the conductivity in the surface region of a thin film. This resulted in our films being $\sim$ 50% more conducting than the corresponding bulk sample, for zero strain. This effect is related to the more disordered atomic configurations observed in the surface layers and the presence of under-coordinated atoms. When strain is applied, either isotropically (bulk) or biaxially (slab), a moderate enhancement in the ionic conductivity is observed, for the studied temperature and strain ranges. Biaxially strained thin films are found to be less conductive than isotropically strained YDC, which has been ascribed to the highly anisotropic diffusion mechanism observed in the thin films. Our findings confirm those from recent experimental studies which employed films of high crystallographic quality and found only a limited impact on the ionic conductivity from tensile strain [266, 277].

7

Properties of cadmium oxide from first principles

7.1 Intrinsic defects and adventitious H doping

The remarkable TCO properties of CdO were first described in 1907 by Badecker [39]. Since then, this material has positioned itself as a prototypical wide band gap transparent semiconductor, which adopts the rock salt (RS) structure (Figure 7.1) with space group $Fm\bar{3}m$–O_h^5 (225). This material has been reported to be an n-type degenerate semiconductor which possesses a small indirect band gap (E_g^{ind} in Figure 7.2) of $\sim 0.84\,\text{eV}$ [297] and a larger direct band gap (E_g^{dir} in Figure 7.2) of $\sim 2.2\,\text{eV}$ [298, 299]. CdO is a highly non-stoichiometric material, and generally possesses large carrier concentrations ($\sim 10^{18} - 10^{20}\,\text{cm}^{-3}$) together with large electron mobilities in the bulk [300]. These high carrier concentrations generate a pronounced Moss-Burnstein (MB) shift which can considerably extend the optical band gap, E_g^{opt} [301] indicated in Figure 7.2. In addition, donor dopants can extend E_g^{opt} above 3.1 eV, making CdO suitable for TCO applications. Mobilities of the order of $\sim 200\ \text{cm}^2\text{V}^{-1}\text{s}^{-1}$ and conductivities as high as $42000\,\text{S}\,\text{cm}^{-1}$ have been reported for doped CdO samples [302], which is an order of magnitude higher than the typical conductivities of the industry standard TCOs. Understanding the defect chemistry of CdO is therefore vital for the development of

improved TCOs.

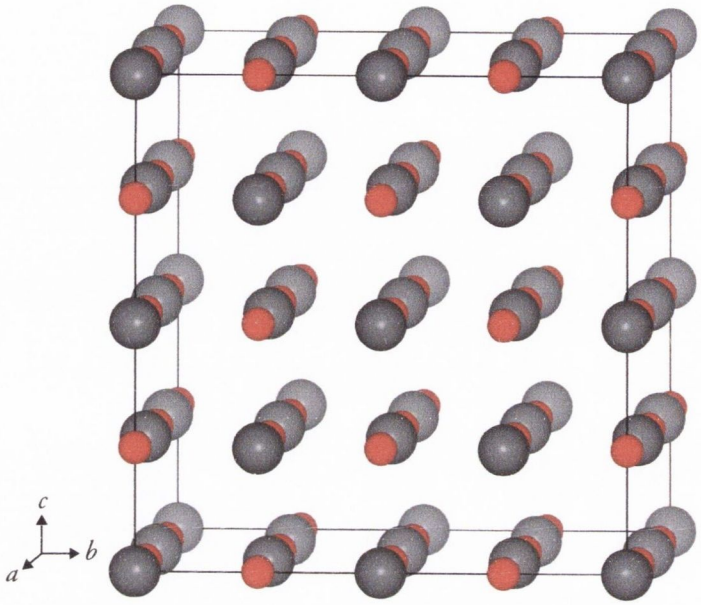

Figure 7.1: Rock salt structure of CdO. Shown in gray are the Cd cations while the oxide ions are in red.

To date, however, there is still uncertainty regarding the nature of the dominant *intrinsic* defects in this material. Cd interstitials (Cd_i) [303, 304] and oxygen vacancies (V_O) [33, 305] have both been put forward as the dominant defects in CdO. Similar to other *n*-type TCOs [306], hydrogen impurities have also been suggested both experimentally [307] and theoretically [308] to act as donors in CdO by means of *adventitious* doping. A recent experimental study by King *et al.* found that intrinsic defects and H impurities *all* act as shallow donors in CdO[309]. This finding is intriguing, as in all other *n*-type TCOs, V_O acts as a *deep* donor, and cation interstitials, while being shallow donors, are generally too high in energy to contribute heavily towards any intrinsic conductivity [310, 311]. This suggests that intrinsic defects behave differently in CdO compared to the other TCOs. The discussion that follows examines the formation of intrinsic defects and hydrogen impurities in CdO using screened hybrid density functional theory (h-DFT). Hydrogen is included along the intrinsic defects given its concomitant presence under experimental conditions. The effects of one electron donors

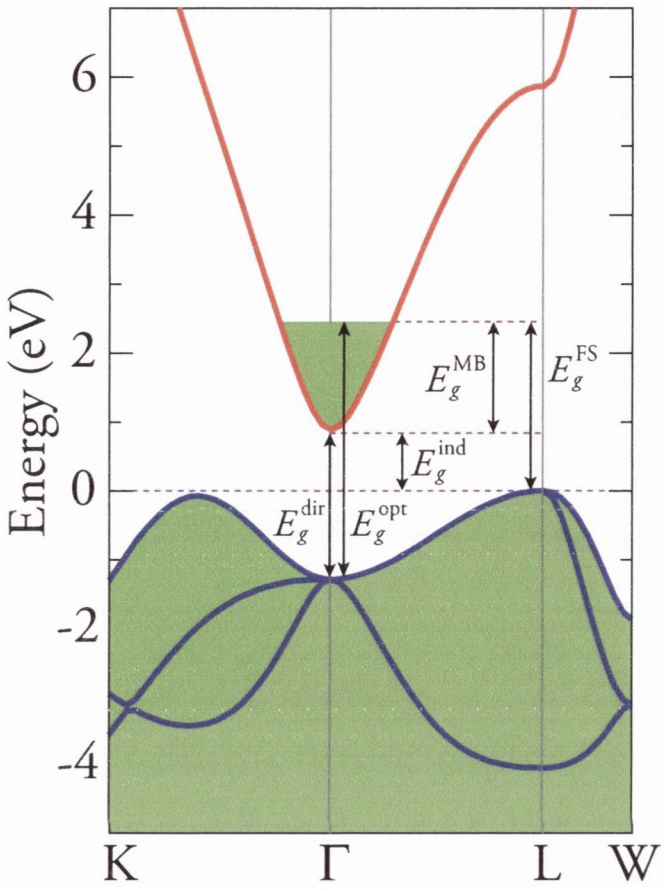

Figure 7.2: Schematic band structure highlighting the Fermi level stabilization energy, E_g^{FS}, The Moss-Burnstein shift, E_g^{MB}, and the optical band gap, E_g^{opt}, for defective CdO. The green shaded areas indicate occupation by electrons. The VBM is set to 0 eV.

typically used as dopants in CdO are discussed in Section 7.2. These dopants include the RE cations Sc, Y and La, as well as, three members from group 13, namely, Al, Ga, In. Anionic dopants are also examined by means of F defects.

7.1.1 Methods

All calculations were performed using the periodic DFT code VASP,[98, 143] in which a plane-wave basis set describes the valence electronic states. The PBE [65] gradient corrected functional was used to treat the exchange and correlation. The PAW [101, 312] method was used to describe the interactions between the cores (Cd:[Kr] and

O:[He]) and the valence electrons. In this way the Cd 4*d* states are explicitly included in the valence. To counteract the self interaction error [313] and the band gap errors inherent to standard DFT functionals such as the PBE functional, higher levels of theory must be used. An often used approach to overcome these errors is to utilize hybrid functionals, which include a certain percentage of exact Fock exchange with the DFT exchange and correlation, as discussed in Chapter 2. Hybrid functionals have been shown to yield improved decriptions of the structure, band gap and defect properties of a number of oxide semiconductors [46, 204, 314–328]. Unfortunately, hybrid functionals are very computationally demanding, and have in some cases been overlooked in favour of less computationally expensive methods, such as the "$+U$" correction [67, 329], or even a range of *a posteriori* corrections to LDA/GGA calculations [330]. In this study we have used the screened hybrid density functional developed by Heyd, Scuzeria and Ernzerhof (HSE06)[75, 215], as implemented in the VASP code [216]. Structural optimizations of bulk CdO were performed using both PBE and HSE06 at a series of volumes in order to calculate the equilibrium lattice parameters. Convergence with respect to k-point sampling and plane wave energy cut off were checked, and for both PBE and HSE06 a cutoff of 400 eV and a k-point sampling of $8 \times 8 \times 8$ were found to be sufficient. Calculations were deemed to be converged when the forces on all the atoms were less than 0.01 eV Å^{-1}. A 2×2×2 simulation cell consisting of 64 atoms was used for our defect calculations. The plane wave cutoff was set at 400 eV and a 2×2×2 Monkhorst-Pack special k-point grid was used in all defect calculations. Structural optimizations were considered to be converged once the forces on all species were less than 0.02 eV Å^{-1}. All defect calculations were spin polarized. Density of states are shown with a Gaussian smearing of 0.02 eV.

The chemical potentials discussed in Chapter 3, μ_i, reflect the specific equilibrium growth conditions, within the global constraint of the calculated enthalpy of the host, in this case CdO: $\mu_{\mathrm{Cd}} + \mu_{\mathrm{O}} = \Delta H_f^{\mathrm{CdO}} = -2.15\,\mathrm{eV}$. The lower limit for μ_{O}, which characterizes a Cd-*rich*/O-*poor* environment, is determined by the formation of metallic Cd: $\Delta\mu_{\mathrm{Cd}} = 0\,\mathrm{eV}$; $\Delta\mu_{\mathrm{O}} = -2.15\,\mathrm{eV}$. The upper limit for μ_{O} (Cd-*poor*/O-*rich* conditions)

is governed by O_2 formation: $\Delta\mu_{Cd} = -2.15\,eV$; $\Delta\mu_O = 0\,eV$. The formation of CdO_2 was also considered, but it was found to not be a chemical potential limit. Under both sets of conditions, the solubilities of H-related species are limited by the formation of H_2O, i.e. $\mu_O + 2\mu_H \leq \Delta H_f^{H_2O} = -2.67\,eV$.

7.1.2 Bulk CdO

The calculated lattice parameters, bond lengths and electronic structure data for the PBE and h-DFT calculations on CdO are presented in Table 7.1. The HSE06 structure is only slightly overestimated with respect to the experimental values [331], and is more accurate than standard DFT functionals [332]. HSE06 has previously been shown to be better at accurately predicting the structure and band gap data of many semiconductors compared to standard DFT functionals. In fact, it has been shown that standard DFT functionals are not able to accurately calculate the band structure features of CdO, even predicting CdO to be a semi-metal [332], and that methods that go beyond GGA/LDA must be employed [309, 333]. Both the PBE and the HSE06 calculated band structure for CdO are shown in Figure 7.3. The valence band maximum (VBM) occurs at L, which is slightly higher than the Σ line (between K and Γ). PBE yields a band structure in which the CBM comes down below the VBM, indicating a semi-metallic system, which is in line with the findings from previous standard DFT results [334].

From the HSE06 band structure (Figure 7.3 (b)) we obtain values of 2.18 eV and 0.89 eV for E_g^{dir} and E_g^{ind}, respectively. These results compare well with recent experimental studies which reported E_g^{dir} to be 2.20 eV [299] and 2.16 eV.[298] The most recent measurement of the E_g^{ind} (0.90 eV)[335] is also in excellent agreement with our HSE06 calculated E_g^{ind}. As discussed in Section 1.3, for an effective TCO material, it is important that the second conduction band (CBM+1) is separated from the CBM by greater than 3.1 eV [41]. This large CBM–CBM+1 separation ensures that any donor electrons in the conduction band are not excited by visible light to the next conduction band, and therefore ensures optical transparency, which is vital for device performance.

Table 7.1: Geometrical and electronic structure data for CdO calculated using GGA-PW91, GGA-PBE, and HSE06, and compared to known experiments. a is the lattice parameter, measured in Å, d_{Cd-O} is the Cd–O bond length in Å, the volume is measured in Å^3, E_g^{dir} is the direct band gap in eV, E_g^{ind} is the indirect band gap in eV, VB width is the width of the main valence band in eV, and d states is the position of the Cd d states relative to the VBM at 0 eV and is measured in eV.

	GGA-PW91[332]	GGA-PBE (This Study)	HSE06 (This Study)	Expt.
a	4.80	4.79	4.72	4.70 [331]
d_{Cd-O}	–	2.39	2.36	2.35 [331]
Volume	110.59	109.90	105.15	103.82 [331]
E_g^{dir}	0.60	0.61	2.18	2.16-2.20 [298, 299]
E_g^{ind}	-0.51	-0.51	0.89	0.84-0.90 [335]
VB width	∼4.00	3.94	4.45	∼5.00[336]
d states	∼-6.60	-5.7 to -7.4	-6.5 to -8.3	∼-8.50 [309]

Similarly, for p-type TCOs, absorption must not occur from bands within ~ 3.1 eV of the VBM to the hole states near the VBM.[42, 43] For CdO, the CBM+1 is ~ 15 eV higher than the CBM, indicating that the conduction band features of CdO are ideal for a candidate TCO.

Our HSE06 calculated effective mass for the CBM is $0.21\,m_e$, and for the VBM is $1.3\,m_e$. To the best of our knowledge the valence band effective masses have never been measured experimentally, however, our conduction band effective mass is in good agreement with the most recent experimental measurements of the effective mass ($0.21\,m_e$ and $0.24\,m_e$) [298, 299]. The experimental valence band width of CdO is ~ 5 eV,[336] which agrees well with our calculated VB width of ~ 4.5 eV. Overall, the HSE06 functional describes the electronic structure features of CdO much better than standard functionals, and yields results in excellent agreement with experiments, and also in good agreement with the results of the computationally intensive, higher level GW quasiparticle calculations of Bechstedt and co workers [337].

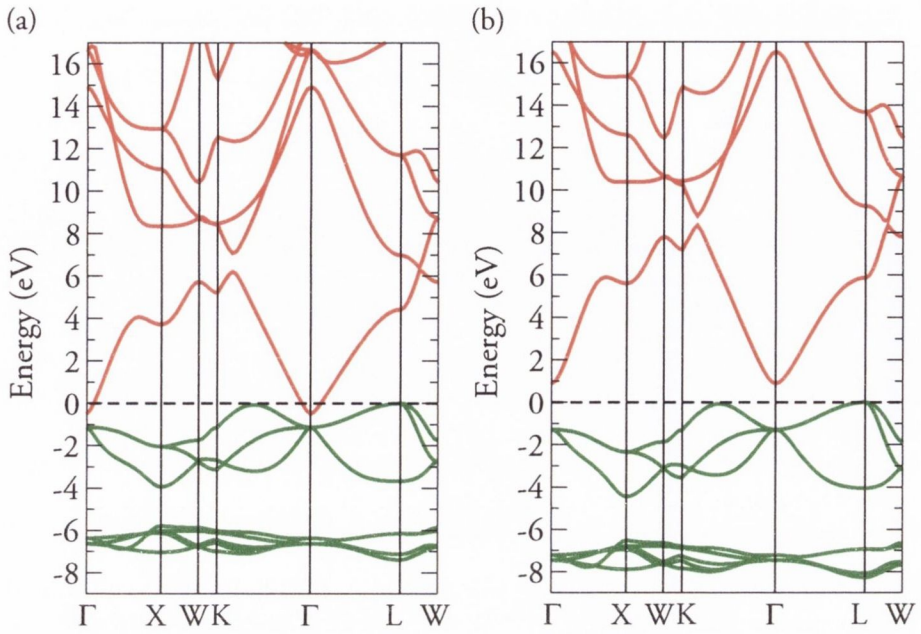

Figure 7.3: (a) PBE and (b) HSE06 calculated band structure for CdO. The VBM is set to 0 eV in both cases and is denoted by a horizontal dashed black line. Green and red bands denote valence and conduction bands respectively. Note how the PBE calculated conduction band comes down below the VBM, indicating a semi-metallic system.

7.1.3 Defect energetics and transition levels

The defects considered in this section include n-type V_O and Cd_i, as well as the p-type oxygen interstitial (O_i) and cadmium vacancy (V_{Cd}). In addition, H was incorporated in a number of lattice positions, namely hydrogen in an oxygen lattice site (H_O) and four different interstitial positions. The interstitial positions tested were the perfect interstitial site, anion antibonding sites 1 Å from an O along the ⟨111⟩ direction (H_i^{AB1}), ⟨110⟩ direction (H_i^{AB2}) and the bond centered site (H^{BC}), as illustrated in Figure 7.4.

A plot of formation energy as a function of Fermi-level position for all intrinsic defects and H related impurities for both Cd-rich/O-poor and Cd-poor/O-rich regimes is displayed in Figure 7.5, see Section 3.3.4 for a discussion of how these diagrams are plotted. For the intrinsic n-type defects, it is clear that the V_O is the most stable defect under both sets of conditions, and will dominate intrinsic conductivity. The Cd_i, which had previously been suggested as the dominant defect [303, 304], is con-

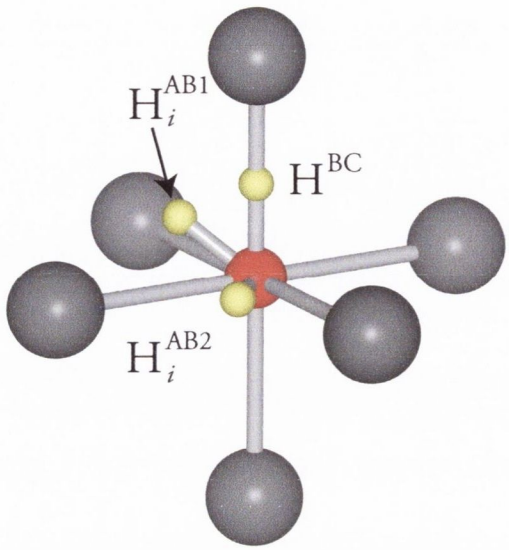

Figure 7.4: Positions of hydrogen intersitials in CdO: diagonal (H_i^{AB1}), facial hydrogen (H_i^{AB2}) and bond centered hydrogen (H^{BC}). Cd, O and H are denoted by grey, red and yellow spheres respectively.

siderably higher in energy and is unlikely to play a large role in the conductivity of CdO. The low formation energies of the V_O under both growth conditions can explain the observed non-stoichiometry of CdO samples [300]. Both V_O and Cd_i exist only in the +2 charge state in the band gap, which is consistent with previous experimental studies which reported that the source of undoped charge carriers in CdO were doubly ionized donors [309]. Interestingly, CdO represents the only wide band gap *n*-type TCO in which V_O acts as a shallow donor. In ZnO [310], SnO_2 [311], Ga_2O_3 [338] and In_2O_3 [339] V_O has been found to be a deep donor, with "undoped" conductivity thought to arise from the presence of adventitious hydrogen [306, 309, 311, 340].

The lowest energy H impurity in CdO under Cd-*rich*/O-*poor* conditions is H_O, which is slightly more stable than H_i^{AB1}, with both defects being lower in energy than V_O as the Fermi level is raised to the CBM and beyond. Both H on the perfect interstitial site and H_i^{AB2} were found to relax to the H_i^{AB1} position. Under Cd-*poor*/O-*rich* conditions, H_i^{AB1} is the most stable defect considered, and will dominate conductivity. The H defects are all in the +1 charge state in the gap, indicating that H behaves exclusively as a shallow donor in CdO. Shallow donor behaviour of H_i and H_O has

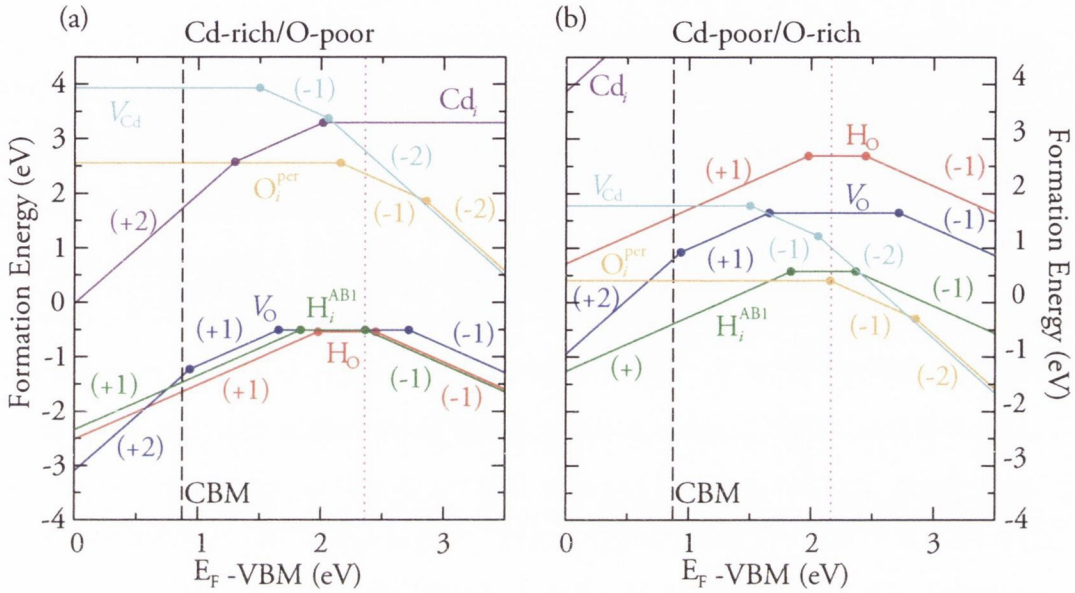

Figure 7.5: Formation energies for intrinsic and hydrogen defects under (a) Cd-rich/O-poor conditions and (b) Cd-poor/O-rich conditions. The solid dots represent the transition levels $\epsilon(q/q\prime)$. The black dashed line indicates the position of the conduction band maximum (CBM), with the purple vertical dotted line represents the maximum achievable Fermi level before compensation occurs.

been noted previously for other wide band gap n-type oxides [306, 309, 311, 340–342]. Our results agree closely with those of King *et al.* who found that native defects and hydrogen impurities *both* act as shallow donors in CdO samples [343].

7.1.4 p-Type CdO?

Recent valence band alignments for wide band gap oxides have indicated that the VBM of CdO is quite high compared to the other wide band gap TCOs [344, 345]. By the doping limit rules [346], this indicates that the VBM of CdO lies in the "p-dopable range", and indicates the possibility of CdO being a bi-polar material, which would be very much sought after for the development of functional TCO p-n junctions. To the best of our knowledge, however, no reports of p-type CdO have ever been published. To investigate the possibility of p-type CdO, we now analyse the formation of O_i and V_{Cd}.

We started our O_i calculations with the O positioned on the perfect interstitial site, however, the O moved towards one of the lattice oxygens, displacing it from its lattice site and forming a peroxide (O–O dumbell-like) species, as shown in 7.6, which we will now denote as O_i^{per}. This type of behaviour has also been noted for ZnO [347, 348], Al_2O_3 [349] and SnO_2 [350, 351]. It is instructive to note that the structure of O_i^{per} is very similar to the structure of the the anions in CdO_2, which has a RS-like structure with peroxide anions, O_2^{2-}, on the regular RS anion sites [352]. Our calculations reveal that this O_i^{per} is the most stable p-type defect under both growth conditions, however, it is higher in energy than the lowest n-type defects under both sets of conditions. Both V_{Cd} and the O_i^{per} exist only in the neutral charge state over the range of the band gap, under both sets of conditions, indicating that they will not act as effective acceptors in this system. These findings explain why p-type CdO samples have never been reported, despite it possessing a relatively high VBM.

7.1.5 Doping limits

Under both sets of growth conditions, compensation by p-type defects is not expected to occur until well above the CBM, as indicated by the vertical dotted line in 7.5 (a) and (b). This limit can be taken as an approximation of the Fermi level stabilization energy, E_g^{FS}, which is the Fermi level at which the formation energy of donor defects and acceptor defects is equal [353]. The definition of E_g^{FS} is based on the amphoteric defect model proposed by Walukiewicz,[353] and means that for Fermi levels above (below) E_g^{FS}, acceptor (donor) defects are favoured [354]. Our computed transition levels only represent a first approximation to the doping limits, as they ignore the effects of band gap renormalization, changes to the parabolicity of the CBM as the number of charge carriers increases [106], and the effect of electron accumulation layers on the band gap [355]. Nevertheless, the results can be used to rationalize the doping behaviour seen experimentally. Taking the Cd-poor/O-rich conditions, our predicted *maximum* Fermi level position above the VBM is 2.15 eV (also indicated by E_g^{FS} in 7.2), which implies a maximum Moss-Burnstein shift (E_g^{MB}) of the order of 1.26 eV.

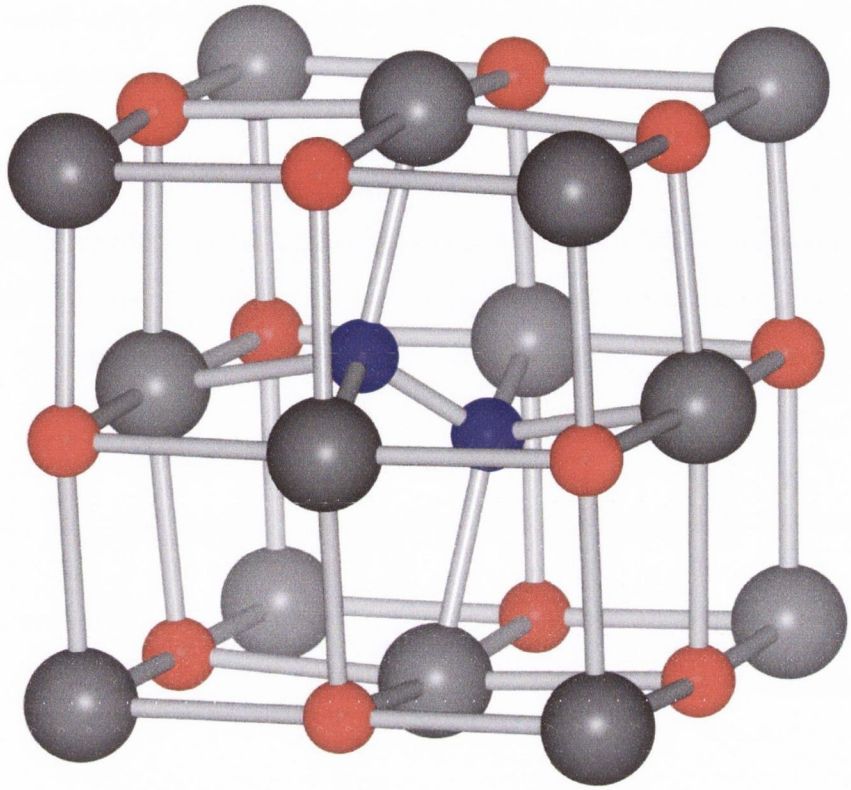

Figure 7.6: Converged structure of an oxygen peroxide, O_i^{per} in the CdO lattice. The two blue spheres denote the O–O dumbell.

Similarly for Cd-rich/O-poor we obtain an E_g^{MB} of 1.43 eV, with the true MB shift expected to lie in between the two extremes. These values are in good agreement with the Fermi level positions reported by Piper *et al.* ($\sim$ 1.15 eV and $\sim$ 1.30 eV) [356, 357], and Speaks *et al.* ($\sim$ 1.00 eV) [354]. This in turn implies maximum *optical* band gaps, E_g^{opt}, of between $\sim$ 3.44 eV and $\sim$ 3.61 eV.

Using our calculated maximum Moss-Burnstein shift, and our calculated effective mass of the CBM, we can estimate the number of charge carriers in "maximally" doped CdO from free electron theory using:

$$E_{BM} = \frac{\hbar^2}{2m^*}(3\pi^2 n_e)^{2/3} \tag{7.1}$$

where m^* is derived from the valence and conduction band effective masses, m_V and m_V according to $\frac{1}{m^*} = \frac{1}{m_C} + \frac{1}{m_V}$, and n_e is the electron carrier concentration. Based on our approximate model, this analysis predicts the maximum carrier concentration to be $\sim 4.34 \times 10^{20}\,\mathrm{cm}^{-3}$ and $\sim 5.25 \times 10^{20}\,\mathrm{cm}^{-3}$ for Cd-poor/O-rich and Cd-rich/O-poor conditions respectively, before compensation by p-type defects occurs. These numbers agree quite well with the saturation carrier concentration reported for CdO (at the E_g^{FS}), which was $\sim 5 \times 10^{20}\,\mathrm{cm}^{-3}$[354].

7.1.6 Discussion

Our h-DFT calculations have shown that the formation energy of V_O is much lower than that of the Cd_i under all growth conditions, indicating that previous studies which identified Cd_i as the dominant defect[303, 304] were misguided. The low formation energy of V_O explains the fact that CdO samples are often found to be highly sub-stoichiometric [300]. Both V_O and Cd_i are found to act as shallow donors in CdO, meaning that the behaviour of V_O in CdO is very different to that reported for V_O in other wide band gap n-type TCOs e.g. ZnO [112, 358, 359], SnO_2 [311], Ga_2O_3 [338] and In_2O_3 [340, 360]. In these n-type TCOs, V_O is found to be stable only in the 0 and +2 charge states, meaning it is a negative-U defect. In CdO however, V_O is stable only as +2 in the band gap, and does not display any negative-U character.

The origin of this can be understood by examining the structure of the V_O in the 0, +1 and +2 charge states. For the 0 (neutral) charge state, the Cd ions neighbouring the vacancy move outwards from the vacancy by 1.7 %, while the nearest neighbour oxygens move towards the vacancy by 1.1 % relative to the bulk bond lengths. For the +1 charge state, the Cd ions move a further 1.4 % and the oxygens move towards the vacancy by a further 0.5 %. This trend is continued for the +2 charge state, with the Cd moving away from the vacancy by a further 1.4 % and the O move inwards by another 0.5 %. These small relaxations are in stark contrast to the large relaxations experienced by, for example, V_O in ZnO [347, 358, 359], which has been shown to experience a 12 % relaxation of the four Zn ions neighbouring a vacancy *towards* the

vacancy site. For the +1 and +2 charge, the Zn ions then relax away from the vacancy by 2 % and 23 % respectively, and it is the large relaxations experienced by the 0 and +2 charge states which stabilize these charge states relative to the +1 charge state, making the V_O a negative-U centre in ZnO. As V_O in CdO does not experience any large lattice distortions, there is no driving force for negative-U behaviour.

At this point it is instructive to think about an oxygen vacancy in Kröger-Vink notation, i.e. $[V_O^{\bullet\bullet} + 2e]$, which means that there is a doubly positive vacancy on an oxygen site, plus two free electrons. The doubly positive vacancy would be expected to *repel* the neighbouring positively charged cations, however, for ZnO the cations move towards the vacancy [347, 358] indicating that there is significant negative charge in the vacancy site. This is explained by the fact that electrons are trapped in the V_O, in an F-centre like fashion in ZnO, complete with polaronic distortion [359]. For the V_O^{+2} in ZnO, the two electrons are now absent from the vacancy, and the Zn ions are strongly repelled away from the vacancy site. The reason that V_O behaves differently in CdO can also be rationalized by considering the nature of the electrons left behind up on V_O formation. Bader [107] analysis of these two electrons show that only 0.46 of an electron is present in the vacancy position, with the other 1.54 electrons delocalized over the Cd and O ions neighbouring the vacancy. This is noticeably less localized than the electrons in the ZnO V_O [310, 359]. The origin of the negative-U behaviour in other wide band gap n-type TCOs, therefore, is the trapping of the electrons in the vacancy position, and this does not occur in the case of CdO. This type of delocalization behaviour in CdO is more in keeping with V_O being a shallow donor, rather than a deep donor. Similarly, the single particle levels (raw eigenvalues of the defects states) for the V_O lie in the bottom of the conduction band in CdO. This is illustrated in 7.7, which shows that the Fermi level is resonant in the conduction band upon V_O formation, with no defect states in the band gap, which is at variance with the deep V_O single particle levels in ZnO, SnO_2, Ga_2O_3 and in In_2O_3 [112, 310, 311, 338, 340, 358–360]. To the best of our knowledge, this type of shallow donor behaviour of V_O in wide band gap oxides has only been reported for one other oxide, Tl_2O_3 [361] which possesses a small

fundamental band gap of $\sim 0.33\,\mathrm{eV}$ and a much larger optical band gap of $> 2.3\,\mathrm{eV}$.

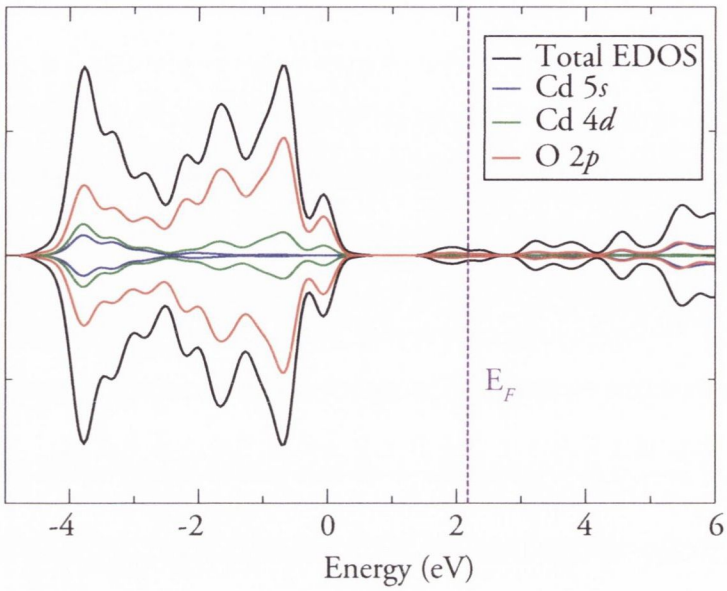

Figure 7.7: The partial density of states for V_O in the 64 atom CdO supercell. The position of the Fermi level, E_F is indicated by the purple vertical dashed line. The VBM is set to 0 eV. The denisty of states includes a Gaussian smearing of 0.2 eV.

We find that H related impurities also have very low formation energies in CdO under all growth conditions, and will always act as shallow donors. For O-*poor*/Cd-*rich* conditions, n-type conductivity in the system will be controlled by the concentration of V_O, H_O and H_i^{AB1}, with H_O slightly more favoured at higher E_F. Under Cd-*poor*/O-*rich* conditions, H_i^{AB1} is the dominant defect, meaning that any H in the growth environment will cause unintentional n-type conductivity under all growth conditions. These findings are in good agreement with the recent experiments of King *et al.* who found that both intrinsic defects *and* H related impurities act as shallow donors in CdO [343].

According to the doping limit rules [346, 353, 362–365], the higher a material's VBM is on an absolute scale, the easier it is to dope the material and make it p-type. This should also mean that native p-type defects *should* have reasonably low formation energies under Cd-*poor*/O-*rich* growth conditions relative to the native n-type defects. Although CdO possesses a high VBM relative to other oxide materials [344, 345], it also possesses a low CBM relative to other oxides, due to its low indirect band gap [344, 345],

Hosono and co workers have recently championed SnO as a possible bipolar material, listing small indirect/forbidden band gaps coupled with larger optical band gaps as the key factors in finding good candidate bipolar semiconductors [366]. By these standards, CdO should represent a very strong candidate for bipolar activity. Our calculations, however, indicate that even though the O_i^{per} has the lowest *neutral* formation energy of the native acceptor defect in CdO under Cd-poor/O-rich conditions, the acceptor ionization levels for this material are deep in the conduction band, indicating that it cannot act as an effective acceptor in CdO. For E_F close to the valence band maximum (which should be optimal for p-type defects), H_i^{AB1} and V_O^{+2} are both lower in energy and will always compensate the native acceptors. Therefore, despite possessing a high VBM, CdO can never show p-type conductivity from intrinsic defects, and it is unlikely that extrinsic acceptors could cause p-type conductivity due to the very low formation energies of the n-type defects. Our calculations indicate that although a high VBM relative to the vacuum is a good indicator of p-type ability, the ultimate behaviour is determined by the defect chemistry. In this respect, high level *ab initio* calculations can prove invaluable.

The doping limits of CdO were examined using the $0/-1$ ionization levels of all the defects considered in order to approximate the point where compensation by acceptors or electron trapping occurs. Our calculations indicate that the point where compensation occurs, which can be likened to the Fermi stabilization energy, E_g^{FS} (also known as the charge neutrality level or alternatively the branch point energy [367, 368]), is situated deep in the conduction band, with calculated limits of $1.26 - 1.43\,eV$ above the CBM depending on the growth conditions. These approximate limits agree quite well with recent experiments that list the E_g^{FS} for CdO to be $\sim 1.15\,eV$ [356], $\sim 1.00\,eV$ [354] and $\sim 1.30\,eV$ [357]. The distance of the E_g^{FS} above the CBM represents the Moss-Burnstein shift possible in doped CdO, and our limits agree well with the large optical band gaps seen experimentally [37, 301, 369–375]. This work therefore demonstrates that the large charge carrier concentrations and big optical band gaps of CdO are made possible by the fact that n-type defects are not compensated by p-type

defects until deep in the conduction band. This type of uncompensated n-type defect chemistry behaviour is also seen for other materials (e.g. InN [376–382] and InAs [383–385] where very large carrier concentrations are sustainable). For In_2O_3 the E_g^{FS} has been reported to be in the range $0.30 - 0.65\,eV$ above the CBM [386, 387]. Taking into account the fact that the effective mass for CdO is reported to be lower than or comparable to that of In_2O_3 [76] and using equation 7.1, then it is clear that CdO can sustain a much higher carrier concentration than In_2O_3. This is the vital factor in doped CdO producing the highest conductivities of any TCO reported previously [302].

7.2 Extrinsic defects in CdO

Having established the nature of the intrinsic dopants in CdO, attention now turns to the substitution of Cd with 3+ cations, as well as the introduction of F as a dopant. The 3+ species included three RE elements, namely Sc, Y and La, as well as, three elements from group 13, Al, Ga and In. These defect calculations were performed on 2×2×2 supercells, as described in Section 7.1.1, where the dopant cations replaced a single Cd ion in the 64-atom supercell (3.125% concentration). In the case of F defects, the options tested were F in the ideal interstitial position, F_i, and as a substitution in an oxygen position F_O. These calculations were performed using the methods described in Section 7.1.1. The solubilities of the dopants presented herein are limited by the formation of secondary phases, i.e. $n\mu_{Me} + m\mu_O = \Delta_f^{MeO_n}$. As a result, it was also necessary to calculate the formation energy of Sc_2O_3, Y_2O_3, La_2O_3, Al_2O_3, Ga_2O_3 and In_2O_3. The solubility of F was determined by the formation of CdF_2, $\Delta H_f^{CdF_2}$.

Experimental studies into the effects of donor doping in CdO have generally yielded samples with high optical transmittance (> 80%) in the visible spectrum, larger optical band gaps than nominally undoped CdO and an increased number of charge carriers [37, 301, 370, 388–390]. However, the extent of these modifications to the properties of pure CdO varies for different dopant species, as well as also being dependent on factors like the substrate deposition media [391], the presence of grain

boundaries, etc. In the case of RE-doped CdO, previous studies have identified both Y [388, 389] and Sc [40, 370, 389] as being efficient donor dopants in this material. In contrast, reports on the properties of La:CdO have shown adverse effects as a result of doping, such as a transition from a semiconducting oxide to an insulator at high dopant concentrations ($\sim$ 30%), with formation of La_2O_3 domains [392, 393]. Within this group of dopants, Y^{3+}, with a 6-coordinate radius of 0.90 Å, is the one that most closely matches that of Cd^{2+} (0.95 Å), while Sc^{3+} (0.75 Å) and La^{3+} (1.03 Å) are more substantially mismatched in terms of size with respect to Cd [131].

A relationship between dopant ionic radius and *n*-type ability has also been observed in the case of the group 13 dopants, where In^{3+} with a radius of 0.80 Å [131] is typically recognized as the best dopant cation in CdO with conductivities in excess of 15×10^4 S/cm and carrier concentrations in the order of $5\times10^{20}cm^{-3}$, both of which represent improvements of an order of magnitude in these values with respect to undoped CdO [394]. In contrast, small dopants like Al^{3+} (0.54 Å[131] and Ga^{3+} (0.62 Å [131]) have been shown effect more modest changes to the conductivity of CdO because they occupy intersitial positions that act as recombination centres for dopant concentrations exceeding 1.5% [395].

Similar to the other dopants that are the subject of this study, reports on F:CdO have have shown that it is a viable dopant for increasing the conductivity and optical transparency of this oxide [334, 390, 396–399]. This donor behaviour of F has been reported in other metal oxides such as ZnO [400, 401], SnO_2 [402] and $BaSnO_3$ [403]. However, the values for the conductivities found in the literature for F:CdO vary by as much as 5 times, from 1.5×10^3 S/cm [397] to 1.1×10^4 S/cm [399] in systems with F concentrations of up to 10%. Similar discrepancies are found in the reported values of the optical BG as a result of the MB shift, with values ranging from 2.3 eV [399] to 2.8 eV [390] for F:CdO.

The following investigation of doped CdO is undertaken in light of these conflicting

reports and, also due to the fact that no simulation studies have been carried out in a comprehensive set of n-type dopants in this material. The most significant aspect in these simulations is the use of state-of-the-art h-DFT simulations using realistic defect concentrations and the use of defect interaction corrections, which have been shown to be necessary in siulations with relatively small supercells [108, 112, 404, 405] that are typically in used in these studies.

7.2.1 Results

The formation energies for the RE dopant defects included in this study are shown in Figure 7.8, Sc_{Cd} (solid black line), Y_{Cd} (solid green ochre line) and La_{Cd} (solid lila line). These defects are shown in the context of the intrinsic defects presented in the previous section, as well as, H-doping, all of which are now represented by thin dashed lines and the same colour scheme from Figure 7.5. The values for the slopes are not explicitly indicated given that these defects can only exist in +1, 0 or -1 states. These results indicate that the best dopant is Y, closely followed by Sc. In both cases these defects are expected to dominate over the intrinsic and H-defects already encountered under O-poor and O-rich conditions. This is in contrast to the formation energy of the +1 charge state of the La defect, which is approximately 1 eV higher than H_i^{AB1} within the band gap. However, despite it being a poor dopant in comparison with Y and Sc, the formation energies of La_{Cd} are considerably lower than the intrinsic Cd_i. La is the only dopant which shows a charge neutral state among these 3+ dopants.

Figure 7.9 presents the formation energies for the group 13 dopants, i.e., Al_{Cd} (solid gray line), Ga_{Cd} (solid beige line) and In_{Cd} (solid pink line). From these plots it is evident that the small dopants, Al and Ga, are not as favourable as In, which is more closely matched with the host cation. Thus, they are not expected to dominate over the native V_O under O-poor conditions as is the case for In_{Cd}. However, the opposite is true under O-rich conditions, where all the dopant defects are found to have lower formation energies than V_O. As with the RE dopants in Figure 7.8, all group 13 dopants were found to be shallow donors in CdO.

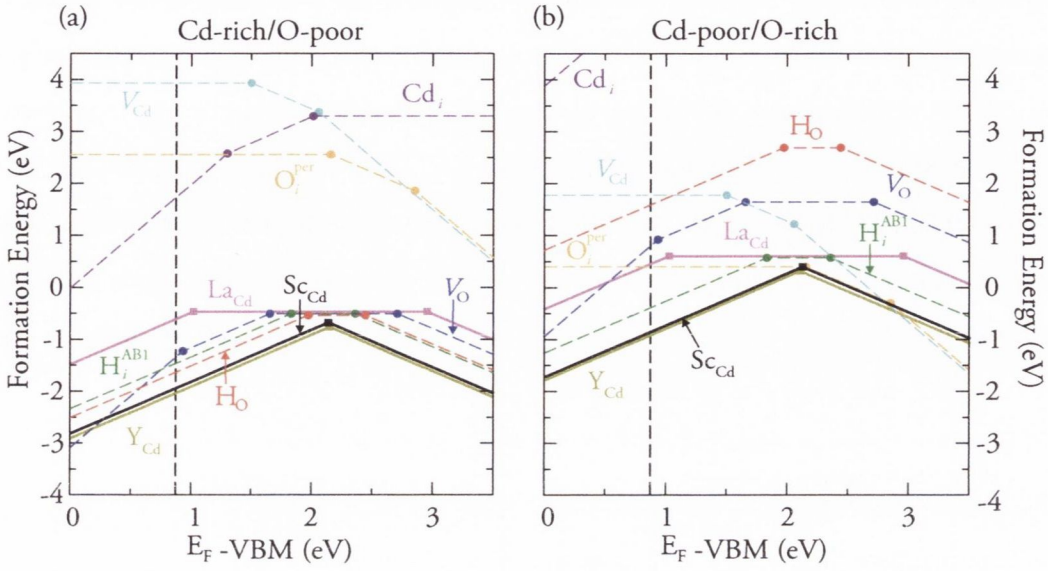

Figure 7.8: Formation energies for the RE dopants included in this study: Sc_{Cd} (solid black line), Y_{Cd} (solid green ochre line) and La_{Cd} (solid lila line). The black dashed line indicates the position of the conduction band maximum (CBM). The intrinsic and H defects are shown as context and are represented using dashed lines.

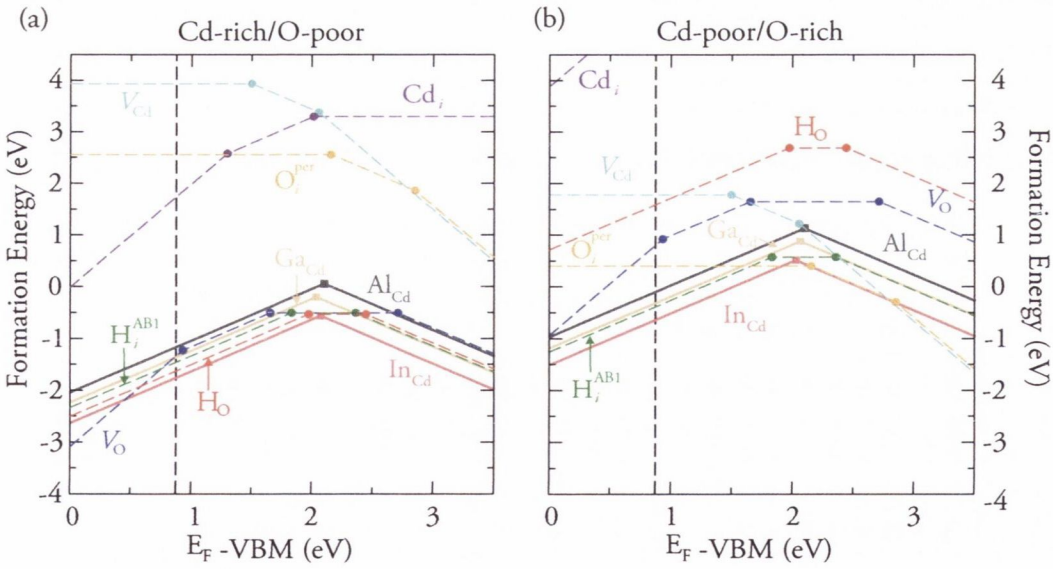

Figure 7.9: Formation energies for the group 13 dopants included in this study: Al_{Cd} (solid gray line), Ga_{Cd} (solid beige line) and In_{Cd} (solid pink line). The black dashed line indicates the position of the conduction band maximum (CBM). The intrinsic and H defects are shown as context and are represented using dashed lines.

Figure 7.10 presents the transition level diagrams for F-doping under O-poor and O-rich conditions. These results indicate that F_O (solid purple line) has the potential to confer excellent n-type properties to CdO and it is expected to dominate the conductivity under all fabriaction environments. This is in line with previous reports for this material [334, 397, 399]. The diagram also indicates that effective F doping is only likely when the F atoms substitute O, because the formation energies for F_i (solid green line) are too high. Similar properties have also been reported in other F-doped TCO materials like $BaSnO_3$ [403] and ZnO [400, 401].

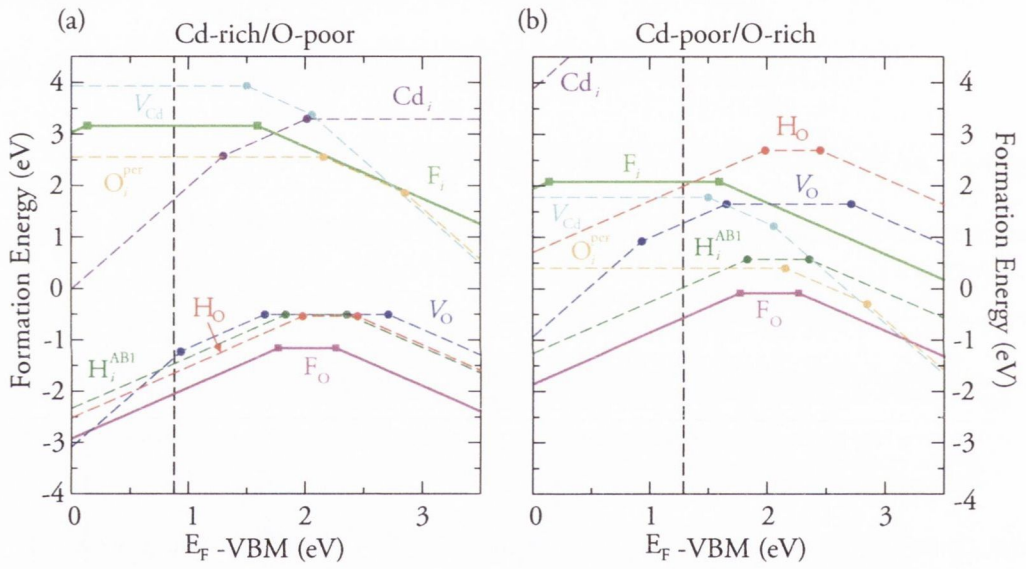

Figure 7.10: Formation energies for F_O (solid purple line) and F_i (solid green line) defects. The solid dots represent the transition levels $\epsilon(q/q\prime)$. The black dashed line indicates the position of the conduction band maximum (CBM). The intrinsic and H defects are shown as context and are represented using dashed lines.

7.2.2 Discussion

A very complete data set for these doped CdO compounds has been assembled by the groups of Profs Freeman and Marks at Northwestern University in the United States, who over the last decade and a half have published a number of studies on CdO doped with four of the species studied here, namely Ga [406], In [301, 369], Sc [370], Y [37]. In

these articles, the authors combined experimental measurements of physical and electronic structure parameters, conductivity measurements, as well as, DFT simulations. A key aspect of these investigations is that all the films were fabricated using Metal Organic Chemical Vapour Deposition (MOCVD), while the simulations were performed using screen exchange LDA (sX-LDA). This consitency in terms of the methods employed greatly facilitates the comparison of the results obtained for each doped CdO system. Figure 7.11 summarizes some of the results that were reported by Jin *et al.*. Shown in this figure are plots of the (a) electronic conductivities (S/cm) and (b) charge carrier concentrations ($\times 10^{20}$cm^{-3}) of CdO doped with Ga, In, Sc and Y as a function of dopant concentration for films deposited MgO (100) from Figures 12b and 14b in Ref. [406]. The data indicates that at relatively low concentrations of dopants, the conductivities observed for Sc:CdO, Y:CdO and In:CdO are likely to be all very similar if even a modest 10% error is assumed. In contrast Ga:CdO displays much lower conductivities over the same concentration range. The carrier concentrations in Figure 7.11 (b) indicate that all dopant species increase the carrier concentration with respect to undoped CdO, as is expected for these shallow donors. The lines in these plots were intended by the original authors to be guides to the eye and it is not immediately clear why no data points are available for In:CdO at low dopant concentrations. For the other dopants the charge carrier concentrations are very similar, which suggests that differences in the conductivities arise from factors like dopant-dependent changes to the band hybridization in CdO. Other data sets for these dopants claim that the solubility of these species in substitutional positions do not exceed 5% as in the case of Y [388], La [392, 393], In [33, 388], Ga [395, 407] and Al [408], which helps to explain the conductivity drops observed for these compounds.

In order to rationalize their experimental data the authors in the Yang *et al.* and Jin *et al.* papers utilized a type of hybrid DFT functional known as screened exchange LDA (sx-LDA), which has been shown to give good agreement with HSE06 results in other metal oxide systems where standard DFT has been shown to fail [205]. The

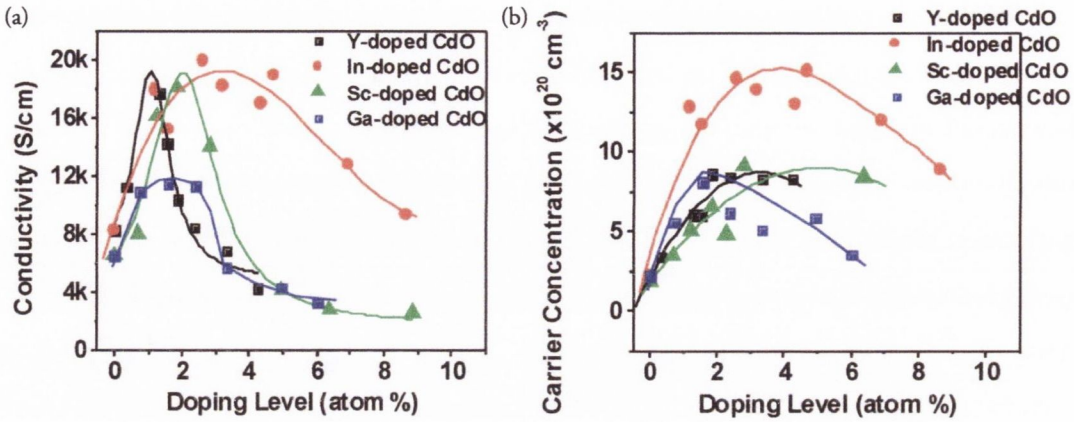

Figure 7.11: Room temparature properties of doped CdO films grown on MgO (100): (a) electronic conductivities and (b) carrier concentrations. From Figures 12b and 14b in Ref. [406].

simulations from Jin *et al.* predicted that the dopants which most closely match the ionic radius of Cd show the best conductivities. Among them, In^{3+} with a radius of 0.80 Å[131] was identified as the best *n*-type dopant for CdO, followed by Y, Sc and Ga. These results were interpreted by examining the lattice distortions induced by the dopants and the changes to the band structure of the doped systems [301]. The authors concluded that from a structural point of view, Cd substitution by dopants like In and Y leads to small distortions due to the fact that there is a small mismatch in their radii. These distortions affect Cd 5*d*– O 2*p* band hybridization by changing the Cd–O bond lengths and these observations were substantiated by plotting the band structure of the doped systems. However, with the HSE data currently available it is not possible to investigate these hybridization effects other than indirectly, by examining the relaxations around the defects. These changes are presented in Figure 7.12 with respect to bulk CdO (red dashed line), where the present results are shown as black symbols, squares for Cd–O and circles for Me–O (Me = Al, Ga, Sc, In, Y, La). The red symbols correspond to the sx-LDA results, where the diamonds represent the Cd–O bond lengths and the triangles are their corresponding Me–O bond lengths. These values were reported by Jin *et al.* [406] (Ga) and Yang *et al.* [37] (Sc, In, Y). There is an excellent level of agreement between the HSE and sx-LDA Me–O bond lengths,

with Y–O being slightly underestimated by sx-LDA with respect to the HSE results reported here. However, the Cd–O bond lengths that are closest to the substitutional defect (nearest neighbour) in the Me:CdO systems calculated using sx-LDA are smaller than those predicted using HSE: -1.71% for Y:CdO, -2.88% for In:CdO, -3.93% for Sc:CdO and -4.14% for Ga:CdO. The size of these differences is large compared to the difference between the experimental and HSE calculated lattice constants, which is 0.42%. The likely source of this discrepancy is the high dopant concentrations in the sx-LDA studies, which were performed on relatively small 16-atom supercells, which makes it is difficult to neglect dopant–dopant interactions [108, 112, 404, 405]. This means that the effects of the dopants on the hybridization of the Cd $5d$– O $2p$ bands is likely underestimated by the sx-LDA studies.

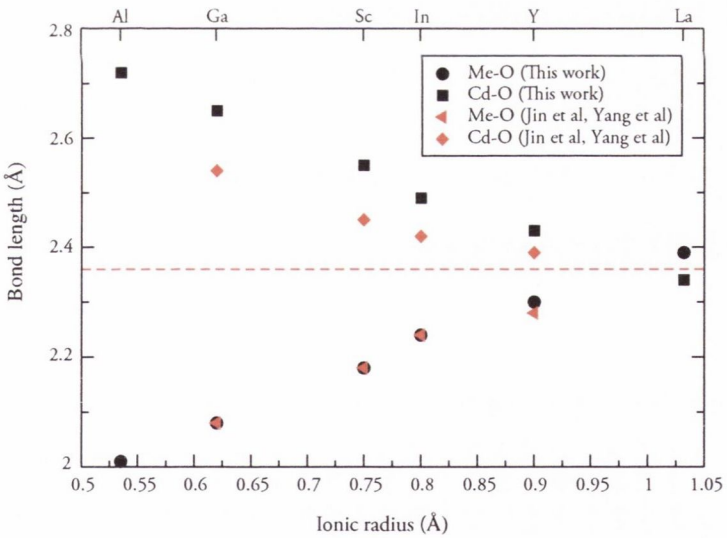

Figure 7.12: Cd–O (nearest neighbour) and Me–O (Me = Al, Ga, Sc, In, Y, La) bond lengths from the present work and from Jin *et al.* Ref. [406] for Ga:CdO and Yang *et al.* [37] for Sc, In and Y. The red line corresponds to the HSE06 Cd–O bond distance for bulk CdO from Table 7.1.

7.3 Summary

We have revealed that V_O is the dominant intrinsic defect in CdO under all growth conditions, acting as a doubly ionized shallow donor. Conductivity in nominally "undoped" CdO is likely to be dominated by V_O and H impurities under all growth conditions. Despite the relatively high VBM of CdO, p-type CdO will never be realized as the formation energy of the p-type defects are too high in energy, their ionization levels are ultra deep, and they are always compensated by n-type defects. We have examined the doping limits of CdO, and find that compensation by p-type defects does not occur until $> 1.2\,\text{eV}$ above the CBM, explaining why the band gap of CdO can experience large Moss-Burnstein shifts which can extend the optical band gap from $\sim 2.2\,\text{eV}$ to a reported $\sim 3.4\,\text{eV}$. To move the field of TCOs forward, alternatives to the expensive and rare In_2O_3 and the toxic CdO must be found. This could be achieved by devising strategies to raise the E_g^{FS} of the abundant TCOs such as SnO_2 or ZnO (or alternatively lower the CBM of these materials), whilst retaining the same characteristic conduction band dispersion and maintaining optical transparency. Whatever strategies may emerge, the defect chemistry of CdO provides a glimpse of the ideal defect chemistry of a candidate TCO, and should serve as a guide to the experimentalist and theoreticians alike in the search for novel TCOs.

In addition, a comprehensive set of extrinsic donors has been studied. In excellent agreement with experiment, it was found that all the dopants act as shallow donors and are likely to increase the charge carrier concentrations in CdO. The results also indicate that within a group there is a strong correlation between dopant size and the formation energy of these defects. F_O was found to be the best donor dopant in this system.

8

Discussion and Conclusions

Throughout this thesis modern theoretical methods and advanced simulation techniques were employed to study the properties of metal oxide materials for industrial applications. The work is divided into the study of the ionic conductivity in ceria-based solid electrolytes used in Solid Oxide Fuel Cells and the defect chemistry in a model Transparent Conducting Oxide, CdO.

The investigation of the ionic conductivity in ceria was carried out in a three-tiered approach: firstly, in Chapters 4 and 5 the content of aliovalent cations ceria was varied in singly doped systems, secondly, ceria solid solutions with multiple dopants were investigated in Chapter 4 and, thirdly Chapter 6 presented a thorough investigation of the effects of strain on doped ceria.

Chapter 4 pertains to the development of reliable interaction potentials for RE-doped ceria using LDA DFT. Special focus was given to the YDC system since it allowed validation of the DFT-derived potentials against neutron diffraction and AC impedance data provided by Dr Stephen Hull and Dr Stefan Norberg. This combined experiment/simulation approach allowed the study of the interactions between defects in YDC. These interactions are typically classified into cation-vacancy and vacancy-vacancy. The results showed that in common with other fluorite-structured materials, such as zirconia-based electrolytes, it is the vacancy-vacancy interactions which ultimately limit the conductivity once the cation-vacancy interactions have been reduced

to a minimum by introducing a dopant species with a similar ionic radius to that of the host Ce^{4+}.

The use of state-of-the-art DFT functionals, in particular HSE06, allowed the correct description of cations with f-electrons, like Nd^{3+}, Sm^{3+}, Gd^{3+} and Ce^{3+}. These advances were then coupled to interaction potentials for these cations, as well as, Zr, Sc and Y, all with common oxygen-oxygen terms, as described in Chapter 5. Having this consistent set of potentials made it possible to simulate ternary mixtures of the form CeO_2-RE'_2O_3-RE''_2O_3. Co-doped ceria compounds like these are particularly interesting as there are numerous reports claiming substantially improved conductivities with respect to their singly-doped counterparts. The results from these simulations showed that these claims are likely to originate from experimental variation in samples and from misinterpretation of the meaning of a critical dopant radius. The work presented made it evident that the properties of co-doped compounds are easily described by the weighted average of the singly doped systems.

Chapter 5 also presented an analysis of the conductivity mechanism in the system CeO_2-ZrO_2-Ce_2O_3 with an equal ratio of Ce^{4+} and Zr^{4+} cations. These solid solutions are of particular importance given their high OSC. In particular, CZO compounds with a pyrochlore-like cation ordering display OSCs that vastly exceed those of ceria. These results presented here demonstrate that cation-ordered CZO displays an ionic conductivity that is several times lower than that of the disordered phase, yet the process of reduction is much less costly energetically. What this implies is that the efficient exchange of oxygen with the atmosphere in TWCs requires that these CZO materials be small in size in order to be less impacted by the low conductivities that it displays.

Using the lattice mismatch between the components of SOFCs to increase the conductivity in ceria-based electrolytes is another approach that has gathered widespread interest. The simulations presented in Chapter 6 show that applying strain to ceria based electrolytes increases the ionic conductivity by up to 40%. Although these gains seem modest when compared to controversial reports that predict up to eight orders of

magnitude increase in related YSZ electrolytes, the results are in line with the latest experimental and computational reports on the subject. This study also brought light on a very important effect which is the enhancement of the conductivity on the surface of thin films.

The work that was carried out on the properties of CdO was presented in Chapter 7. This investigation consisted of two main sections. Firstly, h-DFT calculations were performed on the intrinsic defects in this material, namely oxygen vacancies, oxygen interstitials, cadmium interstitials and cadmium vacancies. The results pointed to a dominance of the n-type oxygen vacancies in both O-rich and O-poor growth conditions. Adventitious hydrogen doping was also investigated along with the intrinsic defects, and it was shown that the defects formed the substitution of oxygen by hydrogen are energetically favourable and are expected to dominate the conductivity of this material, along with oxygen vacancies under O-poor conditions. Other hydrogen defects, such as, hydogen in the interstitial position are expected to be dominant under O-rich conditions. An important corollary from these results is that p-type CdO is an unlikely prospect given the fact that the intrinsic p-type defects, cadmium vacancies and oxygen interstitials, do not act as effective acceptors in this system.

Extrinsic donor dopants were the subject of the second section of the CdO study presented in Chapter 7. For this work, a variety of dopant cations with different sizes were tested, from group 13, Al, Ga and In, from the RE elements Sc, Y and La; anion doping was investigated using fluorine defets in the CdO lattice. The trends observed in the formation energies of the cationic defects are consistent with a reduction of local lattice strain when the dopant cations are of similar size as the host Cd^{2+}. In this case, scandium, yttrium and indium were found to be efficient donors in CdO under all growth conditions. However, the substitution of oxygen by fluorine was predicted to be the n-type defect under all growth conditions.

References

[1] C. R. Karger and W. Hennings, *Renewable and Sustainable Energy Reviews*, 2009, **13**, 583 – 593.

[2] IEA, *Distributed Generation in Liberalised Electricity Markets*, OECD Publishing (Paris), 2002, pp. –.

[3] IEA, *Combined Heat and Power*, OECD Publishing (Paris), 2008.

[4] A. Stambouli and E. Traversa, *Renewable and Sustainable Energy Reviews*, 2002, **6**, 433–455.

[5] S. P. S. Badwal and K. Foger, *Ceramics International*, 1996, **22**, 257–265.

[6] N. P. Brandon, S. Skinner and B. C. H. Steele, *Annual Review of Materials Research*, 2003, **33**, 183–213.

[7] P. Bance, N. P. Brandon, B. Girvan, P. Holbeche, S. O'Dea and B. C. H. Steele, *Journal of Power Sources*, 2004, **131**, 86–90.

[8] A. J. Jacobson, *Chemistry of Materials*, 2010, **22**, 660–674.

[9] X. Changrong, *Green Chemistry and Chemical Engineering*, CRC Press, 2008, pp. 1–71.

[10] J. B. Goodenough, *Annual Review of Materials Research*, 2003, **33**, 91–128.

[11] S. Hull, S. T. Norberg, I. Ahmed, S. G. Eriksson, D. Marrocchelli and P. A. Madden, *Journal of Solid State Chemistry*, 2009, **182**, 2815 – 2821.

[12] B. C. H. Steele, *Solid State Ionics*, 2000, **129**, 95 – 110.

[13] S. Wang, H. Inaba, H. Tagawa, M. Dokiya and T. Hashimoto, *Solid State Ionics*, 1998, **107**, 73 – 79.

[14] S. Wang, H. Inaba, H. Tagawa and T. Hashimoto, *Journal of the Electrochemical Society*, 1997, **144**, 4076–4080.

[15] N. Kim and J. F. Stebbins, *Chemistry of Materials*, 2007, **19**, 5742–5747.

[16] T. Tsai, E. Perry and S. Barnett, *Journal of the Electrochemical Society*, 1997, **144**, L130–L132.

[17] M. Burbano, D. Marrocchelli, B. Yildiz, H. L. Tuller, S. T. Norberg, S. Hull, P. A. Madden and G. W. Watson, *Journal of Physics: Condensed Matter*, 2011, **23**, 255402.

[18] M. Mogensen, N. M. Sammes and G. A. Tompsett, *Solid State Ionics*, 2000, **129**, 63–94.

[19] S. R. Bishop, D. Marrocchelli, W. Fang, K. Amezawa, K. Yashiro and G. W. Watson, *Energy Environ. Sci.*, 2013, **6**, 1142–1146.

[20] D. Marrocchelli, S. R. Bishop, H. L. Tuller and B. Yildiz, *Advanced Functional Materials*, 2012, **22**, 1958–1965.

[21] D. Marrocchelli, S. R. Bishop, H. L. Tuller, G. W. Watson and B. Yildiz, *Physical Chemistry Chemical Physics*, 2012, **14**, 12070–12074.

[22] D. Marrocchelli, S. R. Bishop and J. Kilner, *JOURNAL OF MATERIALS CHEMISTRY A*, 2013, **1**, 7673.

[23] D. A. Andersson, S. I. Simak, N. V. Skorodumova, I. A. Abrikosov and B. Johansson, *Proceedings of the National Academy of Sciences of the United States of America*, 2006, **103**, 3518–3521.

[24] A. Bogicevic and C. Wolverton, *Physical Review B*, 2003, **67**, 024106.

[25] C. R. A. Catlow, *Solid State Ionics*, 1984, **12**, 67 – 73.

[26] D. Y. Wang, D. Park, J. Griffith and A. Nowick, *Solid State Ionics*, 1981, **2**, 95 – 105.

[27] D. R. Ou, T. Mori, F. Ye, T. Kobayashi, J. Zou, G. Auchterlonie and J. Drennan, *Applied Physics Letters*, 2006, **89**, 171911.

[28] H. Inaba and H. Tagawa, *Solid State Ionics*, 1996, **83**, 1 – 16.

[29] G. Balducci, J. Kašpar, P. Fornasiero, M. Graziani and M. S. Islam, *The Journal of Physical Chemistry B*, 1998, **102**, 557–561.

[30] H.-T. Chen and J.-G. Chang, *The Journal of Chemical Physics*, 2010, **132**, 214702.

[31] E. Brandt, Y. Wang and J. Grizzle, *Control Systems Technology, IEEE Transactions on*, 2000, **8**, 767–776.

[32] G. Thomas, *Nature*, 1997, **389**, 907.

[33] B. J. Ingram, G. B. Gonzalez, D. R. Kammler, M. I. Bertoni and T. O. Mason, *J. Electroceram.*, 2004, **13**, 167–175.

[34] K. Hayashi, S. Matsuishi, T. Kamiya, M. Hirano and H. Hosono, *Nature*, 2002, **419**, 462–465.

[35] T. Minami, *Semicond. Sci. Tech.*, 2005, **20**, S35–S44.

[36] R. G. Gordon, *MRS Bull.*, 2000, **25**, 52–57.

[37] Y. Yang, S. Jin, J. E. Medvedeva, J. R. Ireland, A. W. Metz, J. Ni, M. C. Hersam, A. J. Freeman and T. J. Marks, *Journal of the American Chemical Society*, 2005, **127**, 8796–8804.

[38] L. Wang, D. W. Matson, E. Polikarpov, J. S. Swensen, C. C. Bonham, L. Cosimbescu, J. J. Berry, D. S. Ginley, D. J. Gaspar and A. B. Padmaperuma, *Journal of Applied Physics*, 2010, **107**, 043103.

[39] K. Bädeker, *Annalen der Physik*, 1907, **327**, 749–766.

[40] J. E. Medvedeva and A. J. Freeman, *EPL (Europhysics Letters)*, 2005, **69**, 583.

[41] Çetin Kiliç and A. Zunger, *Physical Review Letters*, 2002, **88**, 095501.

[42] X. L. Nie, S. H. Wei and S. B. Zhang, *Physical Review B*, 2002, **65**, 075111.

[43] D. O. Scanlon and G. W. Watson, *Chemistry of Materials*, 2009, **21**, 5435–5442.

[44] M. Burbano, D. O. Scanlon and G. W. Watson, *Journal of the American Chemical Society*, 2011, **133**, 15065–15072.

[45] S. Sheng, G. Fang, C. Li, S. Xu and X. Zhao, *physica status solidi (a)*, 2006, **203**, 1891–1900.

[46] D. O. Scanlon, B. J. Morgan, G. W. Watson and A. Walsh, *Physical Review Letters*, 2009, **103**, 096405.

[47] D. O. Scanlon, B. J. Morgan and G. W. Watson, *Journal of Chemical Physics*, 2009, **131**, 124703.

[48] `http://www.imagesco.com/articles/photovoltaic/photovoltaic-pg4.html`.

[49] N. Sato, M. Ichimura, E. Arai and Y. Yamazaki, *Solar energy materials and solar cells*, 2005, **85**, 153–165.

[50] F. Jensen, *Introduction to Computational Chemistry*, Wiley-VCH Verlag GmbH, Weinheim, Germany, 2nd edn, 2007.

[51] A. Leach, *Molecular Modelling: Principles and Applications*, Prentice Hall: Harlow, England, 2nd edn, 2001.

[52] P. Atkins and J. de Paula, *Physical Chemistry*, Oxford University Press, Oxford, England, 7th edn, 2002.

[53] J. S. Lundeen, B. Sutherland, A. Patel, C. Stewart and C. Bamber, *Nature*, 2011, **474**, 188–191.

[54] J. C. Slater, *Physical Review*, 1951, **81**, 385–390.

[55] P.-O. Löwdin, *Physical Review*, 1955, **97**, 1474–1489.

[56] P. Hohenberg and W. Kohn, *Physical Review*, 1964, **136**, B864–B871.

[57] W. Kohn and L. J. Sham, *Physical Review*, 1965, **140**, A1133–A1138.

[58] W. Koch and M. C. Holthausen, *A Chemist's Guide to Density Functional Theory*, Wiley-VCH Verlag GmbH, Weinheim, Germany, 2001.

[59] D. M. Ceperley and B. J. Alder, *Physical Review Letters*, 1980, **45**, 566–569.

[60] S. H. Vosko, L. Wilk and M. Nusair, *Canadian Journal of Physics*, 1980, **58**, 1200–1211.

[61] J. P. Perdew and Y. Wang, *Physical Review B*, 1992, **45**, 13244.

[62] A. D. Becke, *Physical Review A*, 1988, **38**, 3098.

[63] C. Lee, W. Yang and R. G. Parr, *Physical Review B*, 1988, **37**, 785–789.

[64] J. P. Perdew and W. Yue, *Physical Review B*, 1986, **33**, 8800–8802.

[65] J. P. Perdew, K. Burke and M. Ernzerhof, *Physical Review Letters*, 1996, **77**, 3865–3868.

[66] J. P. Perdew, A. Ruzsinszky, L. A. Constantin, J. Sun and G. I. Csonka, *Journal of Chemical Theory and Computation*, 2009, **5**, 902–908.

[67] S. L. Dudarev, G. A. Botton, S. Y. Savrasov, C. J. Humphreys and A. P. Sutton, *Physical Review B*, 1998, **57**, 1505.

[68] M. Cococcioni and S. de Gironcoli, *Physical Review B*, 2005, **71**, 035105.

[69] S. Li, H. Lu, P. Li, Z. Yang and Z. Guo, *The Journal of chemical physics*, 2008, **128**, 164718.

[70] D. O. Scanlon, A. Walsh, B. J. Morgan and G. W. Watson, *The Journal of Physical Chemistry C*, 2008, **112**, 9903–9911.

[71] B. J. Morgan, D. O. Scanlon and G. W. Watson, *Journal of Materials Chemistry*, 2009, **19**, 5175–5178.

[72] D. O. Scanlon, N. M. Galea, B. J. Morgan and G. W. Watson, *The Journal of Physical Chemistry C*, 2009, **113**, 11095–11103.

[73] C. Adamo and V. Barone, *The Journal of chemical physics*, 2002, **116**, 5933.

[74] J. P. Perdew, M. Ernzerhof and K. Burke, *The Journal of Chemical Physics*, 1996, **105**, 9982.

[75] J. Heyd, G. E. Scuseria and M. Ernzerhof, *Journal of Chemical Physics*, 2003, **118**, 8207–8215.

[76] A. Walsh, J. L. Da Silva and S.-H. Wei, *Physical Review Letters*, 2008, **100**, 256401.

[77] M. Born and K. Huang, *Dynamical theory of crystal lattices*, Oxford Univeristy Press, Oxford, UK, 1954.

[78] P. P. Ewald, *Annalen der Physik*, 1921, **369**, 253–287.

[79] D. M. Heyes, *Physical Review B*, 1994, **49**, 755–764.

[80] A. Aguado and P. Madden, *Journal of Chemical Physics*, 2003, **119**, 7471–7483.

[81] P. A. Madden and M. Wilson, *Chemical Society Reviews*, 1996, **25**, 339–350.

[82] P. Fowler and P. Madden, *Physical Review B*, 1984, **29**, 1035–1042.

[83] P. W. Fowler and P. A. Madden, *Physical Review B*, 1985, **31**, 5443–5455.

[84] P. W. Fowler and P. A. Madden, *The Journal of Physical Chemistry*, 1985, **89**, 2581–2585.

[85] J. H. Harding and N. C. Pyper, *Philosophical Magazine Letters*, 1995, **71**, 113–121.

[86] A. Buckingham, *Advances in Chemical Physics*, 1967, **12**, 107.

[87] G. Papatheodorou and V. Dracopoulos, *Chemical Physics Letters*, 1995, **241**, 345 – 350.

[88] P. A. Madden, K. O'Sullivan, J. A. Board and P. W. Fowler, *The Journal of Chemical Physics*, 1991, **94**, 918–927.

[89] M. J. Castiglione, M. Wilson and P. A. Madden, *Journal of Physics: Condensed Matter*, 1999, **11**, 9009.

[90] S. T. Norberg, I. Ahmed, S. Hull, D. Marrocchelli and P. A. Madden, *Journal of Physics: Condensed Matter*, 2009, **21**, 215401.

[91] P. A. Madden, R. Heaton, A. Aguado and S. Jahn, *Journal of Molecular Structure: THEOCHEM*, 2006, **771**, 9–18.

[92] K. T. Tang and J. P. Toennies, *The Journal of Chemical Physics*, 1984, **80**, 3726–3741.

[93] K. T. Tang and J. P. Toennies, *The Journal of Chemical Physics*, 2003, **118**, 4976–4983.

[94] N. W. Ashcroft and D. N. Mermin, *Solid State Physics*, Rinehart and Winston, New York, 1976.

[95] C. J. Bradley and A. Cracknell, *The Mathematical Theory of Symmetry in Solids*, Clarendon Press, Oxford, England, 1972.

[96] C. Kittel, *Introduction to Solid State Physics*, John Wiley & Sons, Inc., 2005.

[97] C. Herring, *Physical Review*, 1940, **57**, 1169–1177.

[98] G. Kresse and J. Furthmüller, *Physical Review B*, 1996, **54**, 11169–11186.

[99] D. R. Hamann, M. Schlüter and C. Chiang, *Physical Review Letters*, 1979, **43**, 1494–1497.

[100] D. Vanderbilt, *Physical Review B*, 1990, **41**, 7892–7895.

[101] P. E. Blöchl, *Physical Review B*, 1994, **50**, 17953–17979.

[102] R. Feynman, *Physical Review*, 1939, **56**, 340.

[103] F. Murnaghan, *Proceedings of the National Academy of Sciences of the United States of America*, 1944, **30**, 244 – 247.

[104] E. W. Weisstein, *Method of Steepest Descent*, `http://mathworld.wolfram.com/MethodofSteepestDescent.html`.

[105] D. D. Wagman, *Journal of Physical and Chemical Reference Data*, 1982, **11 (Suppl. 2)**, 116.

[106] A. Walsh, J. L. F. D. Silva and S.-H. Wei, *Physical Review B*, 2008, **78**, 075211.

[107] R. F. W. Bader, *Atoms in Molecules: A Quantum Theory*, Oxford University Press, Oxford, 1990.

[108] C. Freysoldt, J. Neugebauer and C. G. V. de Walle, *Physical Review Letters*, 2009, **102**, 016402.

[109] C. G. Van de Walle, D. B. Laks, G. F. Neumark and S. T. Pantelides, *Phys. Rev. B*, 1993, **47**, 9425–9434.

[110] C. G. V. de Walle, D. Laks, G. Neumark and S. Pantelides, *Journal of Crystal Growth*, 1992, **117**, 704 – 709.

[111] C. G. Van de Walle and J. Neugebauer, *Journal of Applied Physics*, 2004, **95**, 3851–3879.

[112] S. Lany and A. Zunger, *Physical Review B*, 2008, **78**, 235104.

[113] A. Walsh, Y. Yan, M. M. Al-Jassim and S.-H. Wei, *Journal of Physical Chemistry C*, 2008, **112**, 12044–12050.

[114] M. Allen and D. Tildesley, *Computer Simulation of Liquids*, Oxford University Press, Oxford, England, 1989.

[115] S. Nosé, *Journal of Chemical Physics*, 1984, **81**, 511–519.

[116] S. Nosé, *Molecular Physics*, 1984, **52**, 255–268.

[117] W. Hoover, *Physical Review A*, 1985, **31**, 1695–1697.

[118] D. J. Evans and B. L. Holian, *The Journal of Chemical Physics*, 1985, **83**, 4069–4074.

[119] G. Martyna, M. Klein and T. M., *Journal of Chemical Physics*, 1992, **97**, 2635–2643.

[120] G. J. Martyna, D. J. Tobias and M. L. Klein, *Journal of Chemical Physics*, 1994, **101**, 4177–4189.

[121] K. Sato, K. Suzuki, K. Yashiro, T. Kawada, H. Yugami, T. Hashida, A. Atkinson and J. Mizusaki, *Solid State Ionics*, 2009, **180**, 1220–1225.

[122] C. H. Cheng, S. F. Lee and C. W. Hong, *Journal of the Electrochemical Society*, 2007, **154**, E158–E163.

[123] E. A. Kümmerle and G. Heger, *Journal of Solid State Chemistry*, 1999, **147**, 485 – 500.

[124] K. Momma and F. Izumi, *Journal of Applied Crystallography*, 2008, **41**, 653–658.

[125] A. Trovarelli, *Catalysis by Ceria and Related Materials*, Imperial College Press, 2002.

[126] B. C. H. Steele and A. Heinzel, *Nature*, 2001, **414**, 345–352.

[127] T. H. Etsell and S. N. Flengas, *Chemical Reviews*, 1970, 339.

[128] S. Sen, H. J. Avila-Paredes and S. Kim, *Journal of Materials Chemistry*, 2008, **18**, 3915–3917.

[129] T. S. Zhang, J. Ma, H. T. Huang, P. Hing, Z. T. Xia, S. H. Chan and J. A. Kilner, *Solid State Sciences*, 2003, **5**, 1505 – 1511.

[130] X. Sha, Z. Lü, X. Huang, J. Miao, Z. Ding, X. Xin and W. Su, *Journal of Alloys and Compounds*, 2007, **428**, 59 – 64.

[131] R. Shannon, *Acta Crystallographica Section A*, 1976, **32**, 751.

[132] R. Fletcher, *The Computer Journal*, 1970, **13**, 317–322.

[133] F. James and M. Roos, *Computer Physics Communications*, 1975, **10**, 343–367.

[134] A. Lazzaro and L. Moneta, *Journal of Physics: Conference Series*, 2010, **219**, 042044.

[135] F. Ercolessi and J. B. Adams, *Europhysics Letters*, 1994, **26**, 583.

[136] A. Aguado and P. A. Madden, *Physical Review B*, 2004, **70**, 245103.

[137] A. Aguado and P. A. Madden, *Journal of Chemical Physics*, 2003, **118**, 5718–5728.

[138] N. Marzari and D. Vanderbilt, *Physical Review B*, 1997, **56**, 12847–12865.

[139] N. Marzari, I. Souza and D. Vanderbilt, *Psi-K Scientific Highlight of the Month*, 2003, **57**, 129.

[140] *The CPMD Consortium, CPMD Version 3.x*, `http://www.cpmd.org`.

[141] D. Marrocchelli, *PhD thesis*, University of Edinburgh, 2010.

[142] S. Jahn and P. Madden, *Physics of the Earth and Planetary Interiors*, 2007, **162**, 129–139.

[143] G. Kresse and J. Hafner, *Physical Review B*, 1994, **49**, 14251–14269.

[144] A. Migani, K. M. Neyman, F. Illas and S. T. Bromley, *Journal of Chemical Physics*, 2009, **131**, 064701.

[145] H. Xu, R. K. Behera, Y. Wang, F. Ebrahimi, S. B. Sinnott, E. D. Wachsman and S. R. Phillpot, *Solid State Ionics*, 2010, **181**, 551 – 556.

[146] R. Grimes, G. Busker, M. McCoy, A. Chroneos, J. Kilner and S. Chen, *Berichte der Bunsen-Gesellschaft*, 1997, **101**, 1204–1210.

[147] S. Vyas, R. W. Grimes, D. H. Gay and A. L. Rohl, *Journal of the Chemical Society, Faraday Transactions*, 1998, **94**, 427–434.

[148] H. Inaba, R. Sagawa, H. Hayashi and K. Kawamura, *Solid State Ionics*, 1999, **122**, 95 – 103.

[149] A. Gotte, K. Hermansson and M. Baudin, *Surface Science*, 2004, **552**, 273 – 280.

[150] A. Gotte, D. Spångberg, K. Hermansson and M. Baudin, *Solid State Ionics*, 2007, **178**, 1421 – 1427.

[151] V. Butler, C. R. A. Catlow, B. E. F. Fender and J. H. Harding, *Solid State Ionics*, 1983, **8**, 109 – 113.

[152] A. Kossoy, Y. Feldman, R. Korobko, E. Wachtel, I. Lubomirsky and J. Maier, *Advanced Functional Materials*, 2009, **19**, 634–641.

[153] A. Kossoy, A. I. Frenkel, Q. Wang, E. Wachtel and I. Lubomirsky, *Adv. Mater.*, 2010, **22**, 1659–1662.

[154] M. Wilson, U. Schönberger and M. W. Finnis, *Physical Review B*, 1996, **54**, 9147–9161.

[155] M. Wilson, S. Jahn and P. A. Madden, *Journal of Physics: Condensed Matter*, 2004, **16**, S2795.

[156] P. Jahn, S. & Madden, *Journal of Non-Crystalline Solids*, 2007, **353**, 3500–3504.

[157] D. Marrocchelli, M. Salanne, P. A. Madden, C. Simon and P. Turq, *Molecular Physics*, 2009, **107**, 443 – 452.

[158] D. Marrocchelli, P. A. Madden, S. T. Norberg and S. Hull, *Journal of Physics: Condensed Matter*, 2009, **21**, 405403.

[159] D. Marrocchelli, P. A. Madden, S. T. Norberg and S. Hull, Solid State Ionics, 2009, pp. 71–78.

[160] D. Marrocchelli, M. Salanne and P. A. Madden, *Journal of Physics: Condensed Matter*, 2010, **22**, 152102.

[161] S. T. Norberg, S. Hull, I. Ahmed, S. G. Eriksson, D. Marrocchelli, P. A. Madden, P. Li and J. T. S. Irvine, *Chemistry of Materials*, 2011, **23**, 1356–1364.

[162] D. Marrocchelli, P. A. Madden, S. T. Norberg and S. Hull, *Chemistry of Materials*, 2011, **23**, 1365–1373.

[163] T. Hisashige, Y. Yamamura and T. Tsuji, *Journal of Alloys and Compounds*, 2006, **408-412**, 1153 – 1156.

[164] S. Sameshima, M. Kawaminami and H. Y, *Journal of the Ceramic Society of Japan*, 2002, **110**, 597–600.

[165] J. Sims and R. Blumenthal, *High temperature science*, 1976, **8**, 99–110.

[166] A. Nakajima, A. Yoshihara and M. Ishigame, *Physical Review B*, 1994, **50**, 13297–13307.

[167] K. Clausen, W. Hayes, J. E. Macdonald, R. Osborn, P. G. Schnabel, M. T. Hutchings and A. Magerl, *Journal of the Chemical Society, Faraday Transactions 2*, 1987, **83**, 1109–1112.

[168] Y. Wang, K. Duncan, E. D. Wachsman and F. Ebrahimi, *Solid State Ionics*, 2007, **178**, 53 – 58.

[169] S. Sameshima, H. Ono, K. Higashi, K. Sonoda, Y. Hirata and Y. Ikuma, *Journal of the Ceramic Society of Japan*, 2000, **108**, 1060–1066.

[170] R. Car and M. Parrinello, *Physical Review Letters*, 1985, **55**, 2471–2474.

[171] M. Burbano, S. T. Norberg, S. Hull, S. G. Eriksson, D. Marrocchelli, P. A. Madden and G. W. Watson, *Chemistry of Materials*, 2012, **24**, 222–229.

[172] M. J. Castiglione and P. A. Madden, *Journal of Physics: Condensed Matter*, 2001, **13**, 9963.

[173] H. Maekawa, K. Kawata, Y. P. Xiong, N. Sakai and H. Yokokawa, *Solid State Ionics*, 2009, **180**, 314 – 319.

[174] C. Tian and S.-W. Chan, *Solid State Ionics*, 2000, **134**, 89 – 102.

[175] B. C. H. Steele and J. Floyd, *Proc. Br. Ceram. Soc*, 1971, **19**, 55.

[176] H. L. Tuller and A. S. Nowick, *Journal of Physics and Chemistry of Solids*, 1977, **38**, 859 – 867.

[177] P. P. Dholabhai, J. B. Adams, P. Crozier and R. Sharma, *Journal of Chemical Physics*, 2010, **132**, 094104.

[178] F. Pietrucci, M. Bernasconi, A. Laio and M. Parrinello, *Physical Review B*, 2008, **78**, 094301.

[179] J. Kilner, *Solid State Ionics*, 1983, **8**, 201 – 207.

[180] G. B. Balazs and R. Glass, *Solid State Ionics*, 1995, **76**, 155–162.

[181] H. Hayashi, R. Sagawa, H. Inaba and K. Kawamura, *Solid State Ionics*, 2000, **131**, 281 – 290.

[182] B. Wang, R. J. Lewis and A. N. Cormack, *Acta Materialia*, 2011, **59**, 2035 – 2045.

[183] E. D. Wachsman, C. A. Marlowe and K. T. Lee, *Energy Environ. Sci.*, 2012, **5**, 5498–5509.

[184] E. D. Wachsman and K. T. Lee, *Science*, 2011, **334**, 935–939.

[185] J. L. Rupp, *Solid State Ionics*, 2012, **207**, 1 – 13.

[186] M. Burbano, D. Marrocchelli and G. Watson, *Journal of Electroceramics*, 2013, **32**, 28–36.

[187] T. Politova and J. Irvine, *Solid State Ionics*, 2004, **168**, 153–165.

[188] J. van Herle, D. Seneviratne and A. McEvoy, *Journal of the European Ceramic Society*, 1999, **19**, 837 – 841.

[189] N. Singh, O. Parkash and D. Kumar, *Ionics*, 2013, **19**, 165–170.

[190] N. K. Singh, P. Singh, D. Kumar and O. Parkash, *Ionics*, 2012, **18**, 127–134.

[191] S. Omar, E. D. Wachsman, J. L. Jones and J. C. Nino, *Journal of the American Ceramic Society*, 2009, **92**, 2674–2681.

[192] S. Omar, E. D. Wachsman and J. C. Nino, *Applied Physics Letters*, 2007, **91**, 144106–3.

[193] X. Sha, Z. Lü, X. Huang, J. Miao, L. Jia, X. Xin and W. Su, *Journal of Alloys and Compounds*, 2006, **424**, 315 – 321.

[194] S. Dikmen, H. Aslanbay, E. Dikmen and O. Sahin, *Journal of Power Sources*, 2010, **195**, 2488 – 2495.

[195] X. Guan, H. Zhou, Z. Liu, Y. Wang and J. Zhang, *Materials Research Bulletin*, 2008, **43**, 1046 – 1054.

[196] J. Ayawanna, D. Wattanasiriwech, S. Wattanasiriwech and P. Aungkavattana, *Solid State Ionics*, 2009, **180**, 1388 – 1394.

[197] P. P. Dholabhai, J. B. Adams, P. A. Crozier and R. Sharma, *Journal of Materials Chemistry*, 2011, **21**, 18991–18997.

[198] J. Ralph, J. Przydatek, J. Kilner and T. Seguelong, *Berichte der Bunsen-Gesellschaft*, 1997, **101**, 1403–1407.

[199] R. M. Kasse and J. C. Nino, *Journal of Alloys and Compounds*, 2013, **575**, 399 – 402.

[200] D.-J. Kim, *Journal of the American Ceramic Society*, 1989, **72**, 1415–1421.

[201] S. Omar, E. D. Wachsman and J. C. Nino, *Solid State Ionics*, 2006, **177**, 3199 – 3203.

[202] A. Chroneos, B. Yildiz, A. Tarancon, D. Parfitt and J. A. Kilner, *Energy Environ. Sci.*, 2011, **4**, 2774–2789.

[203] M. C. Gobel, G. Gregori, X. Guo and J. Maier, *Physical Chemistry Chemical Physics*, 2010, **12**, 14351–14361.

[204] J. L. F. Da Silva, M. V. Ganduglia-Pirovano, J. Sauer, V. Bayer and G. Kresse, *Physical Review B*, 2007, **75**, 045121–10.

[205] R. Gillen, S. J. Clark and J. Robertson, *Physical Review B*, 2013, **87**, 125116.

[206] M. V. Ganduglia-Pirovano, A. Hofmann and J. Sauer, *Surface Science Reports*, 2007, **62**, 219 – 270.

[207] P. R. Keating, D. O. Scanlon and G. W. Watson, *Journal of Physics: Condensed Matter*, 2009, **21**, 405502.

[208] P. R. L. Keating, D. O. Scanlon, B. J. Morgan, N. M. Galea and G. W. Watson, *The Journal of Physical Chemistry C*, 2012, **116**, 2443–2452.

[209] P. R. L. Keating, D. O. Scanlon and G. W. Watson, *J. Mater. Chem. C*, 2013, **1**, 1093–1098.

[210] M. Nolan, J. E. Fearon and G. W. Watson, *Solid State Ionics*, 2006, **177**, 3069 – 3074.

[211] D. A. Andersson, S. I. Simak, B. Johansson, I. A. Abrikosov and N. V. Skorodumova, *Physical Review B*, 2007, **75**, 035109.

[212] R. Heaton, R. Brookes, P. Madden, M. Salanne, C. Simon and P. Turq, *Journal of Physical Chemistry B*, 2006, **110**, 11454–11460.

[213] M. Salanne, C. Simon, P. Turq and P. Madden, *Journal of Fluorine Chemistry*, 2009, **130**, 38–44.

[214] M. Salanne, D. Marrocchelli and G. W. Watson, *The Journal of Physical Chemistry C*, 2012, **116**, 18618–18625.

[215] A. V. Krukau, O. A. Vydrov, A. F. Izmaylov and G. E. Scuseria, *Journal of Chemical Physics*, 2006, **125**, 224106.

[216] J. Paier, M. Marsman, K. Hummer, G. Kresse, I. C. Gerber and J. G. Angyan, *The Journal of Chemical Physics*, 2006, **124**, 154709.

[217] R. J. Heaton, P. A. Madden, S. J. Clark and S. Jahn, *The Journal of Chemical Physics*, 2006, **125**, 144104.

[218] J. C. Slater and J. G. Kirkwood, *Physical Review*, 1931, **37**, 682–697.

[219] V. Haigis, M. Salanne, S. Simon, M. Wilke and S. Jahn, *Chemical Geology*, 2013, **346**, 14 – 21.

[220] S. J. Hong and A. V. Virkar, *Journal of the American Ceramic Society*, 1995, **78**, 433–439.

[221] V. Grover, A. Banerji, P. Sengupta and A. Tyagi, *Journal of Solid State Chemistry*, 2008, **181**, 1930 – 1935.

[222] C.-i. Lee, Q.-L. Meng, H. Kaneko and Y. Tamaura, *Journal of Solar Energy Engineering*, 2012, **135**, 011002–011002.

[223] R. Gerhardt-Anderson and A. S. Nowick, *Solid State Ionics*, 1981, **5**, 547 – 550.

[224] J. V. Herle, T. Horita, T. Kawada, N. Sakai, H. Yokokawa and M. Dokiya, *Journal of the European Ceramic Society*, 1996, **16**, 961 – 973.

[225] C. Huang, W. Wei, C. Chen and J. Chen, *Journal of the European Ceramic Society*, 2011, **31**, 3159 – 3169.

[226] K. Huang, M. Feng and J. B. Goodenough, *Journal of the American Ceramic Society*, 1998, **81**, 357–362.

[227] T. Zhang, P. Hing, H. Huang and J. Kilner, *Solid State Ionics*, 2002, **148**, 567 – 573.

[228] S. Buyukkilic, T. Shvareva and A. Navrotsky, *Solid State Ionics*, 2012, **227**, 17 – 22.

[229] S. Dikmen, P. Shuk and M. Greenblatt, *Solid State Ionics*, 1999, **126**, 89 – 95.

[230] X.-D. Zhou, W. Huebner, I. Kosacki and H. U. Anderson, *Journal of the American Ceramic Society*, 2002, **85**, 1757–1762.

[231] C. Xia and M. Liu, *Solid State Ionics*, 2002, **152-153**, 423 – 430.

[232] P. P. Dholabhai, S. Anwar, J. B. Adams, P. A. Crozier and R. Sharma, *Modelling and Simulation in Materials Science and Engineering*, 2012, **20**, 015004.

[233] B. Grope, T. Zacherle, M. Nakayama and M. Martin, *Solid State Ionics*, 2012, **225**, 476 – 483.

[234] J. Shemilt and H. Williams, *Journal of Materials Science Letters*, 1999, **18**, 1735–1737.

[235] G.-B. Jung, T.-J. Huang and C.-L. Chang, *Journal of Solid State Electrochemistry*, 2002, **6**, 225–230.

[236] L. Aneflous, J. A. Musso, S. Villain, J.-R. Gavarri and H. Benyaich, *Journal of Solid State Chemistry*, 2004, **177**, 856 – 865.

[237] T. S. Zhang, J. Ma, L. B. Kong, S. H. Chan and J. A. Kilner, *Solid State Ionics*, 2004, **170**, 209 – 217.

[238] I. E. Stephens and J. A. Kilner, *Solid State Ionics*, 2006, **177**, 669 – 676.

[239] H. Lang, K. Kiinstler, M. Mangier and G. Tomandl, Solid Oxide Fuel Cells (SOFC VI): Proceedings of the Sixth International Symposium, 1999, p. 233.

[240] P. Li, I.-W. Chen, J. E. Penner-Hahn and T.-Y. Tien, *Journal of the American Ceramic Society*, 1991, **74**, 958–967.

[241] M. Nakayama and M. Martin, *Physical Chemistry Chemical Physics*, 2009, **11**, 3241–3249.

[242] C. B. Gopal and A. van de Walle, *Physical Review B*, 2012, **86**, 134117.

[243] S. Dikmen, *Journal of Alloys and Compounds*, 2010, **491**, 106 – 112.

[244] F.-Y. Wang, S. Chen and S. Cheng, *Electrochemistry Communications*, 2004, **6**, 743 – 746.

[245] H. Yoshida, H. Deguchi, K. Miura, M. Horiuchi and T. Inagaki, *Solid State Ionics*, 2001, **140**, 191 – 199.

[246] H. Yoshida, T. Inagaki, K. Miura, M. Inaba and Z. Ogumi, *Solid State Ionics*, 2003, **160**, 109 – 116.

[247] S. Grieshammer, B. O. H. Grope, J. Koettgen and M. Martin, *Physical Chemistry Chemical Physics*, 2014, –.

[248] S. T. Norberg, S. Hull, S. G. Eriksson, I. Ahmed, F. Kinyanjui and J. J. Biendicho, *Chemistry of Materials*, 2012, **24**, 4294–4300.

[249] G. Balducci, J. Kašpar, P. Fornasiero, M. Graziani, M. S. Islam and J. D. Gale, *The Journal of Physical Chemistry B*, 1997, **101**, 1750–1753.

[250] R. Di Monte and J. Kašpar, *Topics in Catalysis*, 2004, **28**, 47–57.

[251] Z. Kang, *Journal of Alloys and Compounds*, 2006, **408-412**, 1103 – 1107.

[252] T. Wakita and M. Yashima, *Acta Crystallographica Section B*, 2007, **63**, 384–389.

[253] T. Omata, H. Kishimoto, S. Otsuka-Yao-Matsuo, N. Ohtori and N. Umesaki, *Journal of Solid State Chemistry*, 1999, **147**, 573 – 583.

[254] S. N. Achary, S. K. Sali, N. K. Kulkarni, P. S. R. Krishna, A. B. Shinde and A. K. Tyagi, *Chemistry of Materials*, 2009, **21**, 5848–5859.

[255] H. Otobe, A. Nakamura, T. Yamashita and K. Minato, *Journal of Physics and Chemistry of Solids*, 2005, **66**, 329 – 334.

[256] S. Otsuka-Yao-Matsuo, N. Izu, T. Omata and K. Ikeda, *Journal of The Electrochemical Society*, 1998, **145**, 1406–1413.

[257] J. B. Thomson, A. R. Armstrong and P. G. Bruce, *Journal of Solid State Chemistry*, 1999, **148**, 56 – 62.

[258] H.-F. Wang, Y.-L. Guo, G.-Z. Lu and P. Hu, *Angewandte Chemie International Edition*, 2009, **48**, 8289–8292.

[259] P. R. Shah, T. Kim, G. Zhou, P. Fornasiero and R. J. Gorte, *Chemistry of Materials*, 2006, **18**, 5363–5369.

[260] A. Kushima and B. Yildiz, *ECS Transactions*, 2009, **25**, 1599–1609.

[261] A. Kushima and B. Yildiz, *Journal of Materials Chemistry*, 2010, **20**, 4809–4819.

[262] E. Fabbri, D. Pergolesi and E. Traversa, *Science and Technology of Advanced Materials*, 2010, **11**, 054503.

[263] J. Santiso and M. Burriel, *Journal of Solid State Electrochemistry*, 2011, **15**, 985–1006.

[264] A. Orsini, P. Medaglia, S. Sanna, E. Traversa, S. Licoccia, A. Tebano and G. Balestrino, *Superlattices and Microstructures*, 2009, **46**, 223 – 226.

[265] S. Sanna, V. Esposito, D. Pergolesi, A. Orsini, A. Tebano, S. Licoccia, G. Balestrino and E. Traversa, *Advanced Functional Materials*, 2009, **19**, 1713–1719.

[266] S. Sanna, V. Esposito, A. Tebano, S. Licoccia, E. Traversa and G. Balestrino, *Small*, 2010, **6**, 1863–1867.

[267] M. Chu, Y. Sun, U. Aghoram and S. E. Thompson, *Annual Review of Materials Research*, 2009, **39**, 203–229.

[268] N. Sata, K. Eberman, K. Eberl and J. Maier, *Nature*, 2000, **408**, 946–949.

[269] D. Sayle, J. Doig, S. Parker and G. Watson, *Chemical Communications*, 2003, **15**, 1804–1806.

[270] S. Azad, O. A. Marina, C. M. Wang, L. Saraf, V. Shutthanandan, D. E. McCready, A. El-Azab, J. E. Jaffe, M. H. Engelhard, C. H. F. Peden and S. Thevuthasan, *Applied Physics Letters*, 2005, **86**, 131906.

[271] C. Korte, A. Peters, J. Janek, D. Hesse and N. Zakharov, *Physical Chemistry Chemical Physics*, 2008, **10**, 4623–4635.

[272] L. Chen, C. L. Chen, X. Chen, W. Donner, S. W. Liu, Y. Lin, D. X. Huang and A. J. Jacobson, *Applied Physics Letters*, 2003, **83**, 4737–4739.

[273] D. C. Sayle, S. A. Maicaneanu and G. W. Watson, *Journal of the American Chemical Society*, 2002, **124**, 11429–11439.

[274] D. Sayle, C. Catlow, N. Dulamita, M. Healy, S. Maicaneanu, B. Slater and G. Watson, *Molecular Simulation*, 2002, **28**, 683–725.

[275] C. E. Mohn, M. J. Stein and N. L. Allan, *Journal of Materials Chemistry*, 2010, **20**, 10403–10411.

[276] J. Garcia-Barriocanal, A. Rivera-Calzada, M. Varela, Z. Sefrioui, E. Iborra, C. Leon, S. J. Pennycook and J. Santamaria, *Science*, 2008, **321**, 676–680.

[277] D. Pergolesi, E. Fabbri, S. N. Cook, V. Roddatis, E. Traversa and J. A. Kilner, *ACS Nano*, 2012, **6**, 10524–10534.

[278] I. Kosacki, C. M. Rouleau, P. F. Becher, J. Bentley and D. H. Lowndes, *Solid State Ionics*, 2005, **176**, 1319 – 1326.

[279] N. Schichtel, C. Korte, D. Hesse and J. Janek, *Physical Chemistry Chemical Physics*, 2009, **11**, 3043–3048.

[280] M. Sillassen, P. Eklund, N. Pryds, E. Johnson, U. Helmersson and J. Bøttiger, *Advanced Functional Materials*, 2010, **20**, 2071–2076.

[281] T. X. T. Sayle, S. C. Parker and D. C. Sayle, *Journal of Materials Chemistry*, 2006, **16**, 1067–1081.

[282] X. Guo, *Science*, 2009, **324**, 465.

[283] X. Guo, *Scripta Materialia*, 2011, **65**, 96 – 101.

[284] K. Suzuki, M. Kubo, Y. Oumi, R. Miura, H. Takaba, A. Fahmi, A. Chatterjee, K. Teraishi and A. Miyamoto, *Applied Physics Letters*, 1998, **73**, 1502–1504.

[285] G. Dezanneau, J. Hermet and B. Dupé, *International Journal of Hydrogen Energy*, 2012, **37**, 8081 – 8086.

[286] T. Suzuki, I. Kosacki and H. U. Anderson, *Solid State Ionics*, 2002, **151**, 111 – 121.

[287] H. L. Tuller, *Solid State Ionics*, 2000, **131**, 143 – 157.

[288] A. Atkinson and T. Ramos, *Solid State Ionics*, 2000, **129**, 259 – 269.

[289] J. M. Perkins, S. Fearn, S. N. Cook, R. Srinivasan, C. M. Rouleau, H. M. Christen, G. D. West, R. J. H. Morris, H. L. Fraser, S. J. Skinner, J. A. Kilner and D. W. McComb, *Advanced Functional Materials*, 2010, **20**, 2664–2674.

[290] R. A. De Souza, A. Ramadan and S. Horner, *Energy Environ. Sci.*, 2012, 5445–5453.

[291] M. Rushton, A. Chroneos, S. Skinner, J. Kilner and R. Grimes, *Solid State Ionics*, 2013, **230**, 37 – 42.

[292] B. Li, J. Zhang, T. Kaspar, V. Shutthanandan, R. C. Ewing and J. Lian, *Physical Chemistry Chemical Physics*, 2013, **15**, 1296–1301.

[293] H. Nörenberg and G. Briggs, *Surface Science*, 1999, **424**, L352 – L355.

[294] M. Nolan, S. C. Parker and G. W. Watson, *Surface Science*, 2005, **595**, 223–232.

[295] J. Hinterberg, T. Zacherle and R. A. De Souza, *Physical Review Letters*, 2013, **110**, 205901.

[296] D. R. Ou, T. Mori, F. Ye, M. Takahashi, J. Zou and J. Drennan, *Acta Materialia*, 2006, **54**, 3737 – 3746.

[297] F. P. Koffyberg, *Physical Review B*, 1976, **13**, 4470.

[298] P. H. Jefferson, S. A. Hatfield, T. D. Veal, P. D. C. King, C. F. McConville, J. Zúñiga Pérez and V. Muñoz Sanjosé, *Applied Physics Letters*, 2008, **92**, 022101–3.

[299] S. Vasheghani Fahrahani, T. D. Veal, P. D. C. King, J. Zúñiga-Pérez, V. Mũnoz-Sanjoé and C. F. McConville, *Journal of Applied Physics*, 2011, **109**, 073712.

[300] X. Li, T. A. Gessert and T. Coutts, *Applied Surface Science*, 2004, **223**, 138–143.

[301] A. Wang, J. R. Babcock, N. L. Edleman, A. W. Metz, M. A. Lane, R. Asahi, V. P. Dravid, C. R. Kannewurf, A. J. Freeman and T. J. Marks, *Proceedings of the National Academy of Sciences of the United States of America*, 2001, **98**, 7113–7116.

[302] D. R. Kammler, B. J. Harder, N. W. Hrabe, N. M. McDonald, G. B. Gonzalez, D. A. Penake and T. O. Mason, *Journal of the American Ceramic Society*, 2002, **85**, 2345–2352.

[303] A. Cimino and M. Marezio, *Journal of Physics and Chemistry of Solids*, 1960, **17**, 57 – 64.

[304] A. Gulino and G. Tabbi, *Applied Surface Science*, 2005, **245**, 322–327.

[305] R. Haul and D. Just, *Journal of Applied Physics*, 1962, **33**, 487–493.

[306] C. G. Van de Walle, *Physical Review Letters*, 2000, **85**, 1012.

[307] S. F. J. Cox, J. S. Lord, S. P. Cottrell, J. M. Gil, H. V. Alberto, A. Keren, D. Prabhakaran, R. Scheuermann and A. Stoykov, *Journal of Physics: Condensed Matter*, 2006, **18**, 1061–1078.

[308] C. Kiliç and A. Zunger, *Applied Physics Letters*, 2002, **81**, 73–75.

[309] P. D. C. King, R. L. Lichti, Y. G. Celebi, J. M. Gil, R. C. Vilao, H. V. Alberto, J. P. Duarte, D. J. Payne, R. G. Egdell, I. McKenzie, C. F. McConville, S. F. J. Cox and T. D. Veal, *Physical Review B*, 2009, **80**, 081201–4.

[310] S. J. Clark, J. Robertson, S. Lany and A. Zunger, *Physical Review B*, 2010, **81**, 115311.

[311] A. K. Singh, A. Janotti, M. Scheffler and C. G. Van de Walle, *Physical Review Letters*, 2008, **101**, 055502–4.

[312] G. Kresse and D. Joubert, *Physical Review B*, 1999, **59**, 1758–1775.

[313] J. P. Perdew and A. Zunger, *Phys. Rev. B*, 1981, **23**, 5048–5079.

[314] J. Heyd and G. E. Scuseria, *Journal of Chemical Physics*, 2004, **121**, 1187–1192.

[315] J. Heyd and G. E. Scuseria, *The Journal of Chemical Physics*, 2004, **120**, 7274–7280.

[316] J. Heyd, J. E. Peralta, G. E. Scuseria and R. L. Martin, *Journal of Chemical Physics*, 2005, **123**, 174101.

[317] A. Walsh, J. L. F. Da Silva, Y. Yan, M. M. Al-Jassim and S. H. Wei, *Physical Review B*, 2009, **79**, 073105.

[318] S. Chen, Z. G. Gong, A. Walsh and S. H. Wei, *Appl Phys. Lett.*, 2009, **94**, 041903.

[319] J. Allen, D. Scanlon and G. Watson, *Physical Review B*, 2010, **81**, 161103.

[320] D. O. Scanlon and G. W. Watson, *Journal of Physical Chemistry Letters*, 2010, **1**, 3195–3199.

[321] B. G. Janesko, T. M. Henderson and G. E. Scuseria, *Physical Chemistry Chemical Physics*, 2009, **11**, 443–454.

[322] D. O. Scanlon and G. W. Watson, *Journal of Physical Chemistry Letters*, 2010, **1**, 2582–2585.

[323] J. E. Peralta, J. Heyd, G. E. Scuseria and R. L. Martin, *Physical Review B*, 2006, **74**, 073101.

[324] A. Stroppa and G. Kresse, *Physical Review B*, 2009, **79**, 201201(R).

[325] A. Stroppa and S. Picozzi, *Physical Chemistry Chemical Physics*, 2010, **12**, 5405–5416.

[326] D. O. Scanlon and G. W. Watson, *Journal of Materials Chemistry*, 2011, **21**, 3655.

[327] D. O. Scanlon and G. W. Watson, *Physical Review Letters*, 2011, **106**, 186403.

[328] F. Labat, P. Baranek, C. Domain, C. Minot and C. Adamo, *Journal of Chemical Physics*, 2007, **126**, 154703.

[329] B. J. Morgan, D. O. Scanlon and G. W. Watson, *e J. Surf. Sci. Nano Tech.*, 2009, **7**, 395–404.

[330] H. Raebiger, S. Lany and A. Zunger, *Physical Review B*, 2007, **76**, 045209.

[331] H. P. Singh and B. Dayal, *Solid State Comm.*, 1969, **7**, 725–726.

[332] A. Schleife, F. Fuchs, J. Furthmuller and F. Bechstedt, *Physical Review B*, 2006, **73**, 245212–14.

[333] L. F. J. Piper, A. DeMasi, K. E. Smith, A. Schleife, F. Fuchs, F. Bechstedt, J. Zuniga-Perez and V. Munoz-Sanjose, *Physical Review B*, 2008, **77**, 125204–4.

[334] R. Ferro, J. A. Rodríguez, M. Verstraete, V. Solomko and P. Bertrand, *physica status solidi (c)*, 2005, **2**, 3548–3551.

[335] I. N. Demchenko, J. D. Denlinger, M. Chernyshova, K. M. Yu, D. T. Speaks, P. Olalde-Velasco, O. Hemmers, W. Walukiewicz, A. Derkachova and K. Lawniczak-Jablonska, *Physical Review B*, 2010, **82**, 075107.

[336] C. McGuinness, C. B. Stagarescu, P. J. Ryan, J. E. Downes, D. Fu, K. E. Smith and R. G. Egdell, *Physical Review B*, 2003, **68**, 165104.

[337] A. Schleife, C. Rödl, F. Fuchs, J. Furthmüller and F. Bechstedt, *Physical Review B*, 2009, **80**, 035112–10.

[338] J. B. Varley, J. R. Weber, A. Janotti and C. G. V. de Walle, *Applied Physics Letters*, 2010, **97**, 142106.

[339] S. Lany and A. Zunger, *Physical Review Letters*, 2011, **106**, 069601.

[340] S. Limpijumnong, P. Reunchan, A. Janotti and C. G. Van de Walle, *Physical Review B*, 2009, **80**, 193202.

[341] A. Janotti and C. G. Van de Walle, *Nature Materials*, 2007, **6**, 44–47.

[342] P. D. C. King, I. McKenzie and T. D. Veal, *Applied Physics Letters*, 2010, **96**, 062110.

[343] P. D. C. King, T. D. Veal, P. H. Jefferson, J. Zúñiga Pérez, V. Muñoz Sanjosé and C. F. McConville, *Physical Review B*, 2009, **79**, 035203–5.

[344] J. Robertson and S. J. Clark, *Physical Review B*, 2011, **83**, 075205.

[345] Y. Z. Zhu, G. D. Chen, H. Ye, A. Walsh, C. Y. Moon and S.-H. Wei, *Physical Review B*, 2008, **77**, 245209–7.

[346] S. B. Zhang, *Journal of Physics: Condensed Matter*, 2002, **14**, R881.

[347] A. Janotti and C. G. Van de Walle, *Physical Review B*, 2007, **76**, 165202.

[348] A. A. Sokol, S. A. French, S. T. Bromley, C. R. A. Catlow, H. J. J. van Dam and P. Sherwood, *Farad. Discuss.*, 2007, **134**, 267–282.

[349] A. A. Sokol, A. Walsh and C. R. A. Catlow, *Chemical Physics Letters*, 2010, **492**, 44–48.

[350] K. G. Godinho, A. Walsh and G. W. Watson, *Journal of Physical Chemistry C*, 2008, **113**, 439–448.

[351] P. Agoston, C. Korber, A. Klein, M. J. Puska, R. M. Nieminen and K. Albe, *Journal of Applied Physics*, 2010, **108**, 053511.

[352] C. W. W. Hoffman, R. C. Ropp and R. W. Mooney, *Journal of the American Chemical Society*, 1959, **81**, 3830–3834.

[353] W. Walukiewicz, *App. Phys. Lett.*, 1989, **54**, 2094–2096.

[354] D. T. Speaks, M. A. Mayer, K. M. Yu, S. S. Mao, E. E. Haller and W. Walukiewicz, *Journal of Applied Physics*, 2010, **107**, 113706.

[355] P. D. C. King, T. D. Veal, C. F. McConville, J. Zúñiga-Pérez, V. Muñoz-Sanjosé, M. Hopkinson, E. D. L. Rienks, M. Fulsang Jensen and P. Hofmann, *Physical Review Letters*, 2010, **104**, 256803.

[356] L. F. J. Piper, L. Colakerol, P. D. C. King, A. Schleife, J. Zuniga-Perez, P.-A. Glans, T. Learmonth, A. Federov, T. D. Veal, F. Fuchs, V. Munoz-Sanjose, F. Bechstedt, C. F. McConville and K. E. Smith, *Physical Review B*, 2008, **78**, 165127–5.

[357] L. F. J. Piper, P. H. Jefferson, T. D. Veal, C. F. McConville, J. Zuniga-Perez and V. Munoz-Sanjose, *Superlattices and Microstructures*, 2007, **42**, 197–200.

[358] A. Janotti and C. G. V. de Walle, *Applied Physics Letters*, 2005, **87**, 122102.

[359] F. Oba, A. Togo, I. Tanaka, J. Paier and G. Kresse, *Physical Review B*, 2008, **77**, 245202.

[360] P. Ágoston, K. Albe, R. Nieminen and M. Puska, *Physical Review Letters*, 2009, **103**, 245501.

[361] A. B. Kehoe, D. O. Scanlon and G. W. Watson, *Physical Review B*, 2011, **83**, 233202.

[362] W. Walukiewicz, *Journal of Crystal Growth*, 1996, **159**, 244–247.

[363] W. Walukiewicz, *Physica B. Condens. Matt.*, 2001, **302-303**, 123–134.

[364] S. B. Zhang, S. H. Wei and A. Zunger, *Journal of Applied Physics*, 1998, **83**, 3192.

[365] S. B. Zhang, S. H. Wei and A. Zunger, *Physical Review Letters*, 2000, **84**, 1231–1235.

[366] H. Hosono, Y. Ogo, H. Yanagi and T. Kamiya, *Electrochem. Solid State Lett.*, 2011, **14**, H13–H16.

[367] A. Schleife, F. Fuchs, C. Rodl, J. Furthmuller and F. Bechstedt, *Appl Phys. Lett.*, 2009, **94**, 012104.

[368] B. Hoffling, A. Schleife, F. Fuchs, C. Rodl and F. Bechstedt, *Appl Phys. Lett.*, 2010, **97**, 032116.

[369] R. Asahi, A. Wang, J. Babcock, N. Edleman, A. Metz, M. Lane, V. Dravid, C. Kannewurf, A. Freeman and T. Marks, *Thin Solid Films*, 2002, **411**, 101 – 105.

[370] S. Jin, Y. Yang, J. E. Medvedeva, J. R. Ireland, A. W. Metz, J. Ni, C. R. Kannewurf, A. J. Freeman and T. J. Marks, *Journal of the American Chemical Society*, 2004, **126**, 13787–12793.

[371] Z. Zhao, D. L. Morel and C. S. Ferekides, *Thin Solid Films*, 2002, **413**, 203–211.

[372] M. Yan, M. Lane, C. R. Kannewurf and R. P. H. Chang, *Applied Physics Letters*, 2001, **78**, 2342–2344.

[373] O. Vigil, F. Cruz, A. Morales-Acevedo, G. Contreras-Puente, L. Vaillant and G. Santana, *Materials Chemistry and Physics*, 2001, **68**, 249–252.

[374] N. Ueda, H. Maeda, H. Hosono and H. Kawazoe, *Journal of Applied Physics*, 1998, **84**, 6174–6177.

[375] B. Saha, R. Thapa and K. Chattopadhyay, *Solid State Communications*, 2008, **145**, 33 – 37.

[376] L. F. J. Piper, T. D. Veal, I. Mahboob, C. F. McConville, H. Lu and W. J. Schaff, *Phys Rev. B*, 2004, **70**, 115333.

[377] L. F. J. Piper, T. D. Veal, C. F. McConville, H. Lu and W. J. Schaff, *Phys. Stat. Sol. C*, 2006, **3**, 1841–1845.

[378] P. D. C. King, T. D. Veal, P. H. Jefferson, S. A. Hatfield, L. F. J. Piper, C. F. McConville, F. Fuchs, F. J., F. Bechstedt, H. Lu and W. J. Schaff, *Physical Review B*, 2008, **77**, 045316.

[379] L. Colakerol, V. T. D., H. K. Jeong, L. Plucinski, A. DeMasi, T. Learmonth, P. A. Glans, S. Wang, Y. Zhang, L. F. J. Piper, P. H. Jefferson, A. Fedorov, T. C. Chen, T. D. Moustakas, C. F. McConville and K. E. Smith, *Physical Review Letters*, 2006, **97**, 237601.

[380] I. Mahboob, V. T. D., L. F. J. Piper, C. F. McConville, H. Lu, W. J. Schaff, J. Furthmüller and F. Bechstedt, *Physical Review B*, 2004, **69**, 201307(R).

[381] P. D. C. King, T. D. Veal, C. F. McConville, F. Fuchs, J. Furthmüller, F. Bechstedt, P. Schley, R. Goldhahn, J. Schormann, D. J. As, K. Lischka, D. Muto, H. Naoi, Y. Nanishi, H. Lu and W. J. Schaff, *Appl Phys. Lett.*, 2007, **91**, 092101.

[382] W. M. Linhart, T. D. Veal, P. D. C. King, G. Koblmuller, C. S. Gallinat, J. S. Speck and C. F. McConville, *Appl Phys. Lett.*, 2010, **97**, 112103.

[383] L. F. J. Piper, T. D. Veal, M. J. Lowe and C. F. McConville, *Physical Review B*, 2006, **73**, 195321.

[384] J. R. Weber, A. Janotti and C. G. Van de Walle, *App. Phys. Lett.*, 2010, **97**, 192106.

[385] L. O. Olsson, C. M. M. Andersson, M. C. Hakansson, J. Kanski and U. O. Ilver, L.a nd Karlsson, *Physical Review Letters*, 1996, **76**, 3626.

[386] P. D. C. King, T. D. Veal, D. J. Payne, A. Bourlange, R. G. Egdell and C. F. McConville, *Physical Review Letters*, 2008, **101**, 116808.

[387] P. D. C. King, T. D. Veal, A. Schleife, J. Zuniga-Perez, B. Martel, P. H. Jefferson, F. Fuchs, V. Muñoz Sanjose, F. Bechstedt and C. F. McConville, *Physical Review B*, 2009, **79**, 205205.

[388] Y. Dou, R. Egdell, T. Walker, D. Law and G. Beamson, *Surface Science*, 1998, **398**, 241 – 258.

[389] P. Srivastava and Y. Sarma, *Advanced Materials Letters*, 2011, **2**, 290 – 293.

[390] M. Kul, M. Zor, A. S. Aybek, S. Irmak and E. Turan, *Solar Energy Materials and Solar Cells*, 2007, **91**, 882 – 887.

[391] P. D. C. King and T. D. Veal, *Journal of Physics: Condensed Matter*, 2011, **23**, 334214.

[392] A. Dakhel and A. Ali-Mohamed, *Journal of Sol-Gel Science and Technology*, 2007, **44**, 241–247.

[393] A. Dakhel and A. Ali-Mohamed, *Materials Chemistry and Physics*, 2009, **113**, 356 – 360.

[394] B. Zheng, J. Lian, L. Zhao and Q. Jiang, *Applied Surface Science*, 2010, **256**, 2910 – 2914.

[395] R. Deokate, S. Salunkhe, G. Agawane, B. Pawar, S. Pawar, K. Rajpure, A. Moholkar and J. Kim, *Journal of Alloys and Compounds*, 2010, **496**, 357 – 363.

[396] R. Ferro, J. A. Rodríguez, O. Vigil and A. Morales-Acevedo, *Materials Science and Engineering B*, 2001, **87**, 83–86.

[397] R. Ferro and J. A. Rodríguez, *Thin Solid Films*, 1999, **347**, 295–298.

[398] R. Ferro, J. Rodríguez, J. Rickards, J. Cañetas Ortega and R. Trejo-Luna, *Revista mexicana de física*, 2008, **54**, 364 – 367.

[399] K. K. C. P. K. Ghosh, R. Maity, *Solar Energy Materials and Solar Cells*, 2004, **81**, 279–289.

[400] H. Y. Xu, Y. C. Liu, R. Mu, C. L. Shao, Y. M. Lu, D. Z. Shen and X. W. Fan, *Applied Physics Letters*, 2005, **86**, 123107.

[401] Y.-J. Choi and H.-H. Park, *J. Mater. Chem. C*, 2014, **2**, 98–108.

[402] Z. Hu, J. Zhang, Z. Hao, Q. Hao, X. Geng and Y. Zhao, *Applied Physics Letters*, 2011, **98**, 123302.

[403] D. O. Scanlon, *Physical Review B*, 2013, **87**, 161201.

[404] N. D. M. Hine, K. Frensch, W. M. C. Foulkes and M. W. Finnis, *Phys. Rev. B*, 2009, **79**, 024112.

[405] S. Lany and A. Zunger, *Modelling and Simulation in Materials Science and Engineering*, 2009, **17**, 084002.

[406] S. Jin, Y. Yang, J. E. Medvedeva, L. Wang, S. Li, N. Cortes, J. R. Ireland, A. W. Metz, J. Ni, M. C. Hersam, A. J. Freeman and T. J. Marks, *Chemistry of Materials*, 2008, **20**, 220–230.

[407] A. Dakhel, *Solar Energy*, 2008, **82**, 513 – 519.

[408] R. Maity and K. Chattopadhyay, *Solar Energy Materials and Solar Cells*, 2006, **90**, 597–606.